Cosmic Ray Energy Spectrum and Mass Composition Measurement with the Telescope Array Low energy Extension Detector in Hybrid Mode

（**TALE**実験ハイブリッド検出器による
宇宙線のエネルギースペクトルと質量組成測定）

理学研究科

数物系専攻

令和**3**年度

Keitaro Fujita

(藤田 慧太郎**)**

Abstract

The origin and nature of cosmic rays are still unclear, even more than a century has passed since their discovery. Cosmic rays are observed in an energy range from below 10^{8} eV up to greater than 10^{20} eV. The most probable origins of cosmic rays are supernova remnants, and most of cosmic rays observed up to $10^{15} - 10^{17}$ eV are believed to be produced and accelerated in our Galaxy. It is generally thought that heavier components are more abundant in cosmic rays with increasing energies because heavier nuclei are more likely to be accelerated in particle acceleration. The observation data up to 10^{16} eV support this idea. On the other hand, at the energies above about 10^{18} eV they are believed to be originated in extragalactic sources, such as active galactic nuclei or gamma ray bursts. The Telescope Array (TA) experiment, which is observing the ultra high energy cosmic rays ($E > 10^{18}$ eV), has reported that lighter components like the protons are dominated in cosmic rays with energies greater than $10^{18.2}$ eV, and this is consistent with models of extragalactic origin of ultra-high energy cosmic rays. For these reasons, it is suggested that the mass composition of cosmic rays drastically changes around 10^{17} eV, which corresponds to the change of cosmic rays from the galactic to extragalactic components. The Telescope Array Low energy Extension (TALE) experiment was designed to extend the energy threshold of the TA measurement down to 10^{16} eV to focus on the energy region where is considered to be the transition from galactic to extragalactic origin.

The TALE has a hybrid air shower detector for observations of air showers induced by cosmic rays in the atmosphere. The TALE consists of a Fluorescence Detector (FD) station with 10 telescopes located adjacent to the TA Middle Drum FD Station (comprised of 14 telescopes) and a Surface Detector (SD) array comprised of 80 scintillation counters, including 40 of which at 400 m spacing and the other 40 at 600 m spacing. In this thesis, approximately 2 years of the TALE hybrid data are analyzed to measure the cosmic ray energy spectrum and mass composition in the energy range from $10^{16.6}$ eV to $10^{18.4}$ eV. The measured average mass of cosmic rays above $10^{16.6}$ eV first increases up to 10^{17} eV, and and decreases in higher energies. The energy spectrum of cosmic rays also exhibits a change at 10^{17} eV where the power-law index changes from -2.8 to -3.3. These features at around 10^{17} eV may indicate the end of the galactic cosmic ray flux and the start of the transition to extragalactic sources.

Acknowledgements

Firstly, I would like to express my appreciation to my supervisor Professor Shoichi Ogio[1], for the opportunity to be part of the Telescope Array collaboration, and for his continuous support, thoughtful guidance, and encouragement. A special gratitude I give to Associate Professor Yoshiki Tsunesada[1] for his many helpful advice, and tremendous supports.

I would like to thank all of the Telescope Array collaborators for their great help with the science work and pleasant days. I am grateful to Professor Masaki Fukushima[2] and Professor Hiroyuki Sagawa[2] for their great management and for giving me the opportunity to participate in the Telescope Array experiment.

I wish to offer my deep gratitude to Program-specific Assistant Professor Toshihiro Fujii[3], Lecturer Yuichiro Tameda[4], and Assistant Professor Daisuke Ikeda[5] . They have been done the pioneering work on developing the analysis software package for fluorescence detectors, and also they have given me great supports and advice. I would like to thank Assistant Professor Takayuki Tomida[6] for his various support and helpful advice. I would also like to thank Assistant Professor Masahiro Takeda, Assistant Professor Toshiyuki Nonaka[2], Assistant Professor Takeshi Okuda[7], [2], and Dr. Eiji Kido[8] for their important advice and learning the experimental technique at the Telescope Array site, Utah, and the Akeno observatory. I am also grateful to Associate Professor Takashi Sako[2], Assistant Professor Kazumasa Kawata[2], and Associate Professor Shigeharu Udo[5] for their valuable advice and helpful comments.

I would also like to express my gratitude to Lecturer Tareq Abu Zayyad[9] and Dr. JiHee Kim[10] for their helpful discussions and cross-checking of my analysis. I would also like to acknowledge with appreciation to Professor Charles Jui[10], Research Professor John N. Matthews[10], Professor Pierre Sokolsky[10], Professor Gordon Thomson[10], Associate Professor Douglas Bergman[10], Dr. Greg Furlich[10] and Mr. Mathew Potts[10] for their precious discussions, helpful comments, and their kindly support at Utah.

Telescope Array is supported by many staff members that help with issues both technical and administrative work. Without their support, neither this work nor any other would be possible. These people include Mr. Gary McDonough, Mr. Frank Misak, Mr. Jeremy Smith, Research Assistant Professor Robert Cady, Mr. Stan Thomas, Mr. Dave Barr, and Mr. Adrian Baum.

As the past and present members of our laboratory, I would like to thank Dr. Jihyun Kim, Dr. Rosa Mayta Palacios, Dr. Bok Kyun Shin, Ms. Mieko Katsumura, Ms. Haruka Yokota, Mr. Ryota Onogi, Mr. Yuichi Takahashi, Mr. Shoichi Kishigami, Mr. Ryosuke Sahara, Mr. Yoshinori Takagi, Mr. Yugo Omura, Mr. Hiroyuki Oda, Mr. Yuta Tanoue, Mr. Ryota Fujiwara, Mr. Kei Nakai, Mr. Hiroyuki Matsumiya, Ms. Satsuki Koga, Mr. Koki Sato, Mr. Yuto Arai, Mr. Ryosuke Tsuda, Mr. Ryo Fukushima, Mr. Yusuke Kimura, Mr. Ryuhei Arimura, Ms. Aoi Iwasaki, Ms. Misaki Nishioka, Mr. Ichiro Komae, Mr. Jun Shikita, and Mr. Hirofumi Fujimoto for their pleasant communications and encouragements. Especially, Dr. Jihyun Kim, Dr. Rosa Mayta Palacios, Mr. Ryosuke Sahara, Mr. Yugo Omura, and Mr. Ryota Fujiwara gave me many things and shared amazing times in my research life. As the collaborators of other institutes including graduated students, I'm grateful to Mr. Terutsugu Seki, Mr. Mashu Yamamoto, Mr. Ryo Nakamura, Mr. Taichi Inadomi, Mr. Hirokazu Iwakura, Mr. Takafumi Uehama, Mr. Kengo Sano, Mr. Yuya Nakamura, Mr. Yuto Kubota, Mr. Heungsu Shin, Mr. Ryo Higuchu, Mr. Kozo Fujisue, Mr. Fugo Yoshida, Ms. Saori Kasami, Mr. Hyomin Jeong, Mr. Sang Woo Kim, and Mr. Kwangho Lee for their pleasant communications and delightful time in various places.

I gratefully acknowledge the valuable financial support by JST SPRING, Grant Number JPMJSP2139, and a scholarship supported by the Graduate School of Science, Osaka City University. I also gratefully thank the contributions of the computing system at the Institute for Cosmic Ray Research (ICRR), University of Tokyo.

Finally, I am deeply grateful to my family, especially Reiko Fujita for numerous supports and encouragement. I would also like to thank my dear friends for their pleasant communications and encouragement.

[1] *Graduate School of Science, Osaka City University, Osaka, Osaka, Japan*
[2] *Institute for Cosmic Ray Research, University of Tokyo, Kashiwa, Chiba, Japan*
[3] *The Hakubi Center for Advanced Research and Graduate School of Science, Kyoto University, Kitashirakawa-Oiwakecho, Sakyo-ku, Kyoto, Japan*
[4] *Department of Engineering Science, Faculty of Engineering, Osaka Electro-Communication University, Neyagawa-shi, Osaka, Japan*
[5] *Faculty of Engineering, Kanagawa University, Yokohama, Kanagawa, Japan*
[6] *Information Engineering Graduate School of Science and Technology, Shinshu University, Nagano, Nagano, Japan*
[7] *Department of Physical Sciences, Ritsumeikan University, Kusatsu, Shiga, Japan*
[8] *Astrophysical Big Bang Laboratory, RIKEN, Wako, Saitama, Japan*
[9] *Department of Physics, Loyola University Chicago, Chicago, Illinois, USA*
[10] *High Energy Astrophysics Institute and Department of Physics and Astronomy, University of Utah, Salt Lake City, Utah, USA*

The Telescope Array experiment is supported by the Japan Society for the Promotion of Science(JSPS) through Grants-in-Aid for Priority Area 431, for Specially Promoted Research JP21000002, for Scientific Research (S) JP19104006, for Specially Promoted Research JP15H05693, for Scientific Research (S) JP15H05741, for Science Research (A) JP18H03705, for Young Scientists (A) JPH26707011, and for Fostering Joint International Research (B) JP19KK0074, by the joint research program of the Institute for Cosmic Ray Research (ICRR), The University of Tokyo; by the Pioneering Program of RIKEN for the Evolution of Matter in the Universe (r-EMU); by the U.S. National Science Foundation awards PHY-1404495, PHY-1404502, PHY-1607727, PHY-1712517, PHY-1806797, PHY-2012934, and PHY-2112904; by the National Research Foundation of Korea (2017K1A4A3015188, 2020R1A2C1008230, & 2020R1A2C2102800) ; by the Ministry of Science and Higher Education of the Russian Federation under the contract 075-15-2020-778, IISN project No. 4.4501.18, and Belgian Science Policy under IUAP VII/37 (ULB).

This work was partially supported by the grants of the joint research program of the Institute for Space-Earth Environmental Research, Nagoya University and Inter-University Research Program of the Institute for Cosmic Ray Research of University of Tokyo. The foundations of Dr. Ezekiel R. and Edna Wattis Dumke, Willard L. Eccles, and George S. and Dolores Doré Eccles all helped with generous donations. The State of Utah supported the project through its Economic Development Board, and the University of Utah through the Office of the Vice President for Research.

The experimental site became available through the cooperation of the Utah School and Institutional Trust Lands Administration (SITLA), U.S. Bureau of Land Management (BLM), and the U.S. Air Force. We appreciate the assistance of the State of Utah and Fillmore offices of the BLM in crafting the Plan of Development for the site. Patrick A. Shea assisted the collaboration with valuable advice and supported the collaboration's efforts. The people and the officials of Millard County, Utah have been a source of steadfast and warm support for our work which we greatly appreciate.

We are indebted to the Millard County Road Department for their efforts to maintain and clear the roads which get us to our sites. We gratefully acknowledge the contribution from the technical staffs of our home institutions. An allocation of computer time from the Center for High Performance Computing at the University of Utah is gratefully acknowledged.

Contents

Abstract **i**

Acknowledgements **ii**

1 Introduction **1**
- 1.1 Cosmic Rays 1
  - 1.1.1 Energy Spectrum 2
  - 1.1.2 Mass Composition 3
  - 1.1.3 Muon puzzle 5
  - 1.1.4 Anisotropy 6
  - 1.1.5 Galactic to Extragalactic origin 6
- 1.2 Recent Results of Cosmic Ray Measurements 7
- 1.3 Extensive Air Shower 14
  - 1.3.1 Air Shower Phenomenon 15
  - 1.3.2 Characteristic of EAS 17
- 1.4 Techniques for EAS Measurement 23
  - 1.4.1 Particle detection 23
  - 1.4.2 Photon detection 24

2 The Telescope Array Experiment **27**
- 2.1 TA Fluorescence Detector 27
- 2.2 TA Surface Detector Array 30
- 2.3 Telescope Array Low energy Extension (TALE) experiment 31
- 2.4 TALE Fluorescence Detector 32
  - 2.4.1 Telescope and Optics 32
  - 2.4.2 PMT Camera 36
  - 2.4.3 Readout Electronics and Trigger 38
  - 2.4.4 Calibration 41
- 2.5 TALE Surface Detector Array 42
  - 2.5.1 Detector 42
  - 2.5.2 SD Trigger 43
  - 2.5.3 Hybrid Trigger 45
  - 2.5.4 Monitoring 48
- 2.6 Atmospheric Monitoring 50
  - 2.6.1 Atmospheric parameters 51
  - 2.6.2 Atmospheric Attenuation 52
  - 2.6.3 Cloud 54

3 Monte Carlo Simulation **55**
- 3.1 Extensive Air Shower Generation 55
  - 3.1.1 CORSIKA air shower simulation 55
- 3.2 Detector Simulation for the Surface Detectors 56
  - 3.2.1 Dethinning Method 56

3.2.2 Energy Deposition . . . 57
3.2.3 SD Array Response . . . 59
3.3 Detector Simulation for the Fluorescence Detectors . . . 61
3.3.1 Fluorescence Light Emission . . . 61
3.3.2 Cherenkov Light Emission . . . 62
3.3.3 Scattered Light . . . 62
3.3.4 Photon Ray-tracing . . . 64

4 Event Reconstrution 67
4.1 SD Pre Analysis . . . 67
4.2 FD Pre Analysis . . . 68
4.3 Shower Geometry Reconstruction . . . 73
4.3.1 Estimation of the Field of View for Each PMT . . . 74
4.3.2 Shower Detector Plane Determination . . . 76
4.3.3 Hybrid Geometry Fit . . . 77
4.4 Shower Profile Reconstruction . . . 79
4.4.1 X_{max} Determination . . . 79
4.4.2 N_{max} Determination . . . 79
4.4.3 Energy Determination . . . 80
4.5 Profile Constrained Geometry Fit . . . 82
4.6 Event Examples . . . 83
4.7 Resolutions in the Hybrid Mode . . . 84
4.7.1 Monte Carlo Simulation Conditions . . . 85
4.7.2 Quality Cuts . . . 85
4.7.3 Detector Resolutions . . . 86

5 Data Analysis 91
5.1 Data Set . . . 91
5.2 Event Distribution . . . 91
5.3 Time Difference between FD and SD . . . 94
5.4 Data / MC Comparison . . . 94
5.5 Mass Composition . . . 99
5.5.1 $\langle X_{\mathrm{max}} \rangle$ vs. $\log_{10}(E/\mathrm{eV})$ . . . 99
5.5.2 X_{max} Distributions . . . 102
5.6 Energy Spectrum . . . 106
5.6.1 Detector Aperture . . . 107
5.6.2 Detector Exposure . . . 108
5.6.3 Energy Spectrum . . . 109
5.7 Systematic Uncertainties . . . 111
5.7.1 Detector . . . 111
5.7.2 Fluorescence Yield . . . 113
5.7.3 Cherenkov Model . . . 115
5.7.4 Atmospheric Parameters . . . 116
5.7.5 Missing Energy Correction . . . 119
5.7.6 Total Systematic Uncertainties . . . 119
5.8 Comparison with Other Measurements . . . 121
5.8.1 Energy Spectrum Measurements . . . 121
5.8.2 Mass Composition Measurements . . . 122

6 Conclusions 125

A X_{max} distributions with mixture composition fit 127

Bibliography 131

List of Figures

1.1 The cosmic ray spectra with various experiments, available at [2]. . . . 1
1.2 The cosmic ray spectrum measured by various experiments multiplied by $E^{2.6}$ in order to emphasize the knee, the 2nd knee, and the ankle [3]. 2
1.3 $X_{\rm max}$ distributions for proton and iron primaries with energy of $10^{16.5}$ eV (*left*), and of $10^{18.5}$ eV (*right*) simulated by CORSIKA with the hadronic interaction model, QGSJETII-04 [4]. 4
1.4 The averaged $X_{\rm max}$ measured with non-imaging Cherenkov detectors (Tunka, Yakutsk, CASA-BLANCA), and with fluorescence detectors(HiRes/MIA, HiRes, Auger, TA) compared with air shower simulations using the different hadronic interaction models [5]. 4
1.5 Muon measurements converted to the z-scale described in Eq. 1.3. Since the scale depends on the hadronic interaction model, the plots for the different six models are shown. Estimation with Post-LHC models are shown in the top panel, and that with older models are in the bottom panel. The error bars show statistical and systematic uncertainties added in quadrature. Energy scales have been adjusted by a relative calibration. Expectations for z from $X_{\rm max}$ measurements are also shown with a dashed line with a grey band [7]. 5
1.6 Cosmic ray flux map in the equatorial coordinates, observed by Pierre Auger Observatory. Color counters show the cosmic ray flux above 8 $\times 10^{18}$ eV smoothed with a 45 ° radius circle. The galactic center is shown with an asterisk and the galactic plane is shown by a dashed line. [8] 6
1.7 *Left*: Shaded regions show the overlapping contributions of the three populations. *Right*: Mean ln$A$ predicted by several assumptions (H4a, H3a, Global fit, and Global fit with population 4, which contain additional extra-galactic protons) are shown [12]. 7
1.8 The KASCADE array and the KASCADE-Grande array layout [14]. . . 8
1.9 Schematic view of the KASCADE and the KASCADE-Grande stations [14]. 9
1.10 The cosmic ray energy spectra measured by KASCADE-Grande. The black triangles and gray squares show the all particle spectra. Circles show heavy primary spectrum with systematic band indicated by blue shade. Inverted triangles show light primary spectrum with systematic band indicated by red shade [15]. 9
1.11 *Left*: the detector arrangement of the Yakutsk array. Charged particle detectors (open circles), Cherenkov light detectors (filled circles and filled triangles) and the muon detectors (squares) are shown. *Right*: The photo of Cherenkov detector [18]. 10

1.12 The measurements by Yakutsk experiment. *Left*: Cosmic ray energy spectrum (multiplied by E^3). *Right*: The energy dependence of the cosmic ray mass composition. The QGSJETII-03 [19] hadronic interaction model was used in the estimation of $\langle \ln A \rangle$ from measured $X_{\max}$ (conversion of $\langle X_{\max} \rangle$ to $\langle \ln A \rangle$ is discussed in Sec. 5.8.2). 10
1.13 Layout of the Tunka array [20]. 11
1.14 The measurements by Tunka experiment. *Left*: Energy spectrum (multiplied by E^3). *Right*: The energy dependence of the mass composition. Unlike the previous Yakutsk group, the QGSJETII-04 [4] hadronic interaction model was used in the estimation of $\langle \ln A \rangle$ from measured $X_{\max}$. 11
1.15 IceCube Neutrino Observatory with the in-ice array, its sub-array DeepCore, and the cosmic ray air shower array IceTop [23]. 12
1.16 *Left*: All particle energy spectrum (multiplied by E^3) measured by IceTop. Gray band represents the systematic uncertainties. *Right*: Mean $\ln A$ measured by IceTop. Gray band represents the systematic uncertainties [24]. 12
1.17 *Left*: The black points indicate the combined TA energy spectrum [25]. Red points indicate the TALE fluorescence monocular measurement, and blue points are the TA surface detector measurement. *Right*: The $\langle X_{\max} \rangle$ measurement by the TA hybrid detector, shown as black points, compared with the Monte Carlo prediction of QGSJetII-04 hadronic interaction model [11]. Gray band shows systematic band. 13
1.18 *Left*: The Pierre Auger Observatory layout. Each dot corresponds to one of the 1660 surface detector stations. The four fluorescence detector sites are shown, each with the field of view of its six telescopes. The Coihueco site hosts three extra high elevation (HEAT) telescopes. The 750 m array is located a few kilometers from Coihueco [29]. *Right – Top*: FD building at Los Leones site [30]. *Right – Bottom*: One of the SD stations in the Auger site. [29]. 14
1.19 *Left*: Cosmic ray energy spectrum (multiplied by E^3) measured by different five techniques in Pierre Auger Observatory, the 1500 m array using vertical events, inclined events, hybrid events, events detected by the 750 m array and the FD events dominated by Cherenkov light [27]. *Right*: Mean $X_{\max}$ measured by Auger comparing with the predictions for proton and iron MC with the hadronic interaction models of EPOS-LHC [31], Sibyll 2.3c [32] and QGSJetII-04, taken from [28]. . . 14
1.20 Schematic view of the secondary particles generated by a primary cosmic ray proton. Pions and Kaons are produced by the hadron multiple production. The decay of $\pi^0 \to \gamma + \gamma$ initiates electromagnetic cascades. The decay of $\pi^\pm \to \mu^\pm + \nu$ generates muon components of EAS. 16
1.21 The Heitler model [36] for the electromagnetic component cascade. Every steps after the propagation of radiation length, here is λ, the number of particles in the electromagnetic cascade doubles, and the amount of energy per particle decreases in half. 17

1.22 Simulated air shower longitudinal profiles as a function of atmospheric depth in g/cm^2. Black lines indicated proton primary air showers. Red dashed lines indicated iron primary air showers. The variability of iron curves are smaller than proton ones because the cross section of iron nucleus is larger than proton one and electromagnetic cascades initiated by each nuclei are superposed and averaged for iron case. Taken from [37]. 18
1.23 Average air shower behavior of lateral distribution at the ground and longitudinal shower profile of each component, for vertical proton-induced showers at 10^{19} eV, taken from [42]. 19
1.24 Relative fluorescence intensities between about 300 and 430 nm. The sum of the fluorescence yield in this wavelength range differs by -1.66% (Ulrich et al.), by +2.08% (Nagano et al. [47]), and by -1.7% (FLASH [44]) compared to the sum of the fluorescence yield obtained by AIRFLY [48]. Taken from [43]. 20
1.25 The mean ionization loss rate α_{eff} as obtained from CORSIKA simulations is shown for vertical showers of different primary energies and particles (10^{17}, 10^{18}, 10^{19} eV, and proton, iron). The fit is given by Eq. 1.20. Taken from [46]. 21
1.26 Angular distribution of produced Cherenkov photons with respect to the shower axis in a single CORSIKA shower for s = 0.8, 1.0, and 1.2. The Monte Carlo results are compared to the parameterisation, Eq. 1.25. Taken from [46]. 22
1.27 Comparison of the parameterisation Eq. 1.26 and the electron energy spectra of an individual shower obtained with CORSIKA, proton, 10^{19} eV. Taken from [46]. 23
1.28 Visualization for (A) Stereo Observation and (B) Hybrid Observation. The black points indicate the positions of fluorescence telescope and the white squares are the positions of each surface detector. The color represents the relative time difference and time evolve from violet to red. The marker size indicate the number of fluorescence photons / air shower particles. In Fig. (A), both Fluorescence Telescope 1 and Fluorescence Telescope 2, which far 36 km from telescope 1, observed a air shower. Fig. (B) shows that the Fluorescence Telescope and a dozen of surface detectors detected a air shower signals simultaneously. Both events are recorded by the Telescope Array. 25

2.1 Satellite map of the Telescope Array experiment site. Centered roughly around 112.9° W, 39.3° N. The Locations of the TA SDs are shown as red diamonds and the locations of the three TA FD stations are indicated by blue hexagons. Magenta diamonds show the location of the TALE SDs. The TALE fluorescence telescopes are located at the MD site. 28
2.2 *Left*: A photo of Black Rock Mesa fluorescence station. These are three bays, each with four telescopes. The Long Ridge fluorescence station is same structure as BRM station. *Right*: A photo of Middle Drum fluorescence telescopes. 28
2.3 The schematic outline of the MD electronics. The PMT signal is split into discriminator (filter) and delay lines in Channel A and B, and checks if a subcluster level and mirror level trigger conditions are sequentially met. 29

2.4 Trigger patterns of TA SD. The trigger will be issued when any three adjacent SDs with greater than 3 MIP are coincident within 8 μs. 30

2.5 The Telescope Array detectors. Each TA SD location is indicated by white squares and each communication tower location is indicated by black triangles. Dashed line region represents each sub array. The location of the CLF is labeled by the star. The arrows originated from each FD station are represented the edge of FD field of view. In addition, each FD filed of view is plotted beside of location of FD with same color. Northwest array, which is near from MD station, is the TALE SD array. 31

2.6 The layout of the TALE detector. Open square boxes represent the locations of the TALE SD counters and small filled circle correspond to the MD / TALE FD station. The arrows represent azimuthal viewing ranges of both FDs. 32

2.7 Photo of the TA MD (left) and TALE FD (right) building. 33

2.8 Photo of the TALE telescopes. Left one is ring 4 telescope (#17), and right one is ring 3 telescope (#18). Each telescope has the clover-shaped spherical mirror, the black box shaped PMT camera, which supported by orange stands and connected to the electronics crate located at center of both mirrors. 34

2.9 An example event observed with both the TA MD and the TALE FD telescopes. Color represents relative differences of timing detected by each PMT. Marker size represents the number of photons detected by each PMT. 34

2.10 The TA MD (top) and the TALE FD (bottom) mirror reflectance as a function of wavelength. 35

2.11 Photo of a cluster of PMTs with the UV filter at bottom. 36

2.12 Photo of a PMT (Phillips XP3062/FL model) used in the TALE camera. The HV divider and preamplifier are built in, and are stored in the aluminum shield shown in the upper part of the photo. 36

2.13 Top: The UV filter transmittance as a function of wavelength. Bottom: The quantum efficiency of PMT (Phillips XP3062/FL model) as a function of wavelength. 37

2.14 The tube response profile of EMI 9974KAFL model and Phillips XP3062/FL model. Note that the hexagonal shape of the tube is clearly seen in the projection. Phillips XP3062/FL model have a 10 % larger acceptance than EMI 9974KAFL model. 38

2.15 Photo of electronics crates used in the TALE FD. The electronics for two adjacent telescopes are stored in one electronics crate. 39

2.16 Photos of (A): the FADC board and (B): the Trigger/Host board. 16 FADC boards and one trigger/host board are used in each one telescope. A brown shield protects the amplifier and digitization modules for each channel on the left of the FADC board. 40

2.17 Schematic view of the 3-fold coincidence. It is composed of AND circuits and OR circuits. First, each channel has performed the logical AND between itself and the logical OR of the next two channels. This process has done for other channel sets then generate 15 sets of 2-fold coincidence. Same processes has performed for 15 sets of 2-fold coincidence, then judges whether one of 3-fold coincidence are satisfied or not. 40

2.18 An example of the 3-fold coincidence. The channels of 1,2,4 drawn with solid line receive the discrimination signal as high, other dashed lines are represented the discrimination signal as low. This example satisfies the 3-fold coincidence, then the detector trigger is issued. . . . 41
2.19 Photo of the RXF module. The black box contains the Xenon flash lamp itself. The black cylinder at the front of the RXF contains the optical filters (band pass and narrow band). The grey box below the black box contains the electronics for charging and firing the RXF flash lamp. 42
2.20 Photo of the UVLED module mounted at center of TALE mirror. 42
2.21 Photo of the TALE Surface Detector. The TA MD / TALE buildings are seen far from this SD. 43
2.22 Photo of the Middle Drum Communication Tower. The batteries and electronics that controls the TALE SD DAQ are installed at the back side of the solar panels. The wireless antenna to communicate with the SDs is install at the top of steel tower. 44
2.23 (A): Schematic view of the Surface Detector, 1 - Wireless communication antenna, 2 - GPS receiver, 3 - Battery and electronics box, 4 - Solar panel, 5 - Iron roof, 6 - Supporting metal frame. (B) Schematic view of inside of the SD. The wavelength shifting fibers are on the scintillation layers and collected to the PMT face. Each layer are separated by 1mm thick stainless steel. 44
2.24 Event display of an event detected by the TALE SD self trigger. This event was observed on November 07th 2018. On the left is a map of the TALE SD detector with the detector number. The size of the colored circles are proportional to the number of particles detected by the SD and its color shows the arrival timing. The corresponding detector waveforms are shown in the right panel, with an information of total signal in unit of MIP. The Lv. 2 trigger was issued because the SD5608, 5609, 6510, 5508 and 5611 exceeded the threshold of 3 MIP within 32 μs. 46
2.25 The TALE FD event display of an hybrid trigger event example. The size of the colored circles is proportional to the number of photons detected by the PMT and its color shows the arrival timing. The total time duration of this event is less than 500 ns, as shown in right side of color bar. 47
2.26 The TALE SD event display of an event detected by the hybrid trigger. The size of the colored circles on the left plot are proportional to the number of particles detected by the SD and its color shows the arrival timing. The corresponding detector waveforms are shown in the right panel, with an information of total signal in unit of MIP. Only one detector (SD5501) detected the signal above three MIP, then this event was detected by not the SD self trigger, but the hybrid trigger. 47
2.27 Cumulative plots of the observation time as black line and the number of hybrid events at the trigger level as blue line. Left panel are plotted the period before the hybrid trigger installation, and right panel are plotted after installation. Light blue shade in left plot is represents the test period of the hybrid trigger system. The number of hybrid events clearly increase by the hybrid trigger system. 48

2.28 An example of the monitor data for the TALE SD (DET5503). From top to bottom, (1): the GPS status, (2): the communication status between the DAQ PC and this SD, (3): the battery and solar panel status, (4): the temperatures of each measurement points, (5): the pedestal average and standard deviation for upper and lower layers, (6): the single muon histogram's peak for upper and lower layers, and (7): Lv. 0 and Lv.1 trigger rate. 49
2.29 Pedestal and single muon histograms obtained by DET5503. Logarithm scale in upper panel, and same plots but linear scale with narrow range in x axis in bottom panel. Left plots are obtained by the upper layer, and right plots show the lower layer. Narrow distributions in each panels indicate the pedestal histograms, and wider one shows the single muon histograms. Fit results are shown with green curves. 50
2.30 Location relations of the TA site and the GDAS grid, and the radiosonde measurement sites. Star mark indicates the adopted location by the TA measurement. 51
2.31 A picture is LIDAR's optical system (telescope, laser, etc). 53
2.32 Results of the TA LIDAR measurement. Left: the histogram of VAOD 5 km above from the ground. Left: Median of the VAOD as a function of the height above the ground level. The systematic errors and the one σ region of its histogram are also shown [78]. 53

3.1 *Left*: Illustration of the problem caused by the thinning approximation. Dashed lines represent the discarded particles (which would exist in a real shower) and the solid lines represent the weighted particles (thicker lines correspond to larger weights). The surface detector counters are represent by black rectangle at the bottom of figure. *Right*: Illustration of the dethinning algorithm. Taken from [86]. 57
3.2 The energy deposited per counter as a function of the distance from shower core. Simulated air shower initiated by a 10^{19} eV primary proton cosmic ray with a zenith angle of 45° are used. The 10^{-6} level thinned shower is shown in left, and the dethinned shower is shown in right. Both are compared with non-thinned shower. Taken from [87]. 57
3.3 Configuration of the detector and the injected particle used in generating the SD response by the GEANT4 simulation. For each particle, X, Y are the randomly chosen coordinates inside the 6 m $\times$ 6 m square, θ is the (given) zenith angle, and ϕ is the azimuthal angle with randomly chosen . Arrow represents the direction of the injecting particle. 58
3.4 The structure of TA / TALE SD implemented in our simulation software. The components inside of scintillation box are shifted upward to see clearly. 58
3.5 Examples of the energy deposition histograms. X-axis represents the energy deposition in the upper layer, Y-axis represents the energy deposition in the lower layer, and Z-axis (represented by colors) is the frequency. The examples use 1 GeV μ^+ and 1 GeV γ: (a): μ^+ at $\theta = 0°$, (b): μ^+ at $\theta = 60°$, (c): γ at $\theta = 0°$, (d): γ at $\theta = 60°$. 60
3.6 The phase function of the fraction of scattered light plotted as a function of scattering angle. It is used as the scattering phase function. . . . 63
3.7 The structure of TALE FD implemented in our simulation software. . . 64

3.8 The number of fluorescence, Cherenkov, Rayleigh and Mie scattered photons injected into the telescopes. The top panel shows in case of the shower geometry across the F.O.V of telescopes, the bottom panel shows in case of the geometry going toward the FD. 66

4.1 Examples of the SD signals. The dashed lines indicate the edges of the pulses. The horizontal lines represent average pedestal level. 68
4.2 Typical waveforms recorded by the TALE FD. The air shower signal detected by the TALE FD PMT is shown in left panel, and the noise signal is shown in right panel. 69
4.3 The schematic diagram of the weighted triangle filter. 69
4.4 The distribution of significance calculated by the triangle filter fitting. Left panel shows the distribution without air shower signal, right is one with air shower signal. 70
4.5 *Left*: The shower image with the central line of the shower image calculated by the Hough transform represented by magenta line. *Right*: the separation angle β distribution For this example, The PMTs, which are 4° far from the central line, are removed. 71
4.6 Shower track in left panel and timing fit to search for the noise PMT in right. The isolated PMT at (-2.5°, 19 μs) is rejected. 72
4.7 Event display observed by FD comparing before(left) and after(right) PMT selections. The noise PMTs indicated by cross markers are removed by the PMT selection. 73
4.8 Shower detector plane (SDP) with the shower axis and the detector location [89]. 74
4.9 The field of view of all PMTs in the telescope #15 at TALE FD. Color bar represents the sensitivity calculated by ray-trace simulation. 75
4.10 The field of view of each PMTs located at center, edge and corner. Color bar represents the sensitivity calculated by ray-trace simulation. 76
4.11 The schematics of the monocular and the hybrid shower geometry reconstruction. The relations between the measured values, α_i, and the fitting parameters, which are $t_{\rm core}$, $r_{\rm core}$ and ψ, are shown. In the hybrid geometry reconstruction, the parameter $t_{\rm core}$ can be removed by two observables, $t_{\rm SD}$ and $r_{\rm SD}$, as a result the number of the fitting parameter is reduced to two and the shower geometry determination accuracy is improved. 78
4.12 The geometry reconstruction for the same event in hybrid mode (blue fit) and the monocular mode (red fit). The triangle indicates the SD information and the color points are the measured FD data which color represents the arrival time from early (purple) to late (red). 78
4.13 An observed air shower signal and the shower signals estimated by the IMC fitting are shown. The observed data are indicated by points with error bar. The red area shows the contribution of fluorescence light, the blue area represents the Cherenkov light, the purple and green areas shows scattered light of Rayleigh and Mie process, respectively. 80
4.14 Ratio of the calorimetric energy and the total energy as a function of the calorimetric energy. 81

4.15 Fluctuations of χ^2_{geo}, χ^2_{pfl}, and χ^2_{com} for each X_{max} trial as a function of ψ. The best fit values are shown in bottom left in each figure. A trial with ψ = 126.78°, X_{max} = 600 g/cm^2 has a minimum χ^2_{com} among all trials. MC thrown values are 126.615° in ψ, and 585 g/cm^2 in X_{max}, and the best fit by stand alone hybrid geometry fit is ψ = 123.78°. . . . 83

4.16 High energy fluorescence event observed by both the Middle Drum and TALE hybrid detectors. *Left*: SD display. Reconstructed shower direction by hybrid mode is indicated by magenta arrow and crossed point is the reconstructed shower core position. *Top − Right*: FD display. The line fit for the SDP (black line) is overlaid. *Bottom − Middle*: Hybrid geometry fit. The blue triangle makers are FD PMT timing and inverted triangle are SD timing. The red inverted triangle is a detector which is used in Eq. 4.18. *Bottom − Right*: Reconstructed shower profile with relative contributions of fluorescence light, Cherenkov light and scattered light. 84

4.17 One-telescope low energy Cherenkov event. *Left*: SD display. *Top − Right*: FD display. *Bottom − Middle*: Hybrid geometry fit. *Bottom − Right*: Reconstructed shower profile. 84

4.18 Core location distribution of Monte Carlo showers. 85

4.19 TALE Hybrid zenith angle θ reconstruction resolution histograms by evaluating $(\theta_{\text{recon}} - \theta_{\text{thrown}})$. 87

4.20 TALE Hybrid azimuthal angle ϕ angle reconstruction resolution histograms by evaluating $(\phi_{\text{recon}} - \phi_{\text{thrown}}) \cdot \sin\theta_{\text{thrown}}$ 87

4.21 TALE Hybrid impact parameter, R_p, resolution histograms by evaluating $(R_{p\ \text{recon}} - R_{p\ \text{thrown}})/R_{p\ \text{thrown}}$. 88

4.22 TALE Hybrid ψ angle reconstruction resolution histograms by evaluating $(\psi_{\text{recon}} - \psi_{\text{thrown}})$. 88

4.23 TALE Hybrid X_{max} angle reconstruction resolution histograms by evaluating $(X_{\text{max recon}} - X_{\text{max thrown}})$. 89

4.24 TALE Hybrid energy resolution histograms by evaluating $(E_{\text{recon}} - E_{\text{thrown}})/E_{\text{thrown}}$. 89

5.1 TALE Hybrid detector on-time. The vertical dashed gray lines show the dates of the TALE Hybrid data epoch starts. 92

5.2 TALE Hybrid wighted MC event distributions. Left two figures are corresponding to the epoch 1 conditions, which means both the FD and SD operate independently. Right two figures are corresponding to the epoch 2 conditions. 92

5.3 Distribution of the number of data events. Each energy bin size is 0.1 in log scale. These data events are passed after quality cuts and are used in the energy spectrum calculation. 93

5.4 The result of the comparison with the reconstructed shower axis both by the TALE hybrid and TALE monocular reconstruction for the same events. Red points show the mean values of the opening angle distribution. Blue points show one sigma region which includes 68% of the distribution. 94

5.5 TA MD + TALE Hybrid Data/MC Comparisons for # of photo-electrons. 95

5.6 TA MD + TALE Hybrid Data/MC Comparisons for # of PMTs / track-length. 95

5.7 TA MD + TALE Hybrid Data/MC Comparisons for inverse angular speed. 95

5.8 TA MD + TALE Hybrid Data/MC Comparisons for Maximum detected MIP by SD. 96
5.9 TA MD + TALE Hybrid Data/MC Comparisons for number of clustered SDs. 96
5.14 TA MD + TALE Hybrid Data/MC Comparisons for core location of West-East direction. 96
5.10 TA MD + TALE Hybrid Data/MC Comparisons for R_p. 97
5.11 TA MD + TALE Hybrid Data/MC Comparisons for ψ angle. 97
5.12 TA MD + TALE Hybrid Data/MC Comparisons for zenith angle θ. . . 97
5.13 TA MD + TALE Hybrid Data/MC Comparisons for azimuthal angle ϕ. 98
5.15 TA MD + TALE Hybrid Data/MC Comparisons for core location of South-North direction. 98
5.16 TA MD + TALE Hybrid Data/MC Comparisons for X_{max}. 98
5.17 TA MD + TALE Hybrid Data/MC Comparisons for reconstructed energy. 99
5.18 Scatter plot of X_{max} as a function of $\log_{10}(E/\text{eV})$ for all data or MC events that passed the quality cuts. The points with error bar indicate the mean X_{max} in each bin. 100
5.19 TALE Hybrid composition result: the $\langle X_{\text{max}} \rangle$ as a function of energy with the proton and iron MC rails. The gray points are a scatter plot of the observed X_{max}. The black data points with error bars represent the mean X_{max} values binned by energy. The red rail is the fitted line to the proton MC mean X_{max} values (from Fig. 5.18), while the blue rail is the fitted line to the iron MC mean X_{max}. 100
5.20 The observed mean X_{max} fitted by the single line and the broken line function. 101
5.21 X_{max} distribution for data and proton MC and iron MC for energy greater than $10^{16.6}$ eV and less than $10^{17.0}$ eV. In each figure, the data is shown with points, proton MC is filled by red, and iron MC is filled by blue. 102
5.22 X_{max} distribution for data and proton MC and iron MC for energy greater than $10^{17.0}$ eV and less than $10^{17.4}$ eV. In each figure, the data is shown with points, proton MC is filled by red, and iron MC is filled by blue. 103
5.23 X_{max} distribution for data and proton MC and iron MC for energy greater than $10^{17.4}$ eV and less than $10^{17.8}$ eV. In each figure, the data is shown with points, proton MC is filled by red, and iron MC is filled by blue. 103
5.24 X_{max} distribution for data and proton MC and iron MC for energy greater than $10^{17.8}$ eV and less than $10^{18.4}$ eV. In each figure, the data is shown with points, proton MC is filled by red, and iron MC is filled by blue. 104
5.25 The results of KS tests for X_{max} distributions comparison with from the data and proton and iron MC. The horizontal line shows the p-value = 0.05; values below this line indicates incompatible of both data X_{max} distribution and MC one. The observed X_{max} are inconsistent with pure proton and pure iron predictions except for the highest energy bin of proton one. 104
5.26 Example of mixture component fit. The observed X_{max} distribution in energy range of $10^{16.9}$ eV $< E <$ $10^{17.0}$ eV compared with mixture of proton and iron. 105

5.27 Fitted fraction and quality for the scenario with mixture of protons and iron nuclei. The upper panel shows the fractions of each component for each energy bin, and the lower panel shows the p-values obtained by chi-square tests. 106
5.28 The calculated aperture as a function of the energy. *Top*: the TA MD + TALE hybrid detector aperture considering epoch 1 condition. *Bottom*: the TA MD + TALE hybrid detector aperture considering epoch 2 condition. In both figures, red points show the aperture assuming the pure proton primary, and blue points indicate the one of assuming the pure iron primary. 107
5.29 The iron fraction predicted by the H4a model [12]. 108
5.30 The combined exposure over the time period of 11/2017-02/2021. The bottom panel shows the relative differences in the exposure to proton, iron and H4a assumption with respect to the 50 % proton + 50 % iron mixture. The proton and iron points are shifted slightly to allow for greater visibility. 109
5.31 Cosmic ray spectrum measured by the TA MD + TALE hybrid detector. The spectrum has been multiplied by E^3. 110
5.32 The measured energy spectrum fitted by two types of power-law function. Solid line with magenta color in both figures show each power law fitting. 110
5.33 TALE hybrid cosmic ray energy spectrum comparison with measurements by the TALE FD monocular mode [26], by the TA using the FDs at Black Rock Mesa, Long Ridge [96] and Middle Drum [97] sites, and by the TA SD [25]. 111
5.34 Reconstructed energy comparison if the relative timing difference is assumed ± 25 ns shifted from nominal value. Left histograms show the difference for whole energies. Right scatter plots show the differences as a function of energy. 112
5.35 Reconstructed X_{max} comparison if the relative timing difference is assumed ± 25 ns shifted from nominal value. 113
5.36 Reconstructed energy comparison with the fluorescence yield ± 11 % shifted from nominal value. 114
5.37 Reconstructed X_{max} comparison with the fluorescence yield ± 11 % shifted from nominal value. 114
5.38 Angular distribution of Cherenkov photons comparison of Nerling et al. [46], Giller & Wieczorek [101] and Baltrusaitis et al. [102] description. Parameterizations with the shower age = 1, height = 5 km are shown in both description. 115
5.39 Reconstructed energy and X_{max} comparison with Nerling et al. [46] and Giller & Wieczorek [101] Cherenkov model 116
5.40 Reconstructed energy comparison with the VAOD shifted $^{+0.025}_{-0.015}$ from nominal value. 117
5.41 Reconstructed X_{max} comparison with the VAOD shifted $^{+0.025}_{-0.015}$ from nominal value. 117
5.42 Reconstructed energy comparison with the radiosonde atmospheric profile. 118
5.43 Reconstructed X_{max} comparison with the radiosonde atmospheric profile. 118
5.44 Missing energy correction assuming the H4a composition model [12]. . 119

5.45 Systematic uncertainties in the energy scale as a function of energy. Quadratic sum of all contributions are presented. 120
5.46 Systematic uncertainties in $X_{\max}$ as a function of energy. Quadratic sum of all contributions are presented 120
5.47 TALE hybrid energy spectrum with systematic band. For comparison, TALE monocular mode [26], IceTop [24], Yakutsk [16], KASCADE-Grande [15], and Auger Cherenkov-dominated data [104] results are shown. 121
5.48 TALE hybrid $\langle X_{\max} \rangle$ with systematic band. For comparison, 8.5 yrs TA BRM/LR hybrid [11], 7 yrs TA MD hybrid [106], HiRes/MIA [107], and Auger [28] results are shown. The Auger data are take from public data page on [108]. 122
5.49 $\langle \ln A \rangle$ measured by the TALE hybrid detector with systematic band. For comparison, two interpretations by KASCADE [109], IceTop [24], Tunka [21], Yakutsk [110], Auger [28], and 8.5 yrs TA BRM/LR hybrid [11] results are shown. 123

A.1 $X_{\max}$ distribution for data and mixture of proton MC and iron MC for energy greater than $10^{16.6}$ eV and less than $10^{17.0}$ eV. In each figure, the data is shown with points, the mixture fit is shown by solid line with red filled proton MC and blue filled iron MC. 127
A.2 $X_{\max}$ distribution for data and mixture of proton MC and iron MC for energy greater than $10^{17.0}$ eV and less than $10^{17.4}$ eV. In each figure, the data is shown with points, the mixture fit is shown by solid line with red filled proton MC and blue filled iron MC. 128
A.3 $X_{\max}$ distribution for data and mixture of proton MC and iron MC for energy greater than $10^{17.4}$ eV and less than $10^{17.8}$ eV. In each figure, the data is shown with points, the mixture fit is shown by solid line with red filled proton MC and blue filled iron MC. 128
A.4 $X_{\max}$ distribution for data and mixture of proton MC and iron MC for energy greater than $10^{17.8}$ eV and less than $10^{18.4}$ eV. In each figure, the data is shown with points, the mixture fit is shown by solid line with red filled proton MC and blue filled iron MC. 129

List of Tables

2.1 The MD telescope serial numbers are listed with corresponding the HiRes-II mirror serial numbers, the HiRes-I electronics serial numbers, PMT manufacturer, and ring numbers. 30
2.2 The TALE telescope serial numbers are listed with corresponding the HiRes mirror serial numbers, the HiRes-II electronics serial numbers, PMT manufacturer, and ring numbers. The TALE telescope numbers are the sequential numbers from the MD telescope. 33

3.1 Summarized the CORSIKA input parameters 56
3.2 List of calibration data used in the SD simulation. 61

4.1 The criteria for categorizing the PMTs to SOFT and HARD classes. . . 73
4.2 The criteria of judgment by the linear fitting in the 4th PMT selection. . 73
4.3 Fit parameters of missing energy estimation for each primaries are summarized. 82
4.4 Quality Cuts applied in this study. 86
4.5 TALE hybrid event reconstruction resolutions. 86

5.1 Number of data events per each energy bin. These data events are used in calculating the energy spectrum. 93
5.2 Summary of the K-S tests probability performed to compare the TALE hybrid data to the proton and iron Monte Carlo sets. 105
5.3 Fit parameters of broken power law fit to the measured TA spectra. . . 111
5.4 Summary of systematic uncertainties in energy, X_{max} measurements. Lines with multiple entries represent the values at the low and high end of the considered energy range ($\simeq 10^{16.5}$ eV and $\simeq 10^{18.5}$ eV, respectively). 119
5.5 Fit parameters of broken power law fit by other measurements. 121

List of Abbreviations

Auger	Pierre **Auger** Observatory
BRCT	**B**lack **R**ock Mesa **C**ommunication **T**ower
BRM	**B**lack **R**ock **M**esa
CCD	**C**harge **C**oupled **D**evice
CLF	**C**entral **L**aser **F**acility
CORSIKA	**CO**smic **R**ay **SI**mulations for **KA**scade
CMB	**C**osmic **M**icrowave **B**ackground
DAQ	**D**ata **A**c**Q**uisition
EAS	**E**xtensive **A**ir **S**hower
FADC	**F**lash **A**nalog to **D**igital **C**onverter
FD	**F**uorescence **D**etector
FOV	**F**ield **O**f **V**iew
GDAS	**G**lobal **D**ata **A**ssimilation **S**ystem
GPS	**G**lobal **P**ositioning **S**ystem
GZK	**G**reisen **Z**atsepin **K**uzmin
HV	**H**igh **V**oltage
IACT	**I**maging **A**tmospheric **C**herenkov **T**elescope
ICRC	**I**nternational **C**osmic **R**ay **C**onference
IMC	**I**nverse **M**onte **C**arlo
KASCADE	**KA**rlsruhe **S**hower **C**ore and **A**rray **DE**tector
LIDAR	**LI**ght **D**etection **A**nd **R**anging
LR	**L**ong **R**idge
LRCT	**L**ong **R**idge **C**ommunication **T**ower
MC	**M**onte **C**arlo
MD	**M**iddle **D**rum
MDCT	**M**iddle **D**rum **C**ommunication **T**ower
MIP	**M**inumum **I**onization **P**article
NKG	**N**akamura **K**amata **G**reisen
PCGF	**P**rofile **C**onstrained **G**eometry **F**it
PMT	**P**hoto**M**ultiplier **T**ube
RXF	**R**oving **X**enon **F**lasher
SD	**S**urface **D**etector
SDP	**S**hower **D**etector **P**lane
SKCT	**S**melter **K**noll **C**ommunication **T**ower
SLC	**S**alt **L**ake **C**ity
SNR	**S**uper**N**ova **R**emnant
TA	**T**elescope **A**rray
TALE	**T**elescope **A**rray **L**ow energy **E**xtension
UHECR	**U**ltra **H**igh **E**nergy **C**osmic **R**ay
UV	**U**ltra **V**iolet
UVLED	**U**ltra **V**iolet **L**ight **E**mitting **D**iode
VAOD	**V**ertical **A**erosol **O**ptical **D**epth

Chapter 1

Introduction

1.1 Cosmic Rays

In 1912, V. F. Hess discovered cosmic rays which are high energy particles accelerated by astrophysical sources and travel in universe [1]. They are emitted from the Sun, from sources inside our Galaxy, and even from sources outside our Galaxy in the case of the highest energy cosmic rays. The observed cosmic rays energy range is quite broad, in energies from 10^8 eV to beyond 10^{20} eV, as shown in Fig. 1.1. Its arrival rate follows a simple power law, E^{-3}, which is shown by a green dashed line. Historically, there are two known spectral features, a "knee" and a "ankle", which are located at E $\sim 10^{15.6}$ eV and E $\sim 10^{18.7}$ eV, respectively.

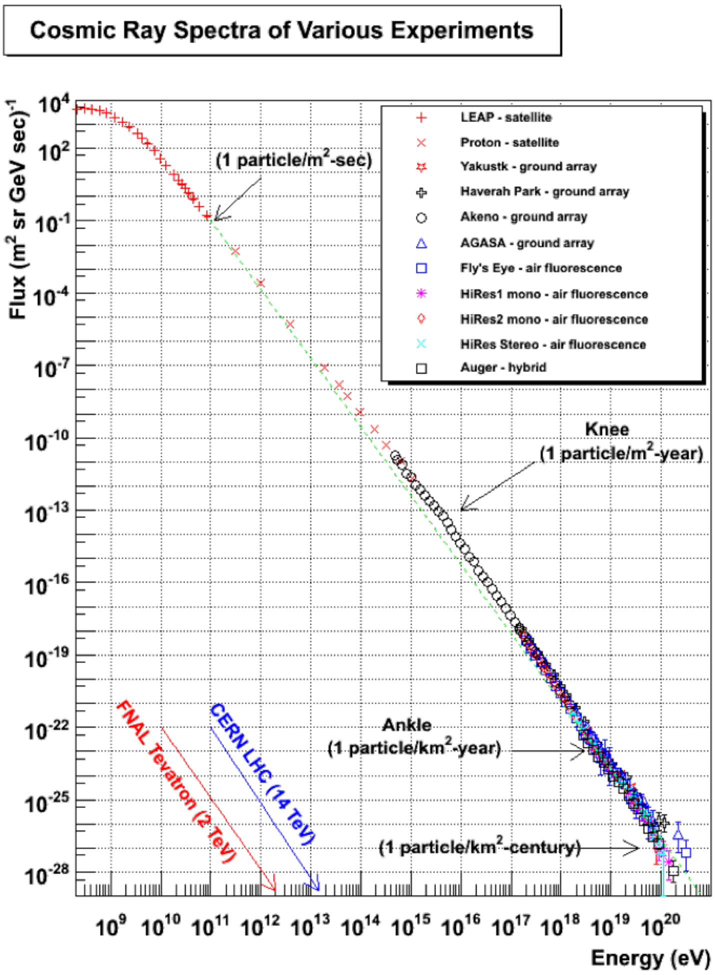

FIGURE 1.1: The cosmic ray spectra with various experiments, available at [2].

1.1.1 Energy Spectrum

In the energy range above 10^{11} eV, where cosmic rays are not affected the solar activity, cosmic ray energy spectrum approximately follows power low structure of $\mathrm{d}\Phi/\mathrm{d}E \propto E^{-\gamma}$, where γ is called a spectral index. The index value is changed from $\gamma \sim 2.7$ to $\gamma \sim 3$ at about $10^{15.6}$ eV, commonly called the knee structure. At around $\sim 10^{17}$ eV, there is a "2nd knee" structure at which the spectrum steepens to $\gamma \sim 3.2$, then harden again to $\gamma \sim 2.6$ at the ankle, about $10^{18.7}$ eV. Finally, the spectrum gets strongly suppressed above $10^{19.6}$ eV, as shown in Fig. 1.2.

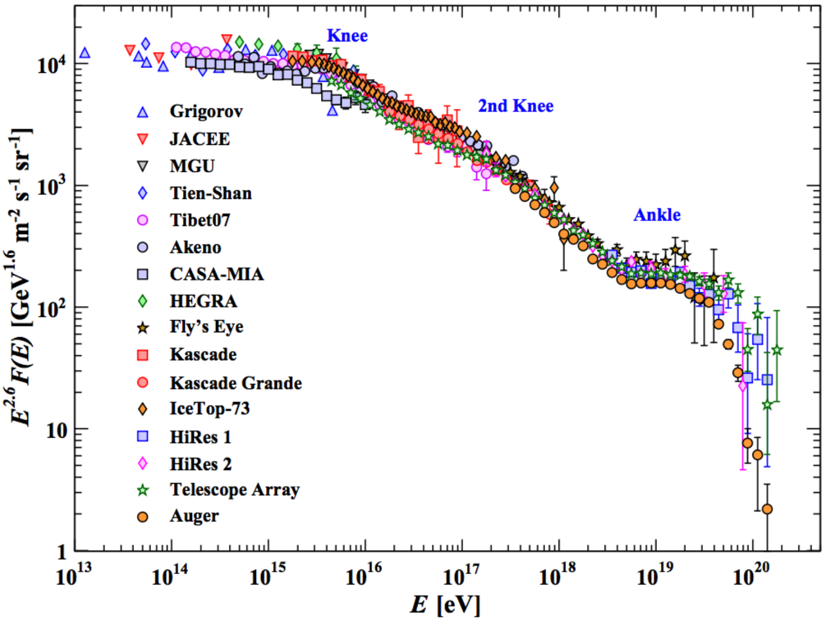

FIGURE 1.2: The cosmic ray spectrum measured by various experiments multiplied by $E^{2.6}$ in order to emphasize the knee, the 2nd knee, and the ankle [3].

Below the knee energy, the low energy cosmic rays are considered to be accelerated by Supernova Remnants (SNRs) in our galaxy. Indeed, the observed high energy gamma rays from several SNRs are considered to be initiated by interacting cosmic rays accelerated the SNR with the surrounding interstellar medium, or the cosmic ray electrons with photon fields.

The knee feature can be explained by the hypothesis the major production mechanism is different for the energies below and above it. The other scenario to explain the knee feature is the steepening of the light components of galactic cosmic rays. This behavior could be due to a limitation of acceleration at the sources or to a more efficient escape from our galaxy or both. In this hypothesis, the beginning of the light components of galactic cosmic rays steepening is expected as the knee energy E_k, where $E_\mathrm{k} \simeq 10^{15.6}$ eV. Both the cosmic ray acceleration at the sources as well as the diffusive propagation in our galaxy depend in general on the rigidities R of the particles, where $R = pc/eZ \simeq E/eZ$ with eZ being the charge of the particle with atomic number Z. Hence, for the charged nuclei case, they can be reached up to Z times higher energy than that of proton when they are accelerated or propagated in a magnetic field. In other words, cosmic ray protons are accelerated up to E_k and then their acceleration is cut off as they escape the sources. The next element, helium, continues and is accelerated until its energy reaches twice that of proton. This trend continues through galactic iron nuclei. So then this hypothesis also naturally explains the 2nd knee feature by the iron knee, and its energy is around $26 \times E_{\mathrm{k}} \sim 10^{17}$ eV. The high energy region, 10^{17} - 10^{18} eV, is expected a place where the transition from galactic cosmic rays to extragalactic cosmic rays, and where the mass composition changes from heavy nuclei to light nuclei with increasing energy.

There are two models for the ankle feature. One is that ankle feature corresponds to the transition from galactic to extragalactic origins. In this case, we expect to observe a anisotropy of the cosmic ray arrival direction on the galactic disk, and also expect that of the mass composition could be changed from heavy nuclei to light nuclei with increasing energy. Alternatively, in the other model the ankle is due to the energy loss of cosmic ray protons via pair production process, shown in Eq. 1.1, of the high energy cosmic ray protons interacting with the Cosmic Microwave Background (CMB) radiation photons.

$$p + \gamma_{\mathrm{CMB}} \rightarrow p + e^{+} + e^{-} \tag{1.1}$$

In this cace we expect the mass composition does not change and continues to dominate cosmic ray protons below and above the ankle.

At the highest energy, there are two hypothesises to explain the suppression feature. One is due to a limitation of acceleration at sources. Another hypothesis predicts that the cosmic ray spectrum drops down rapidly due to the Greisen, Zatsepin, and Kuzmin (GZK) effect. In the GZK model, protons with energy above 6×10^{19} eV interact with the CMB and lose their energy due to the process of photo-pion production shown in Eq. 1.2.

$$\begin{gathered} p + \gamma_{\mathrm{CMB}} \longrightarrow \Delta^{+} \longrightarrow p + \pi^{0} \\ \text{or} \\ p + \gamma_{\mathrm{CMB}} \longrightarrow \Delta^{+} \longrightarrow n + \pi^{+} \end{gathered} \tag{1.2}$$

The Ultra High Energy Cosmic Ray (UHECR) protons propagate through the interstellar medium and continuously experience the above processes. Thus, a theoretical upper limit on the propagation distance for UHECRs are estimated as $\sim$ 50Mpc.

1.1.2 Mass Composition

The mass composition of low energy cosmic rays are observed by direct measurements by experiments mounted on balloons or satellites. On the other hand, direct measurement gets impractical due to the low event rate for high energy cosmic rays. Therefore, the mass composition of cosmic rays is estimated by indirect measurements with obversing the extensive air shower induced by cosmic rays by ground-based telescopes or non-imaging Cherenkov detector arrays.

These ground-based experiments can observe the depth of the maximum at which the air shower particles achieve maximum number of charged particles, so called X_{max}. For a primary proton, one nucleon enters the Earth's atmosphere and interacts with atmospheric molecule, then initiates an air shower. The secondary particles from this first interaction will produce farther particles and the shower will grow. It reaches the maximum shower development when ionization losses dominate over secondary particle productions, and afterwards the number of air shower particles decreases. For a nuclei consisting of A (the mass number) nucleons, the energy per nucleon of the nuclei is smaller than that of a primary proton with same energy of per primary cosmic ray. Each nucleon has an energy E_0/A, where E_0 is primary particle's energy. In this case, the air shower development can be treat as superposition of individual showers initiated by nucleons with energy E_0/A. Since the depth of the shower maximum gets deep with increasing cosmic ray energy, the averaged X_{max} of heavier nuclei than proton are relatively smaller than proton primary at the same energy (Details are describe in Sec. 1.3.2). Moreover, the first interaction depth of heavier nuclei are also smaller than those of protons because their interaction cross sections are larger than that of proton. The difference appears in the depth of shower maximum as shown in Fig. 1.3. Based on these principles, we can evaluate the cosmic ray mass composition by X_{max} measurement indirectly.

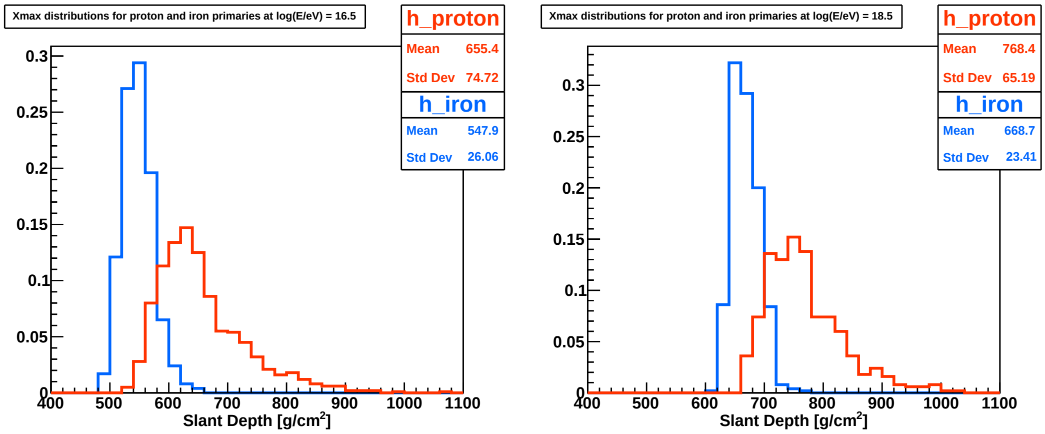

FIGURE 1.3: X_{max} distributions for proton and iron primaries with energy of $10^{16.5}$ eV (*left*), and of $10^{18.5}$ eV (*right*) simulated by CORSIKA with the hadronic interaction model, QGSJETII-04 [4].

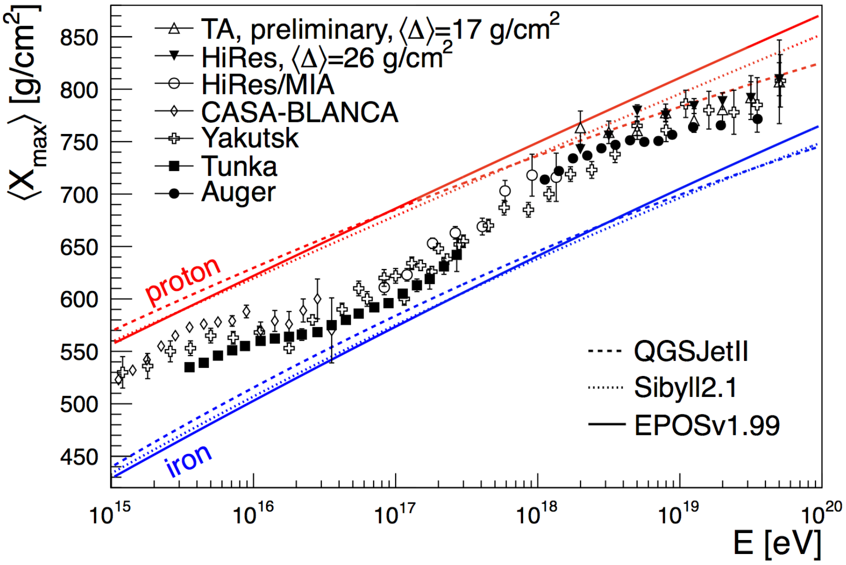

FIGURE 1.4: The averaged X_{max} measured with non-imaging Cherenkov detectors (Tunka, Yakutsk, CASA-BLANCA), and with fluorescence detectors(HiRes/MIA, HiRes, Auger, TA) compared with air shower simulations using the different hadronic interaction models [5].

1.1.3 Muon puzzle

In addition to the X_{max} measurements, the number of muons in the air shower can be used to estimate the mass composition of cosmic rays. The muon component is produced by mesons that produced by the hadron multiple productions, and the number of muons in the air shower is proportional to the mass number of primary, because the hadrons are major component of the primary. However, the observations have shown that the mass composition estimation from X_{max} and that from the number of muons do no agree, especially in the highest energy region. The problem lies in the number of muons predicted by air shower simulations. In order to compare the various measurements and the air shower simulations, Dembinski, H. P et al. [6] introduced the z-scale, which is written as,

$$z = \frac{\ln N_\mu - \ln N_\mu^{\text{proton}}}{\ln N_\mu^{\text{iron}} - \ln N_\mu^{\text{proton}}}, \tag{1.3}$$

where $\ln N_\mu$ is the logarithm of the measured muon abundance, and $\ln N_\mu^{\text{iron}}$ and $\ln N_\mu^{\text{proton}}$ are simulated values for proton and iron showers. Fig. 1.5 shows that the muon measurements above 10^{17} eV suggest a heavier mass composition than predictions of X_{max} measurements, and the averaged composition from muon measurements is heavier than iron. This discrepancy on muon measurements is called the Muon Puzzle.

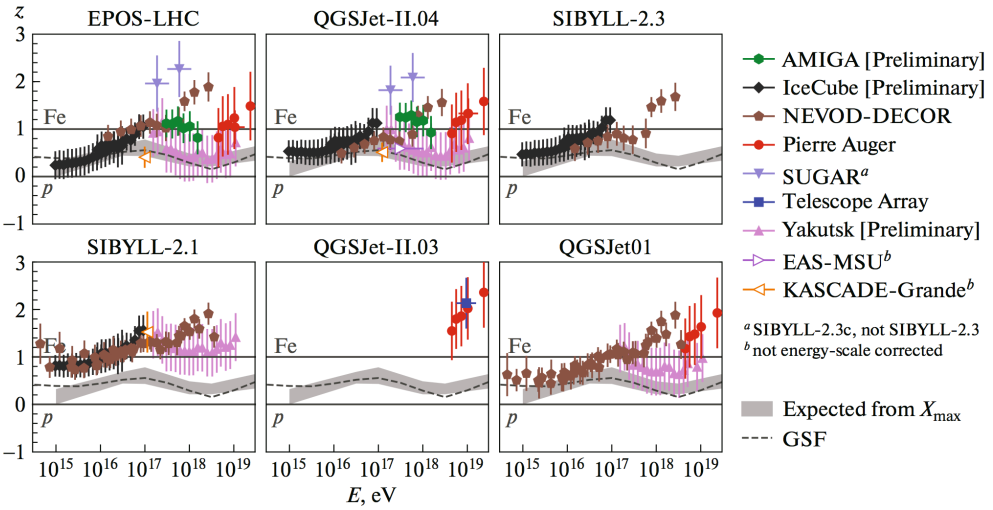

FIGURE 1.5: Muon measurements converted to the z-scale described in Eq. 1.3. Since the scale depends on the hadronic interaction model, the plots for the different six models are shown. Estimation with Post-LHC models are shown in the top panel, and that with older models are in the bottom panel. The error bars show statistical and systematic uncertainties added in quadrature. Energy scales have been adjusted by a relative calibration. Expectations for z from X_{max} measurements are also shown with a dashed line with a grey band [7].

1.1.4 Anisotropy

As noted in the Sec. 1.1.1, we assume that UHECRs come from outside of our galaxy. Possible sources are such as supermassive black holes in active galactic nuclei, jets and lobes of radio galaxies, galaxy clusters, starburst galaxies, gamma-ray bursts, and pulsars. Many experiments have studied the anisotropy for cosmic rays arrival direction and the correlation with possible sources. Here we briefly summarize the recent measurements of the UHECRs anisotropy.

Large Scale Anisotropy

The Pierre Auger Observatory reported a significant dipole anisotropy in arrival directions of cosmic rays with energies above 8 $\times 10^{18}$ eV, and they reported that the major axis of the dipole does not point to the galactic center, shown in Fig. 1.6. This result strongly suggests that UHECRs originate from outside of our galaxy.

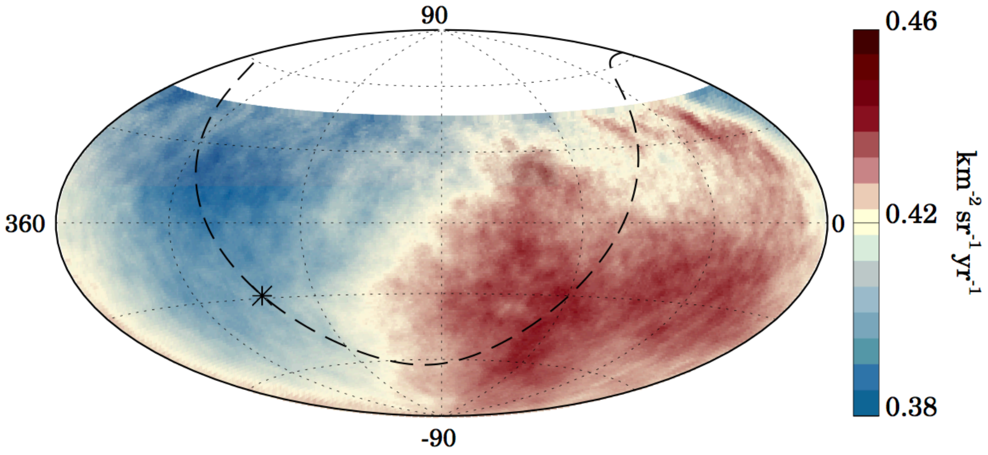

FIGURE 1.6: Cosmic ray flux map in the equatorial coordinates, observed by Pierre Auger Observatory. Color counters show the cosmic ray flux above 8 $\times 10^{18}$ eV smoothed with a 45 ° radius circle. The galactic center is shown with an asterisk and the galactic plane is shown by a dashed line. [8]

Intermediate Scale Anisotropy

An indication of the intermediate scale anisotropy on the arrival directions of UHECRs with energies above 57 EeV in the northern sky has been reported by the Telescope Array experiment using 5 years of data by the surface detector array [9]. Recently, they have also pointed out an indication of an event excess above $10^{19.4}$ eV, and its central direction is close to the Perseus-Pisces supercluster [10].

1.1.5 Galactic to Extragalactic origin

As described in Sec.1.1.1, the 2nd knee is assumed to be corresponding to the acceleration limit of galactic iron cosmic rays. In this hypothesis, cosmic rays around 2nd knee energy have important information that cosmic rays origin expect the transition from galactic to extragalactic. The major component in the higher energy than the 2nd knee is considered to be extragalactic protons. Indeed, the Telescope Array reports that the mass composition with energies from $10^{18.2}$ eV to 10^{19} eV is consistent with the proton component [11]. Therefore, we expect that the mass composition of cosmic rays is drastically changed at the 2nd knee from heavy component dominance to light component dominance with increasing cosmic ray energies. Moreover, The width of X_{max} distributions is expected to be widened because of the mixture of light and heavy components.

In Fig. 1.7, several models predicted by Gaisser et al. [12] are shown. In these models, it is divided the cosmic ray spectrum into three populations to describe the observed ones by various experiments. The first two populations represent cosmic rays from galactic sources and the third population is an extragalactic component. Each population contains several groups of nuclei except for the H4a model, which assumed population 3 as protons only. As first pointed out by Peters [13], in all populations, if cosmic rays reach a maximum energy, E_{max}, which can be accelerated in a source, then the protons will escape first, followed by helium, carbon, etc., according to

$$E_{\text{max}}(Z) = Z \times E_{\text{max}}^{\text{proton}}, \tag{1.4}$$

where Z is the charge of cosmic ray particle. The right panel of Fig. 1.7 shows the mean ln$A$ predictions by each model. As we see, the models with the assumption of protons in the highest energy region, which is the H4a and the Global fit with population 4, show a tendency of the mass composition changing from heavy dominant to light dominant in the energies from 10^{17} eV to 10^{18} eV.

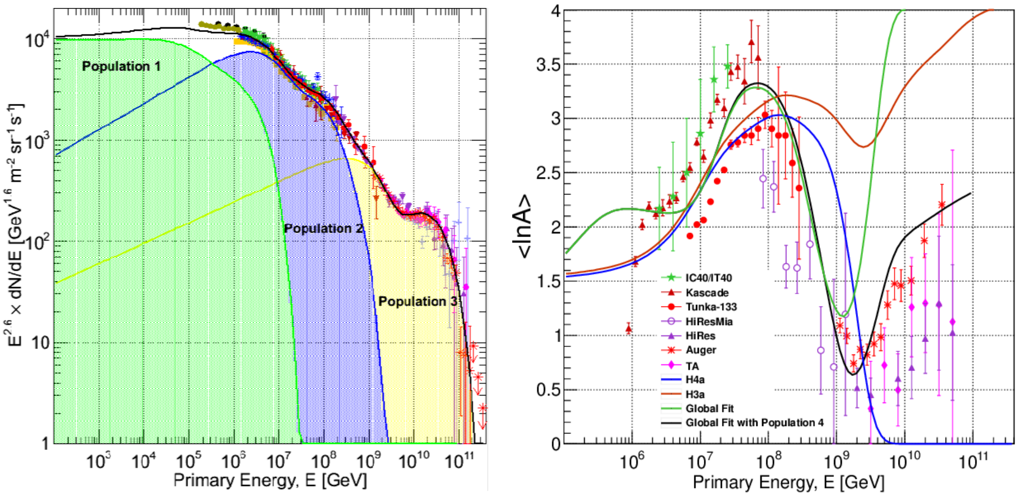

FIGURE 1.7: *Left*: Shaded regions show the overlapping contributions of the three populations. *Right*: Mean ln$A$ predicted by several assumptions (H4a, H3a, Global fit, and Global fit with population 4, which contain additional extra-galactic protons) are shown [12].

1.2 Recent Results of Cosmic Ray Measurements

These are several experiments that had been observed / are observing cosmic rays around the 2nd knee energy. However, we still have no consensus of the interpretation for the transition. Here we introduce these experiments and show recent results.

KASCADE-Grande experiment

The KASCADE-Grande experiment had been operated at the Karlsruhe Institute of Technology in Germany. The KASCADE-Grande consisted of a particle detector array made up of 37 scintillation detectors, which size is 10 m^2, with 137 m spacing, and a detection area was extended to 700 m × 700 m from KASCADE array. Also, KASCADE array consisted of 252 scintillator detectors of 3.2 m^2 spread over an area of 200 m × 200 m, a hadron calorimeter of 20 m × 16 m × 4 m, and a muon tracking detector of 128 m^2. The detectors and array configuration are shown in Fig. 1.8 and 1.9. The KASCADE-Grande experiment had been observed cosmic rays with energies from 10^{16} to 10^{18} eV from 1996 to 2009 [14]. On Fig. 1.10, the black triangles and gray squares indicate the all-particle spectra measured by KASCADE-Grande. They reported that the spectral index is changed from γ_1 = -2.95 ± 0.05 to γ_2 = -3.24 ± 0.08 with the break position at $\log_{10}(E/\mathrm{eV})$ = 16.92 ± 0.10. The group also reported the light and heavy primary spectra. This measurement is based on a ratio of the total number of charged particles (shower size N_{ch}) derived from the measurements of the Grande stations and the total number of muons (N_μ) derived from the measurements of the type-I KASCADE stations in the air shower. As noted in 1.1.3, the number of muons in the air shower is proportional to the mass number of primary, the ratio can be used to separate an electron-rich (light) group and an electron-poor (heavy) group. The measured spectra for both groups are also shown in Fig. 1.10. The change of the spectral index for the electron-poor group is from -2.76 ± 0.02 to -3.24 ± 0.05 with the break position at $\log_{10}(E/\mathrm{eV})$ = 16.92 ± 0.04, and for the electron-rich one is from -3.25 ± 0,05 to -2.79 ± 0,08 with the break position at $\log_{10}(E/\mathrm{eV})$ = 17.08 ± 0.08.

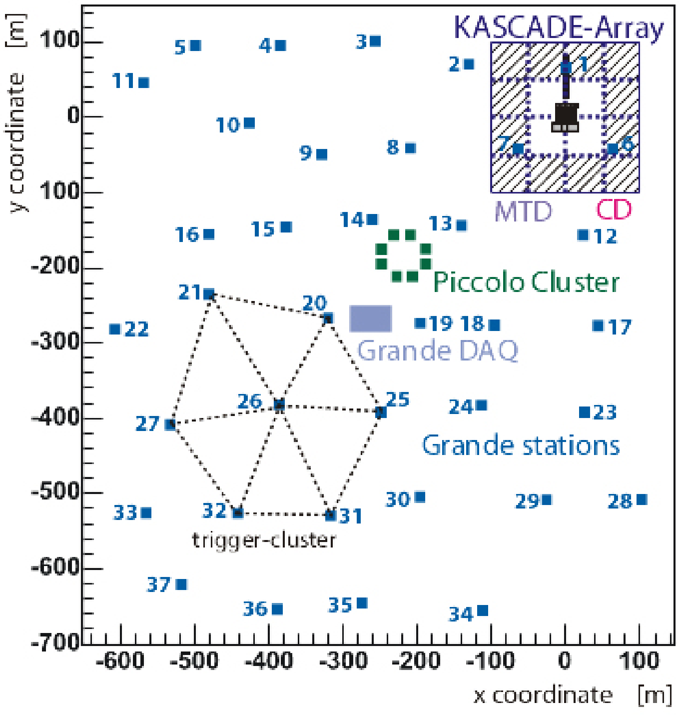

FIGURE 1.8: The KASCADE array and the KASCADE-Grande array layout [14].

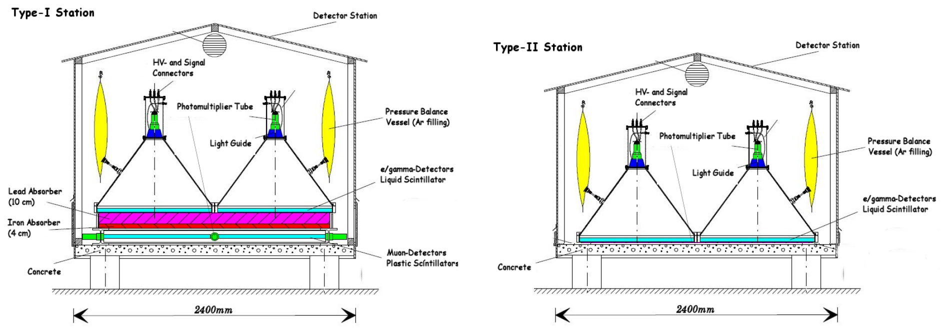

(A) Schematic view of the KASCADE Stations. The type-I stations were installed at nine shaded areas in the KASCADE array in Fig. 1.8. The type-II stations were installed at the center of the KASCADE array indicated as four white squares in Fig. 1.8.

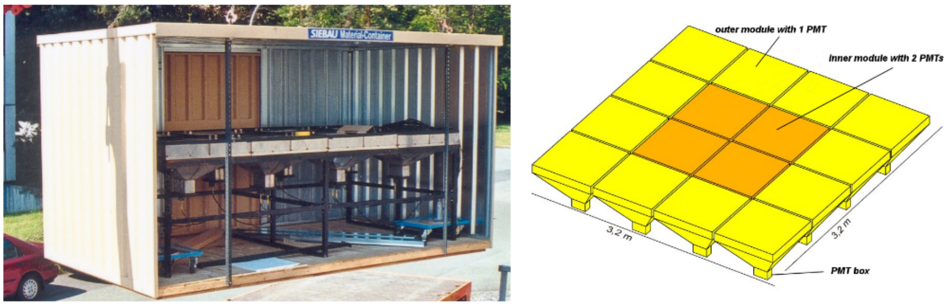

(B) Grande Station Layout. *Left*: inside of a station. *Right*: sketch of 16 scintillators and PMTs.

FIGURE 1.9: Schematic view of the KASCADE and the KASCADE-Grande stations [14].

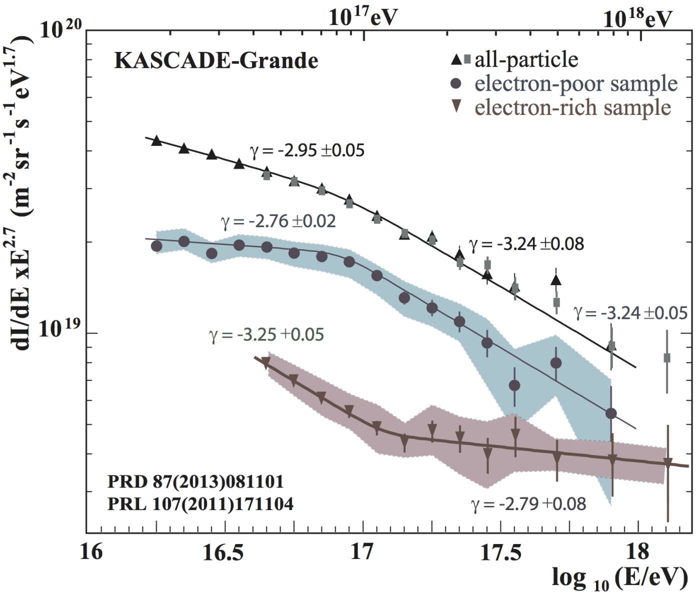

FIGURE 1.10: The cosmic ray energy spectra measured by KASCADE-Grande. The black triangles and gray squares show the all particle spectra. Circles show heavy primary spectrum with systematic band indicated by blue shade. Inverted triangles show light primary spectrum with systematic band indicated by red shade [15].

Yakutsk experiment

Yakutsk experiment is located in Yakutsk, northeast of Russia. An air shower array covers an area of 8.2 km^2 with 58 surface scintillator detectors (the size of each is 2 m^2) and 6 muon detectors (the size of each is 20 m^2) buried underground. In addition, 48 Cherenkov detectors were installed observing the Cherenkov light emitted by air showers. The Cherenkov detector and the array map are shown in Fig. 1.11. This experiment measures cosmic rays with energies above 10^{15} eV. Fig. 1.12 shows measurements of the cosmic ray energy spectrum and the energy dependence of the mass composition by Yakutsk experiment [16, 17].

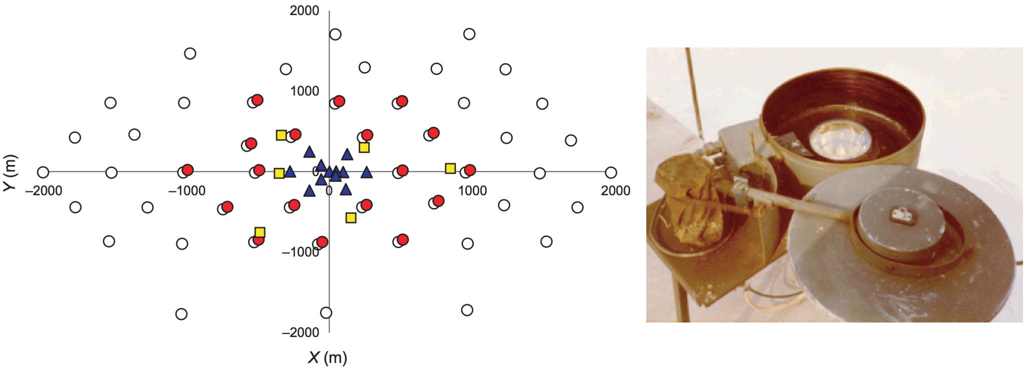

FIGURE 1.11: *Left*: the detector arrangement of the Yakutsk array. Charged particle detectors (open circles), Cherenkov light detectors (filled circles and filled triangles) and the muon detectors (squares) are shown. *Right*: The photo of Cherenkov detector [18].

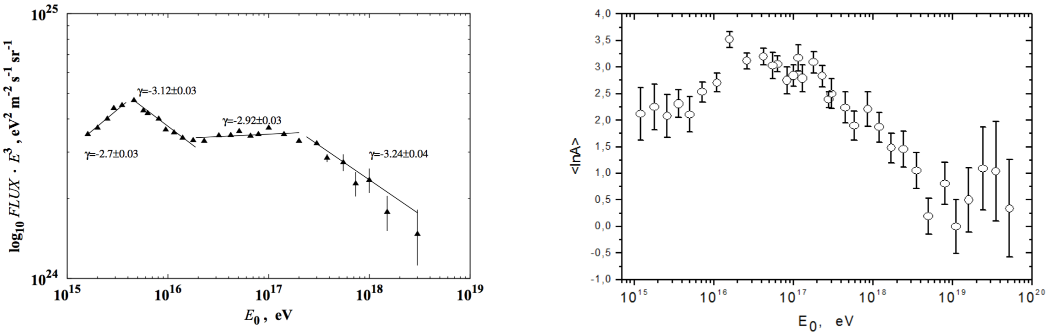

FIGURE 1.12: The measurements by Yakutsk experiment. *Left*: Cosmic ray energy spectrum (multiplied by E^3). *Right*: The energy dependence of the cosmic ray mass composition. The QGSJETII-03 [19] hadronic interaction model was used in the estimation of $\langle \ln A \rangle$ from measured X_{max} (conversion of $\langle X_{\mathrm{max}} \rangle$ to $\langle \ln A \rangle$ is discussed in Sec. 5.8.2).

Tunka experiment

Tunka experiment is located near Lake Baikal in southeastern Russia. It consists of 175 Cherenkov detectors. The detectors are grouped into 25 clusters with 7 detectors each, which made up of 6 hexagonally arranged detectors and one in the center. The distance each the detector in a cluster is 85 m. 19 clusters are arranged with denseness. The detector configuration is shown in Fig. 1.13. This experiment observes cosmic rays with energies from 10^{15} eV to 10^{18} eV. Fig. 1.14 shows measurements of the cosmic ray energy spectrum and the energy dependence of the mass composition by Tunka experiment [20, 21]. The group reported that measured spectrum breaks at 3×10^{17} eV but slightly higher than KASCADE-Grande and Yakutsk results.

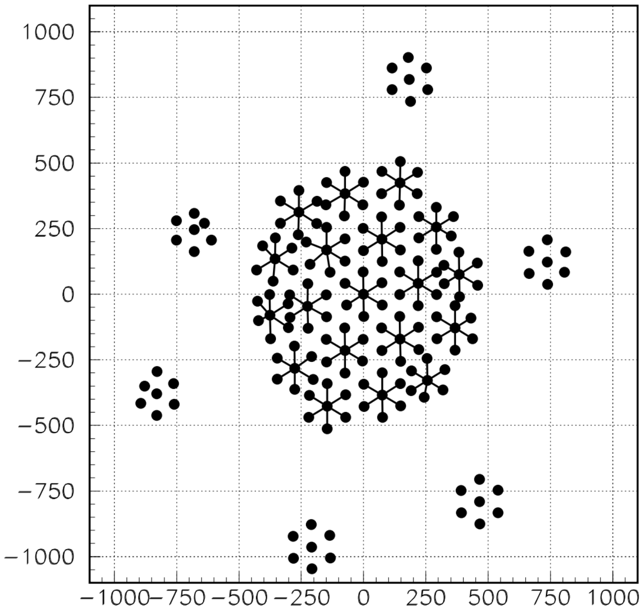

FIGURE 1.13: Layout of the Tunka array [20].

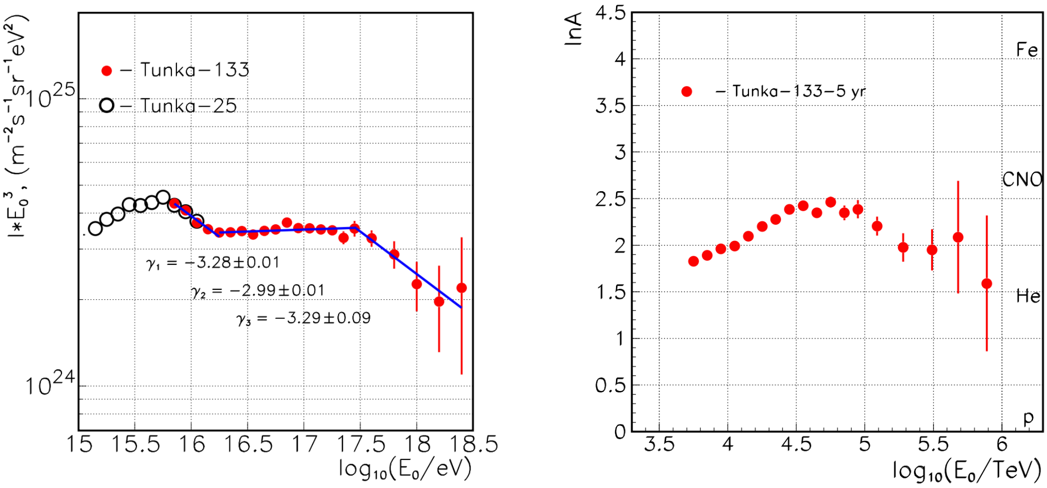

FIGURE 1.14: The measurements by Tunka experiment. *Left*: Energy spectrum (multiplied by E^3). *Right*: The energy dependence of the mass composition. Unlike the previous Yakutsk group, the QGSJETII-04 [4] hadronic interaction model was used in the estimation of $\langle \ln A \rangle$ from measured $X_{\max}$.

IceTop at IceCube Neutrino Observatory

IceCube, a neutrino observatory at the South Pole, is a cubic-kilometer detector in Antarctic ice and located near the Amundsen-Scott South Pole Station. It consists of 5,160 digital optical modules (DOMs). The DOMs are attached to vertical strings and arrayed over a cubic kilometer from 1,450 meters to 2,450 meters depth. A surface charged particle detector array, IceTop, which located on the surface of the ice at 2835 m above sea level, consists of 162 ice-filled tanks, instrumented with PMTs that detect Cherenkov radiation, and arranged in 81 stations on the surface, shown in Fig. 1.15. The target energy range IceTop with IceCube is 300 TeV to 1 EeV energy range [22]. Fig. 1.16 shows their measurements of the cosmic ray energy spectrum and the energy dependence of the mass composition. Yakutsk and Tunka reported that at the low energies, the mass composition increases with energy, and above 10^{17} eV, it begins to decrease. Whereas, IceTop result implies that the heavy components still dominate in energies above 10^{17} eV.

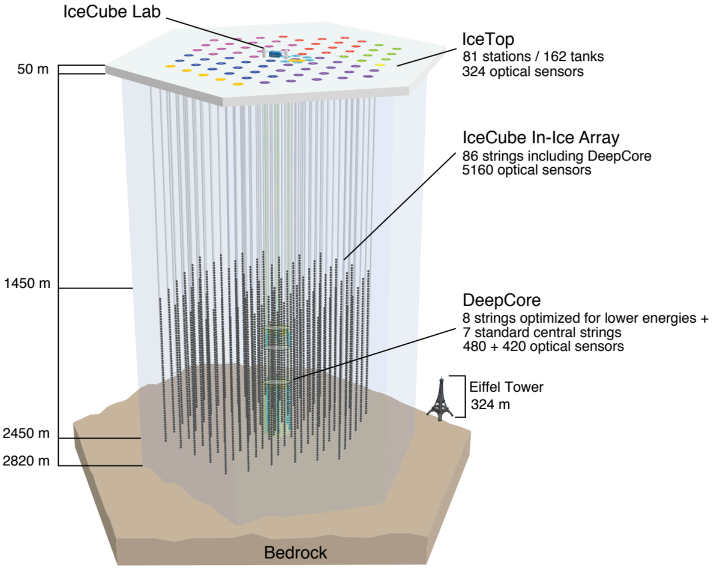

FIGURE 1.15: IceCube Neutrino Observatory with the in-ice array, its sub-array DeepCore, and the cosmic ray air shower array IceTop [23].

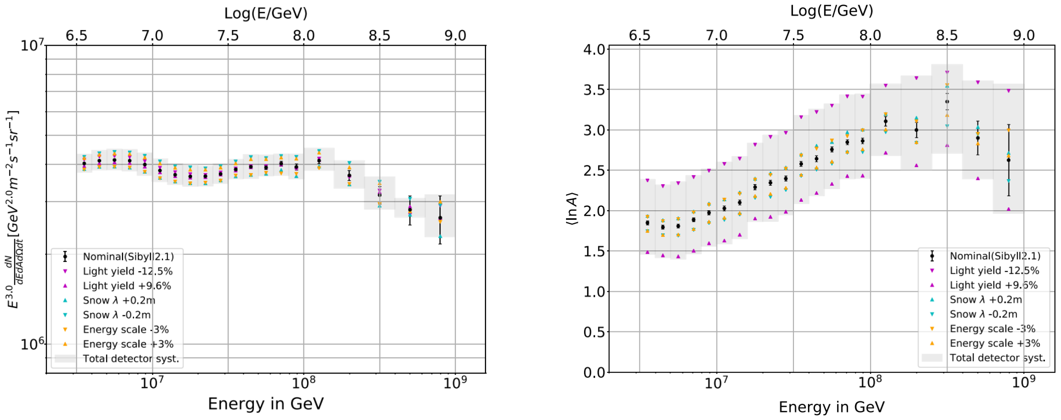

FIGURE 1.16: *Left*: All particle energy spectrum (multiplied by E^3) measured by IceTop. Gray band represents the systematic uncertainties. *Right*: Mean ln$A$ measured by IceTop. Gray band represents the systematic uncertainties [24].

Telescope Array experiment

Telescope Array (TA) experiment is the largest cosmic ray observatory in the northern hemisphere. It is operating of the hybrid detectors made up of surface detector arrays and 60 fluorescence telescopes to observe cosmic rays air showers with energies from 2×10^{15} eV to above 10^{20} eV. Detailed information are described in Chapter 2. Fig. 1.17 shows recent results by the TA collaboration. Cosmic ray spectrum over five orders of magnitude of the energy is obtain from 11 years TA surface detector array data [25] and 22 months of the TALE fluorescence monocular data [26], shown in the left panel. There are some very clear points in the spectrum, namely the knee structure near $\sim 10^{15.5}$ eV, the low energy ankle at $10^{16.22}$ eV, the second knee at $10^{17.04}$ eV, the ankle at $10^{18.69}$ eV, and the suppression at $10^{19.81}$ eV. In the right panel of Fig. 1.17, The black points indicated the $\langle X_{\mathrm{max}} \rangle$ as a function of energy measured by the TA hybrid detector. The TA result indicates the light nuclei are dominant component above $10^{18.2}$ eV.

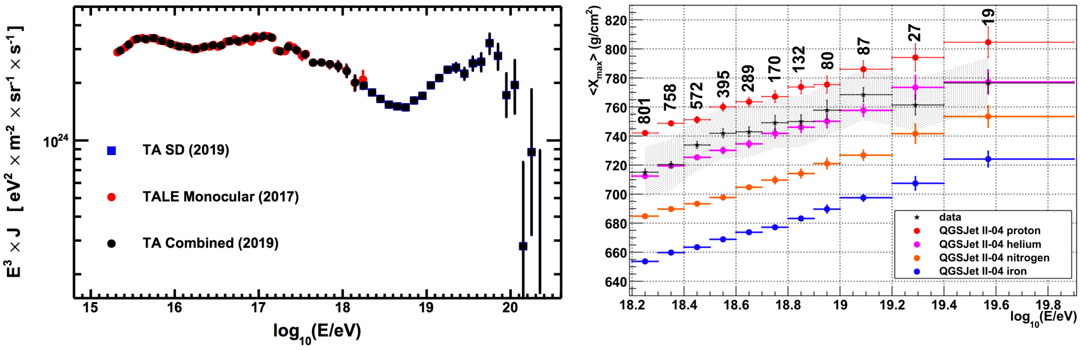

FIGURE 1.17: *Left*: The black points indicate the combined TA energy spectrum [25]. Red points indicate the TALE fluorescence monocular measurement, and blue points are the TA surface detector measurement. *Right*: The $\langle X_{\mathrm{max}} \rangle$ measurement by the TA hybrid detector, shown as black points, compared with the Monte Carlo prediction of QGSJetII-04 hadronic interaction model [11]. Gray band shows systematic band.

Pierre Auger Observatory

The Pierre Auger Observatory is the largest cosmic ray observatory in the world. It is located in the Mendoza, Argentina. It composes of two types of detectors, one is 3000 km^2 air shower array consisting of 1600 water tank surface detector with 1500 m spacing and the other is 27 fluorescence telescopes looking the atmosphere over the surface detector array. They also have a dense array with 750 m spacing and high elevation fluorescence telescopes to observe low energy cosmic ray air showers ($E > 10^{16}$ eV). Their measurements are shown in Fig. 1.19. In the energy spectrum on the left panel, there are breaking points at 2.8×10^{16} eV, 1.58×10^{17} eV, 5×10^{18} eV, 1.4×10^{19} eV, and 4.7×10^{19} eV [27]. The right panel of Fig. 1.19 is the measurement of cosmic ray composition by using hybrid events [28]. The elongation rate of $\langle X_{\mathrm{max}} \rangle$ is 77 g/cm^2/decade below $10^{18.32}$ eV and is 26 g/cm^2/decade at the higher energies. The Monte Carlo prediction of the elongation rates for the each primary component are ~ 60 g/cm^2/decade. Thus, the measurement shows the mass composition changes heavy dominant to light dominant with energies below $10^{18.32}$ eV, and it turns to heavy above this energy.

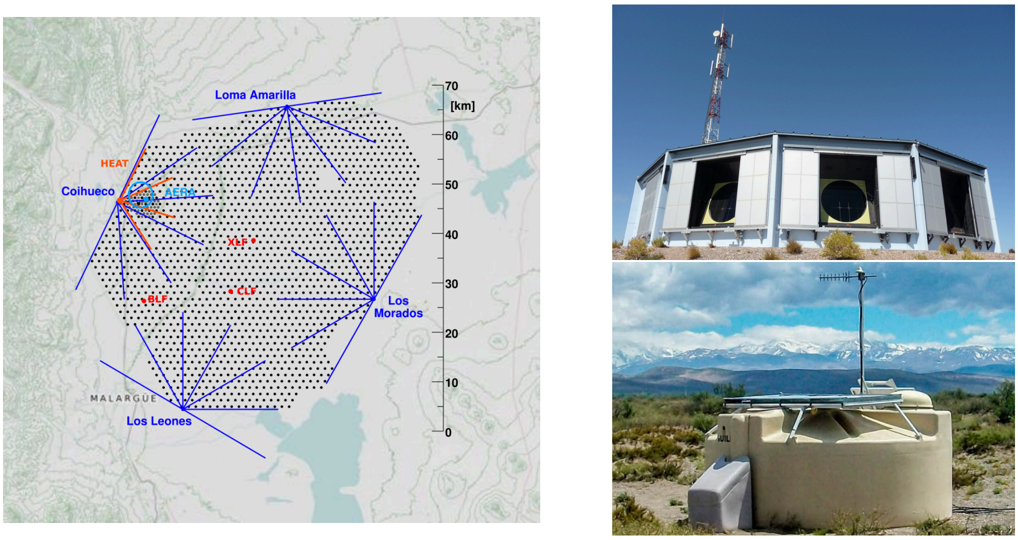

FIGURE 1.18: *Left*: The Pierre Auger Observatory layout. Each dot corresponds to one of the 1660 surface detector stations. The four fluorescence detector sites are shown, each with the field of view of its six telescopes. The Coihueco site hosts three extra high elevation (HEAT) telescopes. The 750 m array is located a few kilometers from Coihueco [29]. *Right – Top*: FD building at Los Leones site [30]. *Right – Bottom*: One of the SD stations in the Auger site. [29].

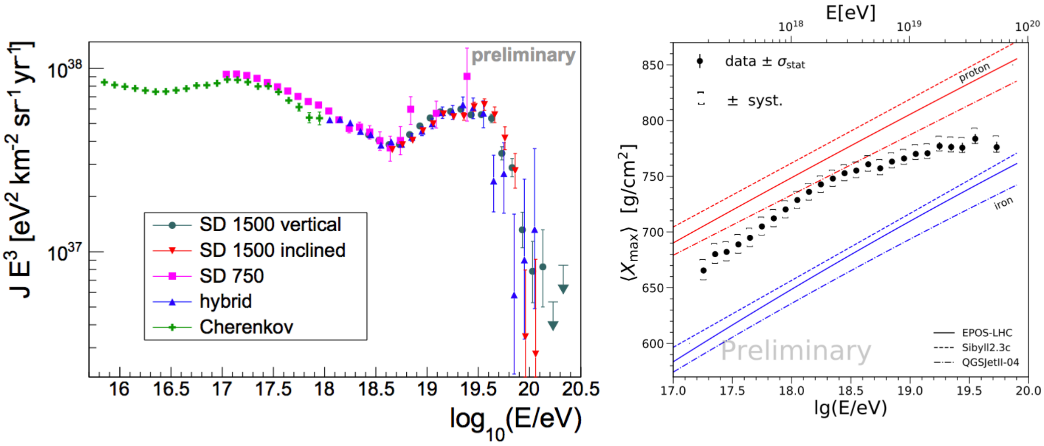

FIGURE 1.19: *Left*: Cosmic ray energy spectrum (multiplied by E^3) measured by different five techniques in Pierre Auger Observatory, the 1500 m array using vertical events, inclined events, hybrid events, events detected by the 750 m array and the FD events dominated by Cherenkov light [27]. *Right*: Mean X_{max} measured by Auger comparing with the predictions for proton and iron MC with the hadronic interaction models of EPOS-LHC [31], Sibyll 2.3c [32] and QGSJetII-04, taken from [28].

1.3 Extensive Air Shower

As described in Sec. 1.1, as the cosmic ray flux follows a power law nature, E^{-3}, the difference of the flux is the over thirty orders of magnitude with energies from 10^9 eV to 10^{20} eV. The relative low energy cosmic rays, below 10^{14} eV, are observed by direct measurements with balloon-based and satellite-based measurements. On the other hand, it is difficult to measure the cosmic rays above this energies by directly.

Since the event rate of the higher energy cosmic rays, we need a larger detection area and a longer exposure time but it is unrealistic to observe by balloons or satellites. Thus, we measure extensive air showers that huge number of secondary particles are generated by interaction with a primary cosmic ray, from which comes from universe, and the atmospheric nuclei.

1.3.1 Air Shower Phenomenon

A primary cosmic ray enters the atmosphere, then it interacts with a atmospheric nucleus and generate the secondary particles. These particles generate farther particles by interacting with atmospheric nuclei. This processes are repeated, again and again, as a result the huge number of particles are generated by the primary cosmic ray. This is called as an extensive air shower (EAS). In general, the extensive air shower consists of hadronic component, muonic component and electromagnetic component.

Hadron and Muon component

The pions and kaons are produced by the hadron multiple production when the hadrons, in which major component of primary cosmic rays, enter and interact with the atmospheric nuclei. Eventually, most of the secondary particles decay into pions. For π^0 case, it decays into two gamma rays immediately because its life time is 8.5×10^{-17} sec. These gamma rays generate the electromagnetic component. For $\pi^{\pm}$ case, its decay modes are

$$\begin{aligned} \pi^+ &\longrightarrow \mu^+ + \nu_\mu \\ \pi^- &\longrightarrow \mu^- + \bar{\nu}_\mu \end{aligned} \tag{1.5}$$

with the life time of $\tau = 2.6 \times 10^{-8}$ sec. $\mu^{\pm}$ also decay like below Eq. 1.6,

$$\begin{aligned} \mu^+ &\longrightarrow e^+ + \bar{\nu}_\mu + \nu_e \\ \mu^- &\longrightarrow e^- + \nu_\mu + \bar{\nu}_e \end{aligned} \tag{1.6}$$

with the life time of 2.2×10^{-6} sec. However, this $\mu^{\pm}$ are relativistic particles, so that most of them survive without decaying even near the ground. On the other hand, since the atmospheric depth is 10 times larger than the mean free path of the hadronic interactions, the huge number of secondary particles are generated by the hadron multiple productions. Fig. 1.20 shows the schematic view of the production of secondary particles through the hadron multiple productions.

Electromagnetic component

The electromagnetic cascades are initiate from gamma rays which come from π^0 decay. This gamma rays produce a electron and a positron by pair creation, furthermore these electron and positron emit a gamma ray via bremsstrahlung. The interaction length of pair creation at the high energy photon is

$$\left(\frac{\mathrm{d}X}{\mathrm{d}E}\right)_{\mathrm{pair}} \simeq -\frac{7}{9}\frac{E}{X_0}, \tag{1.7}$$

where X_0 is the thickness at which the energy of the electron becomes 1/e, so called the radiation length. X_0 is $\sim 38\ \mathrm{g/cm^2}$ in air. For the bremsstrahlung, the interaction

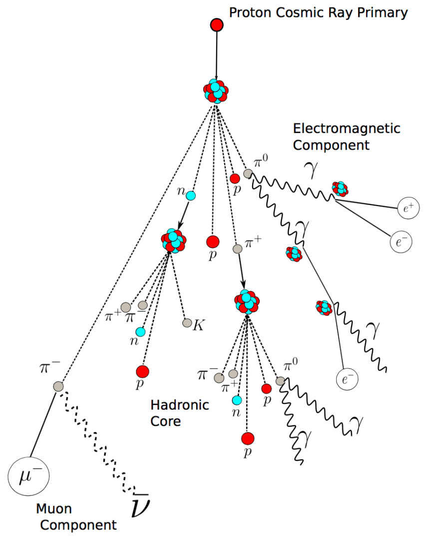

FIGURE 1.20: Schematic view of the secondary particles generated by a primary cosmic ray proton. Pions and Kaons are produced by the hadron multiple production. The decay of $\pi^0 \rightarrow \gamma + \gamma$ initiates electromagnetic cascades. The decay of $\pi^\pm \rightarrow \mu^\pm + \nu$ generates muon components of EAS.

length is calculated by Bethe and Heitler [33] as below,

$$\left(\frac{\mathrm{d}X}{\mathrm{d}E}\right)_{\mathrm{brems}} = -\frac{4N_A Z}{A}\alpha r_e E\left\{\ln(183Z^{-\frac{1}{3}}) + \frac{1}{18}\right\}, \tag{1.8}$$

where α is the fine structure constant, N_A is Avogadro's Number, A is the atomic mass number of the target, Z is the atomic number of the target, r_e is classical electron radius. From this formula transform using with the radiation length of electron,

$$\left(\frac{\mathrm{d}X}{\mathrm{d}E}\right)_{\mathrm{brems}} \simeq -\frac{E}{X_0} \tag{1.9}$$

Therefore, the interaction lengths of a pair creation and a bremsstrahlung are almost similar. Thus, the process of pair production and bremsstrahlung continues and exponentially increase the number of secondary particles in the electromagnetic component. The electromagnetic cascade continues to develop until the average electron energy falls to a level where the ionization energy loss per interaction length becomes larger than the bremsstrahlung energy loss per interaction length. The energy at this boundary is called the critical energy E_c, which is 85 MeV in air [34]. When the energy of secondary particles are below E_c, their energies are lost and absorbed through energy losses without generating secondary particles. As the result, the total number of particles in EAS are decreased. The right panel of Fig. 1.23 shows how the number of secondary particles develop as a function of the altitude for each component. Most of particle are dominated by the electromagnetic component ($e^\pm$ and γ).

1.3.2 Characteristic of EAS

Longitudinal Shower Profile

As described in Sec. 1.3.1, the EAS particles generate further particles above the critical energy, E_c, and are absorbed below E_c. This behavior of increasing and then decreasing of the number of particles in the EAS as a function of atmospheric depth is called longitudinal development. This longitudinal shower development is well described by the Gaisser-Hillas parameterization formula [35],

$$N(x) = N_{\max} \left(\frac{x - X_0}{X_{\max} - X_0} \right)^{\frac{X_{\max} - X_0}{\lambda}} \exp\left(\frac{X_{\max} - x}{\lambda} \right), \tag{1.10}$$

where X_0 is the depth of the first interaction, and λ is interaction length of shower particles, typically $\lambda = 70\ \mathrm{g/cm^2}$.

Here, we consider a very simple toy model of the longitudinal development of a pure electromagnetic cascade initiated by a gamma ray with energy E_0. In this model, the gamma rays produce an electron-positron pair with having a half of its energy after the gamma rays travel the distance of λ, which is a radiation length for the pair production process in the air. Furthermore, Furthermore, the electron and positron emit a gamma ray, which have a half of their energy, via bremsstrahlung after they travel the distance of λ. A primary photon creates an electron and a positron in the first step, and this electron and positron are emit a gamma ray respectively in the second step, i.e., the number of particles increases to four. In this stage, each particle has the energy of $E_0/4$. This branching occurs after the particle travels one radiation length for whichever the splitting process is. After the particles travel x distance, the total number of EAS particles, $N(x)$, and the energy per one particle, $E(x)$, are

$$N(x) = 2^{x/\lambda} \tag{1.11}$$

$$E(x) = \frac{E_0}{2^{x/\lambda}} \tag{1.12}$$

The splitting continues until $E(x) = E_c$. Below $E(x)$, EAS particles are unable to emit a gamma ray via bremsstrahlung. Thus, the maximum number of EAS particles,

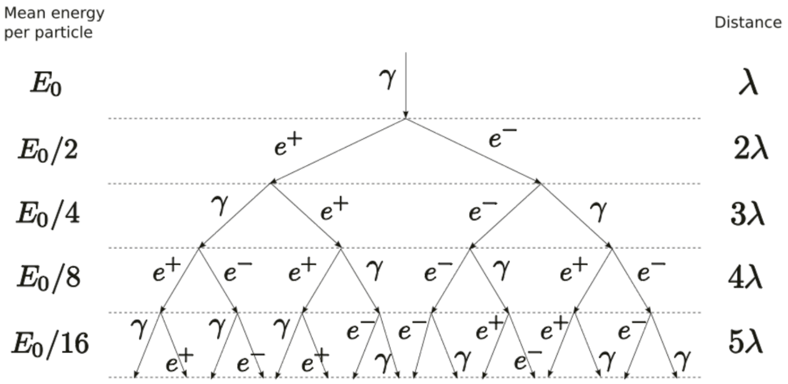

FIGURE 1.21: The Heitler model [36] for the electromagnetic component cascade. Every steps after the propagation of radiation length, here is λ, the number of particles in the electromagnetic cascade doubles, and the amount of energy per particle decreases in half.

$N_{\text{max}} = N(X_{\text{max}})$, at where the depth of the maximum number of EAS particles, and its depth X_{max} are written as

$$N_{\text{max}} = \frac{E_0}{E_c} \tag{1.13}$$

$$X_{\text{max}} = \lambda \frac{\ln(E_0/E_c)}{\ln 2} \tag{1.14}$$

Next is for a nucleus case with atomic number A. We assume the nucleus as a group of A gamma rays for simplify. Since each gamma ray before interaction has the energy of E_0/A, N'_{max} and X'_{max} are

$$N'_{\text{max}} = \frac{E_0/A}{E_c} \times A = \frac{E_0}{E_c} = N_{\text{max}} \tag{1.15}$$

$$\begin{aligned} X'_{\text{max}} = \lambda \frac{\ln(E_0/AE_c)}{\ln 2} &= \lambda \left(\ln \frac{E_0}{E_c} - \ln \mathrm{A} \right) / \ln 2 \\ &= X_{\text{max}} - \frac{\lambda}{\ln 2} \cdot \ln A \end{aligned} \tag{1.16}$$

respectively. Therefore, the shower size of N_{max} is independent on the mass number and the depth of shower maximum, X_{max}, decrease with increasing the mass number. Thus, we can estimate the mass number A by observing the X_{max}. Fig. 1.22 shows the simulated longitudinal developments for proton and iron primary.

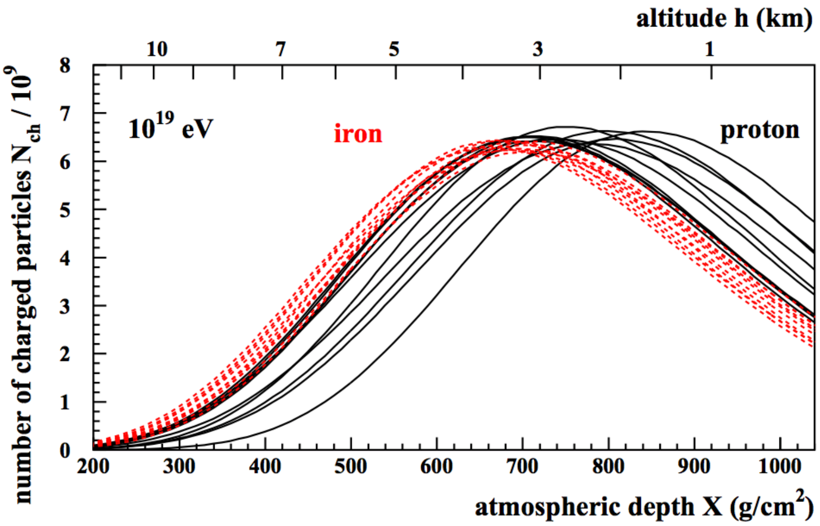

FIGURE 1.22: Simulated air shower longitudinal profiles as a function of atmospheric depth in g/cm^2. Black lines indicated proton primary air showers. Red dashed lines indicated iron primary air showers. The variability of iron curves are smaller than proton ones because the cross section of iron nucleus is larger than proton one and electromagnetic cascades initiated by each nuclei are superposed and averaged for iron case. Taken from [37].

Lateral Density Distribution

The electromagnetic cascades spreads perpendicular to an arrival direction of primary cosmic ray particle by Coulomb scattering, this called a lateral density distribution. The Lateral distributions of EAS are analytically calculated by Nishimura and Kamata [38], and parametrized by Greisen [39], as follows,

$$\rho_{\mathrm{NKG}}(r,s) = C(s)\,\frac{N_e}{r_M^2}\left(\frac{r}{r_M}\right)^{s-2}\left(1+\frac{r}{r_M}\right)^{s-4.5}, \tag{1.17}$$

where r is the distance from shower axis, $C(s)$ is a normalization factor, N_e is the total number of particles at observed altitude, r_M is a Moliere unit, which is the unit of scattering length of a high energy electron when it travels one radiation length ($r_M \simeq 9.8$ g/cm^2), s is a shower age. The shower age represented a level of shower longitudinal development and is defined as,

$$s = \frac{3}{1+2X_{\max}/X}, \tag{1.18}$$

where X is the depth along with the shower axis. Further detail parametrization has done by S. Lafebre et al. (2009) [40] with using air shower simulations by CORSIKA [41] to describe the EAS lateral distribution and that parameterization is used in this thesis. Fig. 1.23 shows the lateral and longitudinal particle profiles of the different shower components, simulated by CORSIKA for proton-induced showers of 10^{19} eV.

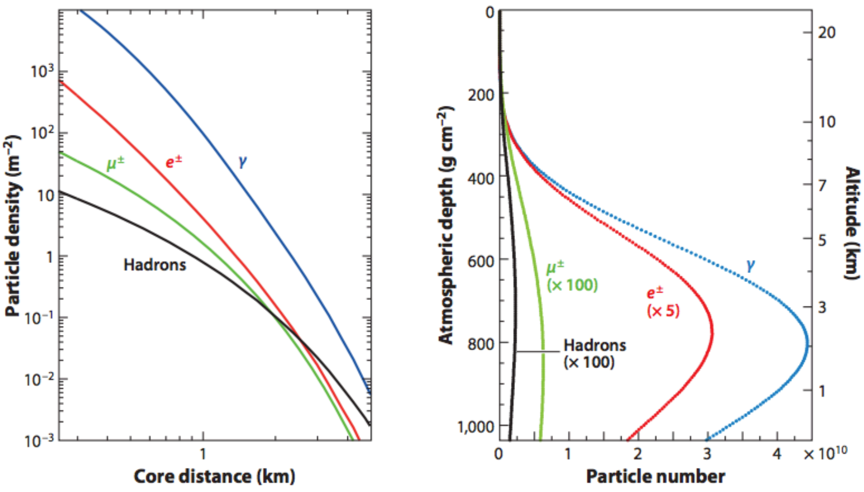

FIGURE 1.23: Average air shower behavior of lateral distribution at the ground and longitudinal shower profile of each component, for vertical proton-induced showers at 10^{19} eV, taken from [42].

Light emission from EAS

When the EAS passes through the atmosphere, it generated two types of light. One is fluorescence light and another is Cherenkov light.

The fluorescence light initiated by EAS is mainly produced by the de-excitation of atmospheric nitrogen molecules, which are excited by energy deposit of electrons/positrons from the air shower. The observed emission is dominated by radiative de-excitation of N_2 and N_2^+ in the wavelength range between about 290 and 430 nm [43]. The radiative de-excitation is competing with quenching processes caused by further non-excited molecules in air. The relative fluorescence intensity has some emission lines between 290 nm and 430 nm. Fig. 1.24 shows the efficiencies of fluorescence photon emissions and the relative intensity measured by various experiments. In this thesis, the FLASH spectrum [44] and the Kakimoto absolute fluorescence yield [45] are used. The number of produced fluorescence photons in the air shower are proportional to the local ionization energy deposit $\mathrm{d}E_{\mathrm{dep}}/\mathrm{dX}$:

$$\frac{\mathrm{d}N_{\gamma}^{\mathrm{Fl}}}{\mathrm{dX}}(X) = y_{\gamma}^{\mathrm{Fl}}(h) \cdot \frac{\mathrm{d}E_{\mathrm{dep}}}{\mathrm{d}X}, \tag{1.19}$$

where y_{γ}^{Fl} is the fluorescence yield in air at altitude h and $\mathrm{d}E_{\mathrm{dep}}/\mathrm{dX}$ is well understand as shown in Fig. 1.25 and described as a function of the shower age s:

$$\alpha_{\mathrm{eff}}(s) = \frac{c_1}{(c_2 + s)^{c_3}} + c_4 + c_5 \cdot s \tag{1.20}$$

with $c_1 = 3.90883$, $c_2 = 1.05301$, $c_3 = 9.91717$, $c_4 = 2.41715$, $c_5 = 0.13180$ [46].

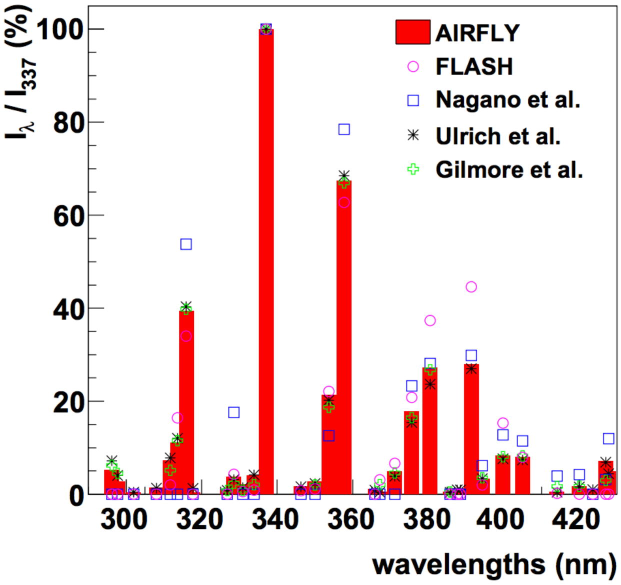

FIGURE 1.24: Relative fluorescence intensities between about 300 and 430 nm. The sum of the fluorescence yield in this wavelength range differs by -1.66% (Ulrich et al.), by +2.08% (Nagano et al. [47]), and by -1.7% (FLASH [44]) compared to the sum of the fluorescence yield obtained by AIRFLY [48]. Taken from [43].

The Cherenkov light are emitted when a charged particle passes a medium with velocity v greater than the speed of light in that medium, c/n, where c is the speed of light in the vacuum, n is the refractive index of the medium [49]. The Cherenkov light are only observed at a particular angle θ with respect to the track of a particle. Here θ is defined as,

$$\theta = \cos^{-1}\left(\frac{c}{nv}\right) \tag{1.21}$$

This θ is $\sim 1.4°$ because the refractive index of the air at 1 atm is n ~ 1.00029. The energy threshold of Cherenkov radiation process for electrons is 21 MeV. The number of Cherenkov photons produced by a charged particle of total energy E and charge

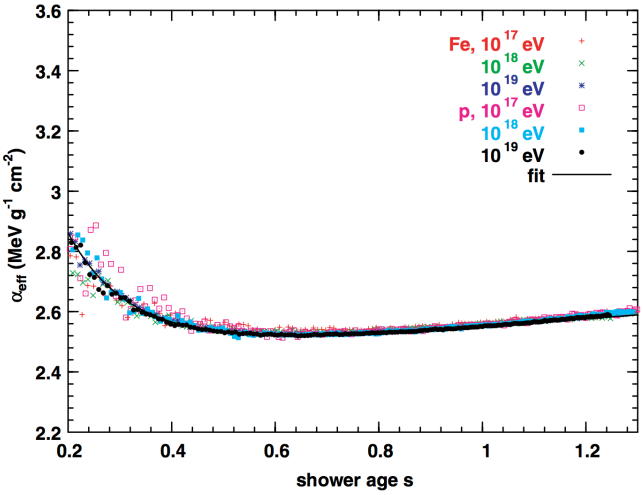

FIGURE 1.25: The mean ionization loss rate $\alpha_{\rm eff}$ as obtained from CORSIKA simulations is shown for vertical showers of different primary energies and particles (10^{17}, 10^{18}, 10^{19} eV, and proton, iron). The fit is given by Eq. 1.20. Taken from [46].

Z in a wavelength interval between λ_1 and λ_2 at the height h is given by

$$\begin{aligned} y_\gamma^{\rm Ch}(E,h) := \frac{{\rm d}N_{\rm Ch}}{{\rm d}X}(E,h) &= \frac{2\pi\alpha Z^2}{\rho(h)}\int_{\lambda_2}^{\lambda_1}\left(1-\frac{1}{n(h)^2\beta^2}\right)\frac{{\rm d}\lambda}{\lambda^2} \\ &\approx \frac{2\pi\alpha Z^2}{\rho(h)}\int_{\lambda_2}^{\lambda_1}\left(2\delta-\frac{m^2c^4}{E^2}\right)\frac{{\rm d}\lambda}{\lambda^2}, \end{aligned} \tag{1.22}$$

where α is the fine structure constant, $\beta = v/c$, ρ is the air density at height h, n is the air refractive index at the height h, and $\delta = n(h) - 1$ [46]. Thus, the total number of Cherenkov photons are written as,

$$\frac{{\rm d}N_\gamma}{{\rm d}X{\rm d}\theta}(X,\theta,h) = A_\gamma(X,\theta,h)N(X) \times \int_{\ln E_{\rm thr}}^{\infty} y_\gamma^{\rm Ch}(E,h)f_e(X,E){\rm d}\ln E, \tag{1.23}$$

where $A_\gamma(X,\theta,h)$ is the angular distribution of produced Cherenkov photons, $N(X)$ is the charged particles at depth X, $E_{\rm thr}$ is the local Cherenkov energy threshold for electrons, $f_e(X,E)$ is the normalized differential electron energy spectrum at depth X

$$f_e(X,E) = \frac{1}{N_{\rm e}}\frac{{\rm d}N_{\rm e}}{{\rm d}\ln E}(X,E) \tag{1.24}$$

The angular distribution of produced Cherenkov photons $A_\gamma(X, \theta, h)$ and the normalized differential electron energy spectrum $f_e(E, s)$ are well reproduced as a function of the shower age s [46],

$$A_\gamma(X, \theta, h) = a_s(s)\frac{1}{\theta_c(h)}\mathrm{e}^{\theta/\theta_c(h)} + b_s(s)\frac{1}{\theta_{cc}(h)}\mathrm{e}^{\theta/\theta_{cc}(h)}$$

$$\begin{aligned}
a_s(s) &= a_0 + a_1 \cdot s + a_2 \cdot s^2 \\
b_s(s) &= b_0 + b_1 \cdot s + b_2 \cdot s^2 \\
\theta_c(h) &= \alpha \cdot E_{\mathrm{thr}}^{-\beta}, \ \text{with}\, E_{\mathrm{thr}} \,\text{in MeV} \\
\theta_{cc}(h) &= \gamma \cdot \theta_c(h), \ \text{with}\, \gamma = \alpha' + \beta'
\end{aligned} \tag{1.25}$$

$$\begin{aligned}
(a_0, a_1, a_2) &= (4.2489 \times 10^{-1}, 5.8371 \times 10^{-1}, -8.2373 \times 10^{-2}) \\
(b_0, b_1, b_2) &= (5.5108 \times 10^{-2}, -9.5587 \times 10^{-2}, 5.6952 \times 10^{-2}) \\
(\alpha, \beta) &= (0.62694, 0.60590) \\
(\alpha', \beta') &= (10.509, -4.9644)
\end{aligned}$$

$$\begin{aligned}
f_e(E, s) &= a_0 \cdot \frac{E}{(E + a_1)(E + a_2)^s} \\
a_1 &= 6.42522 - 1.53183 \cdot s \\
a_2 &= 168.168 - 42.1368 \cdot s \\
a_0 &= k_0 \cdot \exp(k_1 \cdot s + k_2 \cdot s^2) \\
k_0 &= 1.42049 \times 10^{-1} \\
k_1 &= 6.18075 \\
k_2 &= -6.05484 \times 10^{-1}
\end{aligned} \tag{1.26}$$

Fig. 1.26 shows the angular distribution of Cherenkov photons comparison with CORSIKA prediction and Eq. 1.25, and Fig. 1.27 shows the electron energy spectra comparison with CORSIKA prediction and Eq. 1.26.

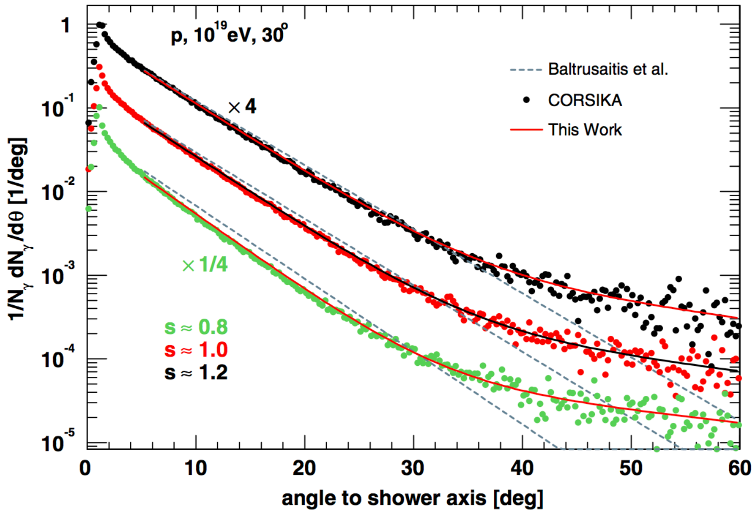

FIGURE 1.26: Angular distribution of produced Cherenkov photons with respect to the shower axis in a single CORSIKA shower for s = 0.8, 1.0, and 1.2. The Monte Carlo results are compared to the parameterisation, Eq. 1.25. Taken from [46].

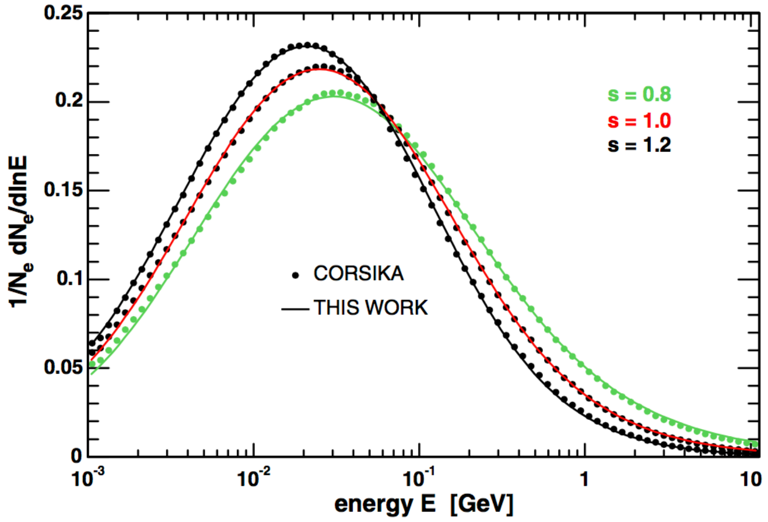

FIGURE 1.27: Comparison of the parameterisation Eq. 1.26 and the electron energy spectra of an individual shower obtained with CORSIKA, proton, 10^{19} eV. Taken from [46].

1.4 Techniques for EAS Measurement

As mentioned above, as the primary cosmic rays produce the EAS and it emits photon signals, we can investigate the cosmic ray properties to detect the EAS particles or photons instead of direct measurements of the primaries. In this section, the techniques of EAS detections are briefly reviewed.

1.4.1 Particle detection

The most commonly used method to detect the EASs is based on the surface detector array made up of particle detector, such as scintillation detectors, water Cherenkov detectors, muon detector. Depending on the energy range the experiment is optimized the distance of each detector, varying from 15 m (KASCADE, Tibet AS-γ) up to more than 1 km (the Telescope Array and the Pierre Auger Observatory). Each detector records the number of particles and the arrival timings at the ground level. The EASs are detected by searching for the time coincidence of signals in neighboring detectors. A best advantage of surface detector array is to observe the cosmic rays with $\sim$ 100% duty cycle.

The arrival direction can be determined from the timing differences recorded by each detector. The cosmic ray energy is determined by estimation of the number of air shower particles apart specific distance from the shower axis, which is optimized with considering the interest energy range and the detector separation [50]. In order to obtain the conversion table or equation to determine the primary cosmic ray energy from the estimated number of particles, a Monte Carlo calculation considering the hadronic interaction model is necessary because it is impossible to launch a test beam with known energy into the device as in particle experiments. Therefore, it is impossible to avoid that the energy determination is affected by the uncertainty of the hadron interaction model.

1.4.2 Photon detection

The large number of Cherenkov photons emitted by EAS particles can be used for efficient detection of the cosmic rays with wide energy range. The Cherenkov technique is useful for both gamma ray astronomy and study of cosmic ray. Imaging atmospheric Cherenkov telescopes (IACTs) can detect the air showers above 20 GeV [51]. They can be reach the high energy region however the IACT observation is limited by effective detection area itself. On the other hand, non-imaging Cherenkov detectors array, which set up is simmer to particle detector array, is able to detect the Cherenkov light at ground with large detection area, which mean this type of detector can reach the high energy region compared with IACT observations. Moreover, recent fluorescence telescopes can observe the cosmic rays above 10^{15} eV by detecting Cherenkov light aggressively [26, 52, 53].

The fluorescence light can be used to detect the cosmic rays above 10^{17} eV. Because 4-5 fluorescence photons produced per mater per charged particle isotropically [45] and the amount of photons are proportional to the number of EAS particles, for a primary cosmic ray with energy of 10^{18} eV, $O(10^3/\mathrm{m}^2)$ photons can be detected from the air shower maximum depth even if photo-detector apart the shower axis from 10 km. Moreover, the number of emitted fluorescence photons follow the ionization energy deposit of the air shower particles in the atmosphere. Therefore, by the detection of fluorescence photons along with the shower axis can be measured the longitudinal shower profile i.e., we can measure the depth of shower maximum X_{max} directly. This fluorescence technique is suggested in the 1960s by Greisen, Chudakov, Suga [54] and others and the fluorescence photons from EAS were detected at the first time by Hara et al. [55] in 1968.

The reconstruction of the air shower longitudinal profile observed with fluorescence telescope is required the air shower geometry. In the shower observations with one fluorescence telescope (monocular observation), the arrival direction can be determined by using the relative photon detection time differences on the shower-detector plane, which is a plane consisting of the fluorescence telescope and a shower axis. In general, the arrival direction resolution is low precise, $\sim 6^\circ$. The reconstruction accuracy can be improved by measuring an air shower simultaneously with two distant telescopes (stereo observation), or observing simultaneously with surface detector array and one fluorescence telescope (hybrid observation). Both methods can reconstruct the arrival direction precisely with less than 1°. The energy determination is by the integration over the ionization energy deposit in the atmosphere. Thus, the systematic uncertainties related with hadronic interaction model is quite small in the fluorescence measurement because the longitudinal shower profile and primary cosmic ray energy can determine without the hadronic interaction dependence.

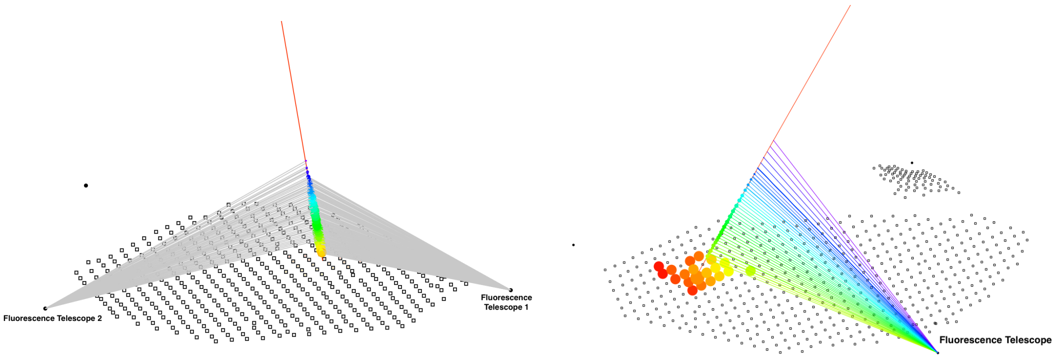

(A) Stereo Observation

(B) Hybrid Observation

FIGURE 1.28: Visualization for (A) Stereo Observation and (B) Hybrid Observation. The black points indicate the positions of fluorescence telescope and the white squares are the positions of each surface detector. The color represents the relative time difference and time evolve from violet to red. The marker size indicate the number of fluorescence photons / air shower particles. In Fig. (A), both Fluorescence Telescope 1 and Fluorescence Telescope 2, which far 36 km from telescope 1, observed a air shower. Fig. (B) shows that the Fluorescence Telescope and a dozen of surface detectors detected a air shower signals simultaneously. Both events are recorded by the Telescope Array.

Chapter 2

The Telescope Array Experiment

The Telescope Array (TA) experiment [56] is an international collaboration with members from Japan, USA, South Korea, Russia, Belgium, Czech Republic, and Slovenia and aims to observe the UHECRs. The TA has the largest hybrid cosmic ray detector in the northern hemisphere in Millard Country, Utah St. The main part of the experiment consists of a surface detector (SD) array that is overlooked by 3 fluorescence detector (FD) stations. TA SD consists of 507 scintillation counters with 1200 m spacing and covering a total of $\sim$ 700 km^2 area on the ground. The three TA FD stations are located at Black Rock Mesa (BRM), Long Ridge (LR), and Middle Drum (MD). These TA FD telescopes are viewing 3° to 31° in elevation. The TA began operation in 2008 and is measuring the cosmic ray spectrum by TA SD [25, 57, 58], TA FD monocular mode [59, 60, 61] and TA hybrid mode [62, 63], the cosmic ray mass composition [11, 64, 65], the cosmic ray anisotropy [9, 66, 67, 10]. In order to study for lower energy cosmic rays, the Telescope Array Low energy Extension (TALE) detectors were constructed with the same techniques of the TA hybrid measurement [68]. Furthermore, the TA×4 experiment, which extends the detection area of the TA SD by a factor of 4, is in progress to focus on the highest energy region (E $>$ 57 EeV) [69, 70]. This chapter focuses on the general description of the TA and the TALE experiments.

2.1 TA Fluorescence Detector

The TA Fluorescence Detectors consist of 38 telescopes in total. There are 12 telescopes, which were newly designed and constructed for the TA experiment, at the BRM fluorescence station and LR fluorescence station respectively. One telescope consists of a spherical mirror 3.3 m in diameter with 18 hexagonal segments mirrors, a camera consisting of 16 × 16 photomultiplier tubes (PMTs) located at the focal plane, and readout electronics that record their PMT signals by 10 MHz FADC devices. Detail description can be found in [71, 72] The total field of view of each station is 108° in azimuthal angle and 3° - 33° in elevation angle overlooking the area of SD array, shown in Fig. 2.5. The left of Fig. 2.2 is a photo of the building of the BRM fluorescence station.

Middle Drum Fluorescence Telescopes

The rest of the 14 telescopes are located at the MD fluorescence station. These telescopes are reutilized from the HiRes-I and the HiRes-II experiments, summarized in Table 2.1. Each 14 telescope consists of a spherical mirror and a camera, as shown in Fig. 2.2 right. The mirror is composed of four segments arranged in a cloverleaf shape with a total area of 5.2 m^2. The camera consists of 16 × 16 PMTs located at the focal plane of the mirror. Each telescope has a field of view of about

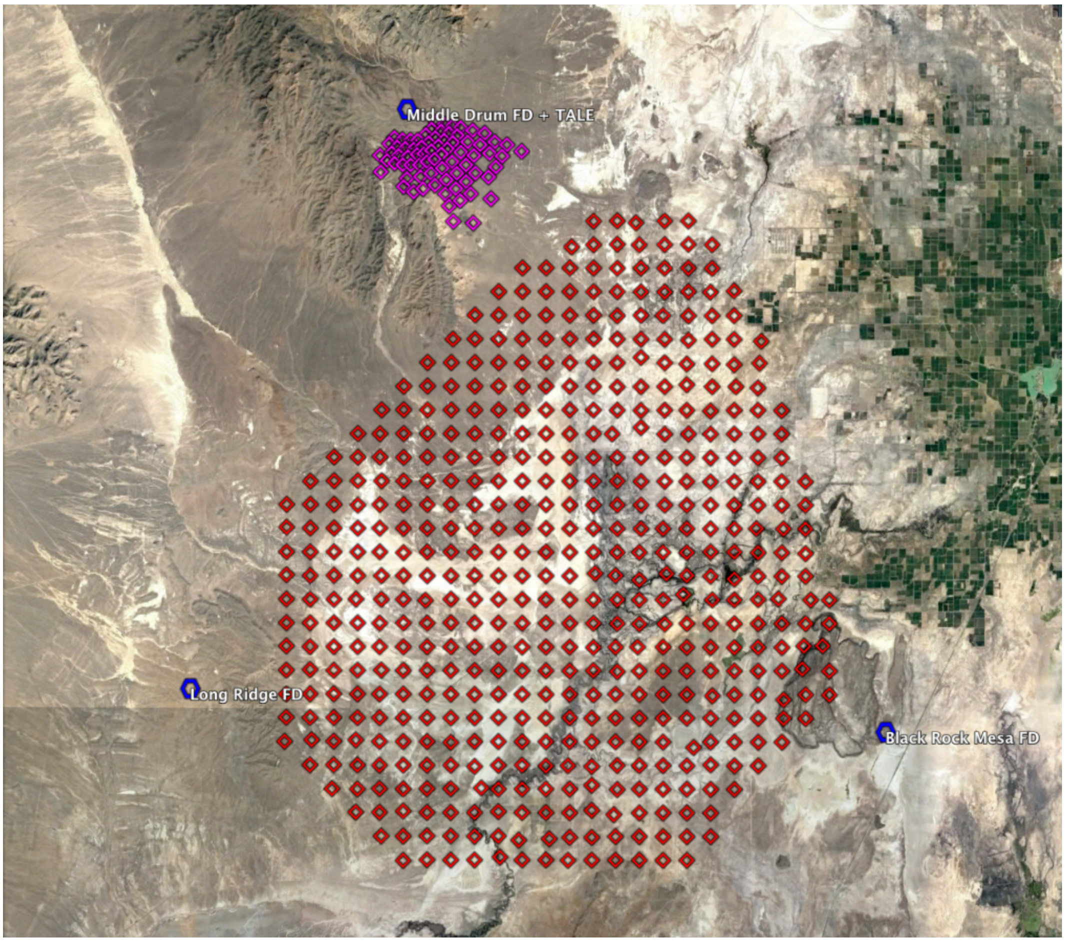

FIGURE 2.1: Satellite map of the Telescope Array experiment site. Centered roughly around 112.9° W, 39.3° N. The Locations of the TA SDs are shown as red diamonds and the locations of the three TA FD stations are indicated by blue hexagons. Magenta diamonds show the location of the TALE SDs. The TALE fluorescence telescopes are located at the MD site.

FIGURE 2.2: *Left*: A photo of Black Rock Mesa fluorescence station. These are three bays, each with four telescopes. The Long Ridge fluorescence station is same structure as BRM station. *Right*: A photo of Middle Drum fluorescence telescopes.

14° in elevation angle and 16° in azimuthal angle. The total field of view of the MD station is 3° - 31° in elevation and about 115° in azimuth. Seven of 14 telescopes view 3° - 17° in elevation, while the remaining seven view 17° - 31° in elevation. We define a “ring” to represent a set of telescopes that view the same elevation. The MD detector has two rings: ring 1 views from 3° - 17° in elevation while ring 2 views 17° - 31° in elevation (In Fig. 2.5, red points on the Top-Left plot shows the MD field of view). The mirror reflectances are measured by a spectrophotometer (KONICA MINOLTA CM-2500d) and the results are shown in Fig. 2.10 left. In front of the PMTs, there is a UV band-pass filter to remove the noise signals. The UV filter is a narrow bandpass filter made of glass and used to restrict the light reflected from the mirror and impinging on the camera face to between 300 and 400 nm wavelength range with high efficiency, shown in the left of Fig. 2.13.

There are two different types of PMTs employed in the MD station and these PMT cameras also are reutilized from the HiRes-I experiment. The PMTs with EMI 9974KAFL model is used in camera 01 - 06 and PMTs with Philips XP3062/FL model is used in camera 07 - 14. The EMI tubes have a thicker, more spherical front face and lower mean quantum efficiency compared to the Philips tubes. Fig. 2.14 shows the non-uniformity of tube profiles for both types.

The PMT signals sent to the trigger circuit are applied to three levels of trigger judgments: tube trigger, subcluster trigger, and mirror level trigger. The tube trigger judges the signal based on an externally set threshold value. Each PMT has a different threshold that is adjusted to keep the trigger rate of each PMT at around 200 Hz. The Signal that exceeds the tube trigger threshold is classified as "hit" and is applied to the next subcluster trigger judgment. The timing of tube trigger issued and the signal integration with 1.2 μs and 5.6 μs time window for hit PMT signals are stored by a sample and hold read-out electronics. A subcluster is a unit of 256 PMTs divided into 16 segments in a 4 × 4 PMTs. The minimum condition for subcluster trigger is that there are at least three tube trigger hit PMTs within 6 μs in the subcluster and at least one adjacent pair. All subcluster trigger information is used in the final trigger judgment, the mirror level trigger. For the mirror level trigger, there must be at least two subclusters triggered by the subcluster trigger within 25 μs. Fig. 2.3 shows a schematic outline of MD telescope data acquisition electronics. Further descriptions for MD telescopes can be found in [73].

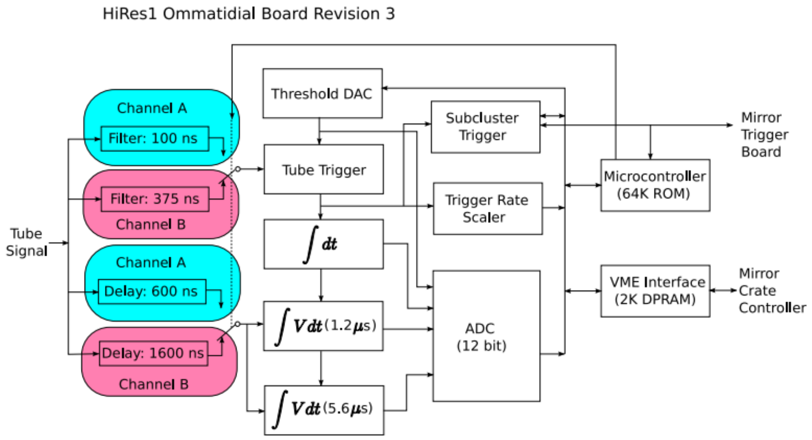

FIGURE 2.3: The schematic outline of the MD electronics. The PMT signal is split into discriminator (filter) and delay lines in Channel A and B, and checks if a subcluster level and mirror level trigger conditions are sequentially met.

MD telescope #	HiRes-II Mirror #	HiRes-I Camera #	PMT	ring #
01	22	01	EMI	1
02	17	06	EMI	2
03	21	03	EMI	1
04	18	04	EMI	2
05	36	09	EMI	1
06	34	11	EMI	2
07	35	07	Philips	1
08	33	08	Philips	2
09	32	02	Philips	1
10	29	10	Philips	2
11	31	05	Philips	1
12	30	12	Philips	2
13	19	13	Philips	1
14	15	14	Philips	2

TABLE 2.1: The MD telescope serial numbers are listed with corresponding the HiRes-II mirror serial numbers, the HiRes-I electronics serial numbers, PMT manufacturer, and ring numbers.

2.2 TA Surface Detector Array

The TA Surface Detector Array consists of 507 SDs arranged on a grid with 1.2 km spacing and the total coverage of the SD array is $\sim 700\ \text{km}^2$. The SD array consists of three sub arrays, each connected to a central data acquisition tower by wireless LAN communication. Each central data acquisition tower is called SKCT (Smelter Knoll Communication Tower), BRCT (Black Rock Mesa Communication Tower), and LRCT (Long Ridge Communication Tower) respectively. Fig. 2.4 shows trigger patterns of TA SD data acquisition. Fig. 2.5 shows the location of each communication tower by black triangles and sub array area by dashed lines. The SD is basically the same as that of the TALE experiment, and is described in Sec. 2.5.1.

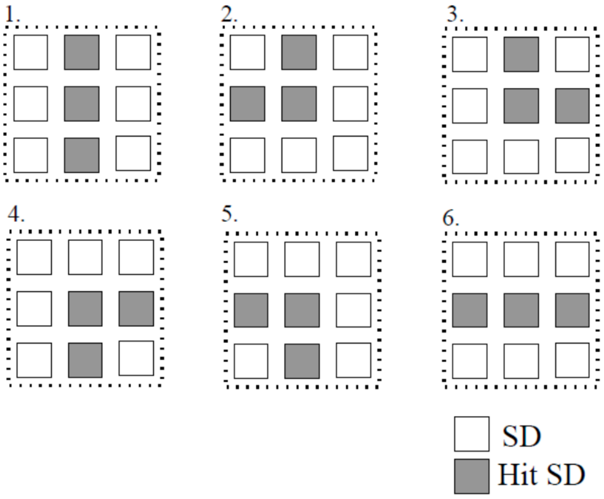

FIGURE 2.4: Trigger patterns of TA SD. The trigger will be issued when any three adjacent SDs with greater than 3 MIP are coincident within 8 μs.

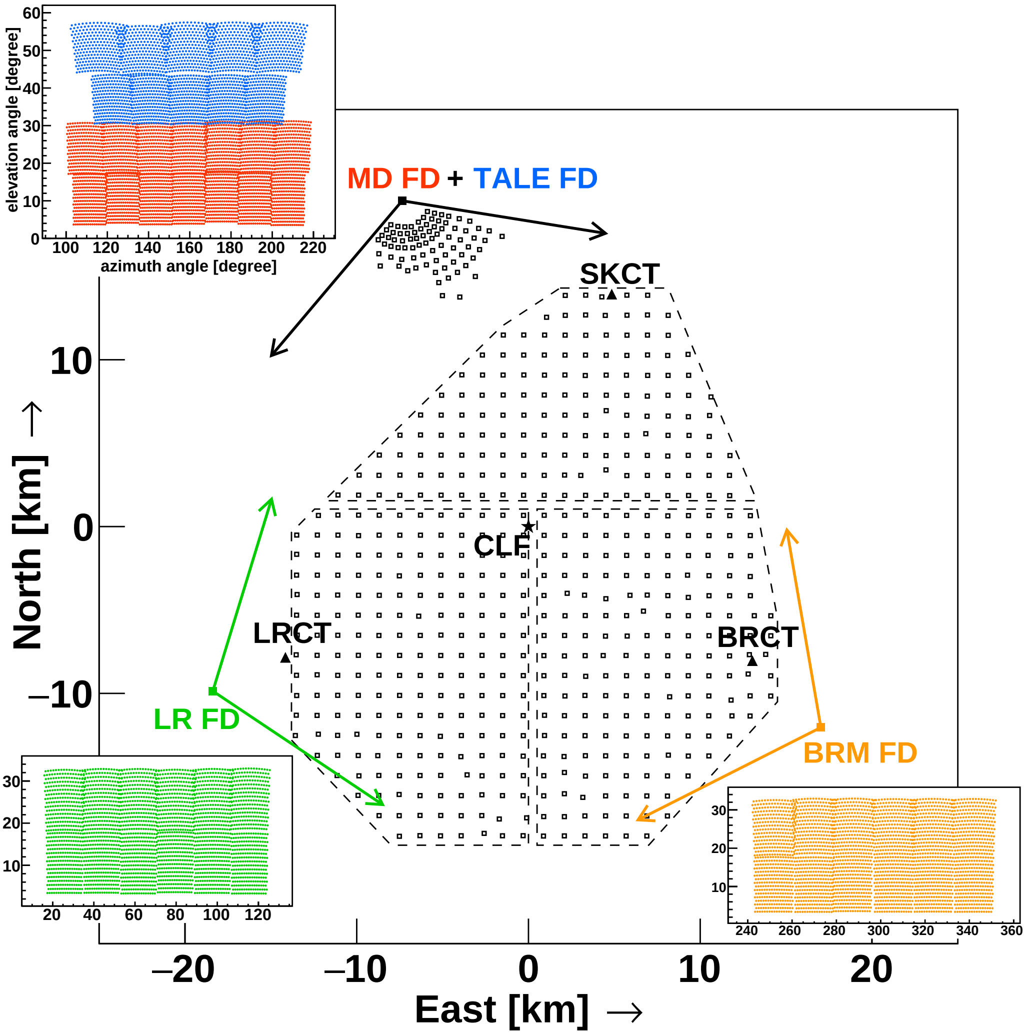

FIGURE 2.5: The Telescope Array detectors. Each TA SD location is indicated by white squares and each communication tower location is indicated by black triangles. Dashed line region represents each sub array. The location of the CLF is labeled by the star. The arrows originated from each FD station are represented the edge of FD field of view. In addition, each FD filed of view is plotted beside of location of FD with same color. Northwest array, which is near from MD station, is the TALE SD array.

2.3 Telescope Array Low energy Extension (TALE) experiment

As described in Sec. 1.1.5, the cosmic ray origins are considered to be the transition from galactic to extragalactic sources around 2nd knee energy. If so, $\langle X_{\mathrm{max}} \rangle$ are expected to be changing from heavy component side to light side drastically, and the X_{max} distribution themselves are expected to be wider than single component X_{max} distribution because galactic primary iron cosmic rays and extragalactic primary proton cosmic rays are compatible around 2nd knee energy region. In order to observe such a changing of $\langle X_{\mathrm{max}} \rangle$ elongation rate and the width of X_{max} distribution with energy dependence by high precise X_{max} measurement, we have extended the observing energy region to lower energies, which is called the Telescope Array Low energy Extension (TALE) experiment. The goal of this thesis is to determine the cosmic rays mass composition and energy spectrum measure with the TALE hybrid detector.

The TALE is located at the north part of the TA site and is aimed at measuring the energy spectrum, mass composition, and anisotropy of cosmic rays above 10^{15} eV. The TALE detector consists of one FD station with ten fluorescence telescopes and an array of 80 scintillation surface detectors, which were deployed to cover a total area of approximately 20 km^2. As described in Sec. 1.3.2, as the height of X_{max} by lower energy cosmic rays are relatively higher than UHECRs, the TALE FD is viewing a high elevation angle of 31° - 59°, which is directly above the field of view of the MD telescopes (shown in Fig. 2.5, blue points on Top-Left plot shows the TALE FD field of view). Moreover, the lateral spread of air showers that induced by target cosmic ray energies at the observation level is compact than one induced by UHECRs. Hence the distance of SD is closer than that of the TA SD. For the TALE SD case, 40 SDs with 400 m spacing and another 40 SDs with 600 m spacing, as shown in Fig. 2.6. The TALE FD began operation in 2013 at the MD station, and the TALE SD started observation in 2017. In addition, an external trigger from the TALE FD to the TALE SD to detect low energy cosmic rays, so-called a hybrid trigger system, was installed in 2018.

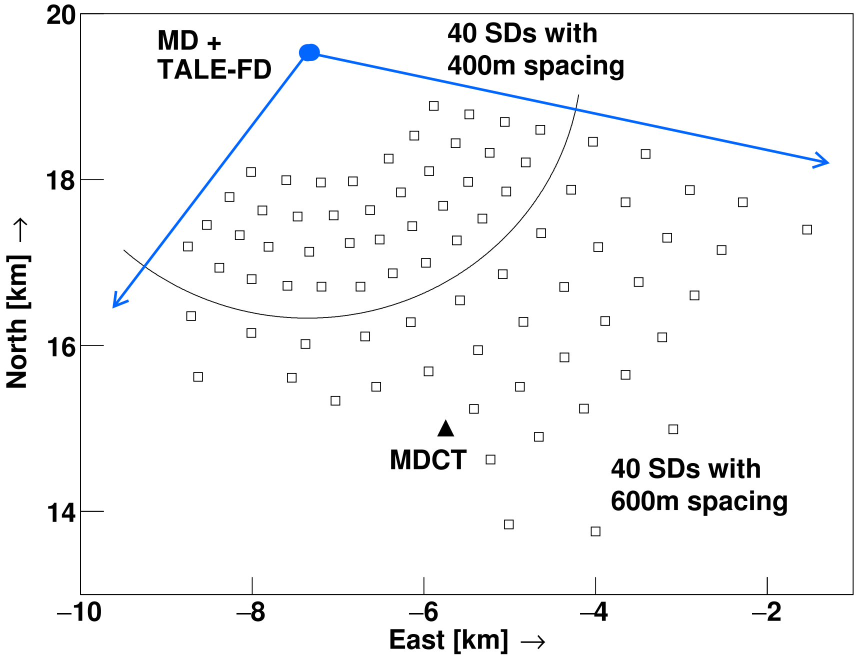

FIGURE 2.6: The layout of the TALE detector. Open square boxes represent the locations of the TALE SD counters and small filled circle correspond to the MD / TALE FD station. The arrows represent azimuthal viewing ranges of both FDs.

2.4 TALE Fluorescence Detector

2.4.1 Telescope and Optics

The TALE Fluorescence Detectors are located next to the MD FD station (Fig. 2.7). The TALE telescopes are also reutilized from the HiRes-I and the HiRes-II experiments, summarized in Table 2.2. As shown in Fig. 2.8, the mirror of the telescope is the same type as the one used at MD telescopes, consisting of four segmented clover-shaped spherical mirrors with an area of 5.2 m^2, and the camera consists of 16 × 16 PMTs at the focal plane of the mirror. Each PMT signal is recorded by a 10 MHz FADC device with an 8-bit resolution. The total field of view of TALE FD is 31° - 59° in elevation angle and about 115° in azimuthal angle. Five of the 10 telescopes view 31° - 45° in elevation (ring 3), while the remaining five view 45° - 59° in elevation (ring 4). As already mentioned in the previous section, the TALE FD views above the TA MD field of view. Thus, using the TA MD and the TALE FD together can observe air showers from 3° - 59° in elevation continuously, such as Fig. 2.9. This enables us to observe the full development of air showers that initiate closer to the observatory.

The mirror reflectances are measured by the same spectrophotometer used in TA FD telescopes measurements and the results are shown in the right panel of Fig. 2.10. Six of 10 mirrors, which reutilized from the HiRes-I mirrors, are slightly low mirror reflectance than others.

FIGURE 2.7: Photo of the TA MD (left) and TALE FD (right) building.

TALE telescope #	HiRes Mirror #	HiRes-II Camera #	HiRes-II Electronics #	PMT	ring #
15	HiRes-I 11	39	25	Philips	4
16	HiRes-I 15	02	26	Philips	3
17	HiRes-II 42	03	01	Philips	4
18	HiRes-II 41	04	02	Philips	3
19	HiRes-I 14	05	03	Philips	3
20	HiRes-I 10	06	04	Philips	4
21	HiRes-II 13	07	05	Philips	3
22	HiRes-II 38	08	06	Philips	4
23	HiRes-I 13	09	07	Philips	3
24	HiRes-I 08	10	08	Philips	4

TABLE 2.2: The TALE telescope serial numbers are listed with corresponding the HiRes mirror serial numbers, the HiRes-II electronics serial numbers, PMT manufacturer, and ring numbers. The TALE telescope numbers are the sequential numbers from the MD telescope.

FIGURE 2.8: Photo of the TALE telescopes. Left one is ring 4 telescope (#17), and right one is ring 3 telescope (#18). Each telescope has the clover-shaped spherical mirror, the black box shaped PMT camera, which supported by orange stands and connected to the electronics crate located at center of both mirrors.

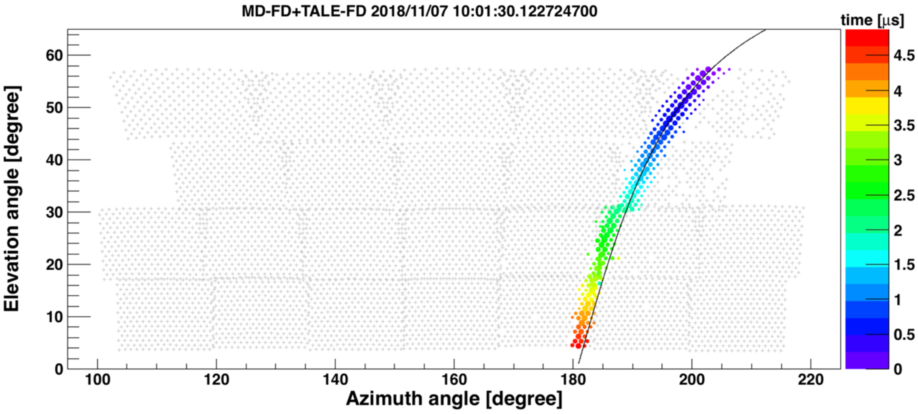

FIGURE 2.9: An example event observed with both the TA MD and the TALE FD telescopes. Color represents relative differences of timing detected by each PMT. Marker size represents the number of photons detected by each PMT.

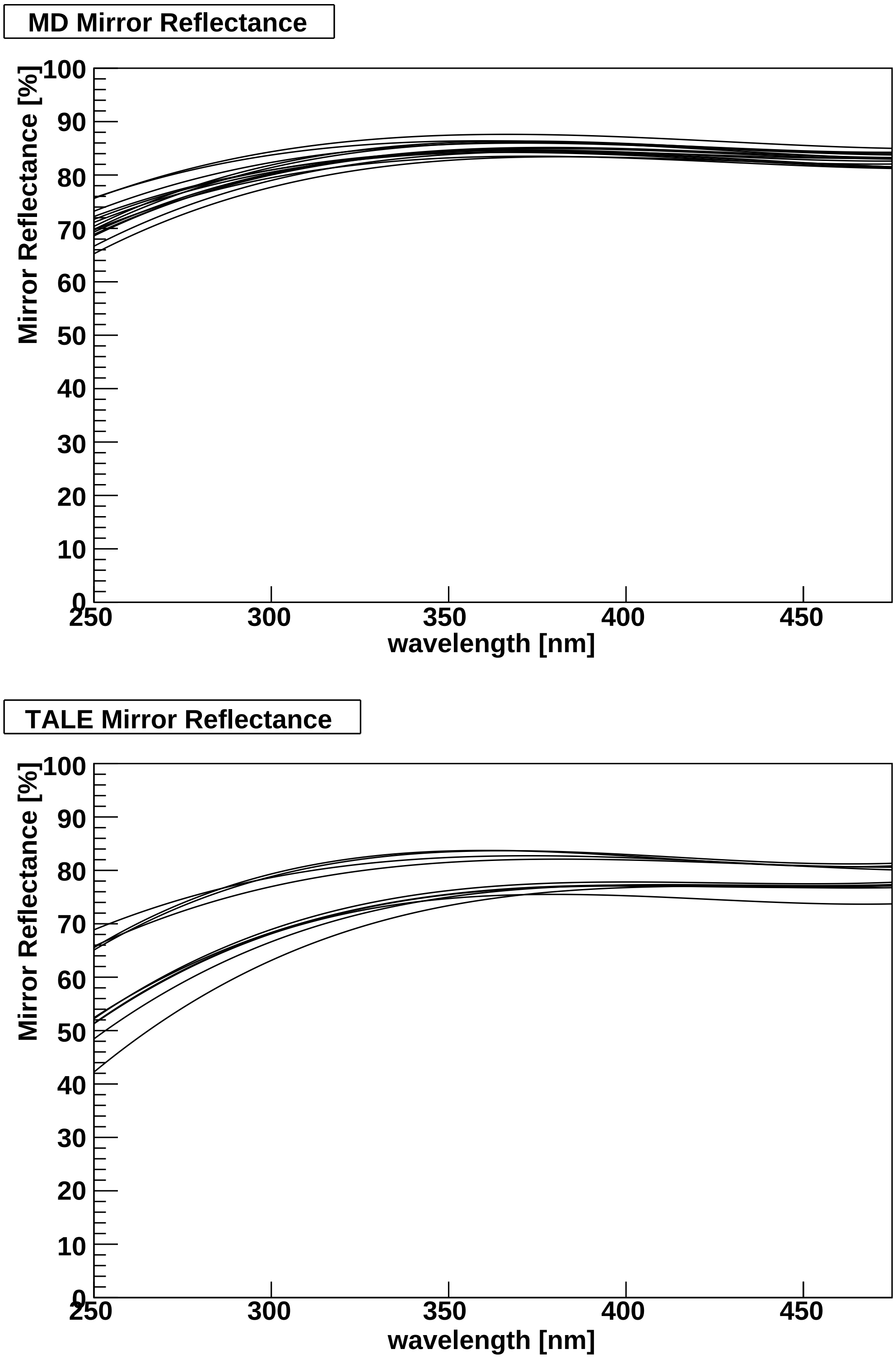

FIGURE 2.10: The TA MD (top) and the TALE FD (bottom) mirror reflectance as a function of wavelength.

2.4.2 PMT Camera

The configuration of the PMT camera is the same as that of the TA-FD station, consisting of 256 PMTs arranged in a 16 ×16 array and equipped with a UV filter at the front of the PMT camera. The PMT camera is installed on the focal plane of the spherical mirror, and the distance between the center of the spherical mirror and the center of the PMT camera is 2.28 m. The size of the PMT camera is 720 × 620 × 360 mm (width × height × depth of the camera). Fig. 2.11 shows a cluster of PMTs with the UV filter seen at the bottom and Fig. 2.13 shows the UV filter transmittance as a function of wavelength. The PMT used is Phillips XP3062/FL (Fig. 2.12), and each PMT has a field of view of 1° × 1°. The size of the PMT is 48 mm and the effective detection area is 1197 mm^2. The quantum efficiency of the PMTs is assumed to have the same value and wavelength dependence for all PMTs, and the values are shown in the right panel of Fig. 2.13. Fig. 2.14 shows the non-uniformity of the PMT.

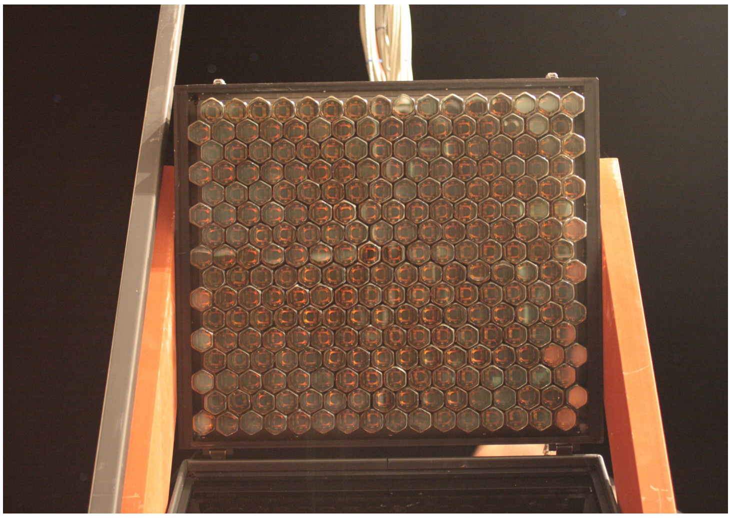

FIGURE 2.11: Photo of a cluster of PMTs with the UV filter at bottom.

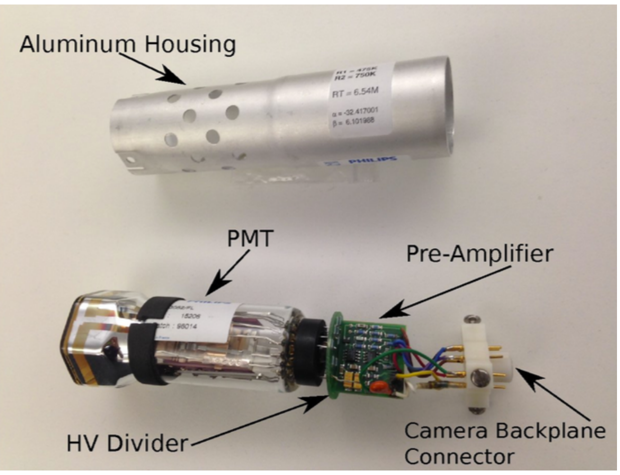

FIGURE 2.12: Photo of a PMT (Phillips XP3062/FL model) used in the TALE camera. The HV divider and preamplifier are built in, and are stored in the aluminum shield shown in the upper part of the photo.

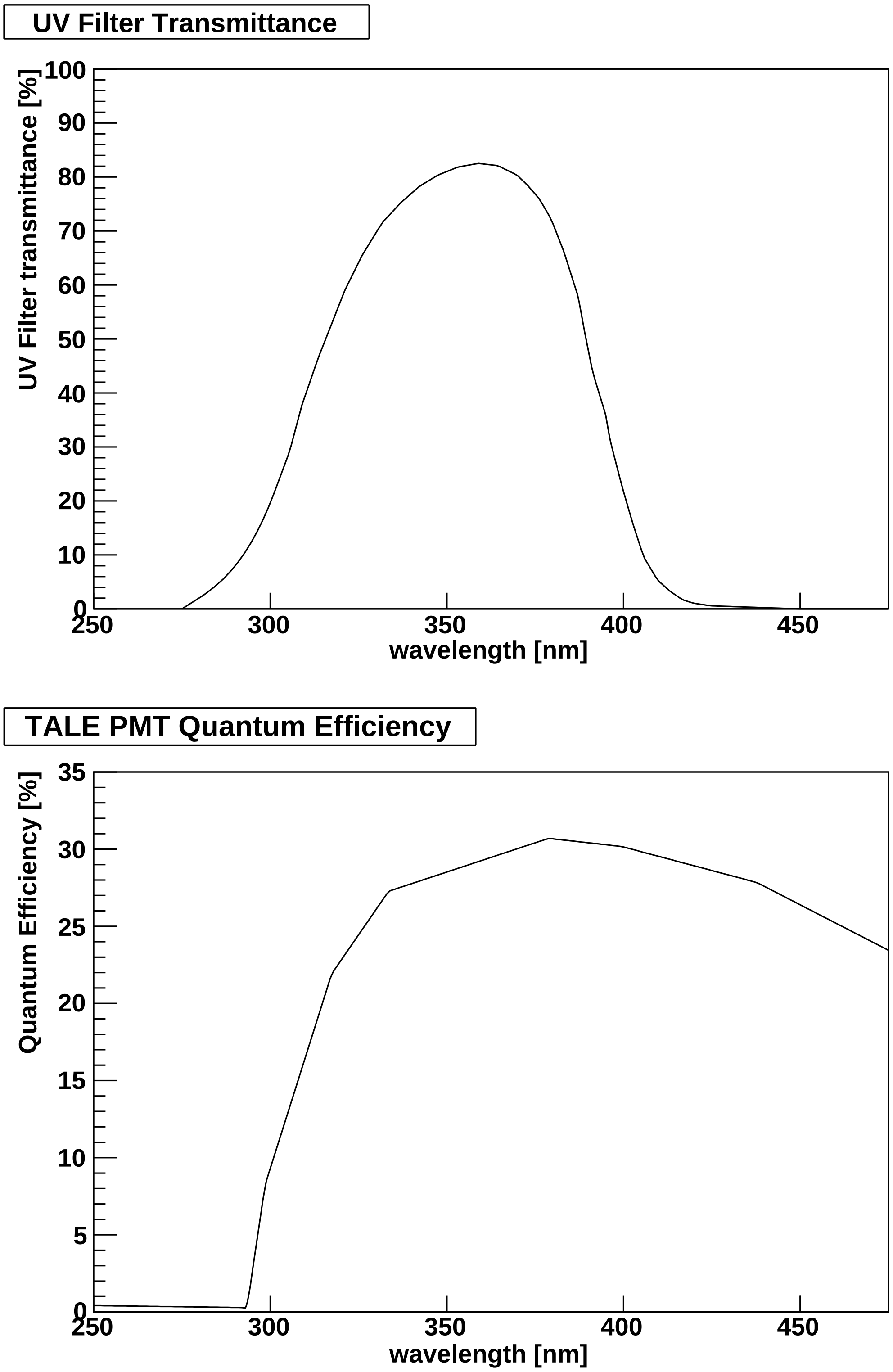

FIGURE 2.13: Top: The UV filter transmittance as a function of wavelength. Bottom: The quantum efficiency of PMT (Phillips XP3062/FL model) as a function of wavelength.

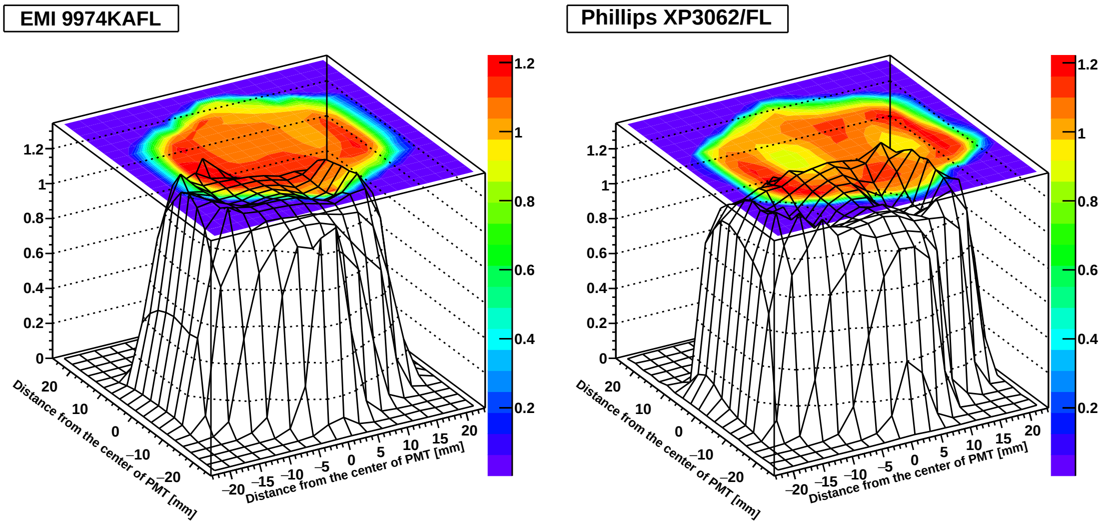

FIGURE 2.14: The tube response profile of EMI 9974KAFL model and Phillips XP3062/FL model. Note that the hexagonal shape of the tube is clearly seen in the projection. Phillips XP3062/FL model have a 10 % larger acceptance than EMI 9974KAFL model.

2.4.3 Readout Electronics and Trigger

Two telescopes share one electronics crate. Each crate consists of link modules, power control boards, 16 FADC boards (Fig. 2.16 left), trigger/host board (Fig. 2.16 right), power supplies, and cooling fans. The photos of the front/backside of the electronics crate are shown in Fig. 2.15. The link module handles all communication and clock distributions to the FADC boards. Each telescope has one link module. The power control boards provide power to the FADC electronics rack, communicate with the link module, and monitor voltages, temperature, humidity, and shutters of the telescope building.

FADC Board

The FADC board is divided into an analog front-end and a digital back-end. The front-end amplifies, digitizes, and stores the 16 PMT signals. In addition, to store the waveforms for the individual PMTs, each FADC board records the analog sum for the column/row of PMT signals. The sum channel signals are digitized and recorded separately with high and low gain channels. In total, each FADC board has 20 channels comprised of 16 PMT signals, a high gain vertical sum, a low gain vertical sum, a high gain horizontal sum, and a low gain horizontal sum, and all channels digitize input signal with 100 ns sampling by an Analog Device AD775 8-bit ADC [74].

The back-end part performs a pulse finding scan and reports the result of those scans to the trigger/host board. The output signals of high gain vertical sum and high gain horizontal sum are scanned whether these signals exceed the threshold. If the sum signal is in exceeds 12 ADC counts above pedestal level, then the signal is discriminated and a trigger bit is set as high, otherwise, the bit is set as low. This bit results are sent to the trigger/host board. On the other hand, the output signals of the low gain vertical sum and low gain horizontal sum are used to correct saturated channels within the camera, and these correction processes are adopted in the reconstruction.

Trigger/Host Board

The TALE Trigger/Host board has two functions, one is that it acts as a HOST device for the 16 FADC boards in each crate, and another is what generates the trigger for the detector. The trigger/host board is comprised of five components; a Trigger DSP (Motorolla 56309), Row Trigger PLD and Column Trigger PLD (Altera EPF8425ALC84), a trigger/timing PLD (Altera EPF8425ALC84), and a communication PLD (Altera EPM7128ELC84). The Trigger DSP and the communication PLD handle the host function of the trigger/host board. All communications from the trigger DSP to each FADC board are via the communication PLD.

Each trigger PLD receives the outputs of 16 discriminator signals from high gain vertical sum channels and 16 discriminator signals from high gain horizontal sum channels respectively, and judges whether the trigger condition is met or not. First, each channel, which receives the discrimination signal, has performed the logical AND between itself and the logical OR of the next two channels. For example, the AND is performed between channel 0 and the result of channel 1 OR channel 2. This is done for each set of channels and form a 15-channel set of 2-fold coincidences. This process is repeated with the 2-fold coincidences in order to form a 14-channel set of 3-fold coincidences. At least one 3-fold coincidence is found, then the detector trigger is issued. This full process of 3 fold coincidence generation is shown in Fig. 2.17 and an example of the satisfaction of the 3 fold coincidence is shown in Fig. 2.18.

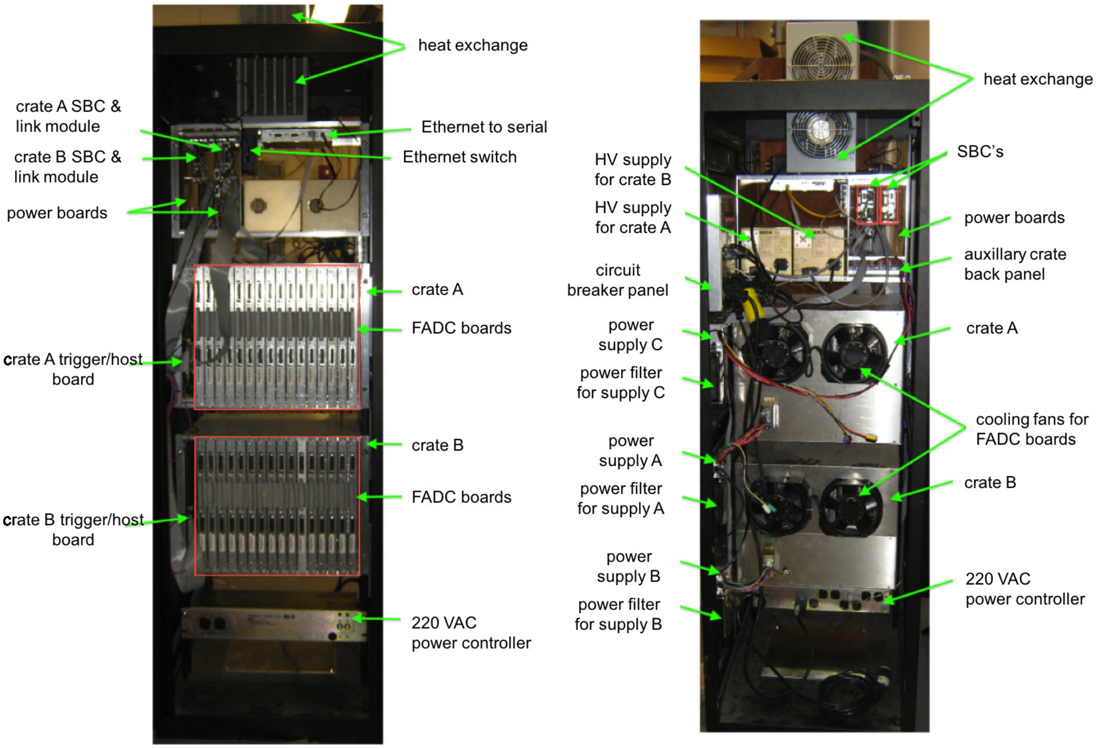

FIGURE 2.15: Photo of electronics crates used in the TALE FD. The electronics for two adjacent telescopes are stored in one electronics crate.

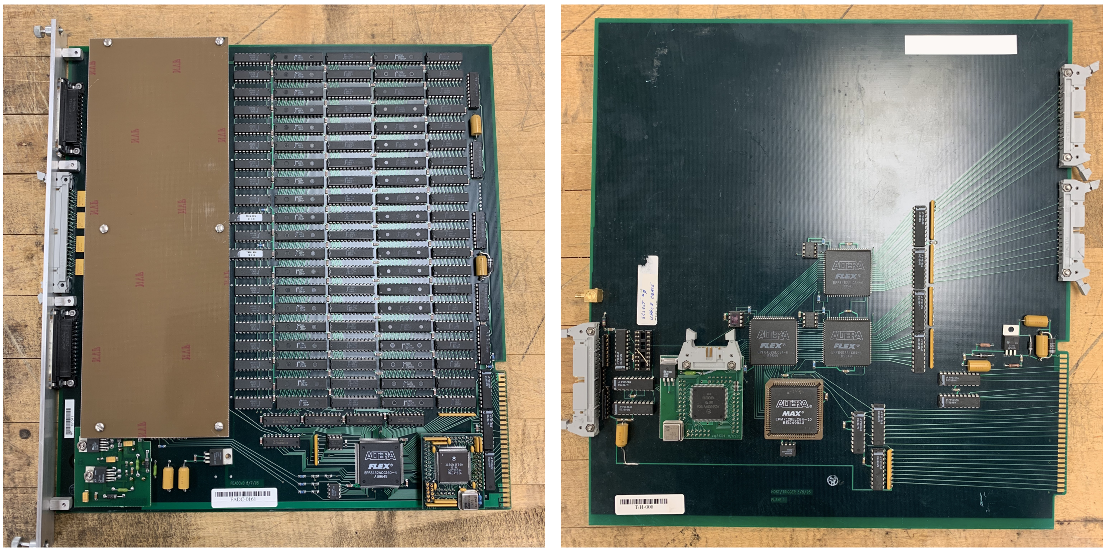

(A) FADC board (B) Trigger/Host board

FIGURE 2.16: Photos of (A): the FADC board and (B): the Trigger/Host board. 16 FADC boards and one trigger/host board are used in each one telescope. A brown shield protects the amplifier and digitization modules for each channel on the left of the FADC board.

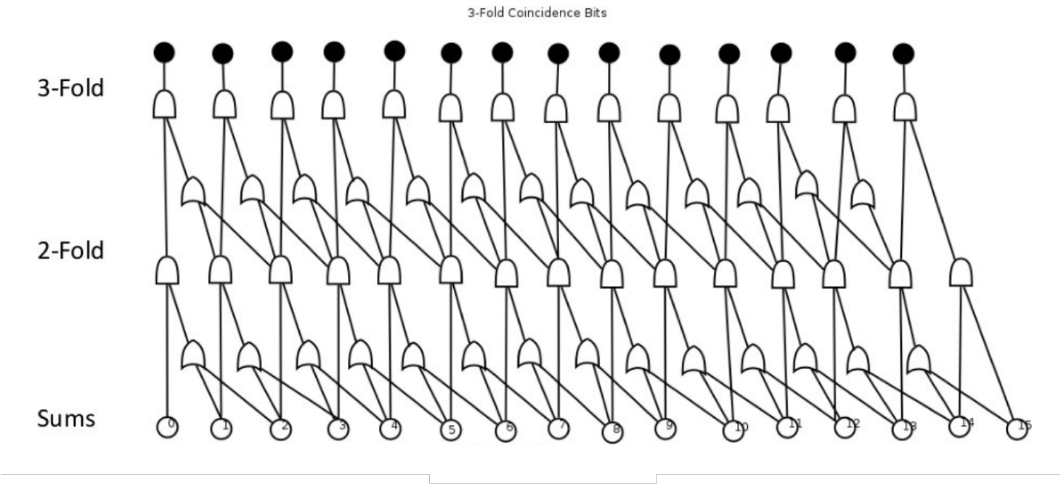

FIGURE 2.17: Schematic view of the 3-fold coincidence. It is composed of AND circuits and OR circuits. First, each channel has performed the logical AND between itself and the logical OR of the next two channels. This process has done for other channel sets then generate 15 sets of 2-fold coincidence. Same processes has performed for 15 sets of 2-fold coincidence, then judges whether one of 3-fold coincidence are satisfied or not.

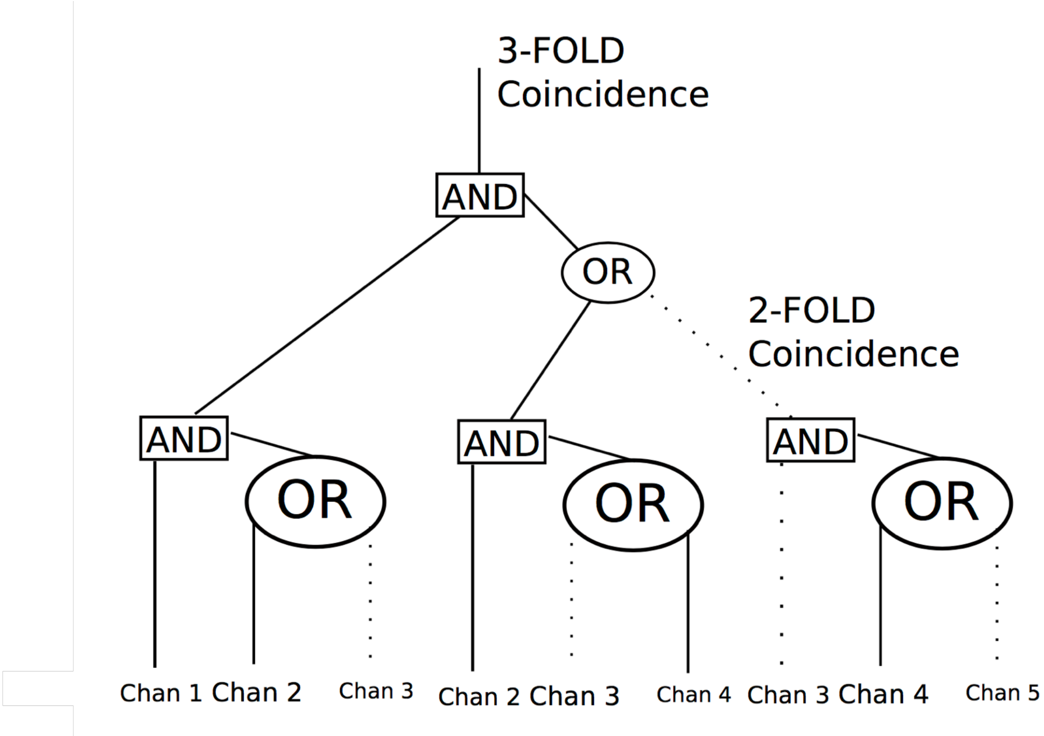

FIGURE 2.18: An example of the 3-fold coincidence. The channels of 1,2,4 drawn with solid line receive the discrimination signal as high, other dashed lines are represented the discrimination signal as low. This example satisfies the 3-fold coincidence, then the detector trigger is issued.

2.4.4 Calibration

The RXF and the UVLED are used to calibrate the optical system for the MD / TALE telescopes. The RXF calibration is performed at the beginning of observation period, i.e., once a month, while the UVLED calibration is performed at the beginning and end of every observation night.

RXF

A Roving Xenon Flasher (RXF), shown in Fig. 2.19, consists of 5 parts: a Xenon flash lamp, a UV band-pass filter (300 - 400 nm), a narrow band filter (355 nm), a neutral density filter, and a teflon diffuser. The RXF emits 1 μs long pulses of light at about 1.5 Hz. Approximately 500 xenon flasher events are recorded in order to get a good measurement of the mean and width of the distribution. The number of photons produced per xenon flasher event varies only slightly from pulse to pulse, about 0.3 %, and the temperature dependence is about -3 % / 10°C between -15 - 40°C.

UVLED

A UVLED module is placed at the center of each mirror to illuminate the PMT cluster. As Fig. 2.20, the UVLED module is mounted at the center of post of the telescope mirror so that it can uniformly illuminate all PMTs. It emits about 500 shots of 355 nm UV light. Their UVLED modules are designed to be temperature stabilized within 1/10°C of 45°C. Compared to the RXF calibration, the UVLED calibration provides nightly PMT gains. Additionally, the PMT gain is balanced to 1 photoelectron / ADC at the beginning of the observation period.

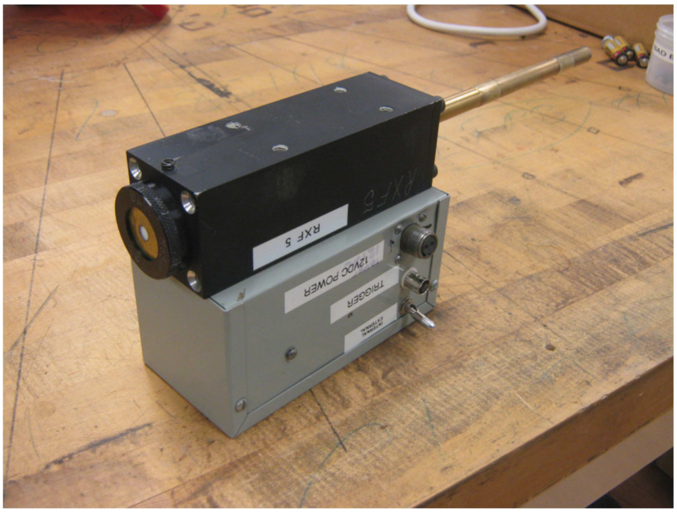

FIGURE 2.19: Photo of the RXF module. The black box contains the Xenon flash lamp itself. The black cylinder at the front of the RXF contains the optical filters (band pass and narrow band). The grey box below the black box contains the electronics for charging and firing the RXF flash lamp.

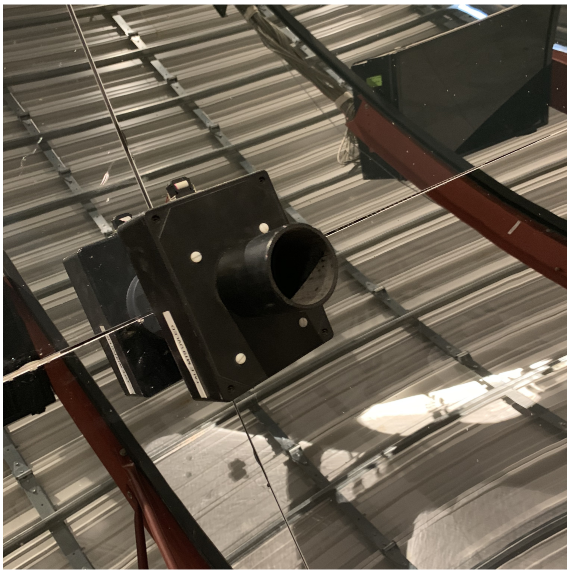

FIGURE 2.20: Photo of the UVLED module mounted at center of TALE mirror.

2.5 TALE Surface Detector Array

2.5.1 Detector

The TALE SD array consists of 80 scintillation counters, including 40 with 400 m spacing and 40 with 600 m spacing, and the total coverage of the TALE SD array is approximately 20 km^2. All SDs are connected to a central data acquisition tower, which is called MDCT (Middle Drum Communication Tower) indicated by a black triangle in Fig. 2.6, by wireless LAN communication with a 2.4 GHz band. The DAQ PC is installed at the MDCT and controls the SD DAQ.

The main component to detect the air shower particles is two layers of a 3m^2 plastic scintillator with 1.2 cm thickness, shown in Fig. 2.23b. Both layers are read out by the PMTs (Hamamatsu R8619) separately. By taking the coincidence of the signals from the upper and lower scintillator layers, the background signal and the signal from the air shower particles can be effectively distinguished. The scintillation lights produced by the charged particles energy deposition are led to the PMTs through wavelength shifting fibers (Kuraray Y-11). The output from the PMTs is digitized by the FADC devices (AD9235BRU-65) with 12-bit resolution, 50 MHz samplings.

The scintillation layers and the PMTs are enclosed in a 1.2 mm thick, 2.3 m × 1.7 m × 10 cm stainless steel box and are covered a 1.2 mm thick iron roof (item 5 in Fig. 2.23a). The SD uses a 12 V deep cycle battery to operate its electronics at 5 W (item 3 in Fig. 2.23a). The battery is automatically charged during the daylight by a 1 m^2, 125 W solar panel, which is shown in Fig. 2.23a, item 4. This ensures a nearly 100% data collection duty cycle.

FIGURE 2.21: Photo of the TALE Surface Detector. The TA MD / TALE buildings are seen far from this SD.

2.5.2 SD Trigger

Whenever the SDs detect signals above a certain intensity, they issue the two types of triggers by themselves, so called a Lv. 0 trigger and a Lv. 1 trigger. The SDs summarize the timing information of the Lv. 1 trigger and send it to the DAQ PC at the central data acquisition tower, in the TALE SD case the MDCT is, every second.

FIGURE 2.22: Photo of the Middle Drum Communication Tower. The batteries and electronics that controls the TALE SD DAQ are installed at the back side of the solar panels. The wireless antenna to communicate with the SDs is install at the top of steel tower.

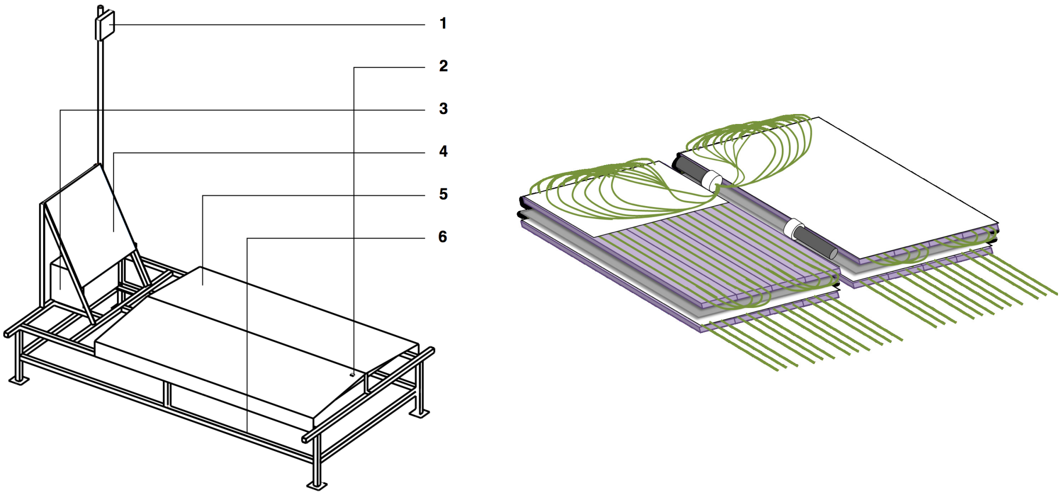

(A) Schematic view of the Surface Detector

(B) Schematic view of inside of the SD.

FIGURE 2.23: (A): Schematic view of the Surface Detector, 1 - Wireless communication antenna, 2 - GPS receiver, 3 - Battery and electronics box, 4 - Solar panel, 5 - Iron roof, 6 - Supporting metal frame. (B) Schematic view of inside of the SD. The wavelength shifting fibers are on the scintillation layers and collected to the PMT face. Each layer are separated by 1mm thick stainless steel.

The central data acquisition tower receives the Lv. 1 trigger summaries from all SDs, then judges the air shower trigger (Lv. 2 trigger).

Lv. 0 trigger

The output signals from PMTs are continuously digitized by the FADC devices. The digitized waveforms are evaluated by a unit of Minimum Ionization Particle (MIP), which corresponds to the energy deposit by ionization loss of a single charged particle. If integrated with 8 slice time windows (= 160 ns) for both signals of upper and lower layers are greater than 0.3 × MIP, which is equivalent to 15 counts in the ADC values, the Lv. 0 trigger is issued. The Lv. 0 trigger rate is around 800 Hz. Once the Lv. 0 trigger is issued, the SD stores the waveform in total 2.56 μs, which starts from before 640 ns of the timing of the Lv. 0 trigger to after 1920 ns of the Lv. 0 trigger timing, to a Lv. 0 trigger list.

Lv. 1 trigger

All stored waveforms in the Lv. 0 trigger lists are integrated with 2.56 μs, which is the length of waveform, and subtract the pedestal. Typically the pedestal is $\sim$ 5 ADC counts. When that value is above 150 ADC counts (equivalent to 3 MIP), the Lv. 1 trigger is issued and the SD stores the timing of Lv. 1 trigger and the average integration of upper and lower layers in a Lv. 1 trigger list. One entry in the Lv. 1 trigger list has 3 Bytes. Each SD sends its own Lv. 1 trigger list to the DAQ PC every second. The Lv. 1 trigger rate is around 20 Hz.

Lv. 2 trigger

The DAQ PC judges the Lv. 2 triggers using by the Lv.1 trigger lists received from the SDs. This trigger is as the air shower event judgment. The DAQ PC sorts the all Lv. 1 trigger lists by time, then scans with the time gate of 32 μs. When it is found that the Lv. 1 trigger timings of any 5 (till Sep. 2019) / 4 (since Oct. 2019) SDs are in the time gate width, the Lv. 2 trigger is issued and calculates a Lv. 2 trigger timing by taking an average of the earliest / latest Lv. 1 trigger timing that were used in the judgment of Lv. 2 trigger. Once the Lv. 2 trigger is issued, the DAQ PC collects the Lv. 0 trigger lists from the SDs that have the Lv. 0 trigger lists within ± 32 μs from the Lv. 2 trigger timing, and store them. This trigger judgment also has performed every second. An example event recorded by Lv. 2 trigger on 07 Nov. 2018 is shown in Fig. 2.24.

2.5.3 Hybrid Trigger

In addition to the SD stand-alone trigger, an external triggering system which sending trigger from the TALE FD to the TALE SD was installed in Nov. 2018, a so called Hybrid Trigger. The arrival directions of air shower can be reconstructed precisely with hybrid mode compared with monocular data, but this needs at least one SD waveform. The shower size at the observation level is compact with decreasing the cosmic ray energies. Thus, it is hard to detect the low energy cosmic rays by the SD trigger because it always requires at least 4 detectors with signals above 3 MIP. Therefore, we installed the hybrid trigger system to collect one or more SD waveforms coincided with the TALE FD shower detection. This allows us to detect the low energy cosmic rays with the hybrid observation.

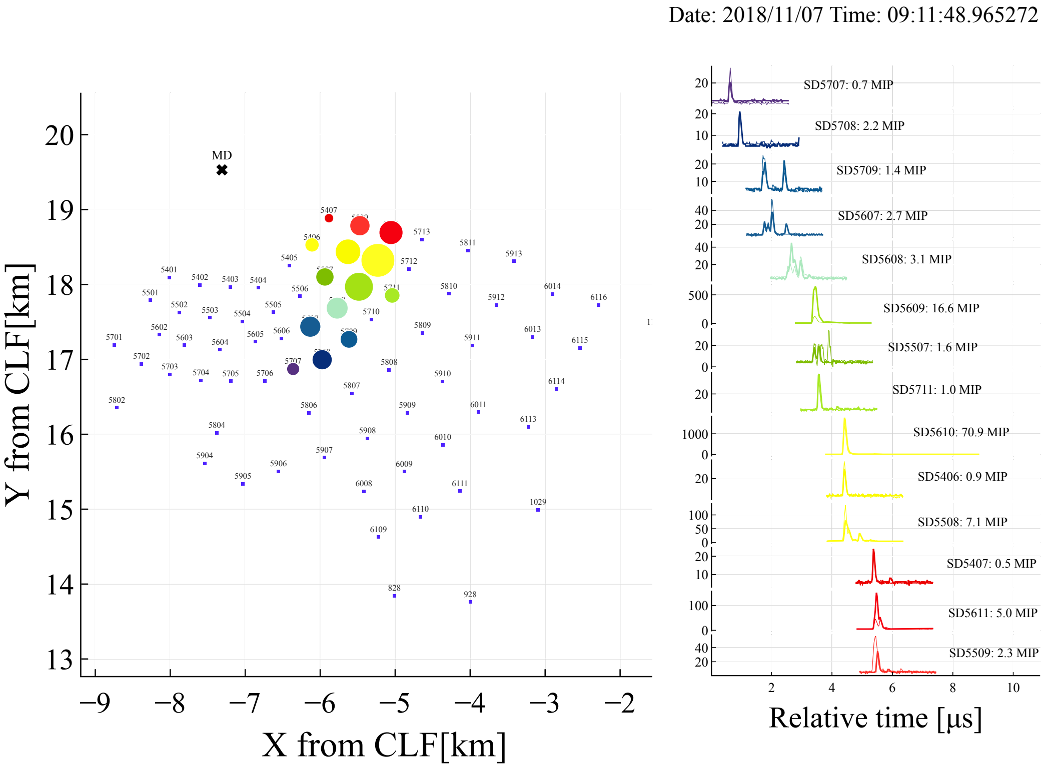

FIGURE 2.24: Event display of an event detected by the TALE SD self trigger. This event was observed on November 07th 2018. On the left is a map of the TALE SD detector with the detector number. The size of the colored circles are proportional to the number of particles detected by the SD and its color shows the arrival timing. The corresponding detector waveforms are shown in the right panel, with an information of total signal in unit of MIP. The Lv. 2 trigger was issued because the SD5608, 5609, 6510, 5508 and 5611 exceeded the threshold of 3 MIP within 32 μs.

The hybrid triggers are sent only if the TALE FD triggered events meet the following criteria,

- A pattern recognition algorithm has performed to select track like events.
- Remove upward going events (laser events for the calibration)
- Calculate a time duration of triggered event after the hit pattern recognition performed, t_{duration}, then
    - all events are send to the SD DAQ PC if $t_{\text{duration}} \geq 500$ ns
    - once in 20 events are send if 200 ns $< t_{\text{duration}} <$ 500 ns
    - once in 200 events are send if $t_{\text{duration}} \leq 200$ ns

The trigger rate of TALE FD itself is around 10 Hz, while the hybrid trigger rate is at kept less than 0.1 Hz by the above criteria. These ensure that the SD DAQ does not fail by increasing trigger rates.

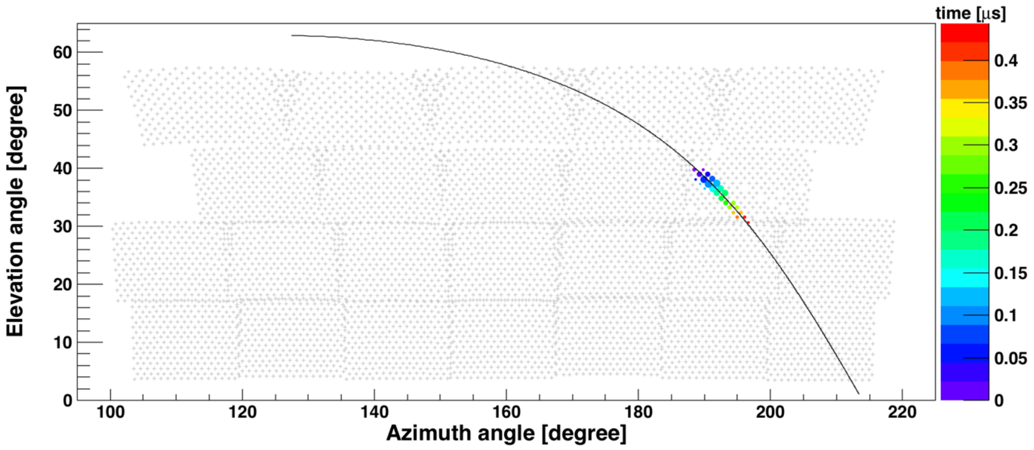

FIGURE 2.25: The TALE FD event display of an hybrid trigger event example. The size of the colored circles is proportional to the number of photons detected by the PMT and its color shows the arrival timing. The total time duration of this event is less than 500 ns, as shown in right side of color bar.

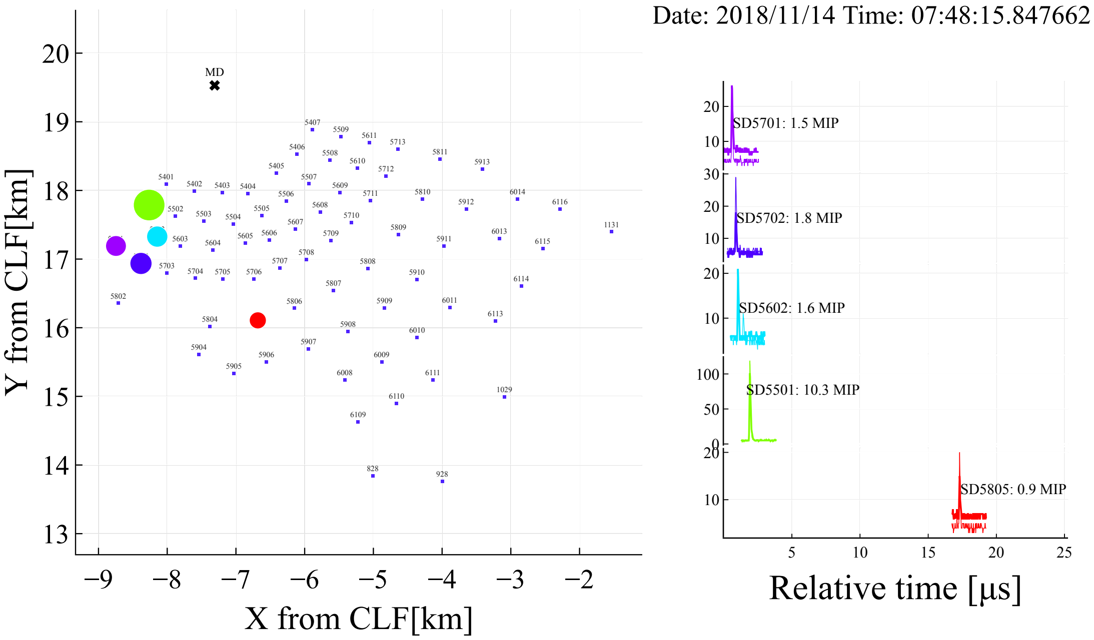

FIGURE 2.26: The TALE SD event display of an event detected by the hybrid trigger. The size of the colored circles on the left plot are proportional to the number of particles detected by the SD and its color shows the arrival timing. The corresponding detector waveforms are shown in the right panel, with an information of total signal in unit of MIP. Only one detector (SD5501) detected the signal above three MIP, then this event was detected by not the SD self trigger, but the hybrid trigger.

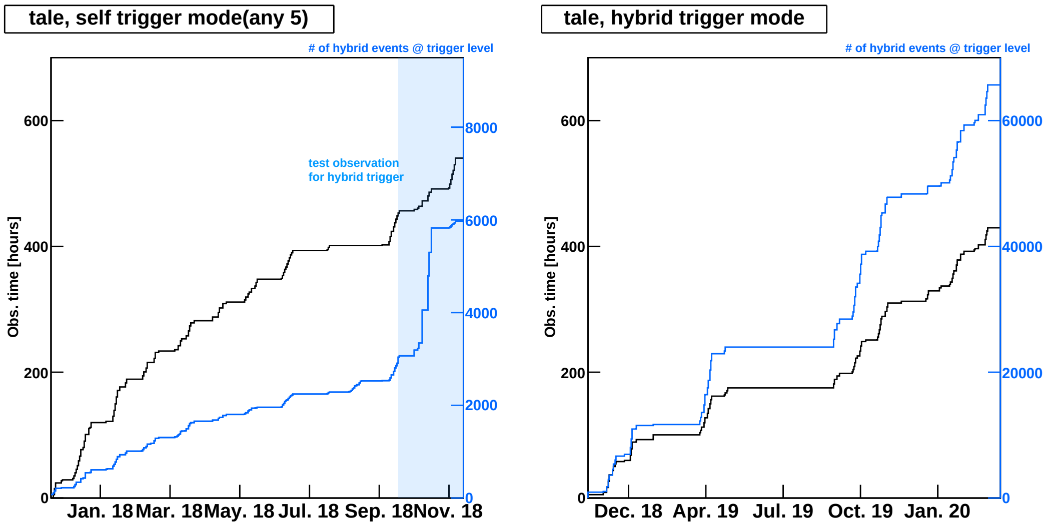

FIGURE 2.27: Cumulative plots of the observation time as black line and the number of hybrid events at the trigger level as blue line. Left panel are plotted the period before the hybrid trigger installation, and right panel are plotted after installation. Light blue shade in left plot is represents the test period of the hybrid trigger system. The number of hybrid events clearly increase by the hybrid trigger system.

2.5.4 Monitoring

Each SD is making monitor data that represent the status of detector itself, and sends them to the DAQ PC. This allows us to check the detector status and to calibrate the sensitivities of detector. There are monitor data in total 3 types, which are taken in intervals with each 1 second, each 1 minute, or every 10 minutes. The data size that is taken in every second is 8 Bytes for each SD, while the others are ~ 9 kBytes in total for each SD. Thus those data are divided into 600 datasets, then send to the DAQ PC over 10 minutes to reduce the load on DAQ PC.

Below are shown the details of monitor data.

- Every second
  - Number of events with signals greater than 3 MIP which corresponds to the Lv. 1 trigger rate
  - GPS time stamps
  - Number of clock counts in 1 second
- Every minute
  - Number of events with signals greater than 0.3 MIP which corresponds to the Lv. 0 trigger rate
  - Battery current and voltage
  - Solar panel current and voltage
  - Temperatures measured at the inside of electronics box, electronics itself and stainless-steel box
- Every 10 minutes

  - Single muon histogram
  - Pedestal histogram
  - GPS module status
  - Number of detected satellites by the GPS module

These monitor data are updated twice a day and operators check whether the SD DAQ and each SD status are stable or not. If something happened, maintenances will be done. Fig. 2.28 shows an example of each monitor data.

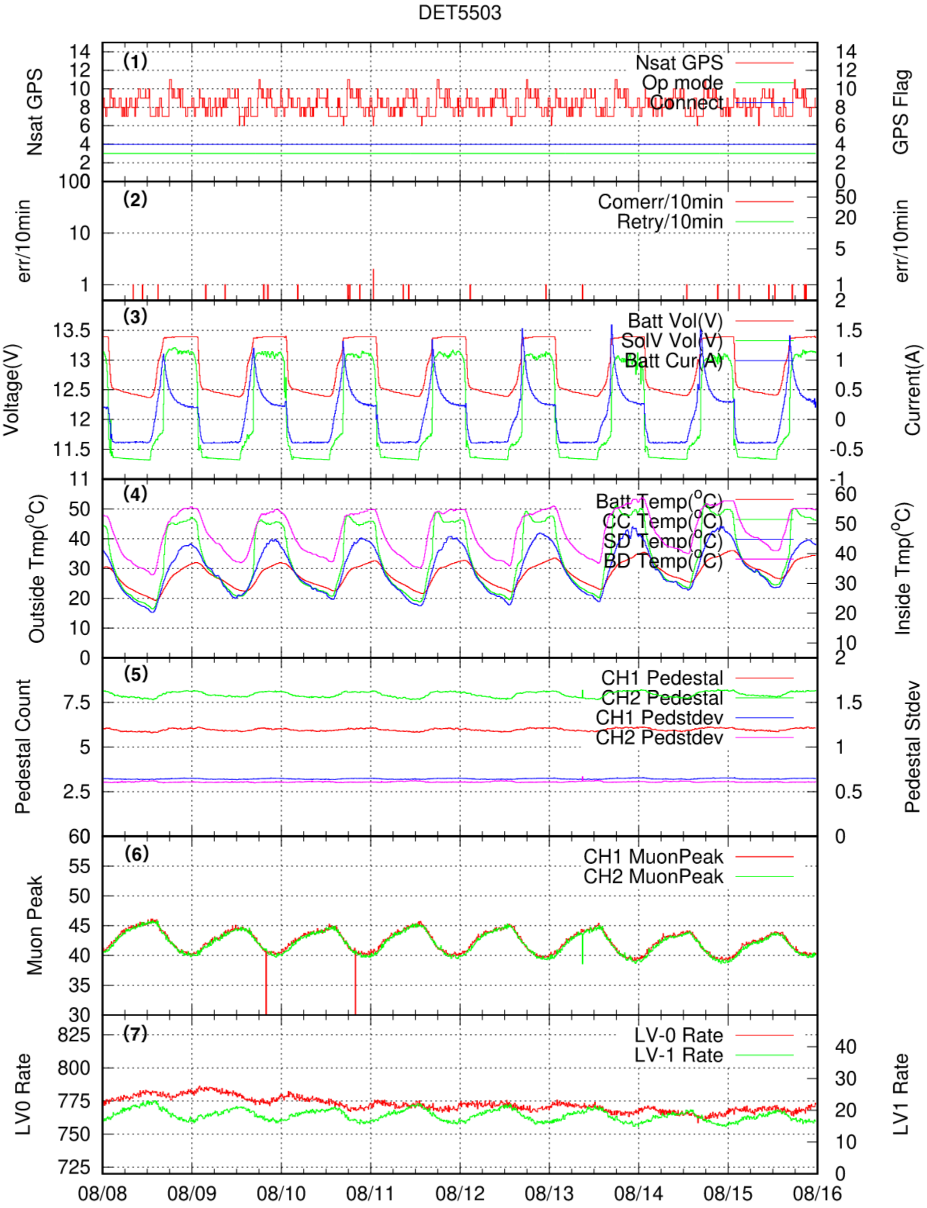

FIGURE 2.28: An example of the monitor data for the TALE SD (DET5503). From top to bottom, (1): the GPS status, (2): the communication status between the DAQ PC and this SD, (3): the battery and solar panel status, (4): the temperatures of each measurement points, (5): the pedestal average and standard deviation for upper and lower layers, (6): the single muon histogram's peak for upper and lower layers, and (7): Lv. 0 and Lv.1 trigger rate.

Single Muon Histogram / Pedestal Histogram

The SD integrates every waveform in Lv. 0 trigger list, and stores as a single muon histogram for upper and lower layers. The gate width of the integration is in total 240 ns, which starts from before 80 ns of the peak timing of waveform to after 160 ns of the peak timing of waveform, i.e., 12 bins ADC sum are stored. Since most of the signals stored in the Lv. 0 trigger lists are considered to be background signals that are not related to air shower particles, the peak height of a single muon histogram can be used to calibrate the sensitivity of each SD signal. On the other hand, The pedestals are also obtained by integration of signals every 8 time slices for each layer. Each SD sends these histograms to the DAQ PC every 10 minutes. Fig. 2.29 shows examplea of the pedestal and single muon histograms obtained by one TALE SD.

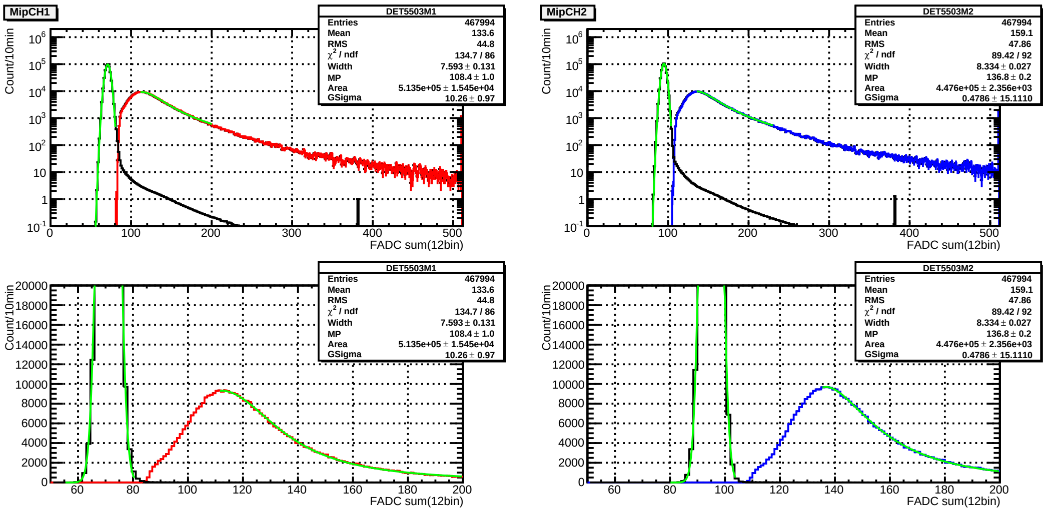

FIGURE 2.29: Pedestal and single muon histograms obtained by DET5503. Logarithm scale in upper panel, and same plots but linear scale with narrow range in x axis in bottom panel. Left plots are obtained by the upper layer, and right plots show the lower layer. Narrow distributions in each panels indicate the pedestal histograms, and wider one shows the single muon histograms. Fit results are shown with green curves.

2.6 Atmospheric Monitoring

The fluorescence light and Cherenkov light produced by air shower particles are scattered and absorbed by atmospheric particles when they propagate through the atmosphere. It is important to monitor the atmospheric conditions to estimate the primary cosmic ray energy from the detected photons.

The TA / TALE FD analyses are used the following three parameters.

- Atmospheric parameters (temperature, pressure, and humidity)
- Atmospheric transparency
- Cloud

Here I introduce measurements of these atmospheric parameters.

2.6.1 Atmospheric parameters

The atmospheric parameters such as pressure, temperature, and humidity are important for the FD measurement. These parameters are used for the calculation of the fluorescence yield, the Cherenkov production, atmospheric depth, transparency of the atmosphere. These parameters should be measured periodically as the atmosphere is changed by time, Those parameters are measured by the radiosonde / the GDAS and we use the public database provided by them.

Radiosonde

The radiosonde measurement is done by a balloon up to 30 km above sea level. There are six launching sites for the radiosonde around the TA site by meteorological instrument. At each site, the characteristics of the atmosphere are measured every 12 hours and they are opened to the public on the website [75]. The atmospheric parameters measured by ELKO site (40.87 North, 115.73 West) and SLC site (40.77 North, 111.97 West) are used in this systematic study because the climate of ELKO is similar to the TA site and SLC site is nearest to the TA site.

GDAS

The Global Data Assimilation System (GDAS) interpolates meteorological data measured with various types of observations, which are at the surface, by balloons (radiosonde included), wind profilers, aircraft reports, buoys, radars, and satellites, in the world [76] and publishes the meteorological data with the one-degree grid in latitude and longitude [77]. Their meteorological databases are summarized every 3 hours as a function of mandatory pressure levels. We adopt the nearest GDAS grid point from the TA site, where is 39 degrees in latitude and -113 degrees in longitude shown as star mark in Fig. 2.30, and use it as a standard atmospheric profile data in this thesis.

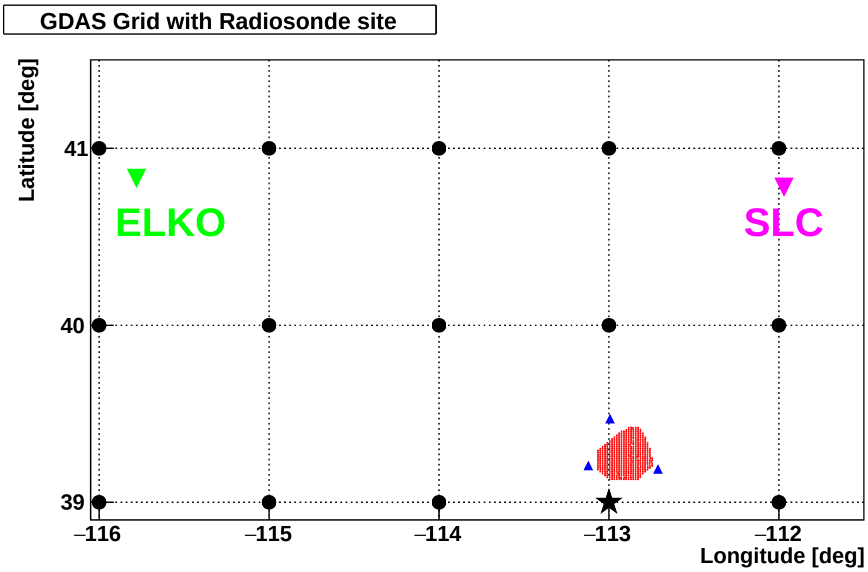

FIGURE 2.30: Location relations of the TA site and the GDAS grid, and the radiosonde measurement sites. Star mark indicates the adopted location by the TA measurement.

2.6.2 Atmospheric Attenuation

The atmospheric attenuation is one of the most important calibration factors because it affects the reconstructed energy directly. Two main components for attenuation have to be considered in the fluorescence measurement. One is coursed by the atmospheric molecules, another is by aerosols. The scattering phenomenon caused by molecules is called Rayleigh scattering. It is well known by atmospheric parameters corresponding to temperature and pressure. Thus, the important thing for measurement of the atmospheric attenuation is the scattering caused by aerosols, called Mie scattering. As the atmospheric aerosols depend on the time, the atmospheric attenuation has to be measured frequently. We have two atmospheric attenuation measurements, one is by a Light Detection And Ranging (LIDAR) system, another is a Central Laser Facility (CLF) system.

LIDAR

The LIDAR system is installed near the BRM FD station. Fig. 2.31 shows a photograph of the LIDAR system. The LIDAR is composed of a YAG laser with 355 nm wavelength, 4 mJ power and 1 Hz frequency(ORION made by ESI), a 30 cm diameter telescope (LX200GPS-30 made by MEADE), a PMT (R3479, made by HAMAMATSU) with a UV filter. The atmospheric attenuation is measured by detecting the backward scattering photons in the laser shooting. The photons are detected by the PMT and digitized by an oscilloscope. The LIDAR system operated before and after observation with 4 types of measurement: 500 vertical shots and 500 horizontal shots with two types of energy, respectively. The details of the operation and analysis can be found in [78].

The attenuation factor of Mie scattering can be measured by the LIDAR system through the detection of back-scattered photon subtracted by the attenuation for the Rayleigh scattering, which can be calculated by the measured atmospheric parameters. The system provides an extinction coefficient that is the inverse of the horizontal attenuation length for each height for every observation day. The data obtained by the horizontal shots can measure the extinction coefficient on the ground. The distribution of the attenuation for the component of the Mie scattering is shown in Fig. 2.32 left. For the index of the attenuation, we define the vertical aerosol optical depth (VAOD)

$$T_{\rm Mie} = \exp(-\mathrm{VAOD}), \tag{2.1}$$

where $T_{\rm Mie}$ is the transparency by the Mie scattering. The measured VAOD is $0.035^{+0.019}_{-0.013}$. The amount of the aerosol is reduced as the altitude increases. Thus, the extinction coefficient $\mathrm{Mie}(h)$ at the several heights h is expressed as

$$\mathrm{Mie}(h) = \exp(-h/H), \tag{2.2}$$

where H is a scale height for the aerosol distribution. This parameter can be obtained by fitting for the attenuation length on the ground and VAOD at each height. The fitted scale height is obtained for 1.0 km The obtained VAOD value is in reasonable agreement with those of HiRes [79].

FIGURE 2.31: A picture is LIDAR's optical system (telescope, laser, etc).

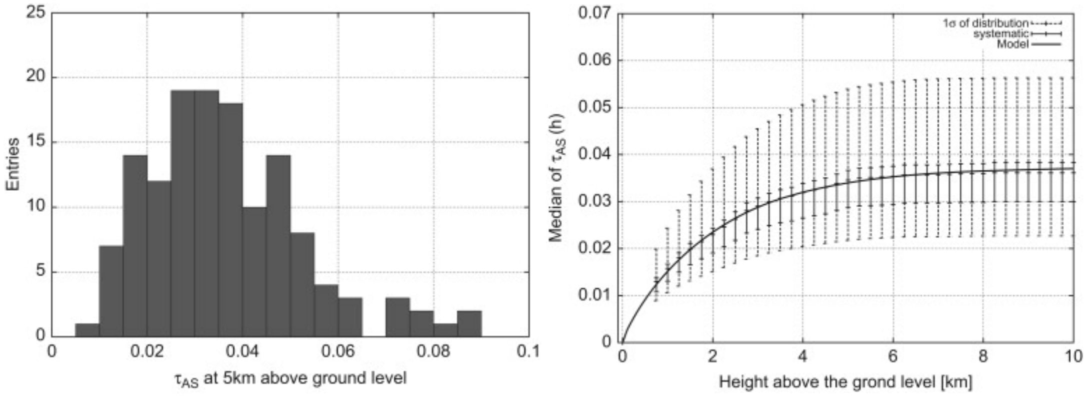

FIGURE 2.32: Results of the TA LIDAR measurement. Left: the histogram of VAOD 5 km above from the ground. Left: Median of the VAOD as a function of the height above the ground level. The systematic errors and the one σ region of its histogram are also shown [78].

CLF

The CLF system is installed at the center of TA site with the same distance 21 km far from all three FD stations, and shots the vertical UV laser (355 nm, 5 mJ) as same as the LIDAR. To detect side scattered photons by three FD stations can be used to measure the atmospheric condition every 30 minutes. The same approach as the LIDAR measurement has performed to the CLF data, then we obtained the preliminary result that the median of measured VAOD and 1σ widths of each side tail is $0.043^{+0.025}_{-0.015}$ [80].

Furthermore, the seasonal variation of the VAOD values has been reported in [81]. In the future, this seasonal dependence of aerosols should be considered in the TA FD analysis.

2.6.3 Cloud

The FD measurements are affected by the cloud because the cloud shields the photons emitted from EAS. There are three methods to measure the amount of the cloud: the weather code (WEAT code) visually recorded by the operator in the MD station, the picture taken by the IR camera at the BRM station, and CCD-fisheye camera installed at BRM, LR, and CLF locations. The WEAT code is adopted because almost all periods of FD observations are covered.

Chapter 3

Monte Carlo Simulation

Measuring the cosmic ray mass composition and energy spectrum require an accurate determination of the detector aperture, which often strongly depend on the cosmic ray energies. In order to estimate performance in hybrid mode, we developed a detector Monte Carlo software. This Monte Carlo software is composed of air shower simulations, air shower particles detection by the SDs on the ground, photon generations, and signal detection by the FD PMT camera. Here the details for air showers and detectors simulations are described.

3.1 Extensive Air Shower Generation

3.1.1 CORSIKA air shower simulation

At first, we simulate air showers by the CORSIKA (COsmic Ray SImulations for KAscade) air shower simulation [41]. The CORSIKA is the most famous to simulate the EASs initiated by high energy cosmic ray particles originally made for KASCADE experiment. The CORSIKA can treat many kinds of primary particles such as protons, light nuclei up to iron, hadrons, photons, with choosing various hadronic interaction models. For the hadron interaction models, GHEISHA, URQMD and FLUKA are available at low energy region, and VENUS, QGSJET, DPMJET, SIBYLL, neXus and EPOS are available in high energy regions. For the electromagnetic interactions, EGS4 or the analytical NKG formula can be used. The CORSIKA enables us to simulate all interaction and trajectory for ALL air shower particles up to the observation level, which can be set by users. Thus, the CORSIKA can be calculated the number of particles and the amount of energy deposit at each depth for each particle type (γ, $e^{\pm}$, $\mu^{\pm}$, ν, and hadrons). These information are important for the FD simulation because the number of produced fluorescence and Cherenkov photons are proportional to the number of charged particles and the amount of energy deposit.

Here the primary cosmic ray particles are simulated only protons or irons because the sensitivity of the mass composition measurement by fluorescence telescope is not enough to separate in the nuclei level clearly. For the hadronic interaction model, the FLUKA [82] and the QGSJETII-04 [4] are chosen in low and high energy regions respectively. The EGS4 [83] is selected as an electromagnetic interaction model.

As the number of air shower particles increases with the cosmic ray energies increasing, much computing time are needed to simulate one air shower for higher energies if tracking trajectories and calculating the interactions for all particles one by one. To reduce computing time, a thinning option is available in the CORSIKA. With the thinning mode, users set a thinning factor, and air shower particles, which after each interaction, with energies below the thinning factor multiply the primary cosmic ray energy are grouped as the weighted particle. Descriptions of the CORSIKA thinning approximation can be found in [84, 85]. Additionally, air shower particles with energies below the E_{cut} are not traced. The E_{cut} can be selected for electromagnetic component and hadronic component. The parameters of air shower simulation are shown in Table. 3.1.

Parameter	Description
Primary Paticle	proton and iron
Interaction Model	FLUKA (low energy, E $<$ 80 MeV) QGSJETII-04 (high energy, E $>$ 80 MeV)
Energy Range	$10^{16.2}$ - $10^{18.5}$ eV
Zenith Angle	0 - 60 degree, uniformly
Azimuthal angle	0 - 360 degree, uniformly
Thinning factor	10^{-6}
E_{cut}	250 keV for electromagnetic component 50 MeV for hadronic component
Number of showers	500 events per dlog(E/eV) = 0.1 (E $< 10^{17}$ eV) 200 events per dlog(E/eV) = 0.1 (E $\geq 10^{17}$ eV)

TABLE 3.1: Summarized the CORSIKA input parameters

3.2 Detector Simulation for the Surface Detectors

3.2.1 Dethinning Method

The thinning approach leads to large fluctuations in the number of air shower particles and the time of arrival of the particles, as a results gives different number densities at the ground than the shower simulation without thinning option. The solid lines in Fig. 3.1 left represent the weighted particle trajectories, and the dashed lines represent the particle trajectories not traced due to the thinning algorithm. Only the detectors, which shown as black rectangle at bottom, on the trajectories represented by the solid line detect large number of particles, while the detectors on the trajectory represented by the dashed line do not detect particles. In order to avoid this problem for the SD simulation, a dethinning method were developed for the TA SD simulation [86], and we also applied to the TALE SD simulation. In the processes of dethinning algorithm, a point on the weighted (w) particle trajectory are chosen, which called the "Arbitrary Vertex" shown in Fig. 3.1 right, at first. From this vertex point, the locations of $w - 1$ particles are restored by a two-dimensional Gaussian distribution with a few degrees (set as $\beta \cdot r$ degrees, where r is the lateral distance from the shower core for the weighted particle and β = 3°/km for electromagnetic particles and 1°/km for muons and hadrons) centered on the trajectory of weighted particle. The energy of each restored particle is calculated by a $\pm$10% fractional Gaussian distribution centered on the energy of parent particle. The lateral distribution of simulated air shower with non-thinned mode compared with 10^{-6} level thinned shower and with dethinned shower are shown in Fig. 3.2. The dethinned method well reproduces the lateral distribution of non-thinned shower.

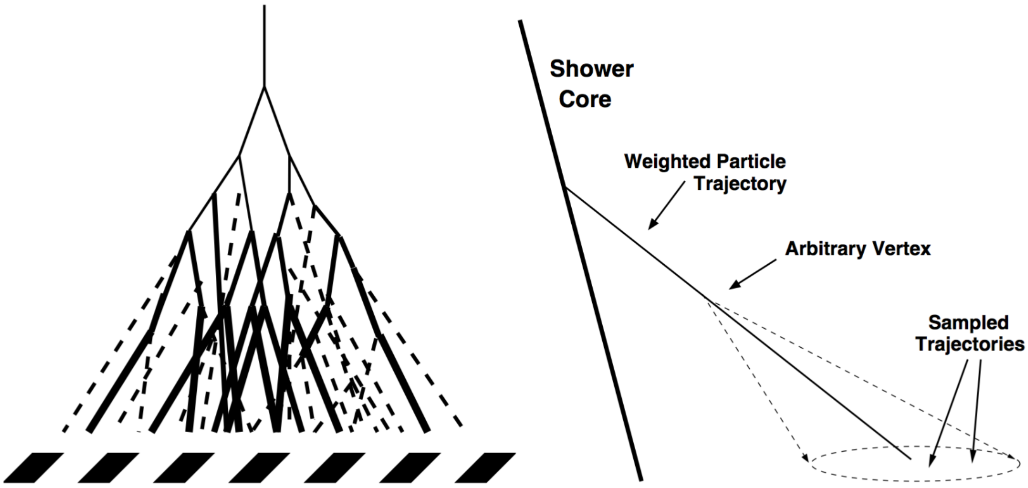

FIGURE 3.1: *Left*: Illustration of the problem caused by the thinning approximation. Dashed lines represent the discarded particles (which would exist in a real shower) and the solid lines represent the weighted particles (thicker lines correspond to larger weights). The surface detector counters are represent by black rectangle at the bottom of figure. *Right*: Illustration of the dethinning algorithm. Taken from [86].

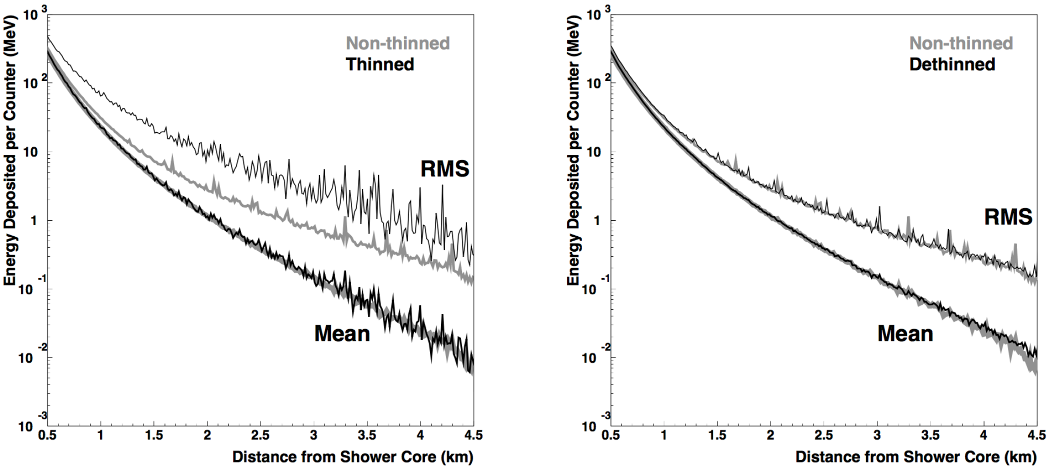

FIGURE 3.2: The energy deposited per counter as a function of the distance from shower core. Simulated air shower initiated by a 10^{19} eV primary proton cosmic ray with a zenith angle of 45° are used. The 10^{-6} level thinned shower is shown in left, and the dethinned shower is shown in right. Both are compared with non-thinned shower. Taken from [87].

3.2.2 Energy Deposition

For the surface detector response simulation, we use GEANT4 package [88]. The GEANT4 can be used to calculate the energy deposition by various type, energy, and zenith angle of particles in the upper and lower scintillation layer. In the detector simulation developed for the TA / TALE SD, a look-up table is prepared for each secondary particle (γ, $e^{\pm}$, $\mu^{\pm}$, p, n, $\pi^{\pm}$), which are consisting of two-dimensional energy deposition histograms in the upper and lower scintillation layer for each energy and secθ slice (see Fig.3.5). Fig. 3.3 shows the configuration of generating the look-up table of the SD response to the secondary particles. Fig. 3.4 shows a detail structure of the SD in the GEANT4 simulation. It includes all of components described in Sec. 2.5.1 such as scintillators, the stainless steel box, the roof, the battery, the solar panel.

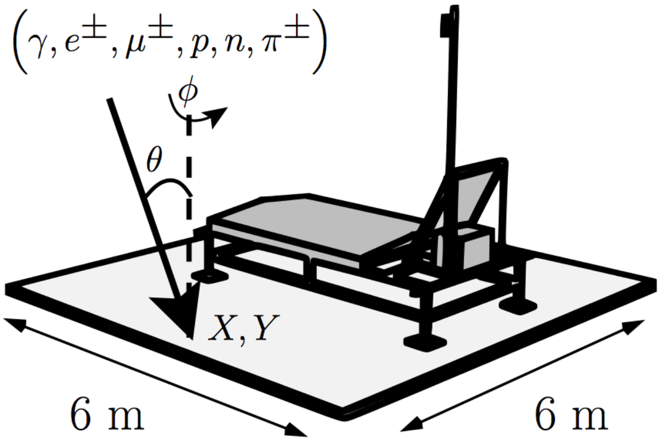

FIGURE 3.3: Configuration of the detector and the injected particle used in generating the SD response by the GEANT4 simulation. For each particle, X, Y are the randomly chosen coordinates inside the 6 m × 6 m square, θ is the (given) zenith angle, and ϕ is the azimuthal angle with randomly chosen . Arrow represents the direction of the injecting particle.

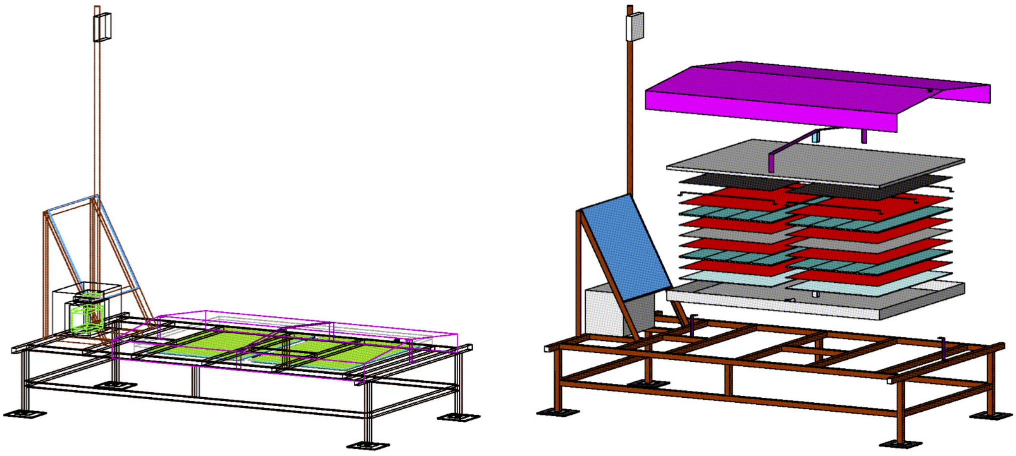

FIGURE 3.4: The structure of TA / TALE SD implemented in our simulation software. The components inside of scintillation box are shifted upward to see clearly.

For the processes of the calculation of energy deposit in the scintillators by secondary particles are described as below,

- Sample a random position X, Y on the ground inside the 6 m × 6 m square, such like Fig. 3.3.
- Sample a random azimuthal angle ϕ.
- Generate the particle with θ, ϕ direction originated from X, Y, then simulate the all possible interaction with inside the detector, the surrounding materials. The results of energy depositions by the initial particle itself and/or the daughter particles inside the upper and lower scintillators are stored.
- Repeat the above steps 1.2×10^6 times.

These procedures are performed for secθ = 1, 1.5, 2.0, 2.5, 3.0, 3.5, 4.0, and for given particle energy. Particle energies are given by followings,

- for γ particle: 63 slices with $\log_{10}(E/\mathrm{eV}) = 0.1$, from $\log_{10}(E/\mathrm{eV}) = 4.7$ to $\log_{10}(E/\mathrm{eV}) = 11.0$
- for $e^{\pm}$, $\mu^{\pm}$, p, n: 50 slices from $\log_{10}(E/\mathrm{eV}) = 6.0$ to $\log_{10}(E/\mathrm{eV}) = 11.0$
- for $\pi^{\pm}$: 49 slices from $\log_{10}(E/\mathrm{eV}) = 6.0$ to $\log_{10}(E/\mathrm{eV}) = 10.9$

To include the effects, where the particles interact inside the detector frame, as well as the back-scattering effects, where the particles hit the ground near the detector and the resulting daughter particles penetrate into the scintillators, the sampling area on the ground (6 m × 6 m) is set as 12 times larger than size of scintillators (1.5 m × 2 m). Examples of the energy deposition histograms produced by above procedure are shown in Fig. 3.5.

Fig. 3.5 (a), (b) show the energy deposition histograms simulated by 1 GeV muons with two zenith angles, 0° and 60° respectively. The energy deposition in the upper layer are indicated in X-axis, and one of in lower layer are indicated in Y-axis. In Fig. 3.5 (a), there is strong peak at where $\log(E_{\mathrm{DEP}}/\mathrm{MeV}) \simeq 0.3$, i.e., $E_{\mathrm{DEP}} \simeq 2$MeV in both layers. While the inclined case, the peak is seen at $E_{\mathrm{DEP}} \simeq 4$MeV in Fig. 3.5 (b) because the particle passes through twice thickness than the vertical case in the detector. In addition, there are two band distributions around 4 MeV in both layers corresponding to that the particle pass through the one side layer and lightly pass another layer. Fig. 3.5 (c), (d) show the energy deposition histograms with simulating 1 GeV γ-rays with zenith angles 0° and 60° respectively. The peak is located at 4 MeV and 8 MeV respectively, twice larger than the vertical muon case. This is because the γ-rays interacts in the roof or the inside of scintillator box then produces the electron / positron pair creation. The band distributions in lower layer corresponds to the energy deposition by the electron / positron generated at the upper layer.

3.2.3 SD Array Response

The look-up table is used to calculate the energy deposition in the SDs by air shower particles simulated with the CORSIKA. In this step, we divide the surface into 6 m × 6 m tiles (one tile corresponds to the Fig. 3.3), and calculate the energy deposition in the SD for each tile up to 8.4 km far from the shower core location. Then, corresponding detector tiles are sampled from 2800 × 2800 tiles with randomly choosing location relation of the shower core and the SD array. The obtained energy deposition are stored as the ADC counts with 12 bit resolution, 50 MHz sampling. The calibration factors discussed in Sec. 2.5.4 are considered here. The background signals are produced based on the Lv. 0 trigger rate, and added to the signals. The calibration data used in our simulation are generated from the actual monitor data discussed in Sec. 2.5.4 , and it consists of 26 types of data shown in Table. 3.2. The stored signals in each SD are applied the same triggering conditions as the actual data described in Sec. 2.5.2, and the signal waveform data is recorded in the same format as the actual data.

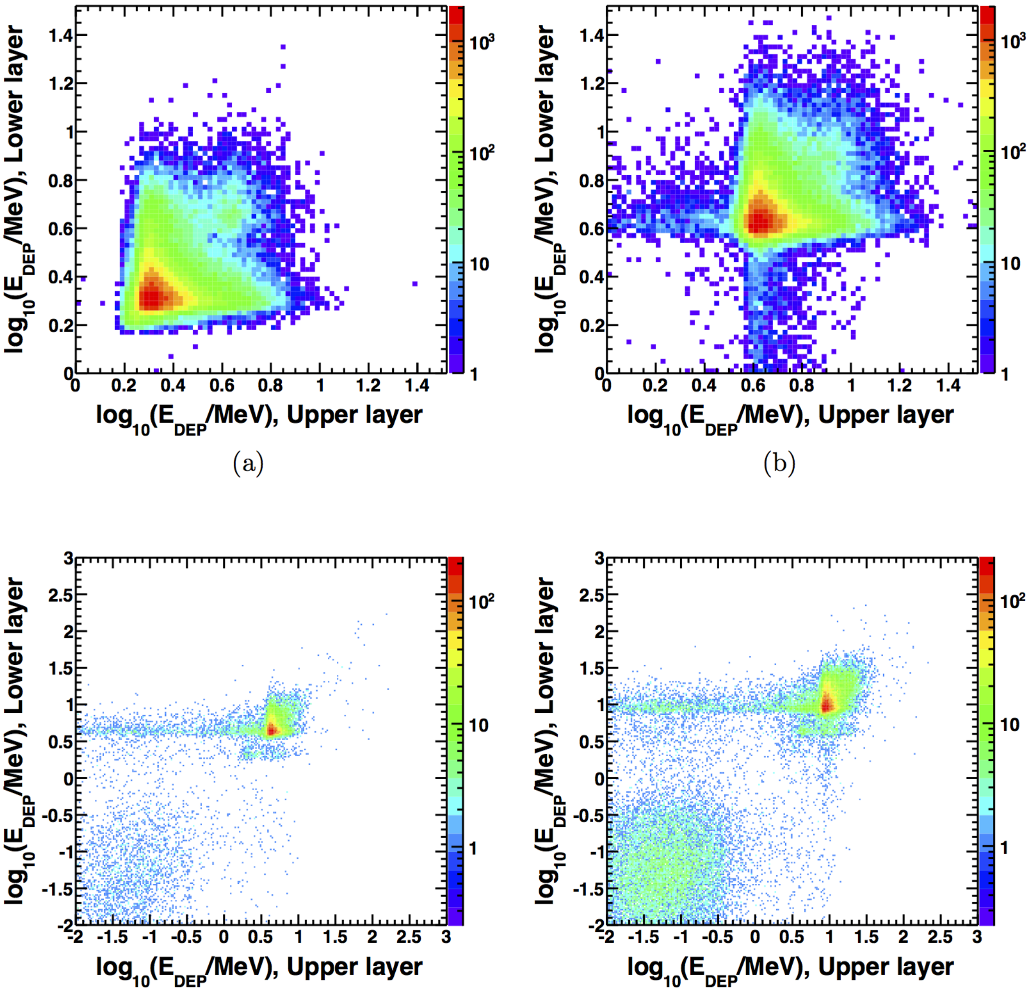

(a) (b)

(c) (d)

FIGURE 3.5: Examples of the energy deposition histograms. X-axis represents the energy deposition in the upper layer, Y-axis represents the energy deposition in the lower layer, and Z-axis (represented by colors) is the frequency. The examples use 1 GeV μ^+ and 1 GeV γ: (a): μ^+ at $\theta = 0°$, (b): μ^+ at $\theta = 60°$, (c): γ at $\theta = 0°$, (d): γ at $\theta = 60°$.

1	time
2	detector number
3	detector status (available or not)
4	conversion factor from energy deposition to photo-electrons in upper layer
5	conversion factor from energy deposition to photo-electrons in lower layer
6	conversion factor from energy deposition to ADC counts in upper layer
7	conversion factor from energy deposition to ADC counts in lower layer
8	single muon peak in upper layer
9	single muon peak in lower layer
10	pedestal average in upper layer
11	pedestal average in lower layer
12	pedestal standard deviation in upper layer
13	pedestal standard deviation in lower layer
14	pedestal peak in upper layer
15	pedestal peak in lower layer
16	left side half width at half maximum for pedestal in upper layer
17	left side half width at half maximum for pedestal in lower layer
18	right side half width at half maximum for pedestal in upper layer
19	right side half width at half maximum for pedestal in lower layer
20	degree of freedom of single muon fitting in upper layer
21	degree of freedom of single muon fitting in lower layer
22	χ^2 of single muon fitting in upper layer
23	χ^2 of single muon fitting in lower layer
24	number of captured satellite
25	PMT linearity in upper layer
26	PMT linearity in lower layer

TABLE 3.2: List of calibration data used in the SD simulation.

3.3 Detector Simulation for the Fluorescence Detectors

3.3.1 Fluorescence Light Emission

In the processes of photon simulation, we divide the shower longitudinal profile into 1g/cm^2 along with the shower axis from the top of atmosphere to easily treat the photon generation. From Eq. 1.19, the number of produced fluorescence photons for each wavelength λ at the i-th segment is

$$N_{i\lambda}^{\mathrm{Fl}} = \frac{\mathrm{d}E_{\mathrm{dep}}}{\mathrm{d}X}\, y_i^{\mathrm{Fl}}(h_i)\, S_\lambda^{\mathrm{Fl}}(h_i)\, \mathrm{d}l_i, \tag{3.1}$$

where i is the segment ID, $\frac{\mathrm{d}E_{\mathrm{dep}}}{\mathrm{d}X}$ is the energy deposit stored in i-th segment calculated by the CORSIKA simulation, $y_i^{\mathrm{Fl}}(h_i)$ is the absolute fluorescence yield at the hight h_i discussed in Sec. 1.3.2, $S_\lambda^{\mathrm{Fl}}(h_i)$ is the fluorescence line spectrum on its height h_i, $\mathrm{d}l_i$ is i-th segment length in g/cm^2 (here is 1 g/cm^2). Here the Kakimoto absolute fluorescence yield [45] and the FLASH spectrum [44] are used. As the fluorescence photons emit isotropically, the number of fluorescence photons $N_{i\lambda}^{\mathrm{Fl,\,tel}}$ injected to the telescope with taking account of the attenuation in the atmosphere are calculated by

$$N_{i\lambda}^{\mathrm{Fl,\,tel}} = N_{i\lambda}^{\mathrm{Fl}}\, T_{i\lambda}^{\mathrm{Rayleigh}}(r_i)\, T_{i\lambda}^{\mathrm{Mie}}(r_i)\, \frac{A_i}{4\pi r_i^2}, \tag{3.2}$$

where r_i is the distance from i-th segment to the telescope, $T_{i\lambda}^{\mathrm{Rayleigh}}(r_i)$ and $T_{i\lambda}^{\mathrm{Mie}}(r_i)$ are a transmittance for the wavelength λ propagating the distance r_i of Rayleigh scattering and Mie scattering respectively, A_i is an effective area of the telescope. The Rayleigh scattering and Mie scattering are described later in Sec. 3.3.3.

3.3.2 Cherenkov Light Emission

The number of Cherenkov photons is also calculated from energy deposit stored in each segment, same as the fluorescence light. From the Eq. 1.22 and 1.23, the total number of Cherenkov photons for each wavelength λ at the i-th segment is

$$N_{i\lambda}^{\mathrm{Ch}} = \frac{1}{\alpha_{\mathrm{eff}}(s)}\, \frac{\mathrm{d}E_{\mathrm{dep}}}{\mathrm{d}X}\, \mathrm{d}l_i\, S_{i\lambda}^{\mathrm{Ch}}(h, s_i) \times \int_{\ln E_{\mathrm{thr}}}^{\infty} y_{\gamma}^{\mathrm{Ch}}(E, h) f_e(E, s)\, \mathrm{d}\ln E, \tag{3.3}$$

where $\alpha_{\mathrm{eff}}(s)$ and the integral term are discussed in Sec. 1.3.2, and $S_{i\lambda}^{\mathrm{Ch}}(h, s_i)$ is the Cherenkov emitted spectrum with the shower age s_i and the hight h_i. As the angular distribution of Cherenkov light is well described as Eq. 1.25, the number of Cherenkov photons injected to the telescope with taking account of the attenuation in the atmosphere are calculated by

$$N_{i\lambda}^{\mathrm{Ch,\,tel}} = N_{i\lambda}^{\mathrm{Ch}}\, T_{i\lambda}^{\mathrm{Rayleigh}}(r_i)\, T_{i\lambda}^{\mathrm{Mie}}(r_i)\, \frac{A_i}{2\pi r_i^2 \sin\theta_i}\, A_{\gamma}(X, \theta_i, h) \tag{3.4}$$

3.3.3 Scattered Light

The produced fluorescence and Cherenkov photons by the air shower particles propagate through the atmosphere and interact with the atmosphere as they propagate. These interactions result in the scattering of light. The first interaction we consider is Rayleigh scattering, which is scattering by air molecules. It depends on the local air density ρ and photon wavelength λ. The second interaction we consider is Mie scattering, which is scattering by dust, or aerosols.

For the case of Rayleigh scattering, transmission coefficient is approximately calculated by

$$T^{\mathrm{Rayleigh}} = \exp\left[-\frac{X_{\mathrm{trans}}}{X_{\mathrm{Rayleigh}}} \left(\frac{400}{\lambda} \right)^4 \right], \tag{3.5}$$

where X_{trans} is the slant depth of photon propagation in the atmosphere in the unit of $\mathrm{g/m^2}$, X_{Rayleigh} is the mean free path of the Rayleigh scattering, which is 2974 $\mathrm{g/cm^2}$ at λ = 400 nm, and λ is the photon wavelength. The angular distribution of Rayleigh scattered light is theoretically given by

$$D^{\mathrm{Rayleigh}}(\theta) = \frac{3}{16\pi}(1 + \cos^2\theta) \tag{3.6}$$

For the transmission coefficient of Mie scattering is calculated by

$$T^{\mathrm{Mie}} = \exp\left[\frac{H_{\mathrm{M}}}{L_{\mathrm{M}}\cos\theta}\left(e^{-h_1/H_{\mathrm{M}}} - e^{-h_2/H_{\mathrm{M}}}\right)\frac{\lambda_{\mathrm{M}}}{\lambda}\right], \tag{3.7}$$

where H_{M} is a scale height that the aerosol density is assumed to decrease exponentially as a function of this height, L_{M} is a horizontal attenuation length at the λ_{M}, h_1 and h_2 are the heights of the scattering point and the receiving point. Here we use H_{M} = 1.0 km, L_{M} = 25 km, λ_{M} = 360 nm. The angular distribution of Mie scattered light, called a phase function $D^{\mathrm{Mie}}(\theta)$, is shown in Fig. 3.6.

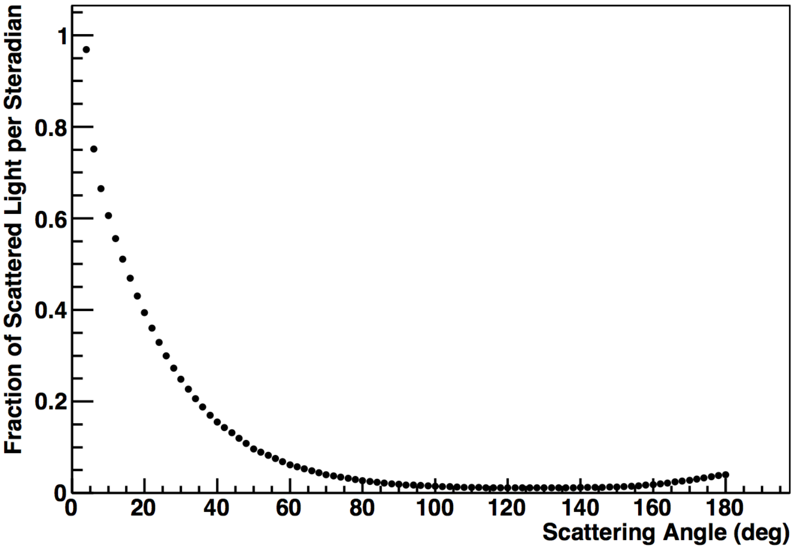

FIGURE 3.6: The phase function of the fraction of scattered light plotted as a function of scattering angle. It is used as the scattering phase function.

Since the Cherenkov photons are accumulated by each segment due to the beaming light (the fluorescence photons are also accumulated however less effective than the Cherenkov photons due to the isotropic light), the scattered photons number is proportional to the integration of Cherenkov photons along the shower axis from the top of atmosphere. The total number of Cherenkov photons for each wavelength λ at the i-th segment $N_{i\lambda}^{\mathrm{Ch,\,total}}$ is calculated the sum of emitted Cherenkov photons in this segment and the integrated Cherenkov photons before this segments as below,

$$N_{i\lambda}^{\mathrm{Ch,\,total}} = N_{i\lambda}^{\mathrm{Ch}} + N_{(i-1)\lambda}^{\mathrm{Ch,\,pass}} \tag{3.8}$$

Thus, the scattered photons by Rayleigh process $N_{i\lambda}^{\mathrm{Rayleigh}}$, Mie process $N_{i\lambda}^{\mathrm{Mie}}$, and the passed photons to next segment are calculated as

$$\begin{aligned} N_{i\lambda}^{\mathrm{Ch,\,pass}} &= N_{i\lambda}^{\mathrm{Ch,\,total}}\, T_{i\lambda}^{\mathrm{Rayleigh}}(\mathrm{d}l_i)\, T_{i\lambda}^{\mathrm{Mie}}(\mathrm{d}l_i) \\ N_{i\lambda}^{\mathrm{Rayleigh}} &= N_{i\lambda}^{\mathrm{Ch,\,total}}\left[1 - T_{i\lambda}^{\mathrm{Rayleigh}}(\mathrm{d}l_i)\right] T_{i\lambda}^{\mathrm{Mie}}(\mathrm{d}l_i) \\ N_{i\lambda}^{\mathrm{Mie}} &= N_{i\lambda}^{\mathrm{Ch,\,total}}\, T_{i\lambda}^{\mathrm{Rayleigh}}(\mathrm{d}l_i)\left[1 - T_{i\lambda}^{\mathrm{Mie}}(\mathrm{d}l_i)\right] \end{aligned} \tag{3.9}$$

Therefore, the number of scattered photons injected to the telescope are calculated by

$$\begin{aligned} N_{i\lambda}^{\text{Rayleigh, tel}} &= N_{i\lambda}^{\text{Rayleigh}}\, T_{i\lambda}^{\text{Rayleigh}}(r_i)\, T_{i\lambda}^{\text{Mie}}(r_i)\, \frac{A_i}{r_i^2}\, D^{\text{Rayleigh}}(\theta_i) \\ N_{i\lambda}^{\text{Mie, tel}} &= N_{i\lambda}^{\text{Mie}}\, T_{i\lambda}^{\text{Rayleigh}}(r_i)\, T_{i\lambda}^{\text{Mie}}(r_i)\, \frac{A_i}{r_i^2}\, D^{\text{Mie}}(\theta_i) \end{aligned} \tag{3.10}$$

3.3.4 Photon Ray-tracing

A “Ray-tracing” technique is used in the TA / TALE FD detector simulation in order to estimate the signal detected at the PMT camera. In the ray-tracing simulation, a trajectory for each photon is calculated for the reflected point on the mirror and injected point on the PMT camera. In order to reproduce the real response, the detailed structure must be implemented in the software. Fig. 3.7 shows a detailed structure of the TALE FD station developed in the simulation software. The combined spherical mirror, supporting columns, cable trays, walls, roofs are implemented.

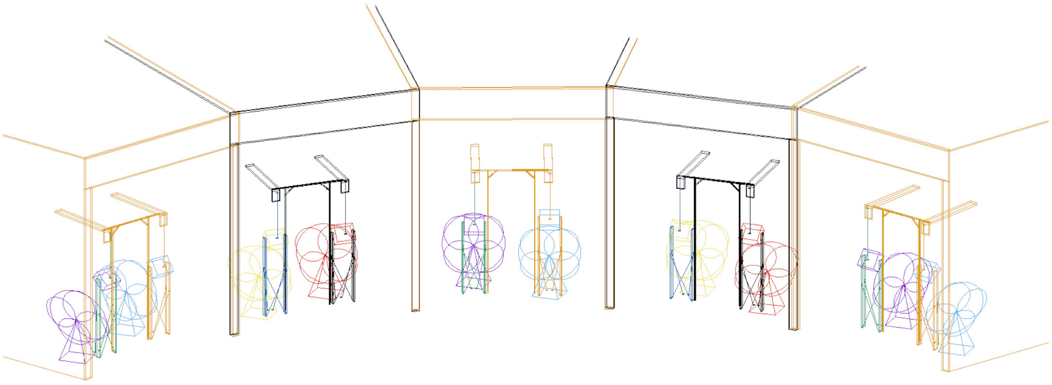

FIGURE 3.7: The structure of TALE FD implemented in our simulation software.

The ray-tracing simulation requires the computing power, because all photons for each wavelength need to calculate their trajectories. For the purpose of a shorter calculation time, the number of photons for ray-tracing is multiplied by the factor of the mirror reflectance, the UV filter transmittance for each telescope and the PMT quantum efficiency. In concrete terms, the number of photons injected to the PMT camera from the i-th segment N_i^{RayTrace} is given by

$$N_i^{\text{RayTrace}} = \int N_{i\lambda}^{\text{photon, tel}}\, R_{i\lambda}^{\text{mirror}}\, \tau_{i\lambda}^{\text{UV}}\, Q_{i\lambda} \mathrm{d}\lambda, \tag{3.11}$$

where $N_{i\lambda}^{\text{photon, tel}} = N_{i\lambda}^{\text{Fl, tel}} + N_{i\lambda}^{\text{Ch, tel}} + N_{i\lambda}^{\text{Rayleigh, tel}} + N_{i\lambda}^{\text{Mie, tel}}$, $R_{i\lambda}^{\text{mirror}}$ is the mirror reflectance, $\tau_{i\lambda}^{\text{UV}}$ is the UV filter transmittance, and $Q_{i\lambda}$ the quantum efficiency of PMT. The PMT response profile factor shown in Fig. 2.14 is considered after the ray-tracing because of the position dependence. For N_i^{RayTrace} photons, the injected position on and time to the PMT camera are calculated one by one. The emitting position of each photon are considered the air shower lateral spread described by S. Lafebre et al. (2009) [40]. The reflection point is determined with a random point inside the mirror effective area. The line is calculated by the emission and reflection point and it corresponds to a ray of the photon. Then, the ray reflects at the mirror and enters the PMT camera by tracing the reflection ray. On the way of tracing, the ray-tracing calculation is finished when the rays intersect the obstructions of telescope or building, or don't inject the PMT camera. After the above processes, the injected photons are converted to the photo-electrons, amplified by each PMT gain and digitized by the FADC device (for the TALE FD), or the integration with the time window (for the TA MD case). The injected time is calculated by the trajectory of ray with considering the response function, the waveform of PMT is generated by the sum of these signals. Repeating the procedure, all PMT signal from the air shower is calculated and stored in each PMTs. Then the trigger judgment is performed.

Fig. 3.8 shows the contributions of fluorescence, Cherenkov, Rayleigh, and Mie scattered photons injected into the telescopes. The red area represents the number of fluorescence photons, the blue area shows the Cherenkov photons, the purple area shows Rayleigh scattered photons, and and the green area shows the Mie scattered photons. The top panel shows the air shower comes across the F.O.V of FD as a result a large number of fluorescence photons are detected. The bottom panel shows the air shower comes toward the FD as a result the Cherenkov photons are dominated.

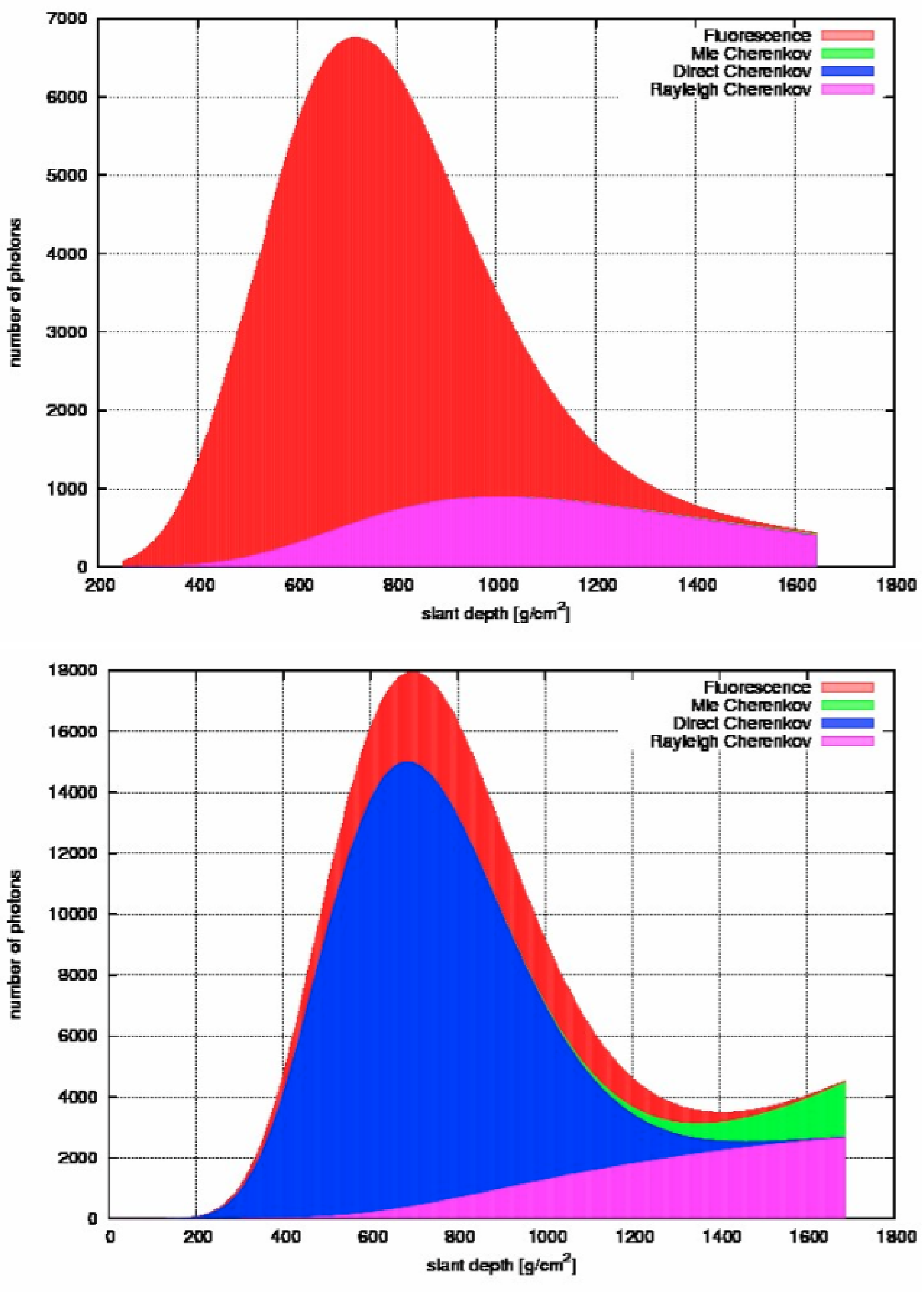

FIGURE 3.8: The number of fluorescence, Cherenkov, Rayleigh and Mie scattered photons injected into the telescopes. The top panel shows in case of the shower geometry across the F.O.V of telescopes, the bottom panel shows in case of the geometry going toward the FD.

Chapter 4

Event Reconstrution

In this section, the overview of the hybrid event reconstruction is discussed. The hybrid reconstruction consists of the following steps: pre analysis for signal selections, determination of a shower detector plane (SDP), shower geometric reconstruction, longitudinal shower profile reconstruction. The hybrid reconstruction of the shower axis is one of the key methods in this thesis. It is based on adding information from one SD to the FD monocular geometry reconstruction. It allows significant improvement in the accuracy of the determination of shower geometries compared with the FD monocular reconstruction. Here we especially concentrate on the event reconstruction processes for the TA MD / TALE FD + TALE SD hybrid data.

4.1 SD Pre Analysis

All triggered SD waveforms are scanned to obtain the particles detection timing and the number of deposited particles by each SD. The first rising time in waveform is used as the timing of the SD. The rising time is obtained by using the S/N ratio. As the pedestal level and its standard deviation for each layer are monitored every 10 minutes, these values are used in this calculation. The waveform is scanned to search a particle signal region that is starting from the bin above 10 $\times\sigma_{\text{ped}}$ to the bin below 3 $\times\sigma_{\text{ped}}$, here σ_{ped} is the standard deviation of pedestal. The first bin of the signal region is used as the rising time, shown in Fig. 4.1. The total deposited particles in the unit with MIP are calculated by the integration value of the signal region by multiplying the conversion factor that comes from the single muon histogram. Then, the SDs that detected signals greater than 3 MIP and are less than 1 km away from the SDP (later described in Sec. 4.3.2) are selected to use the hybrid geometric reconstruction process.

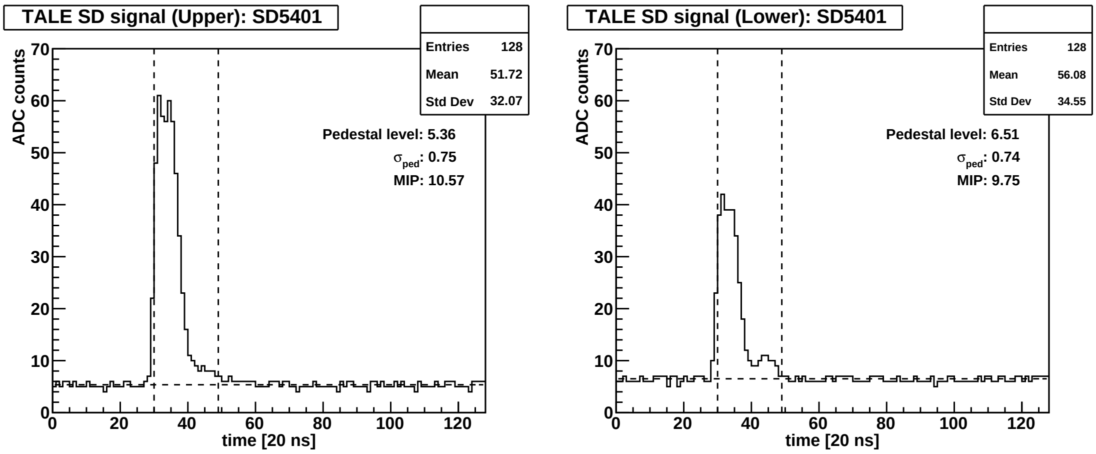

FIGURE 4.1: Examples of the SD signals. The dashed lines indicate the edges of the pulses. The horizontal lines represent average pedestal level.

4.2 FD Pre Analysis

1st Selection

The signal selections for the FD PMT are composed of 4 steps. In the 1st selection, we use a triangle filter to remove the noise hit PMTs. The waveform with air shower signals has a triangle shape as shown in Fig. 4.2 left. In order to calculate the maximum significance $\sigma(w, p)$ with the waveform peak p and width w, all recorded waveforms are fitted by a triangle filter as shown in Fig. 4.3. Here, the significance $\sigma(w, p)$ is defined as below,

$$\sigma(w, p) = \frac{\sum\limits_{i=p-w}^{p+w} F_{\mathrm{sub}}(i)W(i)}{\sum\limits_{i=p-w}^{p+w} P_{\mathrm{rms}}(i)W(i)}, \tag{4.1}$$

where $F_{\mathrm{sub}}(i)$ the i-th bin of waveform subtracted the pedestal mean, $W(i)$ is the weight defined as $W(i) = w - |p - i|$, and P_{rms} is the pedestal fluctuation. The mean and fluctuation of each pedestal is calculated from outside of the pulse region. The filter scan is performed for the peak bin p in all of the bins and the width w from 0 to 30-th bin.

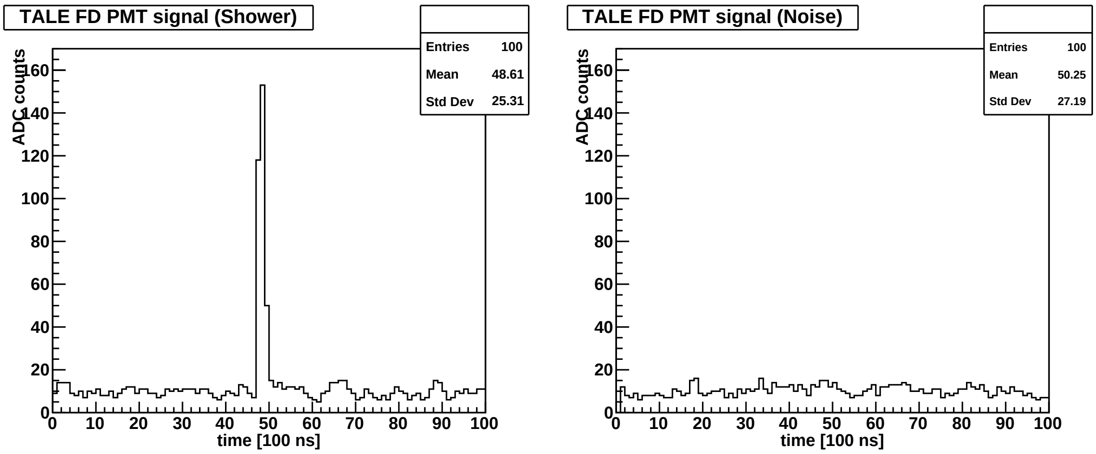

FIGURE 4.2: Typical waveforms recorded by the TALE FD. The air shower signal detected by the TALE FD PMT is shown in left panel, and the noise signal is shown in right panel.

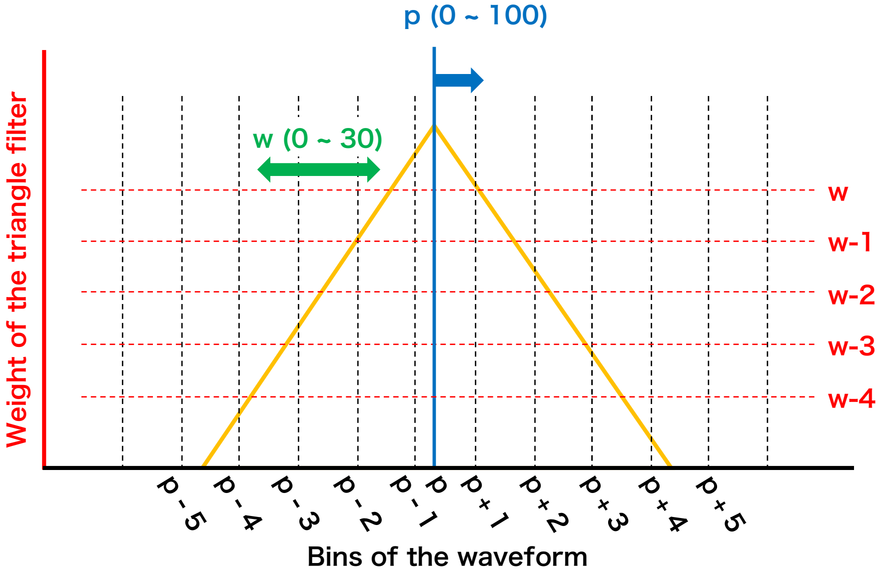

FIGURE 4.3: The schematic diagram of the weighted triangle filter.

When the pair of p and w with maximum significance are found, then the PMT timing T and its error σ_T, and the number of photo-electrons N_{pe} are calculated. Again the waveform is scanned to search for the start bin and end bin of pulse region. The start/end bin corresponds to where the $F_{\text{sub}}(i)$ is less than zero with searching forward/backward from the peak bin. Once the start/end bin are determined, the timing T, timing error σ_T, and the number of photo-electrons N_{pe} are obtained as below,

$$T = \frac{\sum\limits_{i=\text{startBin}}^{\text{endBin}} i \times F_{\text{sub}}(i)}{\sum\limits_{i=\text{startBin}}^{\text{endBin}} F_{\text{sub}}(i)} \times 100 \text{ ns} \tag{4.2}$$

$$\sigma_T^2 = \frac{\sum_{i=\mathrm{startBin}}^{\mathrm{endBin}} (T-i)^2 \times F_{\mathrm{sub}}(i)}{\sum_{i=\mathrm{startBin}}^{\mathrm{endBin}} F_{\mathrm{sub}}(i)} \times 100\ \mathrm{ns} \tag{4.3}$$

$$N_{\mathrm{pe}} = \mathrm{Gain} \times \sum_{i=\mathrm{startBin}}^{\mathrm{endBin}} F_{\mathrm{sub}}(i) \tag{4.4}$$

Here, 100 ns is the bin width corresponding to the 10 MHz sampling. The timing T represents the center of gravity of the pulse. The Gain is the conversion factor from the ADC count to the number of photo-electrons that is obtained by the UVLED calibration as discussed in Sec. 2.4.4.

The distribution of significance $\sigma(w, p)$ is shown in Fig. 4.4 compared with and without shower signals. The significance distribution without air shower signal is almost less than 6σ. Thus, we select the PMTs with significance greater than 6σ as the initial hit PMTs for the next step. The PMTs with less than 6σ are judged whether come from the air shower or not in the 4th selection as discussed later.

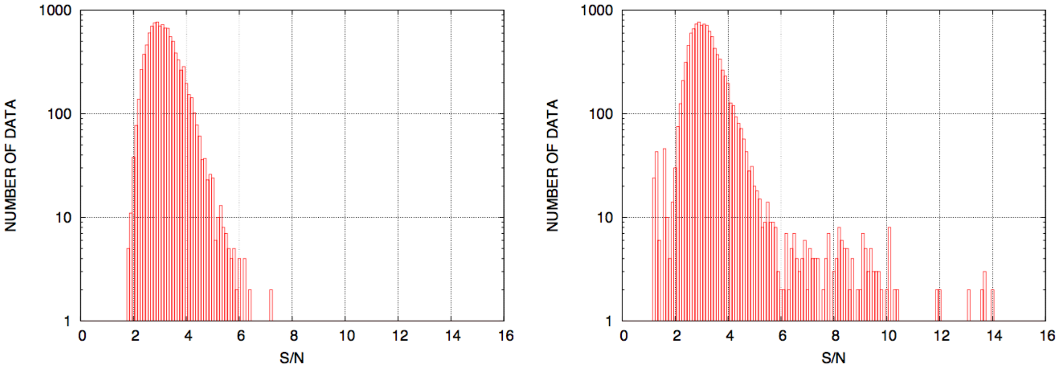

FIGURE 4.4: The distribution of significance calculated by the triangle filter fitting. Left panel shows the distribution without air shower signal, right is one with air shower signal.

By contrast, the TA MD has no FADC devices. Thus, the TA MD case uses another method to calculate the significance of the PMT signal, the PMT timing and its error. The significance calculation for the TA MD is given by

$$\sigma_{\mathrm{MD}} = \frac{N_{\mathrm{pe}}}{\sqrt{40\ \mathrm{p.e.}\ /\mu\mathrm{s}}}, \tag{4.5}$$

where 40 p.e. $/\mu$s comes from the expected number of night sky background photo-electrons at the experimental site.

The PMT timing is stored when the signal exceeds the threshold, as discussed in Sec.2.1. Since the timing of the center of gravity of pulse is required to be accurate geometry reconstruction, it is necessary to add a correction time for each timing recorded by the TA MD. The correction time is well studied in [63, 64], and parametrized as a function of the threshold in mV, the number of photo-electrons in the PMT, and the event inverse angular speed in meter, which is equivalent to the distance between the FD and the shower axis.

The σ_T is also needed to calculate by another way due to the same reason, and given by

$$\sigma_T = \frac{500\ \mathrm{ns}}{\sqrt{N_{\mathrm{pe}}}} \tag{4.6}$$

2nd Selection

Although the 1st selection can remove almost all noise PMTs, the larger signal noise caused by night sky background is remained by only 1st selection. For this reason, further selections are needed to remove the noise PMTs. Since the air shower image detected by the FD is distributed as a line shape, such as Fig 2.9 and Fig. 2.25, this line structure can be used in the 2nd selection. As the number of shower particles is most abundant near the shower axis and decreases far from the axis, the fluorescence and Cherenkov light are dominantly emitted closer to the shower axis. As a result, the PMTs with large signals, which are viewed far from the shower axis, can be considered to noise hits.

Therefore, the central line of the shower image is approximated as the shower axis using the Hough transform algorithm, then the separation angle (β) between this line and the viewing direction of the PMT is calculated. Since the width of shower image depends on the shower geometry (coming or away, near or far) and primary energy, the isolated PMTs in the separation angle distribution are rejected in this selection.

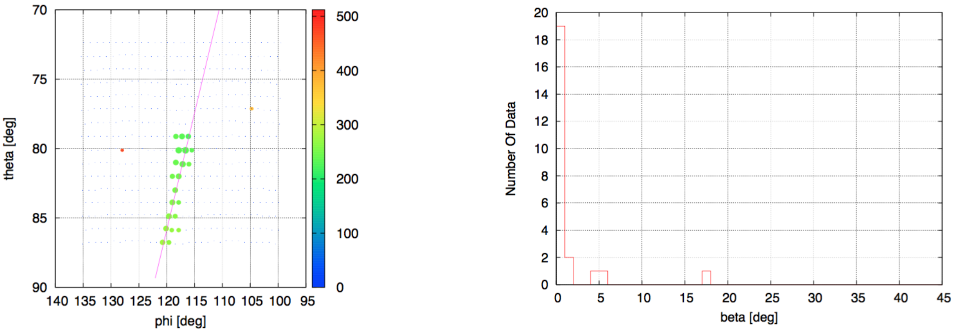

FIGURE 4.5: *Left*: The shower image with the central line of the shower image calculated by the Hough transform represented by magenta line. *Right*: the separation angle β distribution For this example, The PMTs, which are 4° far from the central line, are removed.

3rd Selection

The separated PMTs with noise hit in the shower image are rejected by the 2nd selection. However, the noise PMTs alongside the shower axis are still remained. Thus, we use the PMT timing T calculated by Eq.4.2 to reject the noise hit PMTs in the 3rd selection. The injected timing of each PMT depends on arrival directions and core locations of air showers. The expected arrival time t_i is calculated as

$$t_i = t^* + \frac{1}{c}\frac{\sin\psi - \sin\alpha_i}{\sin(\psi + \alpha_i)} r^*, \tag{4.7}$$

where t^* is the timing at where the center of shower track, ψ is the angle of the shower axis with respect to the direction of the center of the shower track, r^* is the distance from the FD to the shower track center, and α_i is the elevation angle of i-th PMT. These parameters are visualized in Fig. 4.6 left. For the decision by which PMTs are rejected, the residual time ΔT, which is the difference between the observed and expected time, is calculated for all PMTs. Then each residual time is filled into the histogram with 100 ns (for the TALE) / 1 μs (for the TA MD) bin width. The obtained histogram is scanned from the beginning, and the first bin with no entry is as the threshold for the rejection. The PMTs that have a larger residual time than the threshold are rejected in this step.

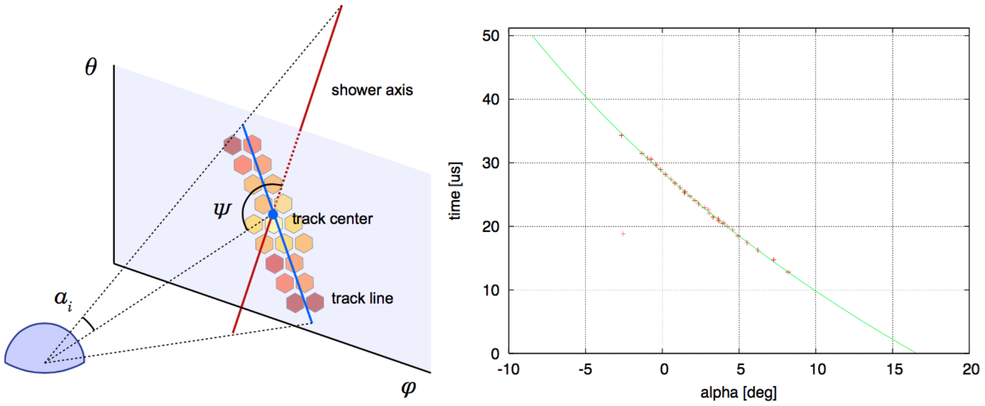

FIGURE 4.6: Shower track in left panel and timing fit to search for the noise PMT in right. The isolated PMT at (-2.5°, 19 μs) is rejected.

4th Selection

Only PMTs with $> 6\sigma$ significance are selected by 1st, 2nd, 3rd selections. For convenience, these PMTs, which passed the 1st, 2nd, 3rd selections, are defined as a tentative Good PMTs. Here, we perform the 4th selection including the PMTs with a small signal less than $< 6\sigma$. This step performs for the removal from the tentative good PMT list, as well as the addition of the rejected PMTs in the previous selections to the tentative good PMT list.

At first, the SDP and fitted timing function $f(\alpha)$, α is the elevation angle on the SDP, are obtained by using all tentative good PMTs. The fitted function is calculated by a hybrid geometry fitting later discussed in Sec. 4.3.3. Second, the timing difference R_i from the fitted function and the opening angle with SDP β_i are calculated for all PMTs, including all rejected PMTs in the previous steps:

$$R_i = |f(\alpha_i) - T_i| \tag{4.8}$$

$$\beta_i = \sin^{-1}(\boldsymbol{n}_i \cdot \boldsymbol{n}_{\mathrm{SDP}}), \tag{4.9}$$

where α_i is the projected elevation angle to the SDP for i-th PMT, $f(\alpha_i)$ is the obtained timing from the fitted function at α_i, $\boldsymbol{n}_i$ is the i-th PMT pointing vector, and $\boldsymbol{n}_{\mathrm{SDP}}$ is the norm vector of SDP. Then, these PMTs are classified by the criteria shown in Table. 4.1. Firstly, the PMTs satisfied with SOFT criterion are applied a judgment routine. Each satisfied PMT is judged by the "linear" fitting of α_i versus T_i with the tentative good PMTs that are within the separation angle $< 5°$ and timing difference < 5 μs. The residual time from the linear fitted function R_{linear}, and the number of used PMTs N_{linear} in linear fitting are used for this judgment. The criteria are shown in Table. 4.2. Once the PMT meets all of these criteria, the PMT is added in the tentative good PMT list. When the tentative good PMT list is updated, then the judgment routine starts over from the beginning. This iteration continues until there is no candidate PMT to judge for the addition/rejection in the SOFT class. Next, the same procedures are applied to the HARD class. This is also repeated until there is no candidate PMT in the class.

Fig. 4.7 shows the event display of actually observed shower candidate at TA FD. Each point represents the PMT direction, color indicates the detected time, and the

	TA FD		TALE FD	
Class	SOFT	HARD	SOFT	HARD
R_i	$< 1.2\mu s$	$< 0.8\mu s$	$< 0.2\mu s$	$< 0.1\mu s$
β_i	$< 4°$	$< 2°$	$< 4°$	$< 2°$

TABLE 4.1: The criteria for categorizing the PMTs to SOFT and HARD classes.

	TA FD	TALE FD
N_{linear}	> 3	
R_{linear}	$< 0.6\mu s$	$< 0.1\mu s$

TABLE 4.2: The criteria of judgment by the linear fitting in the 4th PMT selection.

size of marker is proportional to the number of photo-electrons. The PMTs with $> 3\sigma$ before all selections are filled. After being applied with the 1st to 4th selections are shown in the right panel, the rejected PMTs shows as the cross marker. Therefore, our PMT selections are valid for noise rejections.

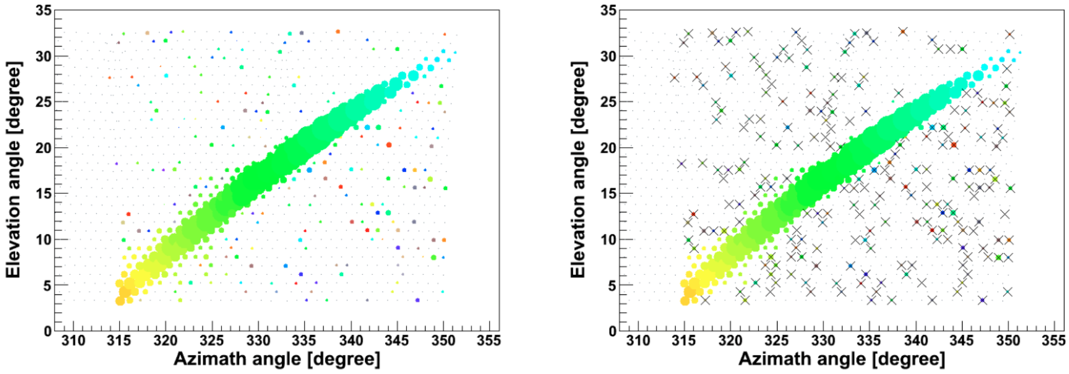

FIGURE 4.7: Event display observed by FD comparing before(left) and after(right) PMT selections. The noise PMTs indicated by cross markers are removed by the PMT selection.

4.3 Shower Geometry Reconstruction

In the geometry reconstruction, we determine a shower geometry that is a core position and an arrival direction of air showers. The reconstruction method using the FD and the SD data, so called "Hybrid Geometry Reconstruction", is described here. In general, the Shower Detector Plane (SDP) that consists of the shower axis and the detector location shown in Fig. 4.8 is determined firstly, then reconstruct the shower axis on the SDP.

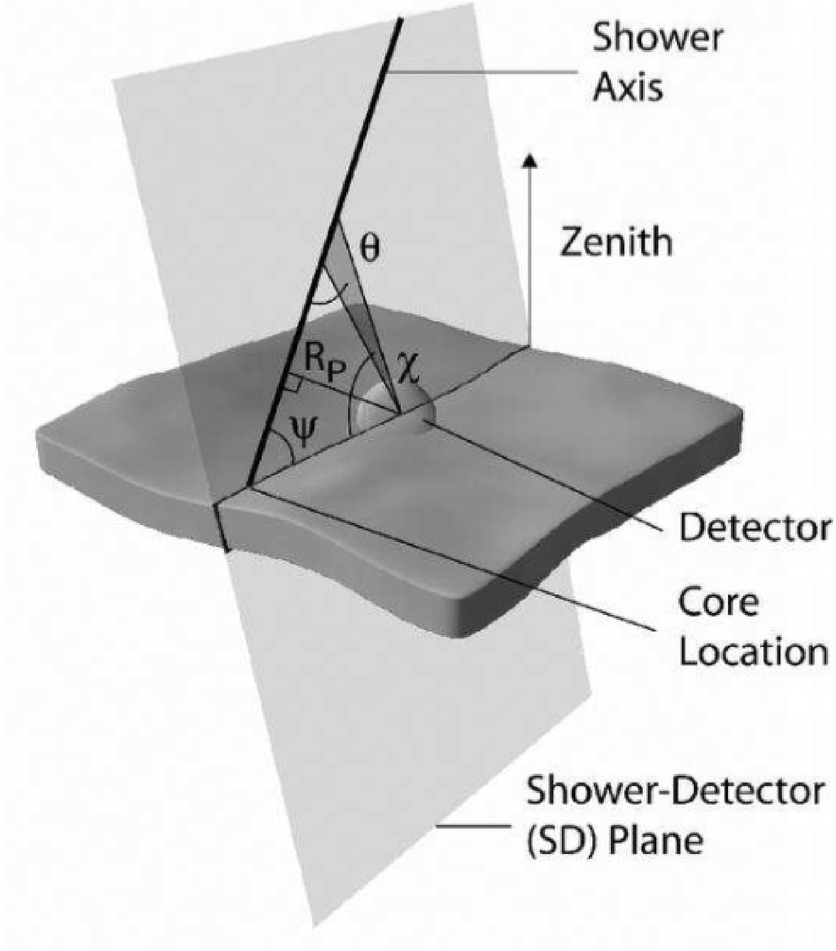

FIGURE 4.8: Shower detector plane (SDP) with the shower axis and the detector location [89].

4.3.1 Estimation of the Field of View for Each PMT

In order to reconstruct the air shower geometry and longitudinal profile precisely, we must know the field of view for each PMT. The field of view of PMT affects the location of PMT camera and the segmented mirror, the overall structure of the telescope including the surrounding obstructions, and the non-uniformity of PMT. Therefore, a ray-trace simulation should be performed and calculated the field of views for every PMT.

In the ray-trace simulation, parallel light is injected into each telescope by 0.125 degree step, and counted the number of photons injected into the PMT. This gives us a sensitivity of each PMT. Examples of the PMT sensitivities and the total directional characteristic of telescope are shown in Fig. 4.10. We calculate a center of gravity of the distribution and use it as the pointing direction for each PMT. The directional characteristics are important to calculate faster in Inverse Monte Carlo as discussed later.

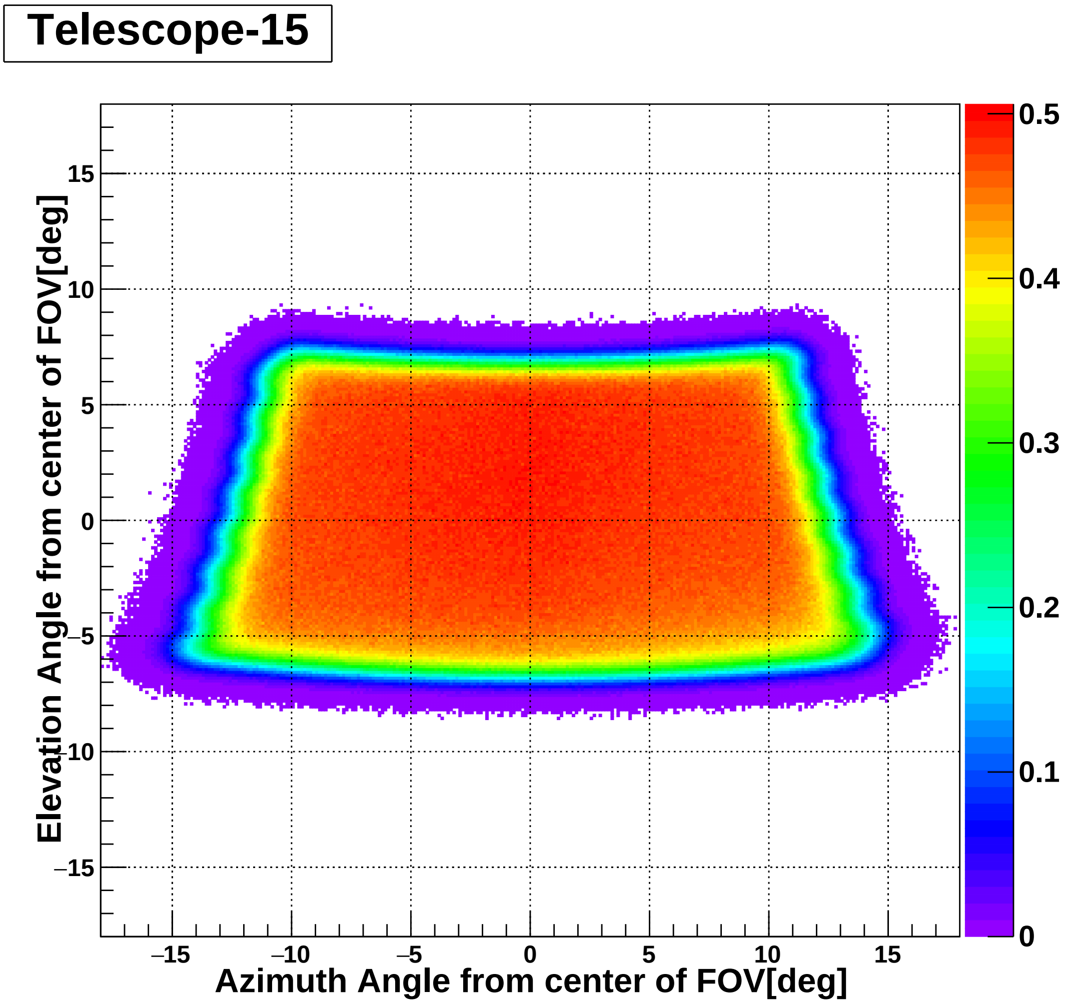

FIGURE 4.9: The field of view of all PMTs in the telescope #15 at TALE FD. Color bar represents the sensitivity calculated by ray-trace simulation.

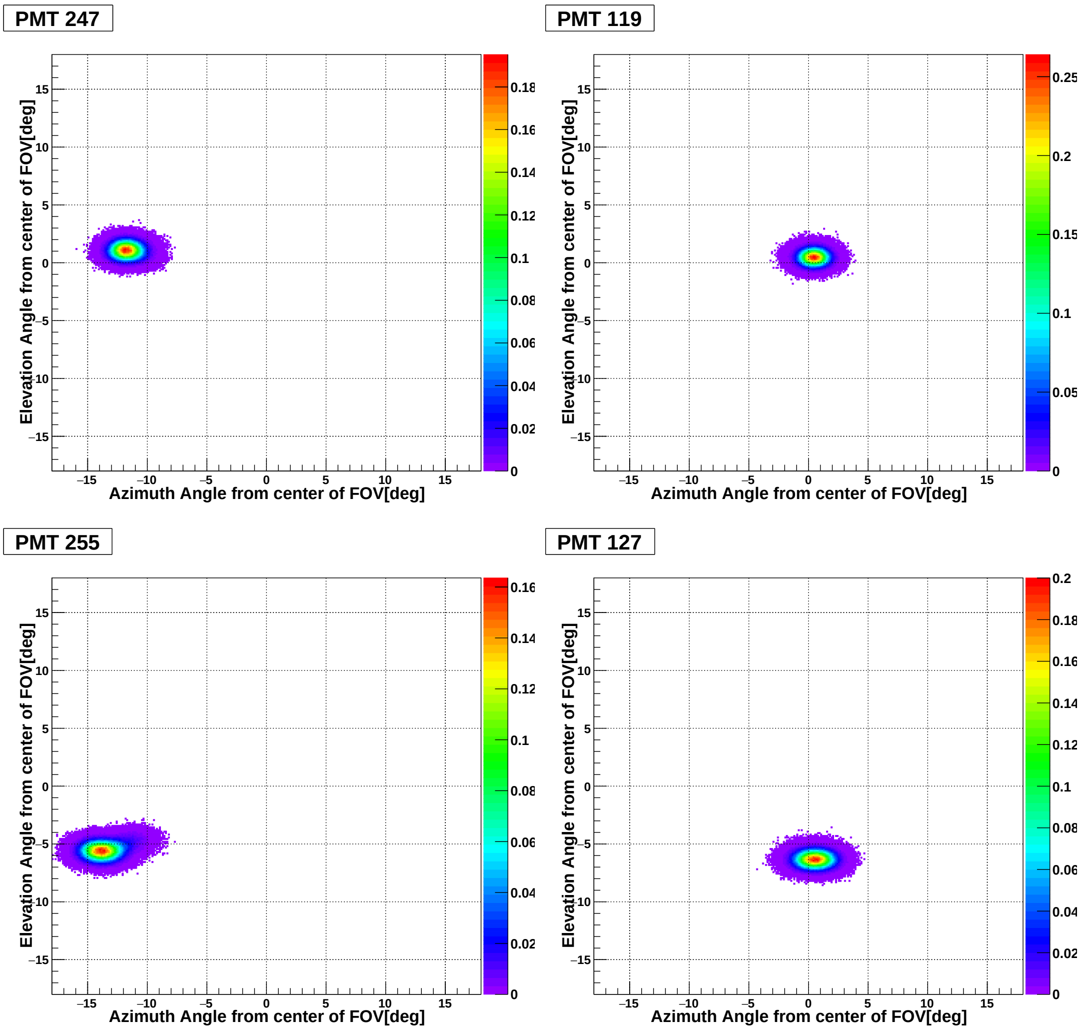

FIGURE 4.10: The field of view of each PMTs located at center, edge and corner. Color bar represents the sensitivity calculated by ray-trace simulation.

4.3.2 Shower Detector Plane Determination

After the good PMTs are selected, we can determine the shower detector plane. In case all of the fluorescence and Cherenkov photons emitted from the shower axis without lateral spread, a normal vector of the SDP is perpendicular to all PMT of line of a sight $\boldsymbol{n}_i$, but in fact, photons are emitting with lateral spread and detected as a track shape with a width. As the PMT direction with larger photons are considered to be closer to the shower axis, the SDP is determined by minimizing the below function with taking account into the number of photo-electrons,

$$\chi^2 = \sum_i \frac{(\boldsymbol{n}_i \cdot \boldsymbol{n}_{\mathrm{SDP}})^2 \cdot w_i}{\sigma_i^2}, \tag{4.10}$$

where $\boldsymbol{n}_i$ is the pointing unit vector of i-th PMT, $\boldsymbol{n}_{\mathrm{SDP}}$ is the unit normal vector of SDP, σ_i is the angular uncertainty related to the field of view of the PMT, which is to be set as a constant $\sigma_i = 1^\circ$ for all PMTs. The w_i is the wight factor of i-th PMT, defined as

$$w_i = \frac{N_{\mathrm{pe},i}}{\sum\limits_i N_{\mathrm{pe},i}} \tag{4.11}$$

4.3.3 Hybrid Geometry Fit

Once the SDP is determined, the shower geometry can be calculated by the time vs angle fit which uses the pointing directions and timings of good PMTs. The parameters and observables used in the fitting function are shown in Fig. 4.11, where $t_{i,\mathrm{exp}}$ and α_i are the expected timing and the elevation angle in the SDP for the i-th PMT respectively, t_{core} is the timing when the air shower reached the ground, r_{core} is the distance from the FD station to the shower core, and ψ is at a shower inclination angle in the SDP. Let the air shower passes through the atmosphere and emits one photon at the location $\boldsymbol{r_p}$ with time t_p. The detected time by the i-th PMT $t_{i,\mathrm{exp}}$ and the core hit time t_{core} are

$$t_{i,\mathrm{exp}} = t_p + \frac{1}{c}|\boldsymbol{r_p}| \tag{4.12}$$

$$t_{\mathrm{core}} = t_p + \frac{1}{c}|\boldsymbol{r_{\mathrm{core}}} - \boldsymbol{r_p}|, \tag{4.13}$$

where $\boldsymbol{r_{\mathrm{core}}}$ is the vector from the FD to the shower core. By removing t_p,

$$t_{i,\mathrm{exp}} - t_{\mathrm{core}} = \frac{1}{c}(|\boldsymbol{r_p}| - |\boldsymbol{r_{\mathrm{core}}} - \boldsymbol{r_p}|) \tag{4.14}$$

According to the law of sines,

$$|\boldsymbol{r_p}| = \frac{r_{\mathrm{core}}}{\sin(\psi + \alpha_i)} \cdot \sin\psi \tag{4.15}$$

$$|\boldsymbol{r_{\mathrm{core}}} - \boldsymbol{r_p}| = \frac{r_{\mathrm{core}}}{\sin(\psi + \alpha_i)} \cdot \sin\alpha_i \tag{4.16}$$

Thus, the expected time at the i-th PMT is

$$t_{i,\mathrm{exp}} = t_{\mathrm{core}} + \frac{1}{c}\frac{\sin\psi - \sin\alpha_i}{\sin(\psi + \alpha_i)} r_{\mathrm{core}} \tag{4.17}$$

For an event that has the timing information of one SD near the shower core, t_{core} is expressed by

$$t_{\mathrm{core}} = t_{\mathrm{SD}} + \frac{1}{c}(r_{\mathrm{core}} - r_{\mathrm{SD}})\cos\psi, \tag{4.18}$$

where t_{SD} is the timing of the leading edge of the SD signal discussed in Sec. 4.1. This is an advantage of the hybrid reconstruction technique. Even if only one air shower signal is recorded by the SD coincided with the FD event, the fitting parameter t_{core} can be removed by two observables, t_{SD} and r_{SD}. Hence, the expected time $t_{i,\mathrm{exp}}$ is

$$t_{i,\mathrm{exp}} = t_{\mathrm{SD}} + \frac{1}{c}(r_{\mathrm{core}} - r_{\mathrm{SD}})\cos\psi + \frac{1}{c}\frac{\sin\psi - \sin\alpha_i}{\sin(\psi + \alpha_i)} r_{\mathrm{core}} \tag{4.19}$$

The quantity to be minimized in the fitting is written as

$$\chi^2_{\mathrm{geo}} = \sum_i \frac{(t_{i,\mathrm{exp}} - T_i)^2}{\sigma^2_{T_i}}, \tag{4.20}$$

where σ_{T_i} is the fluctuation of the signal timing calculated by Eq. 4.3. In case there are several SD candidates, Eq. 4.20 is minimized for each SD, and it is adopted the shower geometry with the least χ^2_{geo} among all trials. In Fig. 4.12, an example of a shower reconstructed by the hybrid and the monocular reconstructions and the reconstructed shower geometry parameters in both cases are shown.

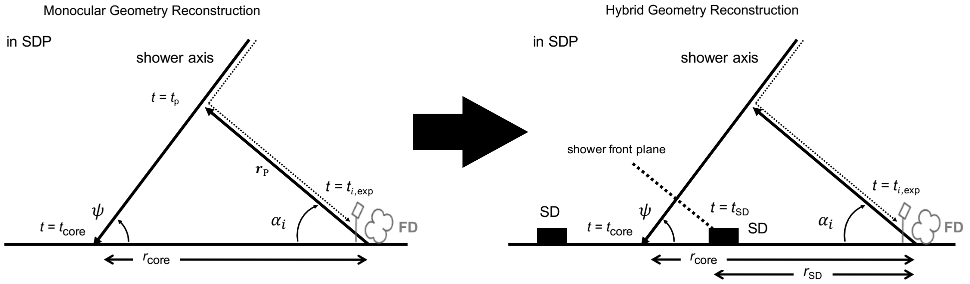

$$t_{i,\mathrm{exp}} = t_{\mathrm{core}} + \frac{1}{c}\frac{\sin\psi - \sin\alpha_i}{\sin(\psi + \alpha_i)}\, r_{\mathrm{core}}$$

$$t_{i,\mathrm{exp}} = t_{\mathrm{core}} + \frac{1}{c}\frac{\sin\psi - \sin\alpha_i}{\sin(\psi + \alpha_i)}\, r_{\mathrm{core}}$$

$$t_{\mathrm{core}} = t_{\mathrm{SD}} + \frac{1}{c}(r_{\mathrm{core}} - r_{\mathrm{SD}})\cos\psi$$

FIGURE 4.11: The schematics of the monocular and the hybrid shower geometry reconstruction. The relations between the measured values, α_i, and the fitting parameters, which are t_{core}, r_{core} and ψ, are shown. In the hybrid geometry reconstruction, the parameter t_{core} can be removed by two observables, t_{SD} and r_{SD}, as a result the number of the fitting parameter is reduced to two and the shower geometry determination accuracy is improved.

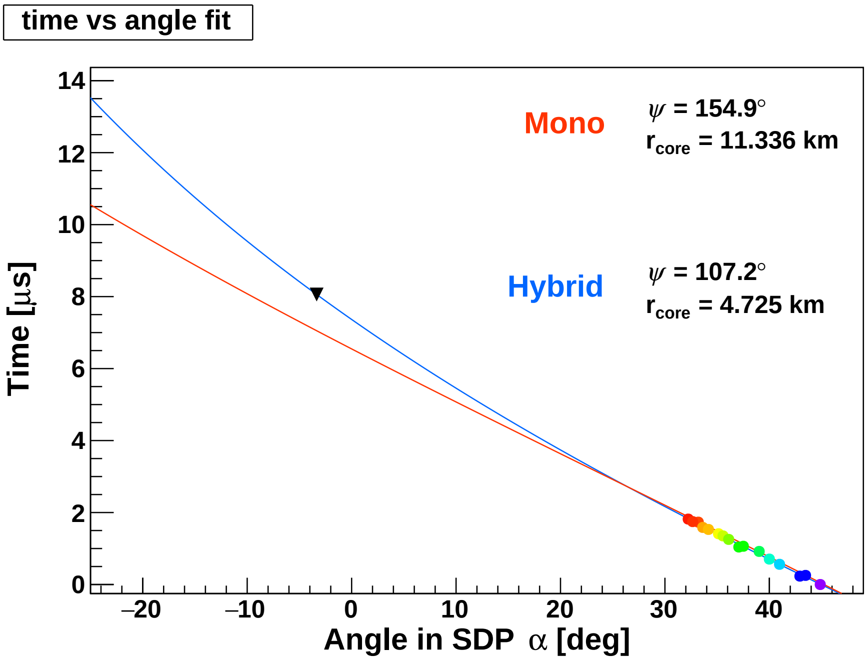

FIGURE 4.12: The geometry reconstruction for the same event in hybrid mode (blue fit) and the monocular mode (red fit). The triangle indicates the SD information and the color points are the measured FD data which color represents the arrival time from early (purple) to late (red).

4.4 Shower Profile Reconstruction

With the shower geometry obtained, the shower longitudinal profile is calculated by the "Inverse Monte Carlo" (IMC) method [90]. This inverse Monte Carlo technique iteratively explores the shower profile parameter space. As discussed in Sec. 3.3, the fluorescence technique detects the Cherenkov and scattered photons as well as the fluorescence light. Therefore, the IMC searches for an optimum solution of the shower profile parameter by repeating Monte Carlo simulations and comparing observed data with MC simulation including all photon emission and scattered processes.

4.4.1 X_{max} Determination

In this IMC procedure, we use the Gaisser-Hillas parameterization formula discussed in Eq. 1.10 as the shower longitudinal profile curve. The first interaction point, X_0, and the interaction length, λ, are fixed at 0 g/cm^2 and 70 g/cm^2 in this thesis respectively. The scanned values are the X_{max} and N_{max}.

For each trial, we calculate the energy deposit along the shower axis from Gaisser-Hillas function with variable X_{max} and $N_{\mathrm{max}} = 1$. Then, we estimate the number of fluorescence and Cherenkov photons along with the shower axis. This performs in the same way as Eq. 3.1 and Eq. 3.3. Using the atmospheric parameters measured by the GDAS and the LIDAR system, the number of fluorescence, Cherenkov and scattered photons injecting the telescopes are calculated.

Next, we perform the ray-trace simulation to estimate the expected number of photo-electrons for each PMT taking into account the calibration factors as the mirror reflectance, the UV filter transmittance and the quantum efficiency. Here we use a database of the directional characteristic for each PMT shown in Fig. 4.10 to reduce the computing time. Hence, the number of expected photo-electrons in i-th PMT $N_{\mathrm{pe},i}^{\mathrm{exp}}$ is

$$N_{\mathrm{pe},i}^{\mathrm{exp}} = \int_X N^{\mathrm{RayTrace}}(X) \cdot S_i(\boldsymbol{r}) \mathrm{d}X, \tag{4.21}$$

where $N^{\mathrm{RayTrace}}(X)$ is number of photons injected into the telescope from the depth X, same description in Eq. 3.11, and $S_i(\boldsymbol{r})$ is the sensitivity of i-th PMT. Then, we evaluate this simulated shower by the following χ^2 function,

$$\chi^2_{\mathrm{pfl}} = \sum_i \frac{1}{\sigma_i^2} \left(\frac{N_{\mathrm{pe},i}}{\sum\limits_i N_{\mathrm{pe},i}} - \frac{N_{\mathrm{pe},i}^{\mathrm{exp}}}{\sum\limits_i N_{\mathrm{pe},i}^{\mathrm{exp}}} \right)^2 \tag{4.22}$$

While changing X_{max}, we search for the optimum X_{max} with the minimization of χ^2_{pfl}.

4.4.2 N_{max} Determination

In the previous X_{max} estimation, we compared the number of expected photo-electrons with N_{max} = 1 air showers and observed signals. Therefore, we can easily calculate N_{max} to take the ratio of the total number of detected photo-electrons to the simulated one,

$$N_{\mathrm{max}} = \frac{\sum\limits_i N_{\mathrm{pe},i}}{\sum\limits_i N_{\mathrm{pe},i}^{\mathrm{exp}}} \tag{4.23}$$

Fig. 4.13 shows the comparison of an observed shower profile curve and the corresponding IMC fitting result. The contributions of the different emission and scattering mechanisms are drawn by different colors.

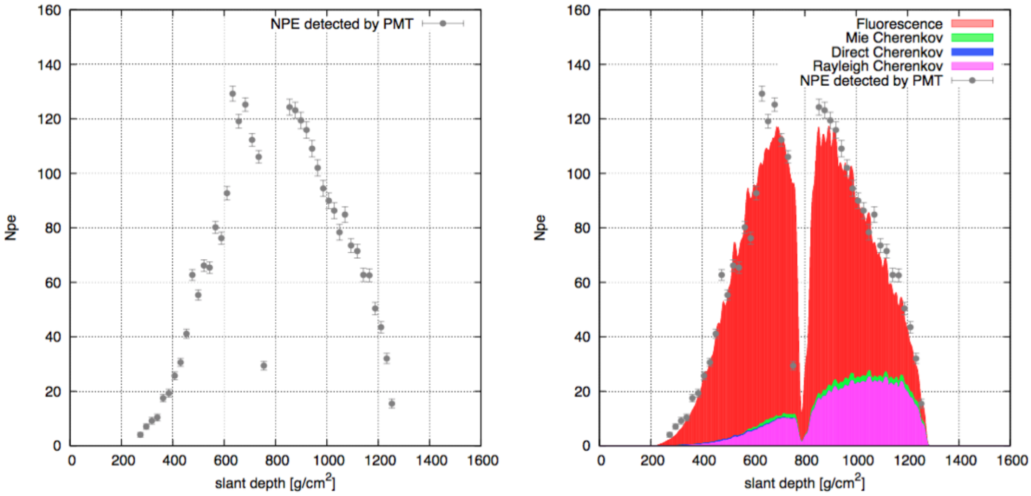

FIGURE 4.13: An observed air shower signal and the shower signals estimated by the IMC fitting are shown. The observed data are indicated by points with error bar. The red area shows the contribution of fluorescence light, the blue area represents the Cherenkov light, the purple and green areas shows scattered light of Rayleigh and Mie process, respectively.

4.4.3 Energy Determination

We can calculate a calorimetric energies, which are the electromagnetic component energies, by summation of the energy deposited along the shower axis. Substituting the $X_{\max}$ and $N_{\max}$ obtained by the inverse Monte Carlo method for the Gaisser-Hillas function and integrating, the E_{cal}, can be calculated as,

$$E_{\mathrm{cal}} = \int_{X_0}^{\infty} \alpha_{\mathrm{eff}}(X) N_{\max} \left(\frac{X - X_0}{X_{\max} - X_0} \right)^{\frac{X_{\max} - X_0}{\lambda}} \exp\left(\frac{X_{\max} - X}{\lambda} \right) \mathrm{d}X, \tag{4.24}$$

where $\alpha_{\mathrm{eff}}(X)$ is the mean ionization loss rate of the air shower particles at the slant depth X, which values is discussed in Eq. 1.20. Note that this E_{cal} is not primary cosmic ray energy, a missing energy correction is needed.

Missing Energy Correction

We obtained the calorimetric energy of the shower, which is a visible energy calculated from the fluorescence and Cherenkov lights detected by telescopes. However, some portion of energies are carried by low energy muons and neutral particles, mainly neutrinos and neutrons, because they do not emit the fluorescence and Cherenkov photons. Therefore, the fluorescence technique is unable to measure the energies of these neutral particles, and the total calorimetric energy E_{cal} are smaller than primary energy E_0. The discrepancy of energies are defined as “Missing Energy” E_{miss}. Here, we will correct for the missing energy through studying Monte Carlo simulations.

The relation between the calorimetric energy, missing energy and E_0 is

$$E_{\text{cal}} = E_0 - E_{\text{miss}}. \tag{4.25}$$

We examined more than thousands CORSIKA showers consisting of pure proton / helium / nitrogen / iron showers to calculate the missing energy of the shower. The calorimetric energy are estimated from an integration of energy deposits by the electromagnetic components. The ratio of the calorimetric energy and the total energy induced by four primary cosmic rays are parameterized by,

$$\frac{E_{\text{cal}}}{E_0} = a_1 + a_2 \log_{10}\frac{E_{\text{cal}}}{\text{eV}} + a_3\left(\log_{10}\frac{E_{\text{cal}}}{\text{eV}}\right)^2 + a_4\left(\log_{10}\frac{E_{\text{cal}}}{\text{eV}}\right)^3 \tag{4.26}$$

and shown in Fig. 4.14. Each parameter is summarized in Table. 4.3. The proton primary cosmic rays result in less missing energy than the other primaries. This is because air showers initiated by the nucleus primary cosmic rays are likely to have more muons and neutrinos than showers initiated by protons.

The total missing energy correction is carried out based on the evolving mixed composition predicted by the H4a model [12]. Given the calorimetric energy of a shower, we use the iron fraction predicted by the H4a model and weigh the missing energy correction by the proton and iron fractions at that energy. We then calculate the total energy of the shower for the observed data.

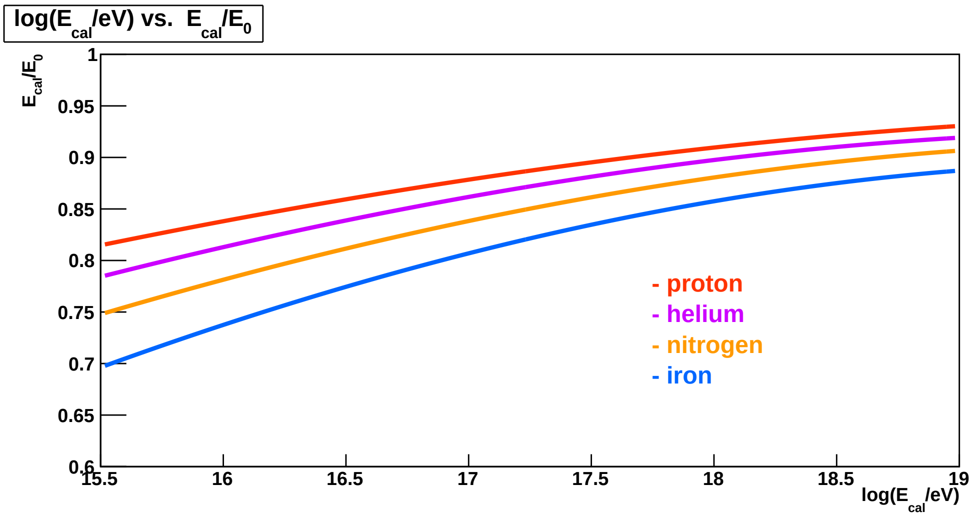

FIGURE 4.14: Ratio of the calorimetric energy and the total energy as a function of the calorimetric energy.

	proton	helium	nitrogen	iron
a_1	-3.133015×10^{-1}	-6.765687×10^{-1}	-9.278369×10^{-1}	-1.400836
a_2	6.016149×10^{-2}	7.710172×10^{-2}	8.701277×10^{-2}	1.084654×10^{-1}
a_3	3.181522×10^{-3}	4.398199×10^{-3}	5.163767×10^{-3}	6.609775×10^{-3}
a_4	-1.527511×10^{-4}	-2.124121×10^{-4}	-2.453553×10^{-4}	-3.147523×10^{-4}

TABLE 4.3: Fit parameters of missing energy estimation for each primaries are summarized.

4.5 Profile Constrained Geometry Fit

The low energy events observed by TALE have track lengths and time duration that are too short for independent geometry reconstruction, even if we reconstruct with the hybrid mode discussed in Sec. 4.3.3. Therefore, we use a "Profile Constrained Geometry Fit" (PCGF) that simultaneously reconstruct the shower geometry and the shower profile. The PCGF was invented at the HiRes experiment for the fluorescence dominated events [91, 92] and is currently used by TALE FD monocular reconstruction for the Cherenkov dominated data [26].

Technically, a scan in the angle ψ is performed. The initial ψ is determined by the stand-alone hybrid geometry fit. The scan range is $\pm7.5^\circ$ from the initial point, and the scan performs by 0.5° step. For each fixed value of ψ, the one remaining parameter, r_{core} is calculated by the hybrid geometry reconstruction. Then for given shower geometry, a set of six independent IMC fits are performed. The six IMCs differ only in the value of X_{max} used in each fit. In each fit, X_{max} is fixed to one of: 500.0, 550.0, 600.0, 650.0, 700.0, or 750.0 g/cm^2, and not allowed to vary during the fit. 10^{16} eV iron showers have an average X_{max} of $\sim$ 500 g/cm^2, and 10^{19} eV proton showers have an average of $\sim$ 750 g/cm^2 based on the Monte Carlo simulations. The range of X_{max} values used in the reconstruction is chosen with these numbers. The χ^2_{geo} (Eq. 4.20) and χ^2_{pfl} (Eq. 4.22) are calculated for each trial, and a combined $\chi^2_{\text{com}} = \chi^2_{\text{geo}} + \chi^2_{\text{pfl}}$ is evaluated optimum solution roughly. The minimum point of combined χ^2_{com} found in rough search can then be used as a starting point for a further refined search. Fig. 4.15 shows an example of rough scan for a MC event. The thrown value of ψ angle is shown as the vertical dashed lines in each plot.

The "rough" search over ψ provides us with an initial guess for the actual minimum point. A refined search is now done in the neighborhood of this initial point. The refined search is performed by the amoeba minimization routine, which implements the downhill simplex method [93]. While slightly changing the ψ and X_{max}, the most likely shower geometry and profile with minimized χ^2_{com} is selected as a final reconstruction result.

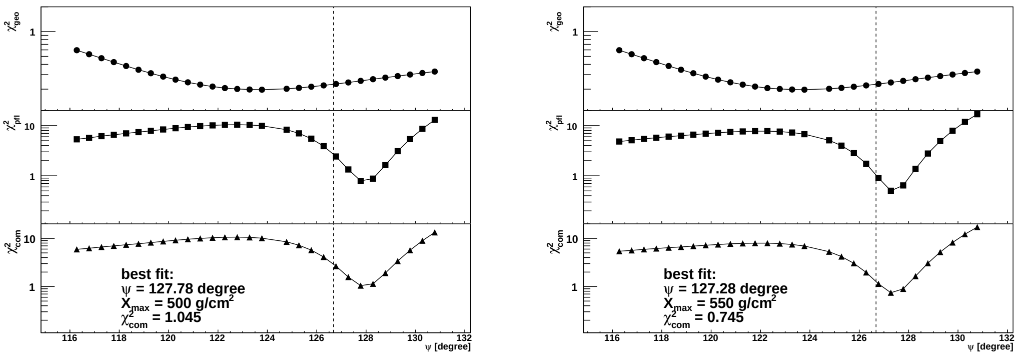

(A) PCGF scan with $X_{\text{max}} = 500\ \text{g/cm}^2$

(B) PCGF scan with $X_{\text{max}} = 550\ \text{g/cm}^2$

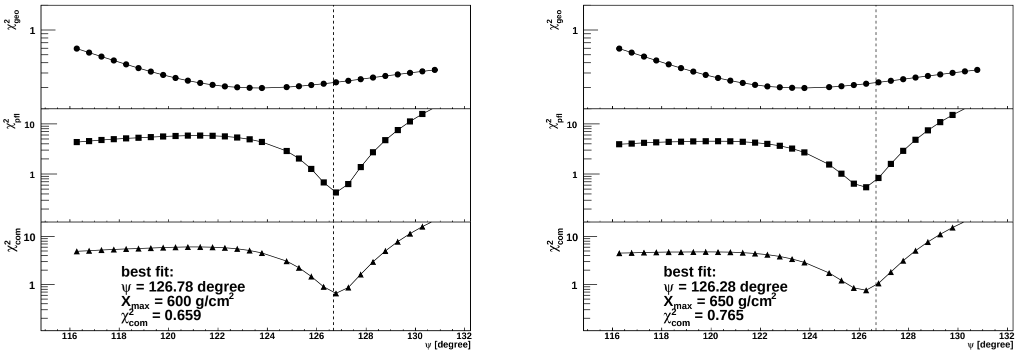

(C) PCGF scan with $X_{\text{max}} = 600\ \text{g/cm}^2$

(D) PCGF scan with $X_{\text{max}} = 650\ \text{g/cm}^2$

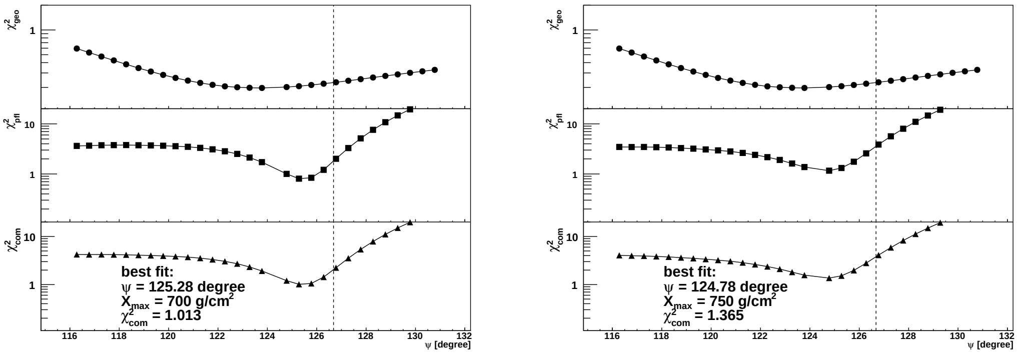

(E) PCGF scan with $X_{\text{max}} = 700\ \text{g/cm}^2$

(F) PCGF scan with $X_{\text{max}} = 750\ \text{g/cm}^2$

FIGURE 4.15: Fluctuations of χ^2_{geo}, χ^2_{pfl}, and χ^2_{com} for each X_{max} trial as a function of ψ. The best fit values are shown in bottom left in each figure. A trial with $\psi = 126.78°$, $X_{\text{max}} = 600\ \text{g/cm}^2$ has a minimum χ^2_{com} among all trials. MC thrown values are 126.615° in ψ, and 585 g/cm² in X_{max}, and the best fit by stand alone hybrid geometry fit is $\psi = 123.78°$.

4.6 Event Examples

The TALE FD observes three different classification of events: Cherenkov, fluorescence, and mixed signal events. The Cherenkov events have the majority of the measured signal come from the Cherenkov light, whereas fluorescence events have the majority of the measured signal come from fluorescence light. Mixed events have a geometry where both fluorescence and Cherenkov contribute to the measured signal. An example of a fluorescence event observed by TA MD and TALE FD is shown in Fig. 4.16, while an Cherenkov event observed by TALE FD is shown in Fig. 4.17.

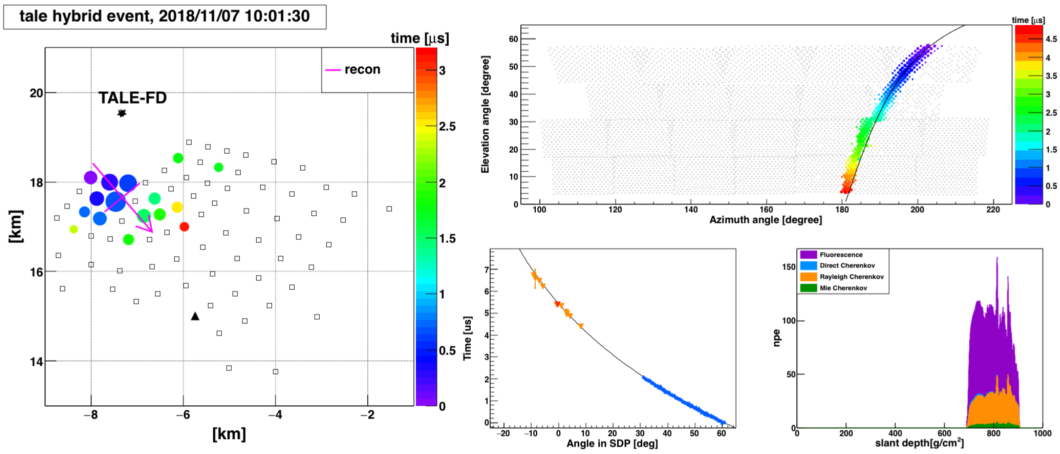

FIGURE 4.16: High energy fluorescence event observed by both the Middle Drum and TALE hybrid detectors. *Left*: SD display. Reconstructed shower direction by hybrid mode is indicated by magenta arrow and crossed point is the reconstructed shower core position. *Top – Right*: FD display. The line fit for the SDP (black line) is overlaid. *Bottom – Middle*: Hybrid geometry fit. The blue triangle makers are FD PMT timing and inverted triangle are SD timing. The red inverted triangle is a detector which is used in Eq. 4.18. *Bottom – Right*: Reconstructed shower profile with relative contributions of fluorescence light, Cherenkov light and scattered light.

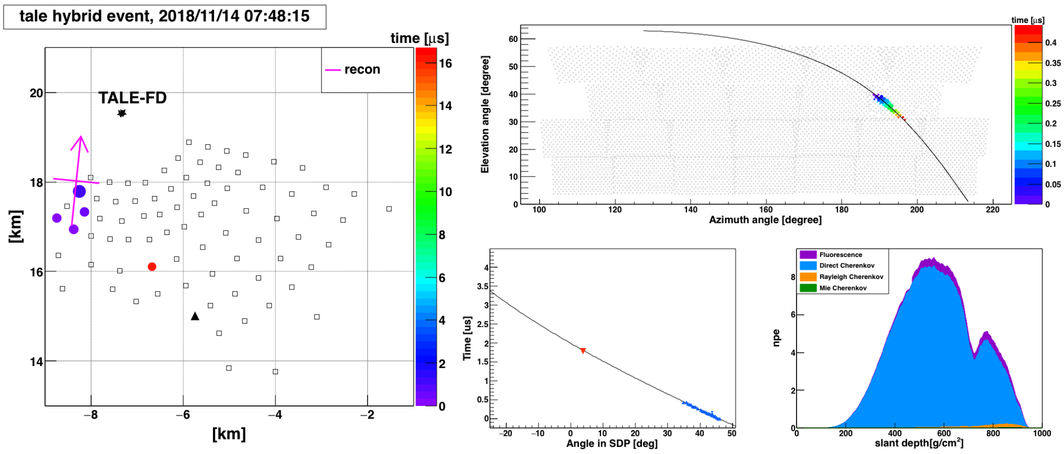

FIGURE 4.17: One-telescope low energy Cherenkov event. *Left*: SD display. *Top – Right*: FD display. *Bottom – Middle*: Hybrid geometry fit. *Bottom – Right*: Reconstructed shower profile.

4.7 Resolutions in the Hybrid Mode

To determine the resolution, the Monte Carlo events were processed through exactly the same reconstruction programs as the data. We compared reconstructed values to thrown values to determine how well Monte Carlo events are reconstructed.

We examined several reconstructed parameters: distance (impact parameter, R_p), ψ angle (angle in the SDP), X_{max} and energy using all events that passed quality cuts, which is discussed later.

4.7.1 Monte Carlo Simulation Conditions

The Monte Carlo simulation conditions for the resolution studies are described here. As discussed in Sec. 3.1.1, we simulated the air showers by the CORSIKA for proton and iron primaries. The energy range is from $10^{16.35}$ - $10^{18.55}$ eV followed by a broken power low structure, which spectrum index is -2.9 below $10^{17.1}$ eV and is -3.2 above $10^{17.1}$ eV. Zenith angle and Azimuthal angle ranges are 0 - 60 degrees and 0 - 360 degrees with uniformly random distributions, respectively. The core position is uniformly random distributed within a semi-circle of 9 km radius shown in Fig. 4.18. All of the calibration factors with time dependence are applied to SD and FD detector simulations.

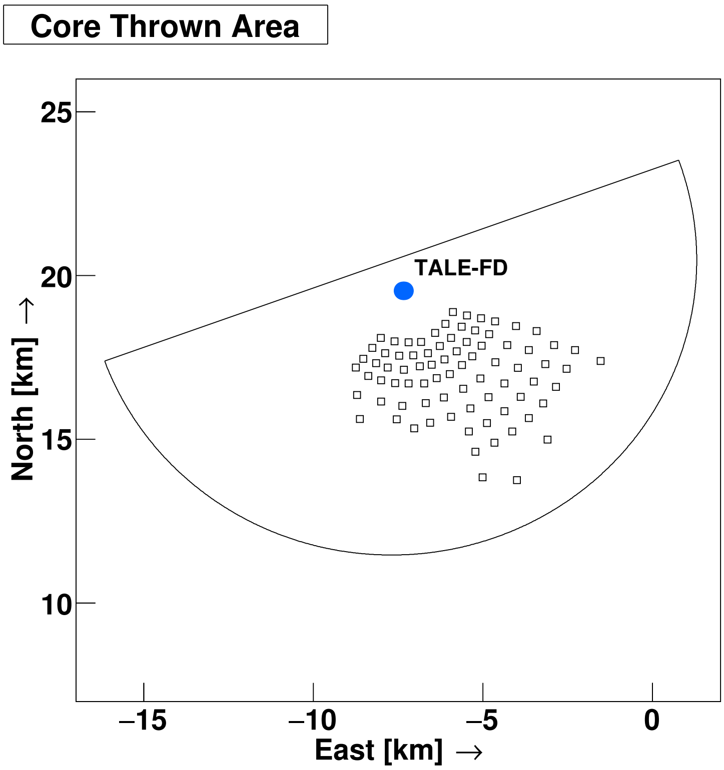

FIGURE 4.18: Core location distribution of Monte Carlo showers.

4.7.2 Quality Cuts

The fluorescence events dominate at energies above $10^{17.5}$ eV , the Cherenkov events dominate at below 10^{17} eV, and mixed events in between. The fluorescence and Cherenkov events have very different characteristics. Mixed events might be more similar to CL or FL events depending on the direct CL contribution to the total signal. Therefore, a different event selection criteria are applied for the different types of events, as summarized in Table 4.4, in order to remove poorly reconstructed events and ensure good detector resolution. Here we define fluorescence events as fractional contribution to the total signal of Fluorescence Light (FL) > 0.75, and Cherenkov events as fractional contribution to the total signal of FL ≤ 0.75.

Variable	CL	FL
No saturated PMTs in FD	applied	
SD detected ≥ 3 MIPs	applied	
X_{max} bracketing cut	applied	
Angular track-length [deg]	track $> 6.5°$	-
Event duration [ns]	> 100 ns	-
# of PMTs	> 10	-
# of Photo-electrons / # of PMTs	> 50	-
# of Photo-electrons	-	> 2000

TABLE 4.4: Quality Cuts applied in this study.

4.7.3 Detector Resolutions

Here the shower geometrical and profile resolutions of the TALE hybrid detector are estimated by comparing the reconstructed parameter and MC thrown one. The difference of the parameters for the proton primarily case are shown in the top-right panel of Fig. 4.19 - 4.24. The Gaussian fit had been performed drawn with the black curve to evaluate the reconstruction bias and resolution. Here, the bias and resolution are defined as the mean and one sigma value obtained by the Gaussian fitting respectively, and its results are shown in the white box under the statistic box. The reconstruction biases and resolutions as a function of MC thrown energy are also shown in the bottom-right panel. Each point represents an MC event. The parameter differences for all events are binned by the thrown energy. The mean and one sigma of each bin obtained by the Gaussian fitting are shown in black. For the iron primary ones are shown in the left panel of Fig. 4.19 - 4.24. The TALE hybrid detector reconstruction resolutions are summarized in Table 4.5.

Parameter	proton MC	iron MC	Figure
θ	0.5°	0.4°	4.19
ϕ	0.5°	0.5°	4.20
R_p	3.0%	3.3 %	4.21
ψ	1.1°	0.9°	4.22
X_{max}	29 $\mathrm{g/cm^2}$	27 $\mathrm{g/cm^2}$	4.23
E	10.2%	8.8%	4.24

TABLE 4.5: TALE hybrid event reconstruction resolutions.

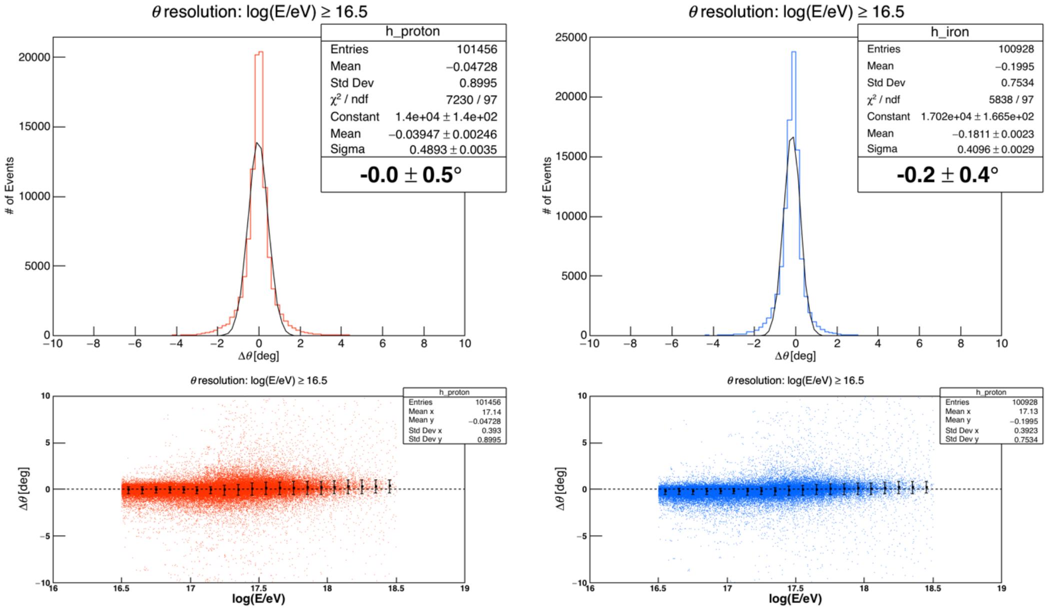

FIGURE 4.19: TALE Hybrid zenith angle θ reconstruction resolution histograms by evaluating $(\theta_{\text{recon}} - \theta_{\text{thrown}})$.

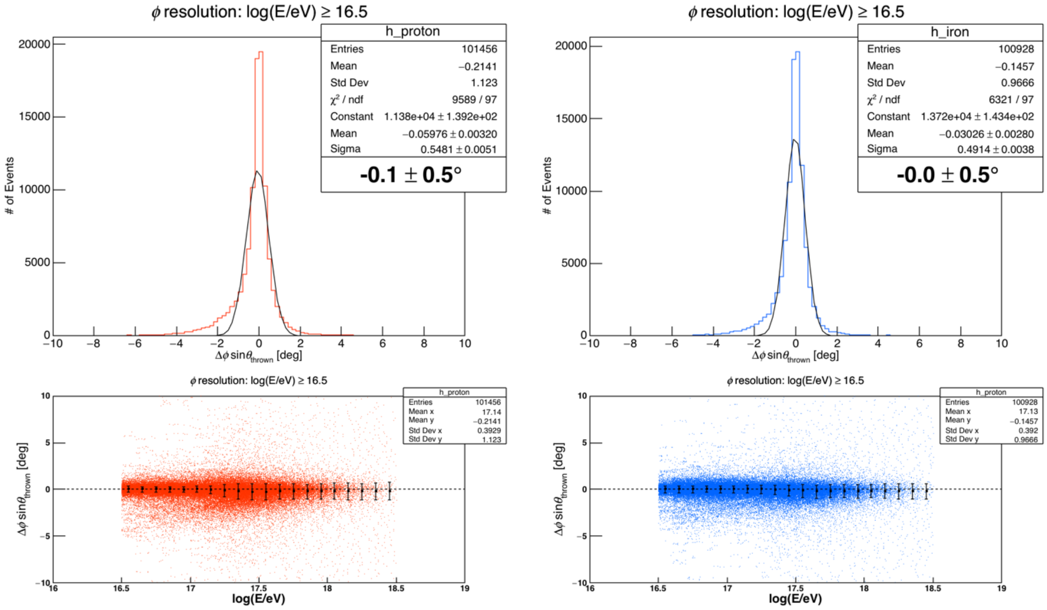

FIGURE 4.20: TALE Hybrid azimuthal angle ϕ angle reconstruction resolution histograms by evaluating $(\phi_{\text{recon}} - \phi_{\text{thrown}}) \cdot \sin\theta_{\text{thrown}}$.

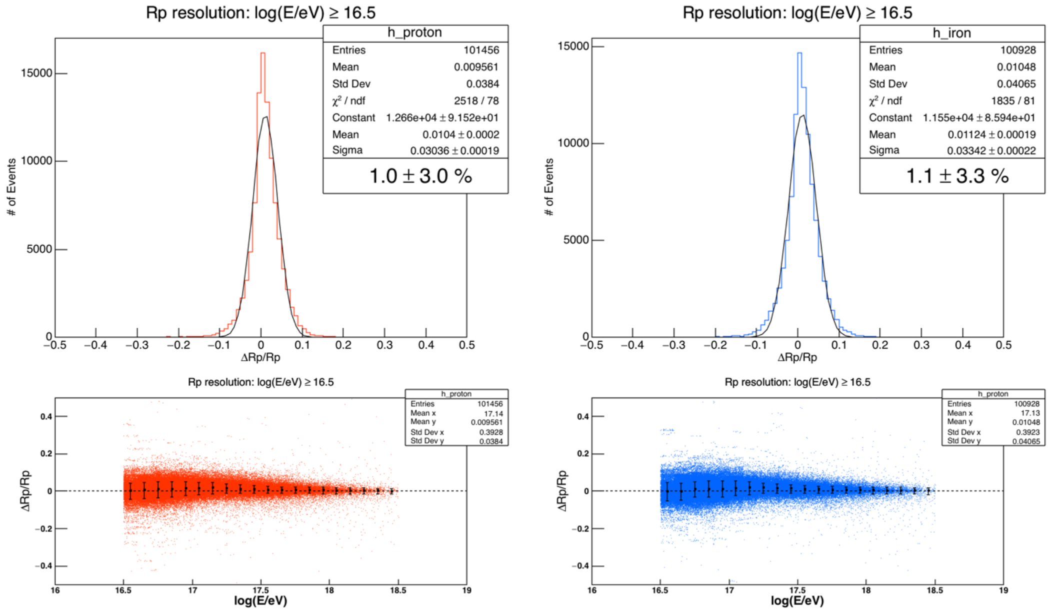

FIGURE 4.21: TALE Hybrid impact parameter, R_p, resolution histograms by evaluating $(R_{p\text{ recon}} - R_{p\text{ thrown}})/R_{p\text{ thrown}}$.

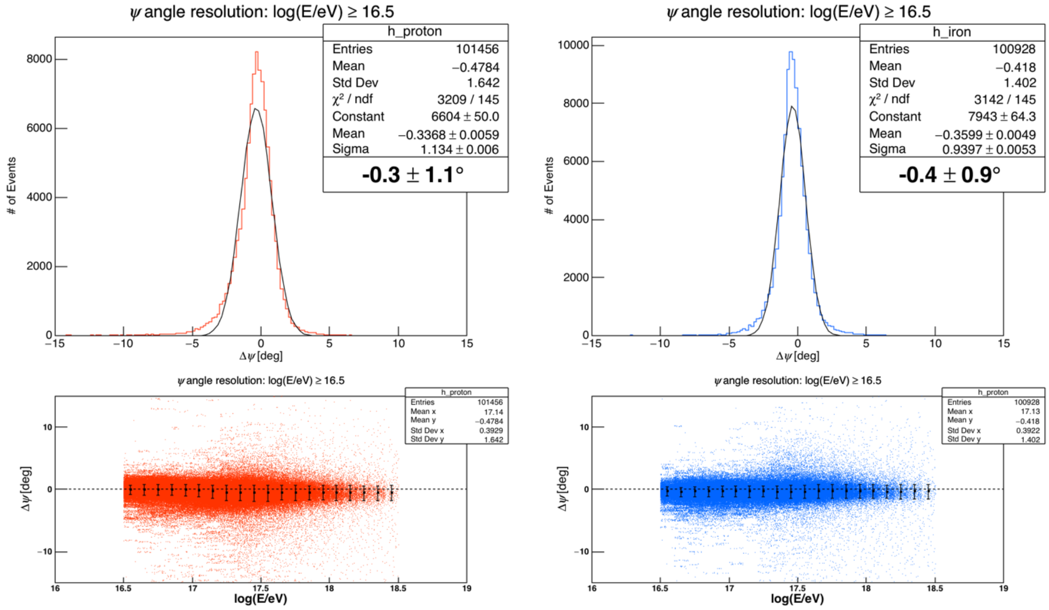

FIGURE 4.22: TALE Hybrid ψ angle reconstruction resolution histograms by evaluating $(\psi_{\text{recon}} - \psi_{\text{thrown}})$.

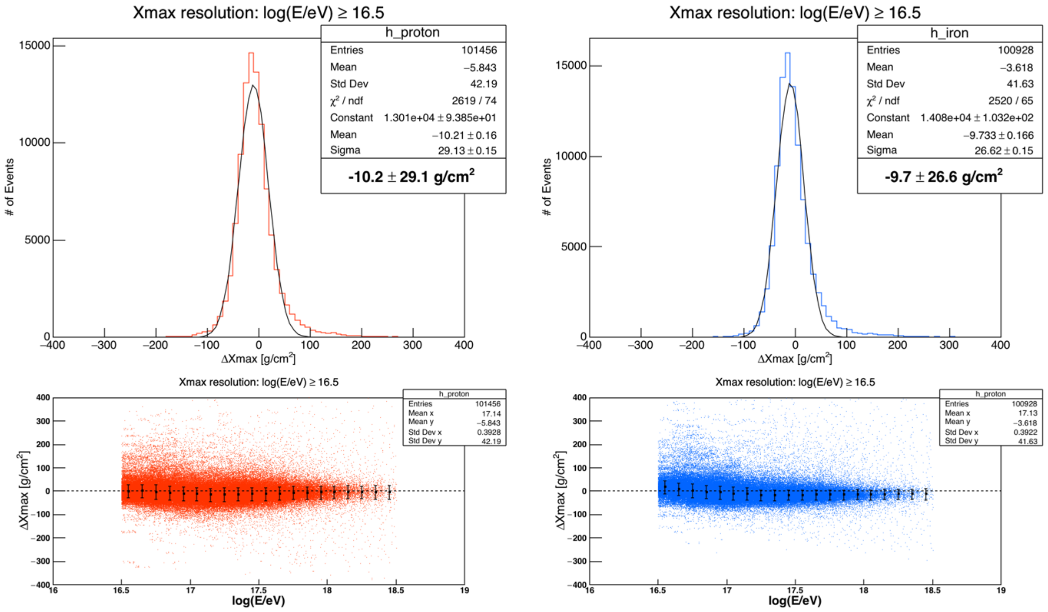

FIGURE 4.23: TALE Hybrid X_{max} angle reconstruction resolution histograms by evaluating $(X_{\text{max recon}} - X_{\text{max thrown}})$.

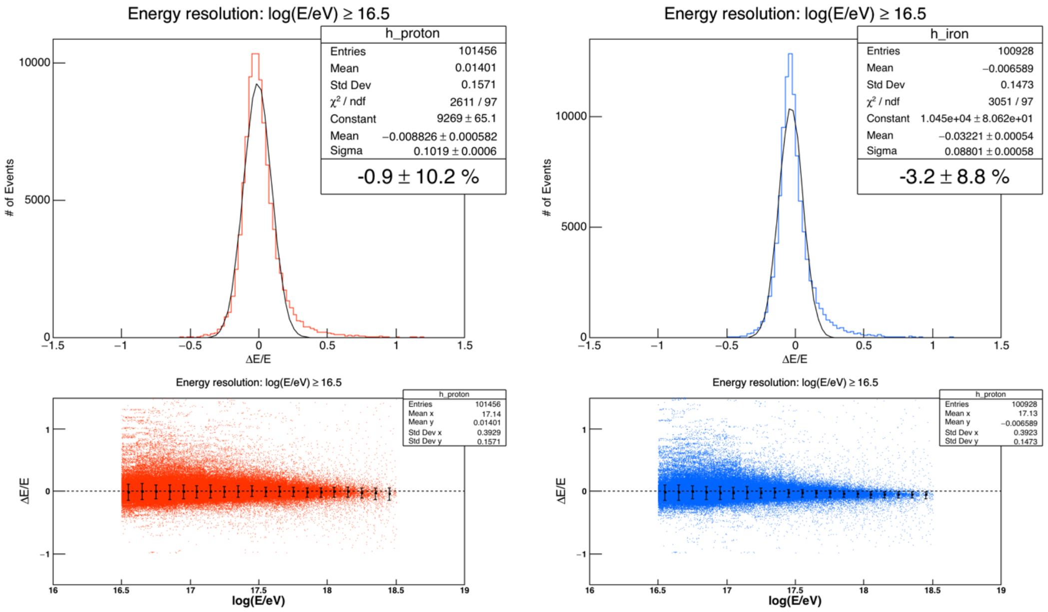

FIGURE 4.24: TALE Hybrid energy resolution histograms by evaluating $(E_{\text{recon}} - E_{\text{thrown}})/E_{\text{thrown}}$.

Chapter 5

Data Analysis

In this chapter, we will discuss the results of cosmic ray mass composition and energy spectrum measured with the TALE Hybrid detector. Here we analyzed for data collected by the TA MD + TALE detector from Nov. 2017 to Feb. 2020. Firstly, we confirm that our data and Monte Carlo distributions agree with each other. This is important in how we understand the cosmic rays and our detector response. Next, we discuss the cosmic ray mass composition with observed X_{max}. Then, we evaluate the energy spectrum.

5.1 Data Set

The TALE Hybrid data are split into two time periods, called an epoch, due to the installation of the hybrid triggering system. These distinct epochs are important as they affect the amount of data collected and change the analysis reconstruction and how the simulated events need to be handled. A Detector On-time is calculated from the time each telescope was permitted to issue the trigger during the observation run. Each data file records how long each telescope is active and this is summed for each run period. It is important to calculate the detector on-time accurately for the cosmic ray energy spectrum measurements.

The different epochs are:

Epoch 1 (2017/11/19 - 2018/11/13):
The TALE FD and TALE SD independently had been operated with each self trigger. The total on-time is 550.2 hours in 96 days.

Epoch 2 (2018/11/14 - Present):
The current TALE hybrid epoch. The hybrid trigger system works, and the trigger rate of hybrid events increased further, shown in Fig. 2.27. The total on-time is 429.6 hours in 77 days before the observation cancelled due to the COVID-19.

For this thesis, both epoch 1 and epoch 2 util Feb. 2020 are used in the mass composition and energy spectrum analysis.

5.2 Event Distribution

25 million events were generated by our MC programs with a spectral index of $\gamma = 1$, for each primary. However, the observed cosmic ray flux follows a $\gamma \approx 3$. A $\gamma = 1$ was chosen to fill out events at the highest energies with increased statistics. Both the thrown MC events and reconstructed MC events with quality cuts were weighted according to TA combined spectrum from the ICRC 2019 [25] to match

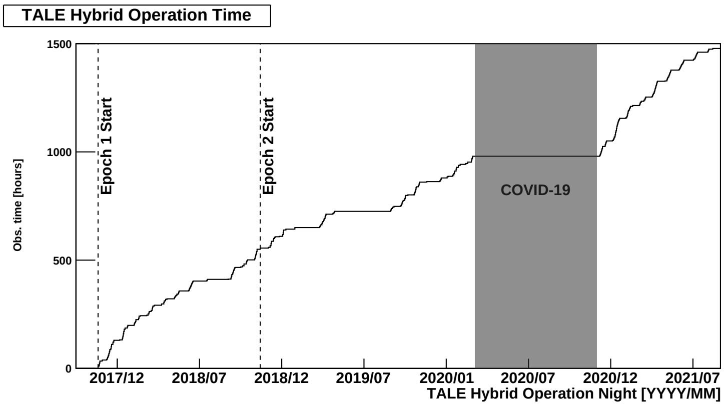

FIGURE 5.1: TALE Hybrid detector on-time. The vertical dashed gray lines show the dates of the TALE Hybrid data epoch starts.

the form of the observed spectrum. The results of the weighting of the thrown and reconstructed event distributions are shown in Fig. 5.2. The spectral break of the 2nd knee at $\log_{10}(E/eV) = 17.1$ is seen in the thrown distribution. Upper-Left panel in Fig. 5.2 shows the proton MC thrown and reconstructed proton MC events with considering the epoch 1 triggering condition. Upper-Right panel in Fig. 5.2 shows the proton MC distributions with considering the epoch 2 triggering condition. The same figures for iron MC case are shown in the bottom two panels in Fig. 5.2.

In addition, the distribution for the reconstructed events after the quality cuts applied is shown in Fig. 5.3 and the number of data events per energy bin are listed in Table 5.1. The number of events increases in epoch 1 compared to epoch 0, especially the low energy region because of the installation of hybrid trigger.

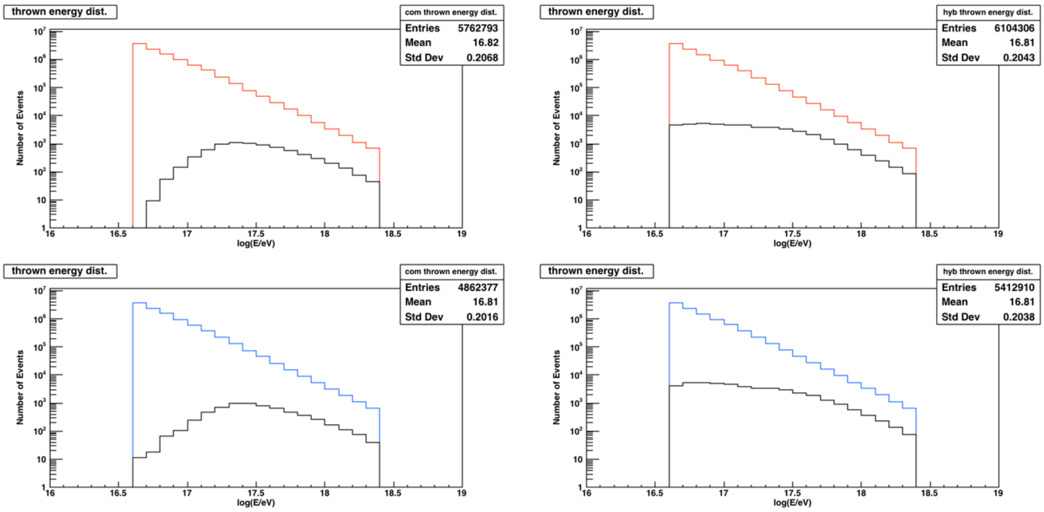

FIGURE 5.2: TALE Hybrid wighted MC event distributions. Left two figures are corresponding to the epoch 1 conditions, which means both the FD and SD operate independently. Right two figures are corresponding to the epoch 2 conditions.

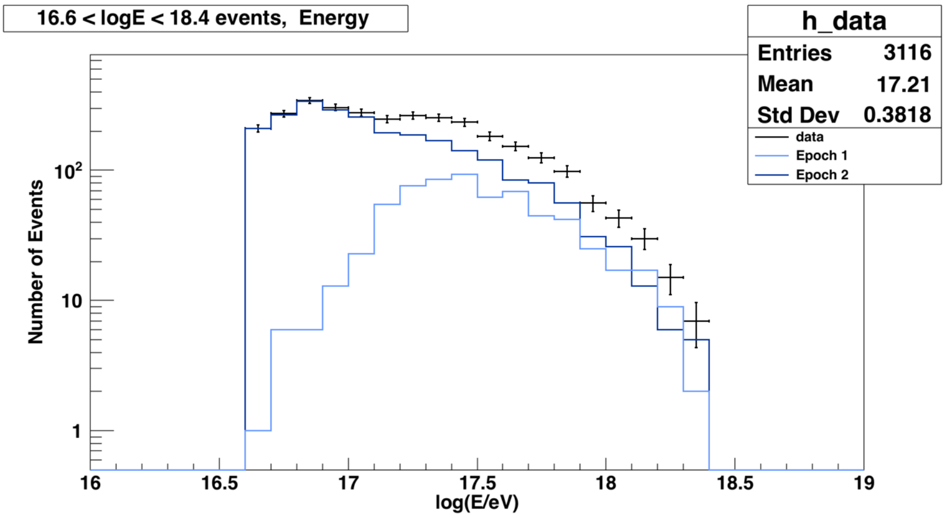

FIGURE 5.3: Distribution of the number of data events. Each energy bin size is 0.1 in log scale. These data events are passed after quality cuts and are used in the energy spectrum calculation.

$\log_{10}(E/\mathrm{eV})$	Number of events
16.6 - 16.7	210
16.7 - 16.8	272
16.8 - 16.9	343
16.9 - 17.0	304
17.0 - 17.1	278
17.1 - 17.2	248
17.2 - 17.3	264
17.3 - 17.4	254
17.4 - 17.5	234
17.5 - 17.6	182
17.6 - 17.7	153
17.7 - 17.8	125
17.8 - 17.9	98
17.9 - 18.0	56
18.0 - 18.1	43
18.1 - 18.2	30
18.2 - 18.3	15
18.3 - 18.4	7

TABLE 5.1: Number of data events per each energy bin. These data events are used in calculating the energy spectrum.

5.3 Time Difference between FD and SD

Since the FD and SD use the GPS, the time of both detectors is almost synchronized. But the precision synchronization of less than 100 ns is required for the hybrid reconstruction. Therefore, we estimate the time difference between the FD and SD by the observed data. Here we obtain the time difference by comparing the reconstructed arrival direction of air shower by the TALE hybrid reconstruction and by TALE FD monocular reconstruction. About 2400 events are remained by both reconstructions after applied the quality cuts. The dependence of time difference assumptions between FD and SD of the opening angle between the reconstructed shower axis for the TALE monocular reconstruction data and that for the TALE hybrid data is shown in Fig. 5.4. The time difference shows the smallest opening angle difference in around 225 ns. Thus, the value of 225 ns is used as the time difference between the FD and SD.

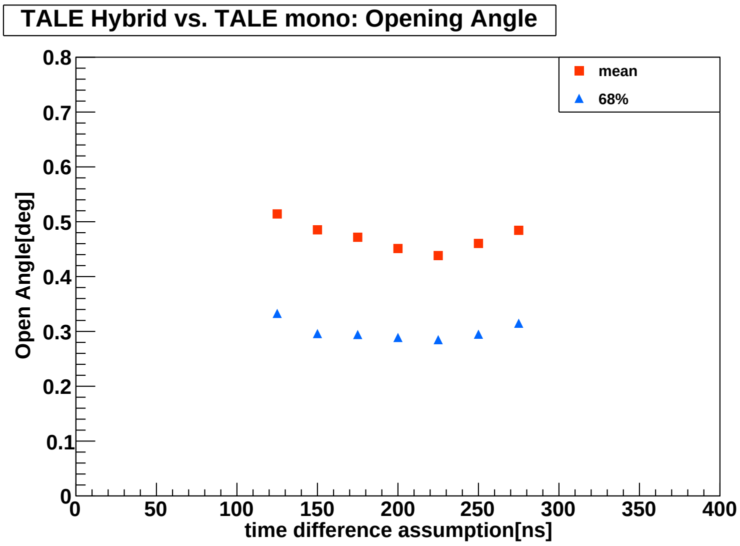

FIGURE 5.4: The result of the comparison with the reconstructed shower axis both by the TALE hybrid and TALE monocular reconstruction for the same events. Red points show the mean values of the opening angle distribution. Blue points show one sigma region which includes 68% of the distribution.

5.4 Data / MC Comparison

Data / MC comparisons were performed with the TALE hybrid detector events to show that our MC describes the observed events well. We analyze data and Monte Carlo events using the same reconstruction programs and apply the quality cuts discussed in Sec. 4.7.2, then check whether observable distributions of various parameters agree with each other. This is an important step to understand our detector. For this analysis, events with energies above $10^{16.6}$ eV were used. The Data / MC comparison plots for the reconstructed parameters are shown in Fig. 5.6 - 5.17. In each figure, Data / MC comparison plots are plotted split in the reconstructed energy (except for Fig. 5.16 - 5.17). The plot with $16.6 < \log_{10}(E_{\mathrm{recon}}/\mathrm{eV}) < 17.5$ is on left, and plot with $17.5 < \log_{10}(E_{\mathrm{recon}}/\mathrm{eV}) < 18.4$ is on right. The bottom panel of the histograms is the bin-by-bin ratio of data to MC. Black plots represent the distributions of observation data, and red or blue plots represent the expected distributions estimated from MC simulations for primary protons and irons, respectively. The distributions of each MC are normalized to the number of observed data. These plots are in reasonable agreement between data and MC simulations.

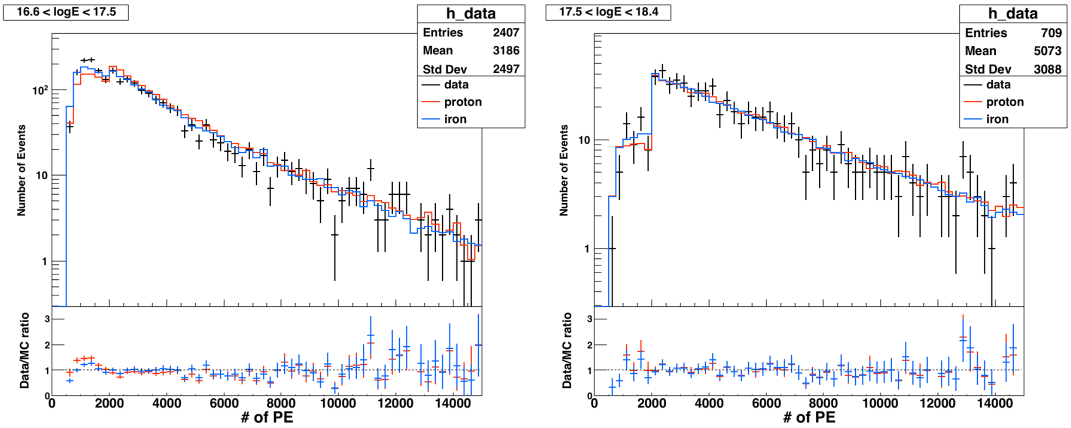

FIGURE 5.5: TA MD + TALE Hybrid Data/MC Comparisons for # of photoelectrons.

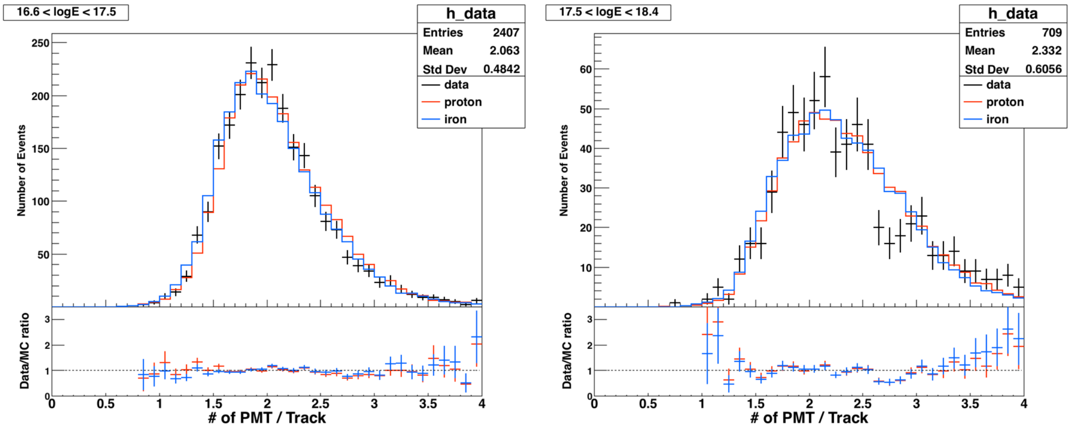

FIGURE 5.6: TA MD + TALE Hybrid Data/MC Comparisons for # of PMTs / track-length.

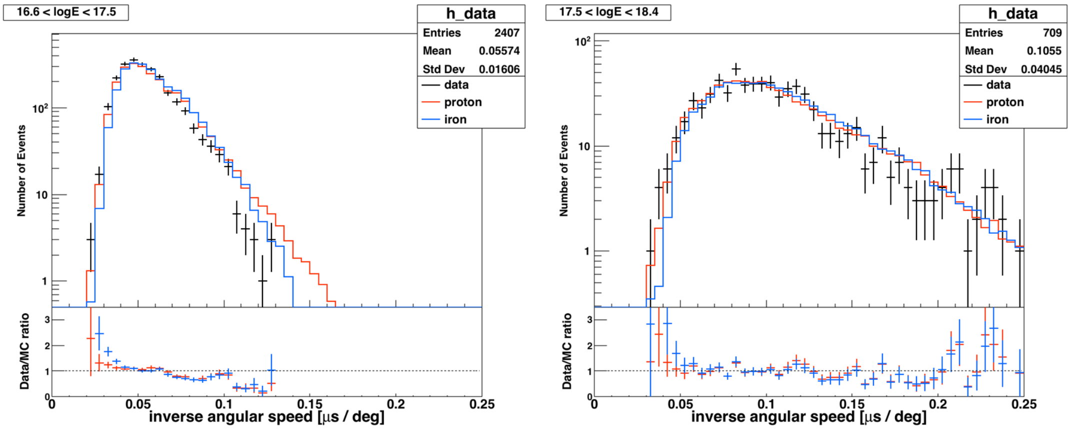

FIGURE 5.7: TA MD + TALE Hybrid Data/MC Comparisons for inverse angular speed.

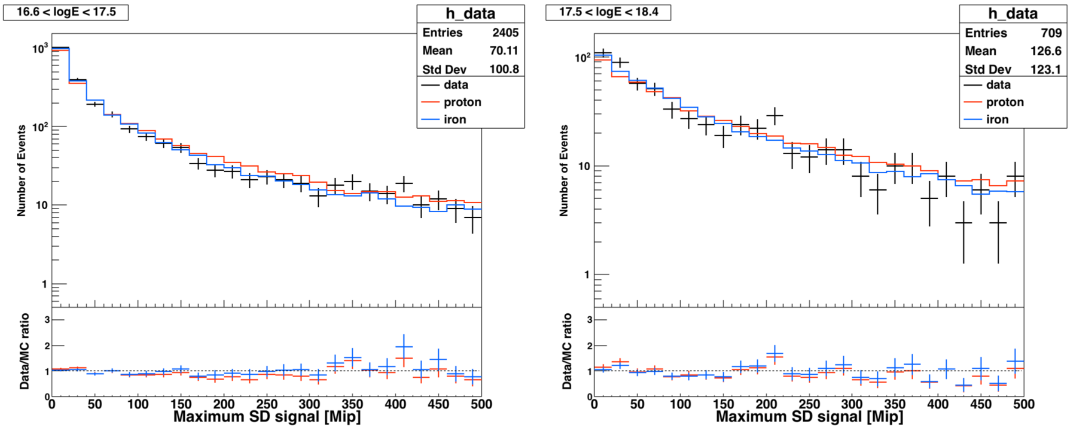

FIGURE 5.8: TA MD + TALE Hybrid Data/MC Comparisons for Maximum detected MIP by SD.

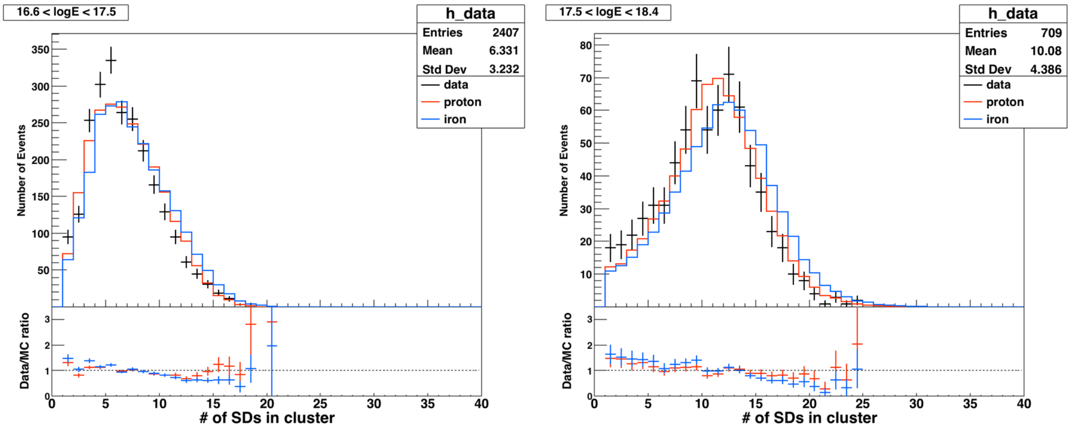

FIGURE 5.9: TA MD + TALE Hybrid Data/MC Comparisons for number of clustered SDs.

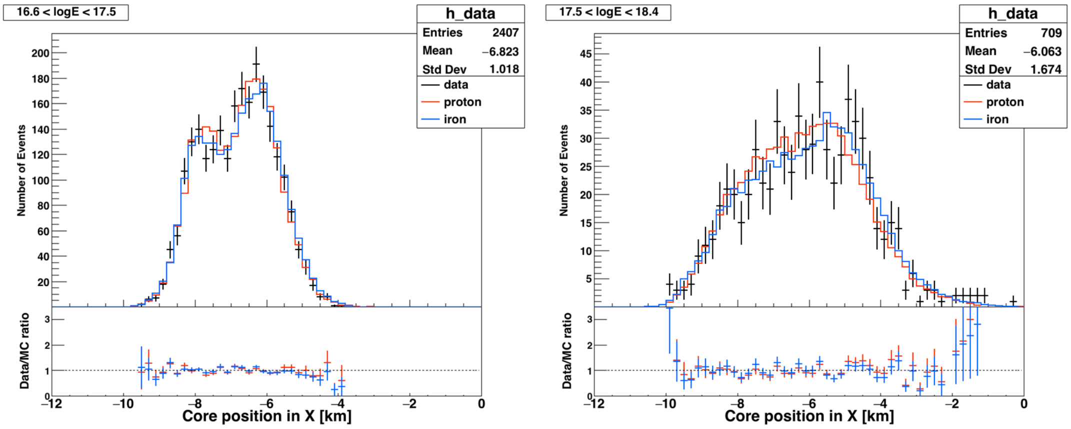

FIGURE 5.14: TA MD + TALE Hybrid Data/MC Comparisons for core location of West-East direction.

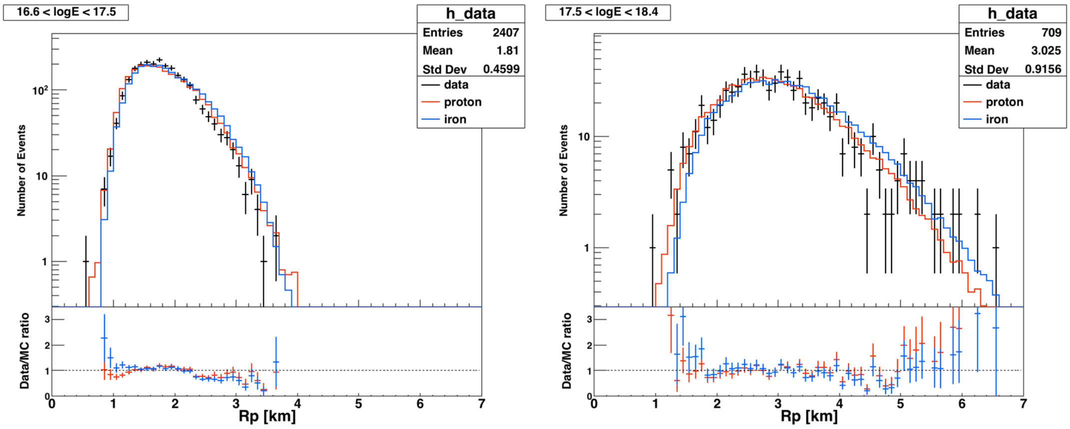

FIGURE 5.10: TA MD + TALE Hybrid Data/MC Comparisons for R_p.

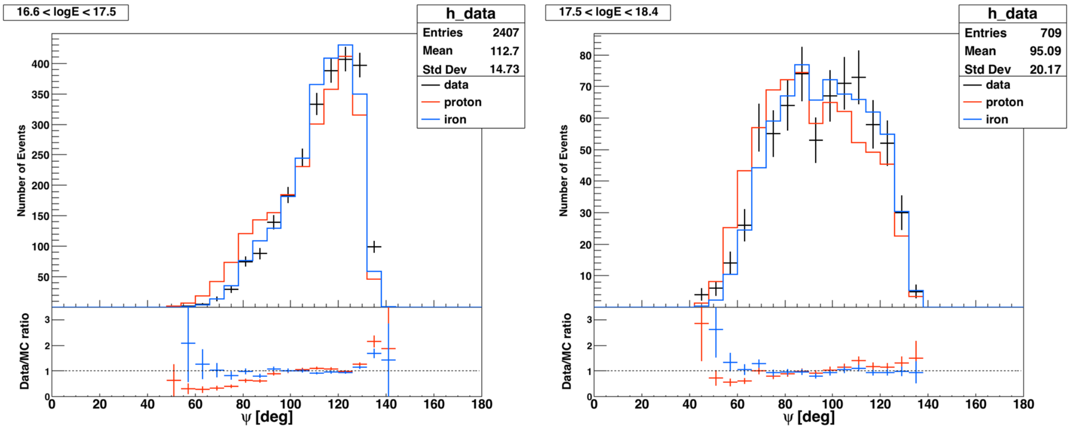

FIGURE 5.11: TA MD + TALE Hybrid Data/MC Comparisons for ψ angle.

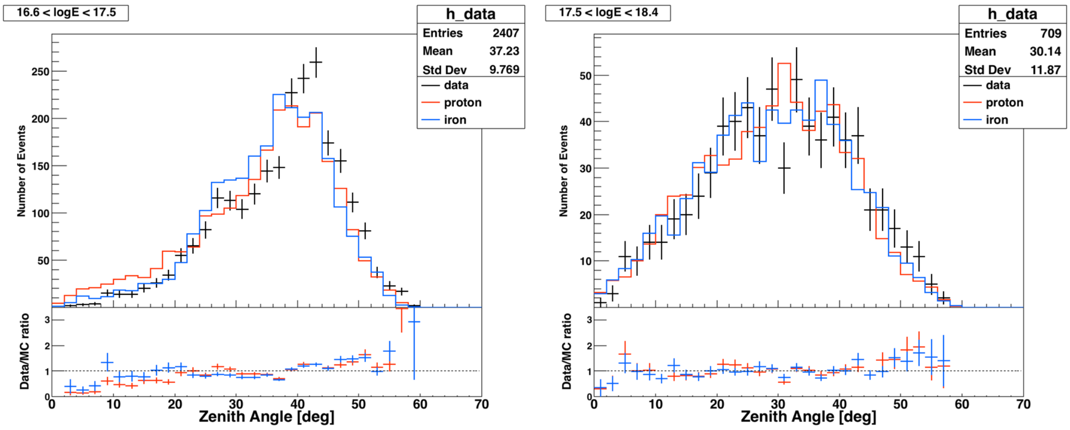

FIGURE 5.12: TA MD + TALE Hybrid Data/MC Comparisons for zenith angle θ.

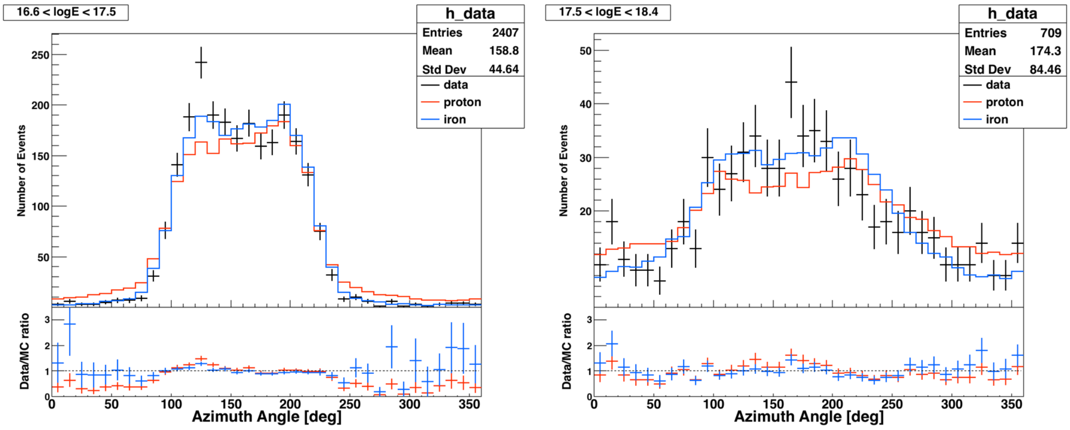

FIGURE 5.13: TA MD + TALE Hybrid Data/MC Comparisons for azimuthal angle ϕ.

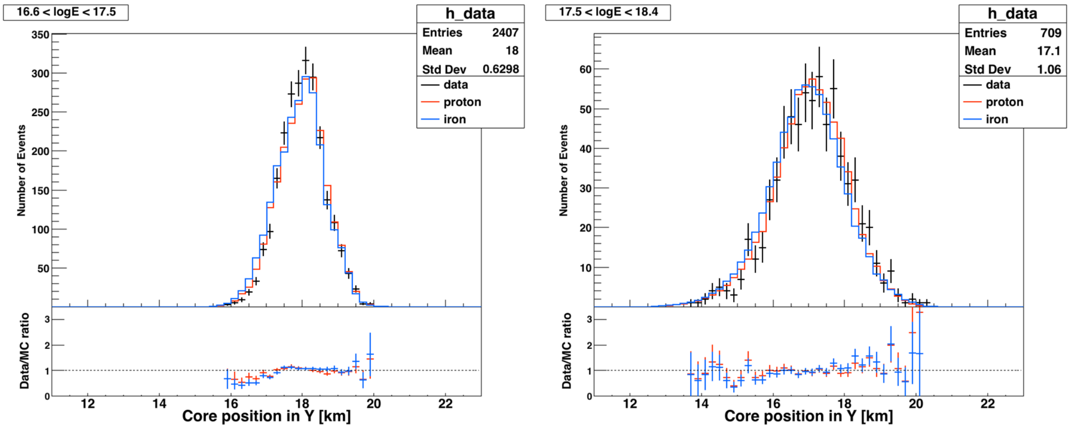

FIGURE 5.15: TA MD + TALE Hybrid Data/MC Comparisons for core location of South-North direction.

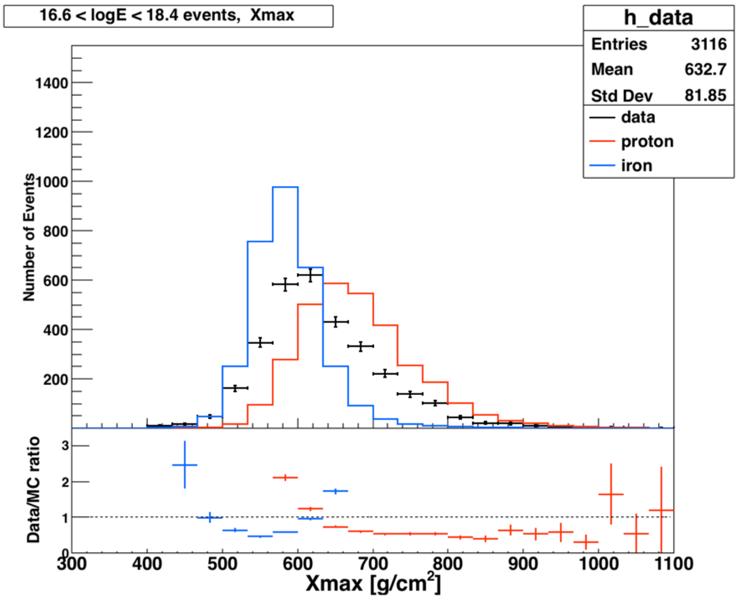

FIGURE 5.16: TA MD + TALE Hybrid Data/MC Comparisons for X_{max}.

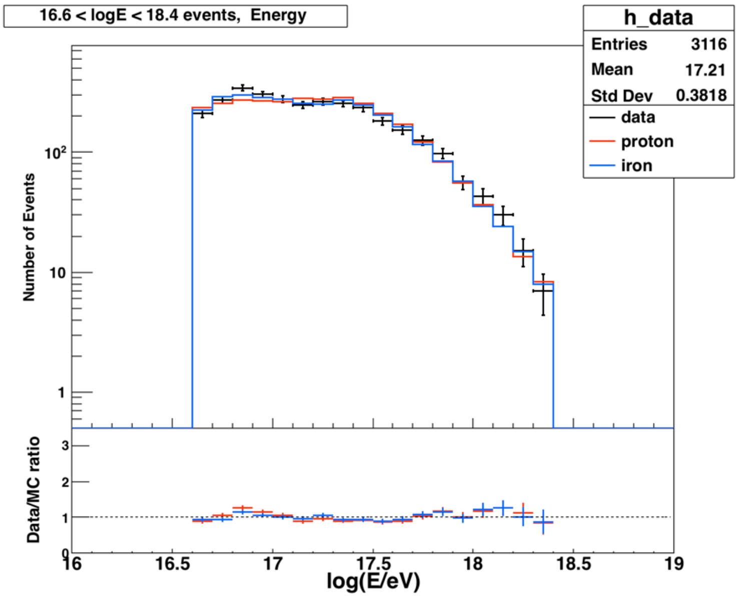

FIGURE 5.17: TA MD + TALE Hybrid Data/MC Comparisons for reconstructed energy.

5.5 Mass Composition

In the previous section, as our MC simulations have been confirmed the reasonable agreement with measured data, we are going to compare the $X_{\max}$ distributions measured by the TALE hybrid detector with the predicted ones by MC simulations for each primary.

As discussed in Sec. 1.1.2, it is hard to determine the mass composition of a cosmic ray on an event by event basis because $X_{\max}$ distributions for proton and iron MC overlap. However, $X_{\max}$ distributions resulting from proton and iron MC have significant differences. Proton showers tend to develop deeper in the atmosphere than iron simulations. Additionally, proton showers have larger fluctuations in $X_{\max}$ resulting in wider $X_{\max}$ distributions. Therefore, both the mean and width of $X_{\max}$ distributions are sensitive to the mass composition of cosmic rays. Moreover, the most complete information can be seen in the full distributions. Here, quantitative comparisons will be discussed between the observed Xmax and the proton and iron MC ones.

5.5.1 $\langle X_{\max} \rangle$ vs. $\log_{10}(E/\mathrm{eV})$

Firstly, it is shown the mean $X_{\max}$ for proton MC and iron MC as a function of $\log_{10}(E/\mathrm{eV})$ in the top of Fig. 5.18. The points with error bars represent the mean $X_{\max}$ and RMS in each energy bin. The line is a fit to the mean $X_{\max}$ values. The slope of the line, or elongation rate, is 61 g/cm^2 / energy decade for the proton, 48 g/cm^2 / energy decade for iron. As expected, this shows that proton and iron MC have a steady elongation rate, even if the detector simulation is included. Note that the measured elongation rate takes into account the detector and reconstruction bias that is included in the MC, and therefore does not represent the true elongation rate of cosmic rays. The bottom of Fig. 5.18 shows a scatter plot of the observed $X_{\max}$.

Fig. 5.19 shows the comparison of the data mean $X_{\max}$ with the elongation rates of the proton and iron MC. The proton and iron “rails”, which are taken from the top panel of Fig. 5.18, indicate the mean X_{max} of pure proton and pure iron compositions. The measured composition appears to be getting heavier with energies around 10^{17} eV, then changing to lighter composition with increasing energy.

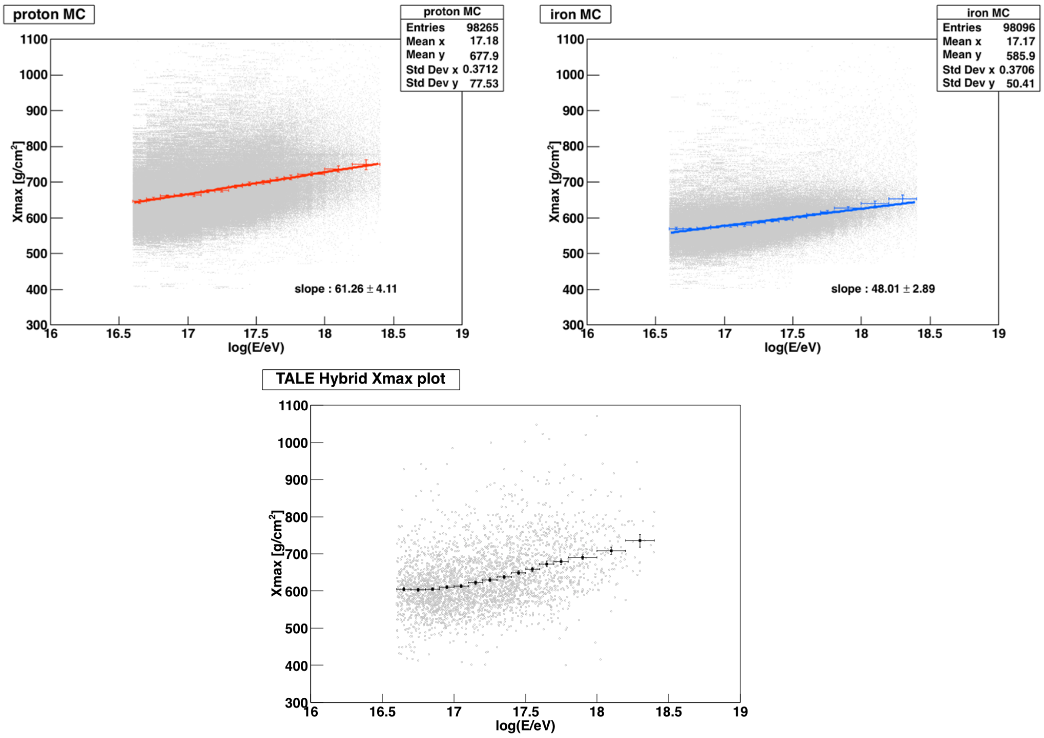

FIGURE 5.18: Scatter plot of X_{max} as a function of $\log_{10}(E/\mathrm{eV})$ for all data or MC events that passed the quality cuts. The points with error bar indicate the mean X_{max} in each bin.

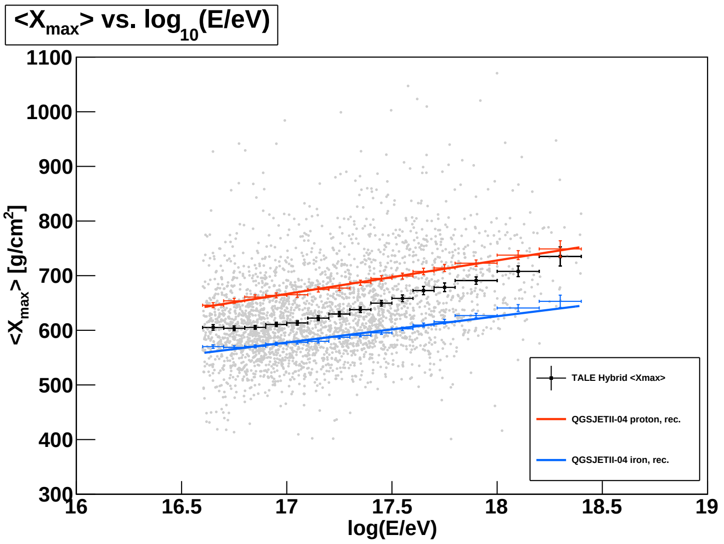

FIGURE 5.19: TALE Hybrid composition result: the $\langle X_{\mathrm{max}} \rangle$ as a function of energy with the proton and iron MC rails. The gray points are a scatter plot of the observed X_{max}. The black data points with error bars represent the mean X_{max} values binned by energy. The red rail is the fitted line to the proton MC mean X_{max} values (from Fig. 5.18), while the blue rail is the fitted line to the iron MC mean X_{max}.

In order to evaluate this evolution of composition, we performed (A) a single line fit and (B) a broken line fit to the observed mean X_{max}, as shown in Fig. 5.20. In the broken line fit, we define a break point in energy, E_{broken}, and elongation rates of before and after the break point, D_{10}^{before} and D_{10}^{after} in unit of [g/cm^2 / energy decade]. The reduced χ^2 of the single line fit is χ^2 / ndf = 14.599 / 14 $\simeq$ 1.04, while that of the broken line fit is χ^2 / ndf = 3.469 / 12 $\simeq$ 0.29. The fitting result is favored a broken structure. We obtained the broken structures with $\log_{10}(E_{\mathrm{break}}/\mathrm{eV}) = 17.1 \pm 0.1$, $D_{10}^{\mathrm{before}} = 26 \pm 15$, and $D_{10}^{\mathrm{after}} = 92 \pm 10$, respectively. On the other hand, the elongation rates for proton and iron MC are $D_{10}^{\mathrm{P}} = 61 \pm 4$ g/cm^2 / energy decade and $D_{10}^{\mathrm{Fe}} = 48 \pm 3$ g/cm^2 / energy decade respectively. The measured elongation rate below E_{broken}, $D_{10}^{\mathrm{before}} = 26 \pm 15$ is less than the MC predictions with assuming the pure composition, while one of above E_{broken}, $D_{10}^{\mathrm{after}} = 92 \pm 10$ is larger than the elongation rate of pure component. This implies that the mass composition becomes light to heavy components below $10^{17.1}$ eV, and again lighter in higher energies.

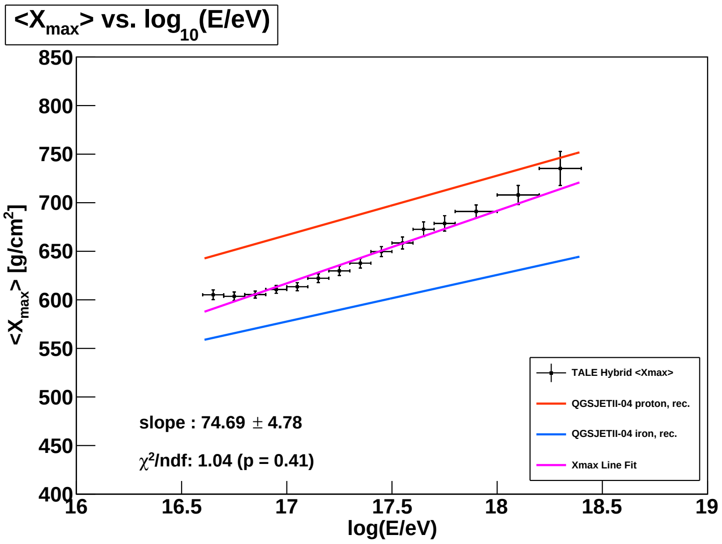

(A) Single line fit

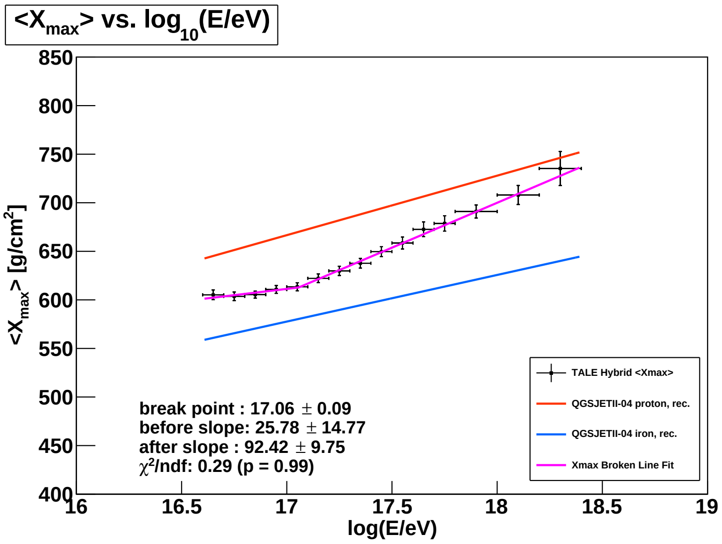

(B) Broken line fit

FIGURE 5.20: The observed mean X_{max} fitted by the single line and the broken line function.

5.5.2 X_{max} Distributions

The measured X_{max} data are binned by energy into 15 energy bins. Below $10^{17.8}$ eV, there are sufficient statistics to use 0.1 decade width energy bins, to provide $>$ 100 events per bin. Above $10^{17.8}$ eV the bin width is widened to include more events. Fig. 5.21 - 5.24 show the X_{max} distributions measured in this analysis. The distributions for reconstructed proton and iron MC events are shown as well. For each energy bin, the histograms of MC ones are normalized by the number of entries of the observed data.

In order to evaluate the compatibility between the observed X_{max} distribution and MC expected X_{max} distributions, we performed the Kolmogorov-Smirnov test (KS test). Fig. 5.25 shows the probabilities calculated by the KS tests with each energy bin comparing observed X_{max} distributions with expected X_{max} distributions by MC proton and iron primaries. This result shows that MC proton and iron distributions are excluded with the 95% confidence level in all of the energy bins except for the highest energy of proton primary. This indicates that the observed X_{max} distributions are unable to reproduce only by pure proton or pure iron composition.

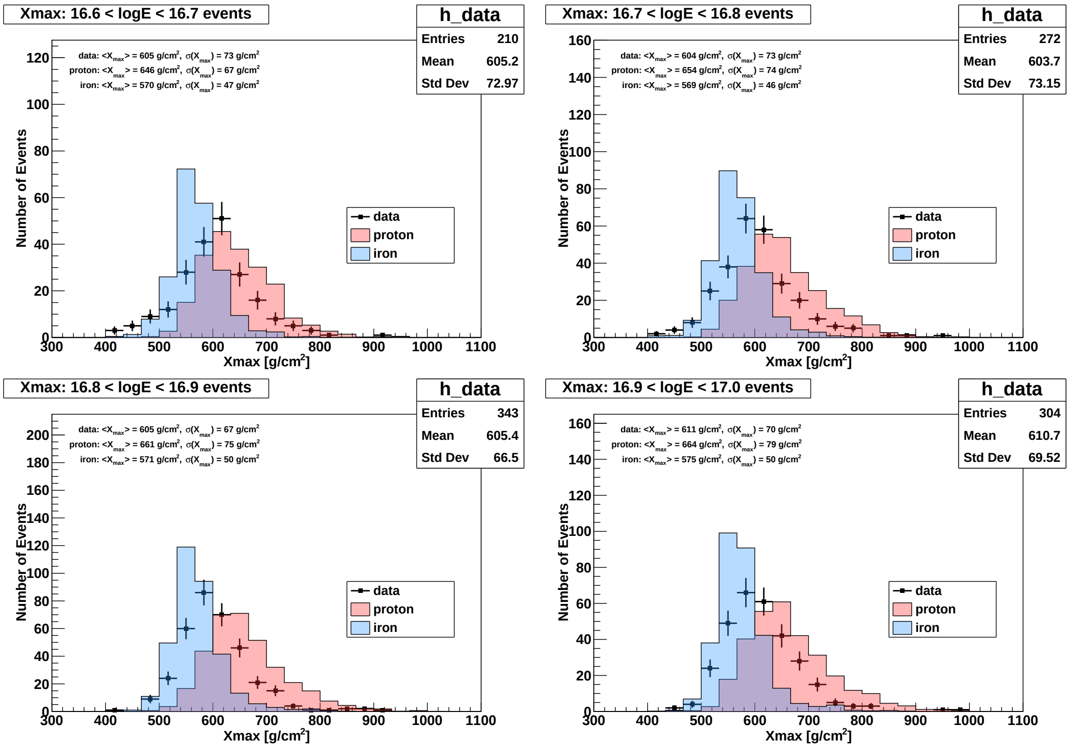

FIGURE 5.21: X_{max} distribution for data and proton MC and iron MC for energy greater than $10^{16.6}$ eV and less than $10^{17.0}$ eV. In each figure, the data is shown with points, proton MC is filled by red, and iron MC is filled by blue.

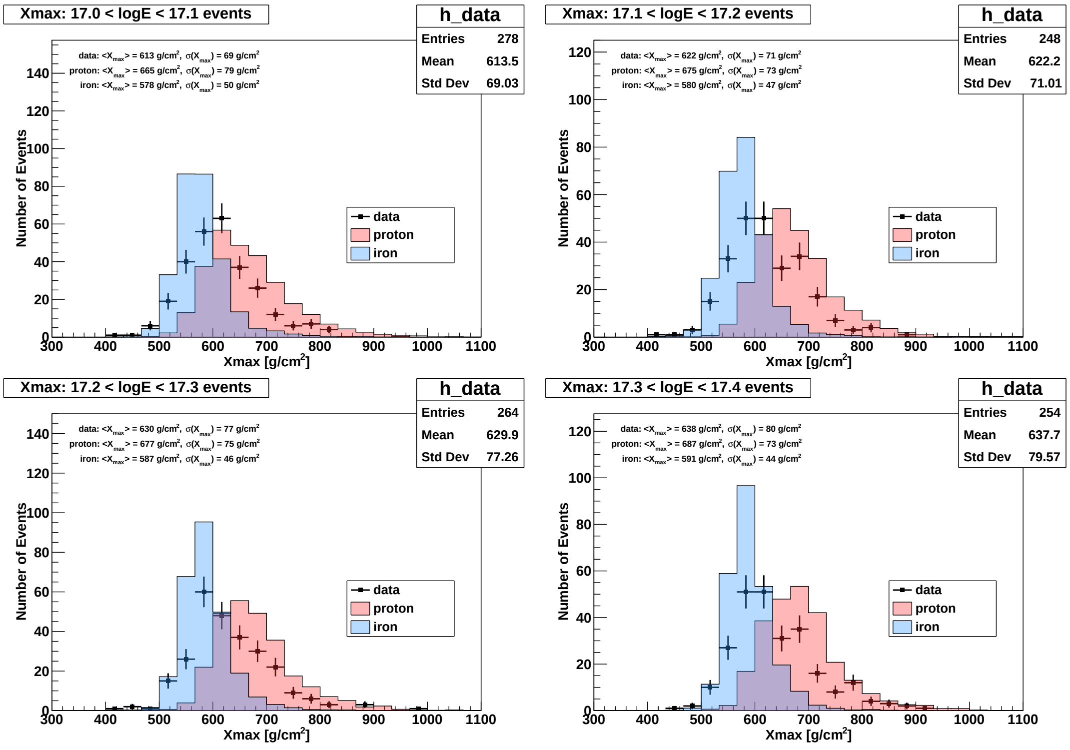

FIGURE 5.22: X_{max} distribution for data and proton MC and iron MC for energy greater than $10^{17.0}$ eV and less than $10^{17.4}$ eV. In each figure, the data is shown with points, proton MC is filled by red, and iron MC is filled by blue.

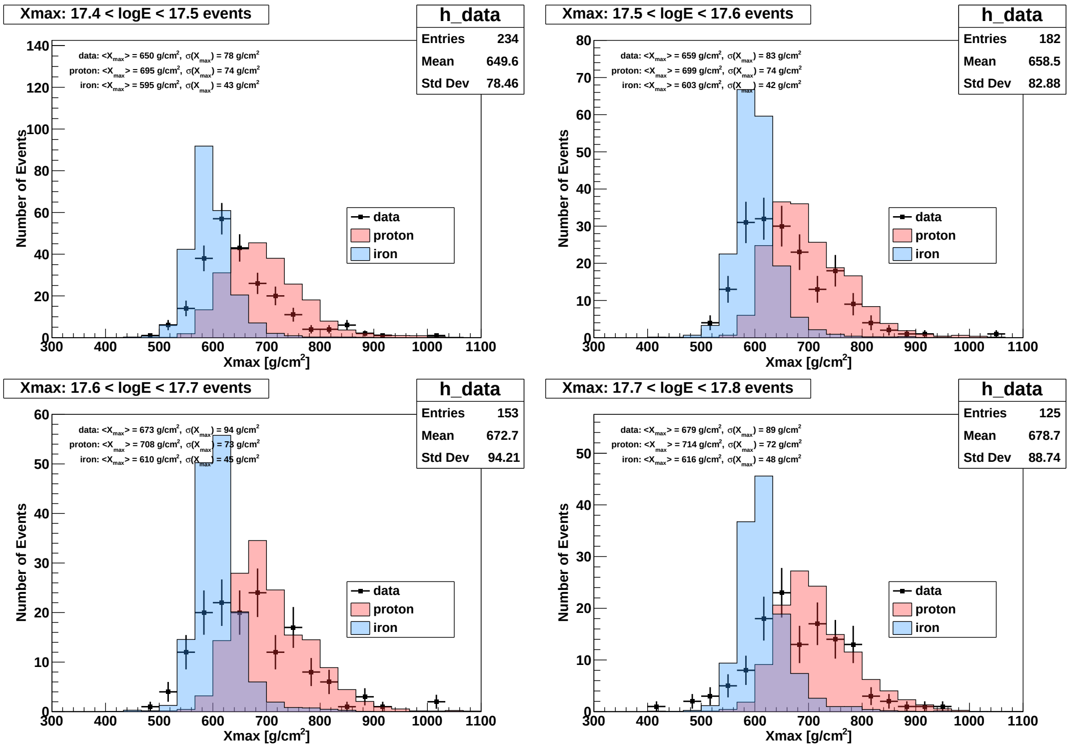

FIGURE 5.23: X_{max} distribution for data and proton MC and iron MC for energy greater than $10^{17.4}$ eV and less than $10^{17.8}$ eV. In each figure, the data is shown with points, proton MC is filled by red, and iron MC is filled by blue.

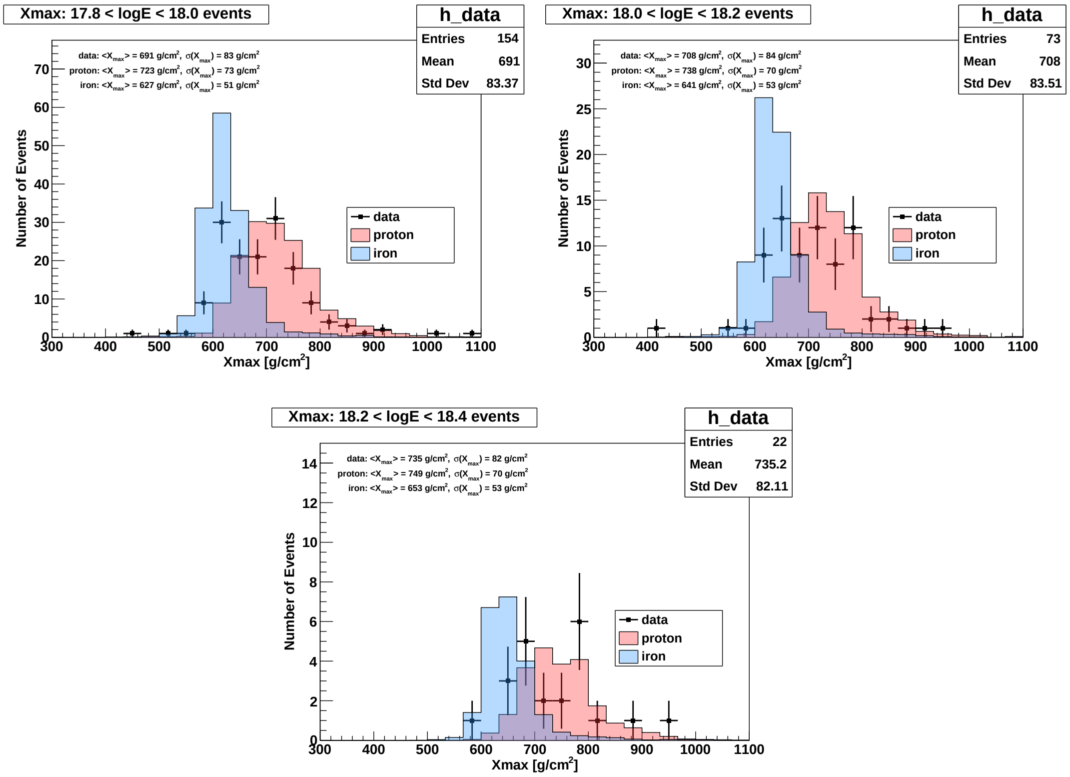

FIGURE 5.24: $X_{\max}$ distribution for data and proton MC and iron MC for energy greater than $10^{17.8}$ eV and less than $10^{18.4}$ eV. In each figure, the data is shown with points, proton MC is filled by red, and iron MC is filled by blue.

FIGURE 5.25: The results of KS tests for $X_{\max}$ distributions comparison with from the data and proton and iron MC. The horizontal line shows the p-value = 0.05; values below this line indicates incompatible of both data $X_{\max}$ distribution and MC one. The observed $X_{\max}$ are inconsistent with pure proton and pure iron predictions except for the highest energy bin of proton one.

$\log_{10}(E/\mathrm{eV})$	proton K-S Probability	iron K-S Probability
16.6 - 16.7	2.876×10^{-09}	8.318×10^{-17}
16.7 - 16.8	7.723×10^{-19}	3.899×10^{-17}
16.8 - 16.9	2.918×10^{-31}	3.274×10^{-21}
16.9 - 17.0	2.576×10^{-21}	7.035×10^{-22}
17.0 - 17.1	6.323×10^{-17}	1.966×10^{-22}
17.1 - 17.2	3.576×10^{-21}	1.278×10^{-20}
17.2 - 17.3	4.780×10^{-19}	1.303×10^{-19}
17.3 - 17.4	3.108×10^{-23}	5.269×10^{-21}
17.4 - 17.5	6.673×10^{-18}	6.518×10^{-27}
17.5 - 17.6	3.690×10^{-11}	5.443×10^{-25}
17.6 - 17.7	1.610×10^{-09}	1.203×10^{-22}
17.7 - 17.8	1.161×10^{-05}	6.126×10^{-22}
17.8 - 18.0	8.195×10^{-06}	7.078×10^{-14}
18.0 - 18.2	3.305×10^{-04}	1.516×10^{-07}
18.2 - 18.4	1.913×10^{-01}	4.765×10^{-04}

TABLE 5.2: Summary of the K-S tests probability performed to compare the TALE hybrid data to the proton and iron Monte Carlo sets.

Next, we examine a test of mixture of the protons and iron nuclei. Using the method outlined by Barlow & Beeston [94] and implemented in ROOT [95] as the TFractionFitter class, we find the fractions of proton and iron which best fit the data in all energy bins. Fig. 5.26 shows the example of X_{max} distribution of the data, mixture, and contributions of proton and iron. All mixture fit results are shown in Appendix A. The fractions of proton and iron found to best fit the data are 49% proton and 51% iron, with an agreement in the means and widths of the data and mixture distributions than pure compositions. The $\langle X_{\mathrm{max}} \rangle$ of the data and proton-iron mixture are 611 $\mathrm{g/cm^2}$ and 618 $\mathrm{g/cm^2}$ respectively and the $\sigma(X_{\mathrm{max}})$, which is the width of X_{max} distribution, are 70 $\mathrm{g/cm^2}$ and 79 $\mathrm{g/cm^2}$. The fractions of each element as a function of energy are shown in Fig. 5.27. These two components fit result also indicates that the observed mass composition becomes lighter with increasing energy.

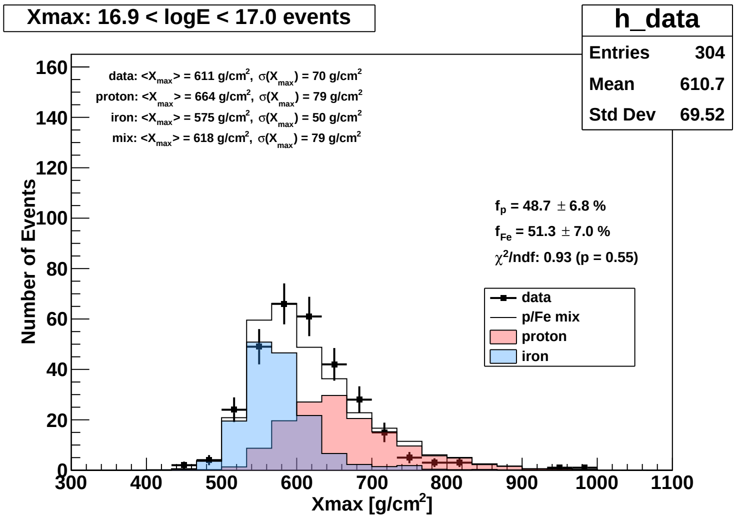

FIGURE 5.26: Example of mixture component fit. The observed X_{max} distribution in energy range of $10^{16.9}$ eV $< E < 10^{17.0}$ eV compared with mixture of proton and iron.

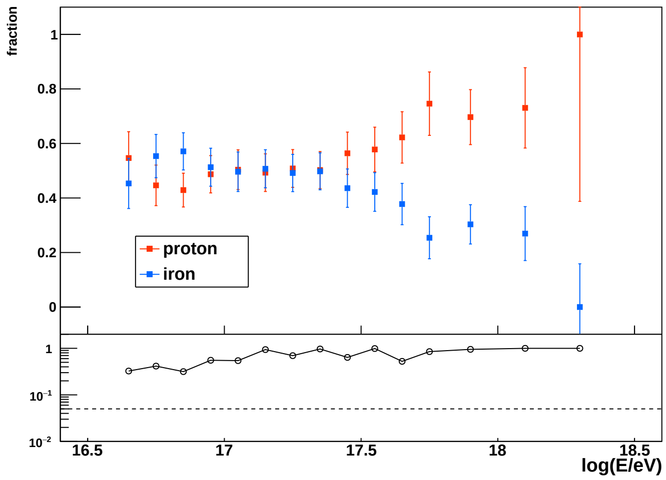

FIGURE 5.27: Fitted fraction and quality for the scenario with mixture of protons and iron nuclei. The upper panel shows the fractions of each component for each energy bin, and the lower panel shows the p-values obtained by chi-square tests.

5.6 Energy Spectrum

Calculation of the cosmic ray energy spectrum requires the number of observed event for each given energy bin, the detector aperture, and the observation time. This can be written as

$$J(E_i) = \frac{N(E_i)}{A\Omega(E_i) \cdot T \cdot \Delta E_i}, \tag{5.1}$$

where $J(E_i)$ is the flux of cosmic rays, $N(E_i)$ is the number of events in a given energy bin, $A\Omega(E_i)$ is the energy-dependent geometric aperture, T is the time period of the observation, and ΔE_i is energy interval, which expressed with the bin size b_i:

$$\Delta E_i = E_i(10^{b_i/2} - 10^{-b_i/2}) \tag{5.2}$$

To calculate the energy spectrum from the reconstructed energy distribution shown in Fig. 5.3 , we need to consider the bin-to-bin migrations of events due to the energy and zenith angle dependence of the detector acceptance, as well as the effects of the detector resolution. In order to take in account of these effects, the ideal measurement formula (Eq. 5.1) is modified as

$$J(E_i) = \frac{N_{\text{data}}(E_{\text{rec},i})}{\frac{N_{\text{MC}}(E_{\text{rec},i})}{N_{\text{MC}}(E_{\text{gen},i})} A_{\text{gen}}\Omega_{\text{gen}} \cdot T \cdot \Delta E_i}, \tag{5.3}$$

where $N_{\text{data}}(E_{\text{rec},i})$ and $N_{\text{MC}}(E_{\text{rec},i})$ are the number of data and MC events in the energy bin E_i, $N_{\text{MC}}(E_{\text{gen},i})$ is the number of generated MC events in the energy bin E_i, $A_{\text{gen}}\Omega_{\text{gen}}$ is a geometrical aperture in which the MC events are generated, and T is the detector on-time discussed in Sec. 5.1. Note that $N_{\text{data}}(E_{\text{rec},i})$ and $N_{\text{MC}}(E_{\text{rec},i})$ are evaluated by the reconstructed energies, while $N_{\text{MC}}(E_{\text{gen},i})$ are evaluated by the MC generated energies. As already discussed in Sec. 5.2, $N_{\text{data}}(E_{\text{rec},i})$ is shown in Fig. 5.3.

5.6.1 Detector Aperture

For the hybrid measurements, the aperture significantly depends on energy. Since the higher energy events are brighter, they can be seen farther away. On the other hand, the lower energy events are only observed relatively nearby. Thus, the aperture of hybrid detector is estimated by MC simulation. The geometrical aperture in this study can be written as

$$\begin{aligned} A_{\mathrm{gen}}\Omega_{\mathrm{gen}} &= \frac{\pi R^2}{2} \times \int_0^{\theta_{\mathrm{max}}} 2\pi \sin\theta \cos\theta \, \mathrm{d}\theta \\ &= (\pi R \sin\theta_{\mathrm{max}})^2/2, \end{aligned} \tag{5.4}$$

where R is the semi-circle radius, 9 km, and $\theta_{\mathrm{max}} = 60^\circ$. Thus, $A_{\mathrm{gen}}\Omega_{\mathrm{gen}} \simeq 299.79$ km^2 ·sr. Hence, the detector aperture $A\Omega(E)$ is calculated as,

$$A\Omega(E_i) = A_{\mathrm{gen}}\Omega_{\mathrm{gen}} \times \frac{N_{\mathrm{MC}}(E_{\mathrm{rec},i})}{N_{\mathrm{MC}}(E_{\mathrm{gen},i})} \tag{5.5}$$

The second ratio term for proton and iron MC cases are corresponding to Fig. 5.2. For this analysis, we must consider the acceptance for each data epoch because the detection efficiencies are completely different as shown in Fig. 5.3. The calculated detector apertures are shown in Fig. 5.28.

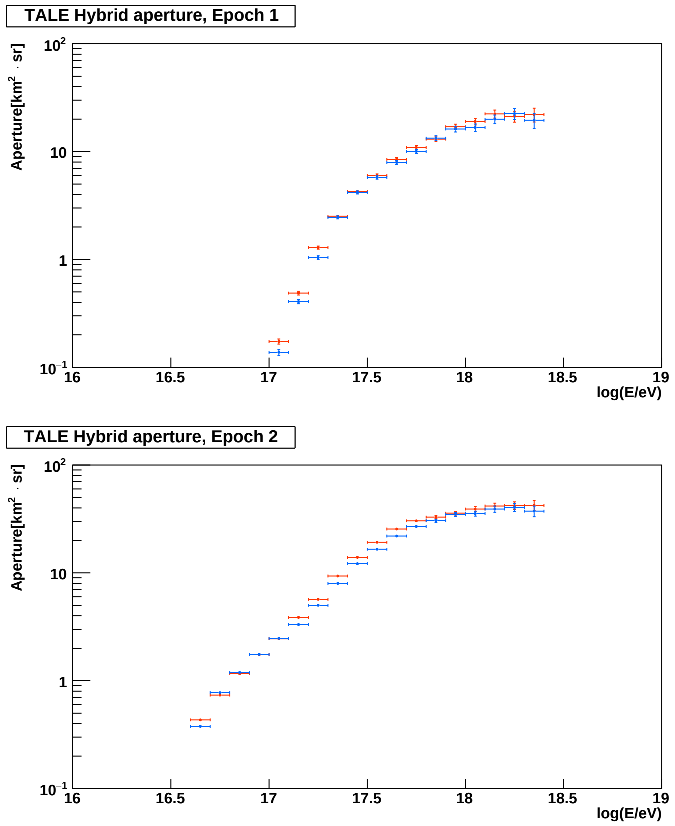

FIGURE 5.28: The calculated aperture as a function of the energy. *Top*: the TA MD + TALE hybrid detector aperture considering epoch 1 condition. *Bottom*: the TA MD + TALE hybrid detector aperture considering epoch 2 condition. In both figures, red points show the aperture assuming the pure proton primary, and blue points indicate the one of assuming the pure iron primary.

5.6.2 Detector Exposure

The exposure is defined as the product of the detector aperture and the detector on-time discussed in Sec. 5.1, and is given by

$$\epsilon(E_i) = A\Omega(E_i) \cdot T \tag{5.6}$$

Since both data epochs have no overlap of observation periods, the combined exposure of the TALE hybrid detector $\epsilon^{\mathrm{total}}(E_i)$ is simply taking a summation of each data epoch exposure,

$$\epsilon^{\mathrm{com}}(E_i) = A\Omega_{\mathrm{Epoch1}} \cdot T_{\mathrm{Epoch1}} + A\Omega_{\mathrm{Epoch2}} \cdot T_{\mathrm{Epoch2}} \tag{5.7}$$

As shown in Fig. 5.28, calculated apertures depend on assumed compositions. We take in account for the composition dependence of detector aperture with mixed composition predicted by the H4a model [12]. Fig. 5.29 shows a iron fraction predicted by H4a model. Once the iron fraction is obtained, we can evaluate the detector aperture with mixed composition,

$$A\Omega^{\mathrm{mix}} = A\Omega^{\mathrm{iron}} \left(R + f \cdot (1 - R) \right) \tag{5.8}$$

$$R = \frac{A\Omega^{\mathrm{proton}}}{A\Omega^{\mathrm{iron}}}, \tag{5.9}$$

where f is the assumed iron fraction shown in Fig. 5.29. The obtained exposures for each composition assumptions are shown in Fig. 5.30.

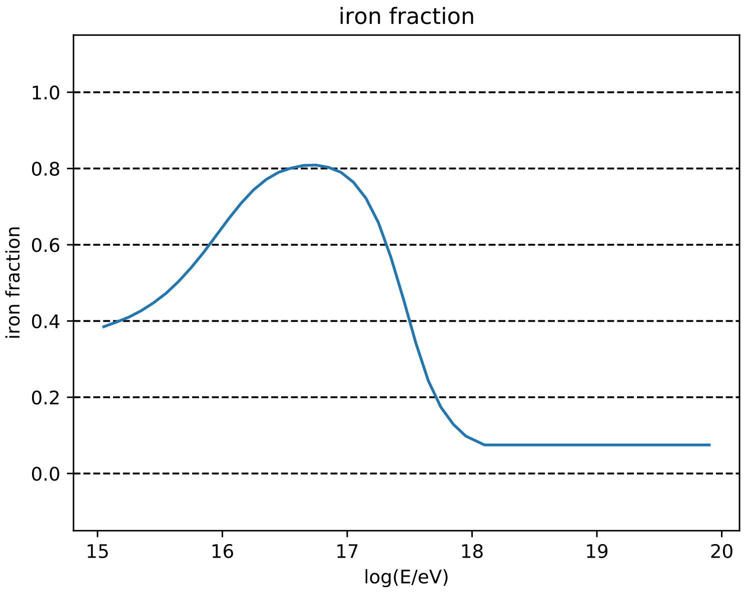

FIGURE 5.29: The iron fraction predicted by the H4a model [12].

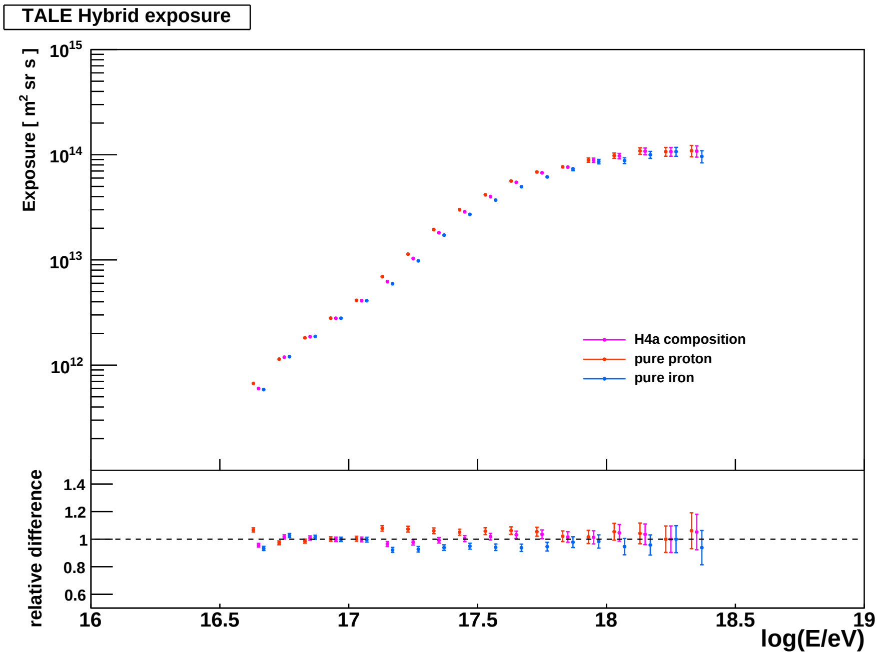

FIGURE 5.30: The combined exposure over the time period of 11/2017-02/2021. The bottom panel shows the relative differences in the exposure to proton, iron and H4a assumption with respect to the 50 % proton + 50 % iron mixture. The proton and iron points are shifted slightly to allow for greater visibility.

5.6.3 Energy Spectrum

The cosmic ray spectrum as a function of energy is calculated from Eq. 5.3. Fig. 5.31 shows the cosmic ray spectrum measured by the TA MD + TALE hybrid detector multiplied by E^3 to be clearly seen a spectrum structure. Note that the missing energy correction and aperture for calculation of the energy spectrum is assuming H4a composition prediction.

To evaluate the spectrum features for observed one, we had done by two different power law fits. The first fit is a single power law function written as

$$J(E) = A \cdot E^{\gamma}, \tag{5.10}$$

where A is the power law normalization constant, and γ represents the spectral index. The second fit is a one broken power function written as

$$J(E) = A \left\{ \begin{array}{ll} E^{\gamma_1} & (E < E_{\text{break}}) \\ E_{\text{break}}^{\gamma_1-\gamma_2} \cdot E^{\gamma_2} & (E \geq E_{\text{break}}), \end{array} \right. \tag{5.11}$$

where E_{break} represents the location of breakpoints in $\log_{10}(E/\text{eV})$, and γ_i represents the spectral indices. The fitting results are shown in Fig. 5.32. The single power law fitting is excluded by a value of the reduced chi-square, χ^2 / ndf = 3.02 (p-value = 1.8 $\times 10^{-4}$), while the broken power law function is better fitted than single one with χ^2 / ndf = 1.41 (p-value = 0.16). The fitted break point, $E_{\text{break}} = 17.04 \pm 0.01$ indicates the spectrum feature of 2nd knee, which has been observed in other measurements.

In Fig. 5.33, 2 yrs TALE FD monocular measurement [26], 11 yrs TA-SD measurement [25], 9.5 yrs BRM and LR FD monocular measurement [96], and 3yrs of Middle Drum FD monocular measurement [97] are shown for comparison. These spectra are in good agreement with each other.

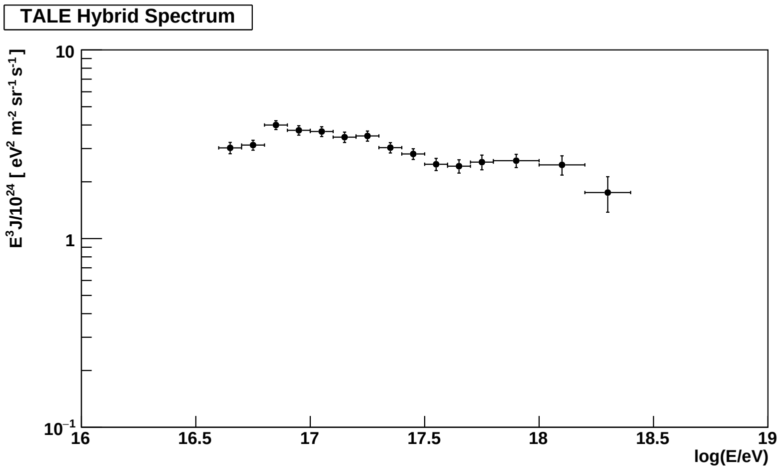

FIGURE 5.31: Cosmic ray spectrum measured by the TA MD + TALE hybrid detector. The spectrum has been multiplied by E^3.

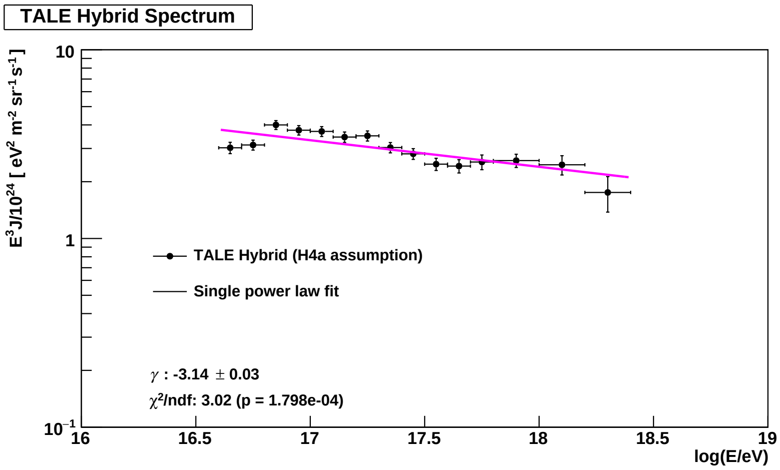

(A) Single power law fit

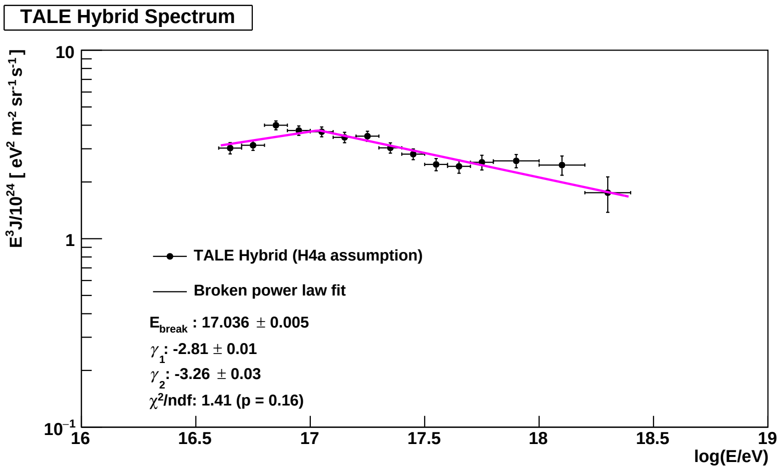

(B) Broken power law fit

FIGURE 5.32: The measured energy spectrum fitted by two types of power-law function. Solid line with magenta color in both figures show each power law fitting.

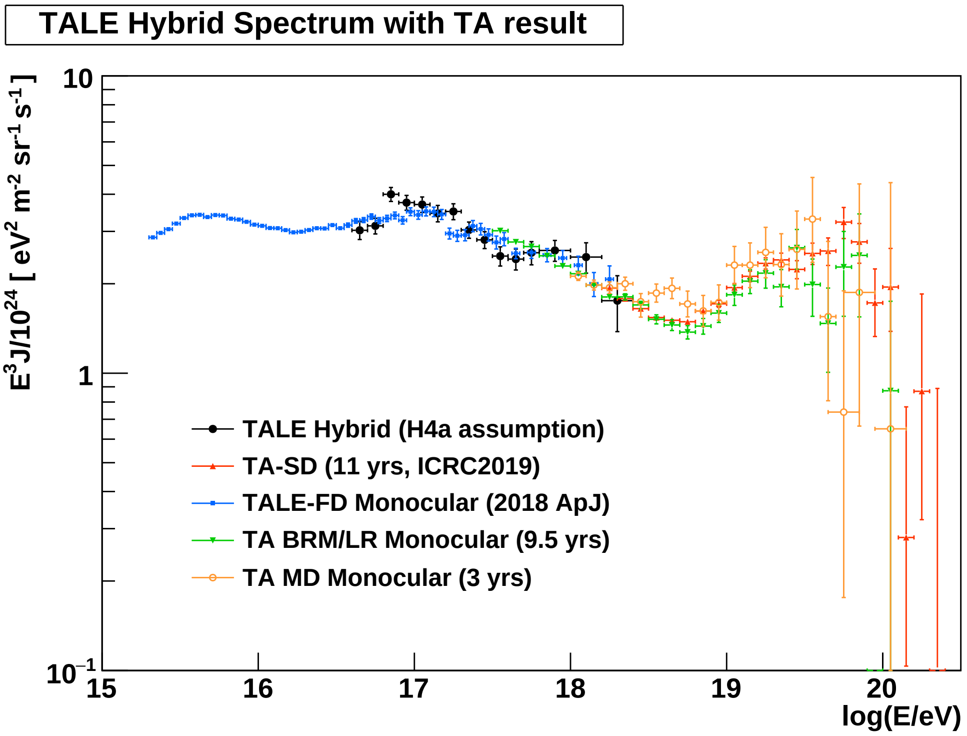

FIGURE 5.33: TALE hybrid cosmic ray energy spectrum comparison with measurements by the TALE FD monocular mode [26], by the TA using the FDs at Black Rock Mesa, Long Ridge [96] and Middle Drum [97] sites, and by the TA SD [25].

	γ_1	$\log_{10}(E_{\text{break}}/\text{eV})$	γ_2
TALE Hybrid	-2.81 ± 0.01	17.04 ± 0.01	-3.26 ± 0.03
TALE Monocular [26]	-2.92 ± 0.01	17.04 ± 0.04	-3.19 ± 0.02
TA SD [25]	-	-	-3.28 ± 0.02
TA BRM / LR FDs [96]	-	-	-3.29 ± 0.01

TABLE 5.3: Fit parameters of broken power law fit to the measured TA spectra.

5.7 Systematic Uncertainties

The systematic uncertainties for energy and $X_{\max}$ measurements take into account the effects of the detector, the experimental environment, and the physics models employed in event reconstruction. In this section, we discuss systematic uncertainties on the energy scale and the $X_{\max}$ determinations for this hybrid measurement.

5.7.1 Detector

Photonic Scale

This includes effects such as PMT gain, UV filter transmission, and telescope mirror reflectivity. The estimation is based on previous studies by the HiRes collaboration [98]. It is based on a portable, high-stability (∼ 0.5%) xenon flash lamp carried to each telescope on a monthly basis. As already mentioned in Table. 2.2, the

TALE FD uses the refurbished HiRes-II telescopes, then we estimate the energy scale uncertainty due to the photonic scale as 10%.

This photonic scale uncertainty is independent of the shower longitudinal profile. Thus, the uncertainty for X_{max} measurement caused by this can be estimated from the elongation rates of the mean X_{max} shown in Fig. 5.18, and we estimate the ± 5 g/cm^2 as X_{max} uncertainty due to the photonic scale uncertainty.

Relative Timing Difference between FD and SD

As discussed in Sec. 5.3, we estimated the relative timing difference between the FD and the SD by comparing with the arrival direction obtained by monocular reconstruction and by hybrid reconstruction with varying the timing difference. Since the sampling rate of SD electronics is 20 ns, the resolution of this estimation is also the same. Here, we take a conservative approach and estimate the systematic uncertainties by shifting ± 25 ns from the relative timing difference determined in Sec. 5.3. The distribution of differences on reconstructed energies and on X_{max} between the nominal and with timing shifted analysis for the observed events shows the systematics uncertainties. Fig. 5.34 and 5.35 show the results of differences for energies and X_{max}, respectively. In general, the estimated energy is proportional to the core distance, which is a distance between the FD and the shower core. The hybrid geometry fit robustly determines the shower core because the SD timing and location are used in the reconstruction. Thus, as we see in Fig. 5.34, the systematic uncertainty due to the relative timing difference is negligible for the TALE hybrid energy measurement. While for the X_{max} determination, the systematic shifts can be seen in Fig. 5.35 due to slightly changing the inclination angle of shower axis by shifting the relative timing. For this reason, we estimate the systematic uncertainty due to the relative timing difference as ± 3.5 g/cm^2.

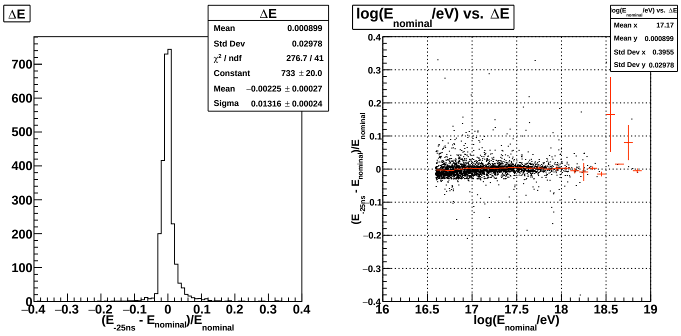

(A) Comparison to -25 ns shifted

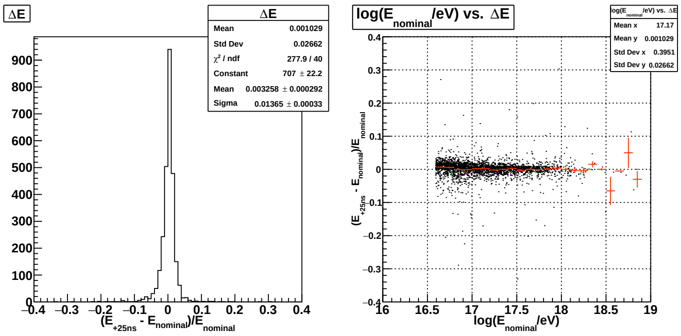

(B) Comparison to +25 ns shifted

FIGURE 5.34: Reconstructed energy comparison if the relative timing difference is assumed ± 25 ns shifted from nominal value. Left histograms show the difference for whole energies. Right scatter plots show the differences as a function of energy.

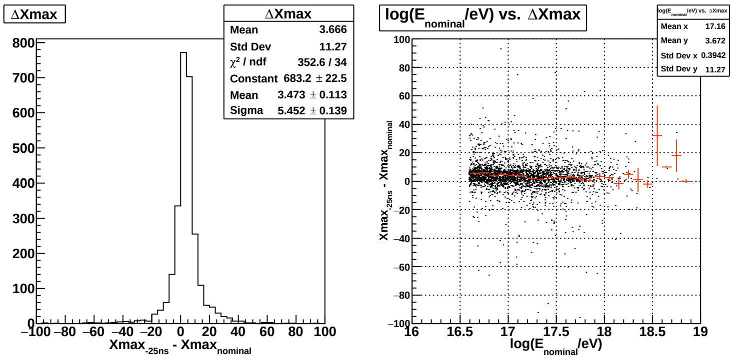

(A) Comparison to -25 ns shifted

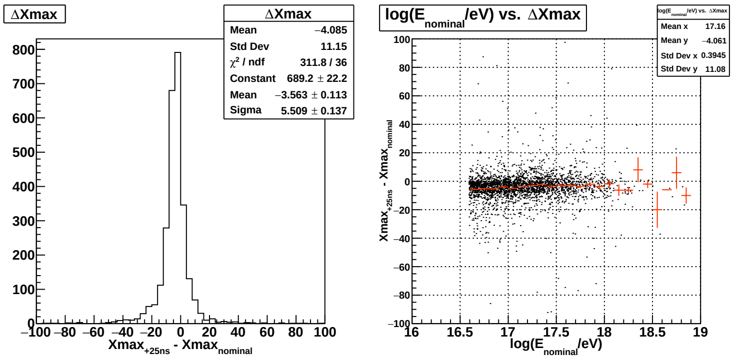

(B) Comparison to +25 ns shifted

FIGURE 5.35: Reconstructed X_{max} comparison if the relative timing difference is assumed ± 25 ns shifted from nominal value.

5.7.2 Fluorescence Yield

We use the fluorescence yield model that the absolute fluorescence yield measured by Kakimoto et al. [45] and the fluorescence line spectrum measured by the FLASH experiment [44]. Therefore the fluorescence yield model used in the TA FD analysis is expressed as

$$\mathrm{FY}_{\mathrm{TA}}(\lambda) = \frac{K \cdot f_{\mathrm{FLASH}}(\lambda)}{\int_{300}^{400} f_{\mathrm{FLASH}}(\lambda) \mathrm{d}\lambda}, \tag{5.12}$$

where $f_{\mathrm{FLASH}}(\lambda)$ is the FLASH spectrum with λ nm, K is the total fluorescence yield reported by Kakimoto et al. [45]. The systematic uncertainty for the absolute fluorescence yield is ± 10 % [45], and the temperature and humidity dependences also give 3 % and 5 % uncertainties respectively [99]. Thus, we conclude the systematic uncertainty for the fluorescence yield is ± 11 %. To investigate this effect, we compared the reconstructed energies and X_{max} with ± 11 % scaling for the absolute fluorescence yield.

Fig. 5.36 and 5.37 show the results of differences of reconstructed energies and Xmax, respectively. As we see, the systematic differences have the energy dependence because the observed low energy events are dominated by the Cherenkov light. Above $10^{17.5}$ eV, the systematic shifts in the energy scale is $\sim$ 10 % the same as absolute fluorescence yield uncertainty. From these results, we estimate that the systematic uncertainties due to the fluorescence yield uncertainty have the energy dependence and the maximum uncertainties are ± 10 % in the energy scale and ± 5 g/cm^2 in X_{max} measurement.

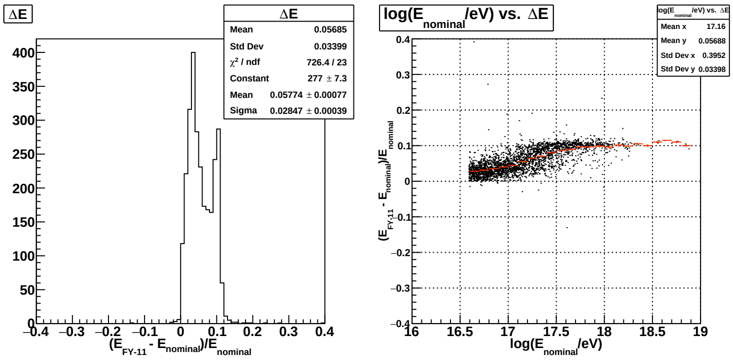

(A) Comparison to -11 % shifted in fluorescence yield

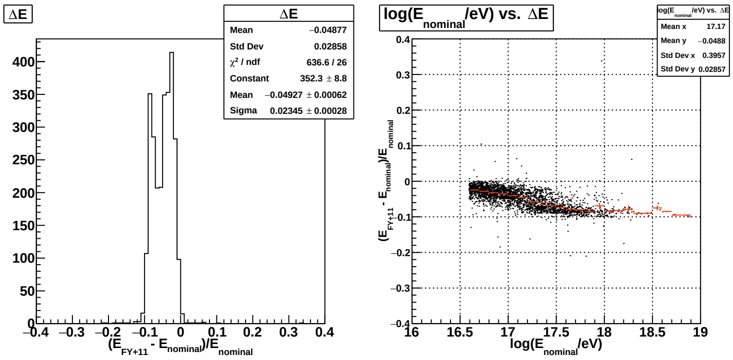

(B) Comparison to +11 % shifted in fluorescence yield

FIGURE 5.36: Reconstructed energy comparison with the fluorescence yield ± 11 % shifted from nominal value.

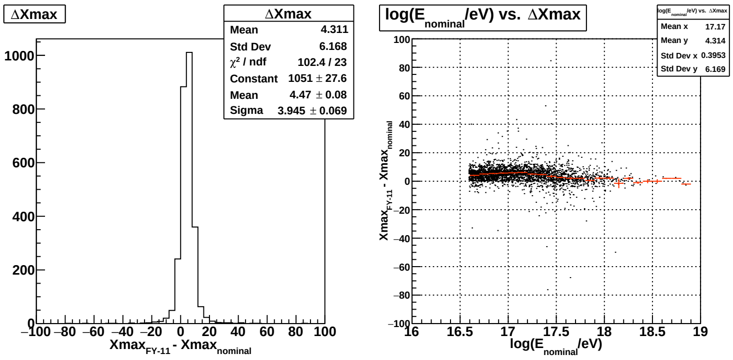

(A) Comparison to -11 % shifted in fluorescence yield

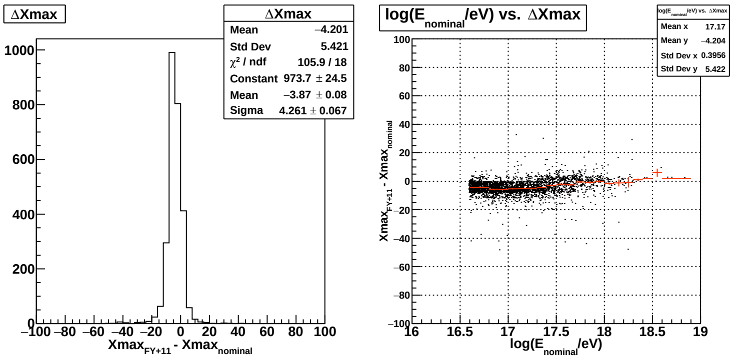

(B) Comparison to +11 % shifted in fluorescence yield

FIGURE 5.37: Reconstructed $X_{\max}$ comparison with the fluorescence yield ± 11 % shifted from nominal value.

5.7.3 Cherenkov Model

There are several models for the angular distribution of Cherenkov emission [46, 100, 101, 102]. Here we estimate the systematic uncertainty by reconstructing the observation data using Giller & Wieczorek [101] description of the angular distribution for Cherenkov photons instead of Nerling et al. [46] description. The difference of angular distribution for both description are shown in Fig. 5.38. Both models are parameterized the angular distribution of Cherenkov emission by using the CORSIKA with Cherenkov option. As we see, Nerling et al. [46] description are slightly higher at large angles than Giller & Wieczorek [101] one. Moreover, the angle to shower axis less than 10 degrees is also shown both differences as shown in the upper-right figure in Fig. 5.38, which is zoomed in the θ range from 0 to 10 degrees.

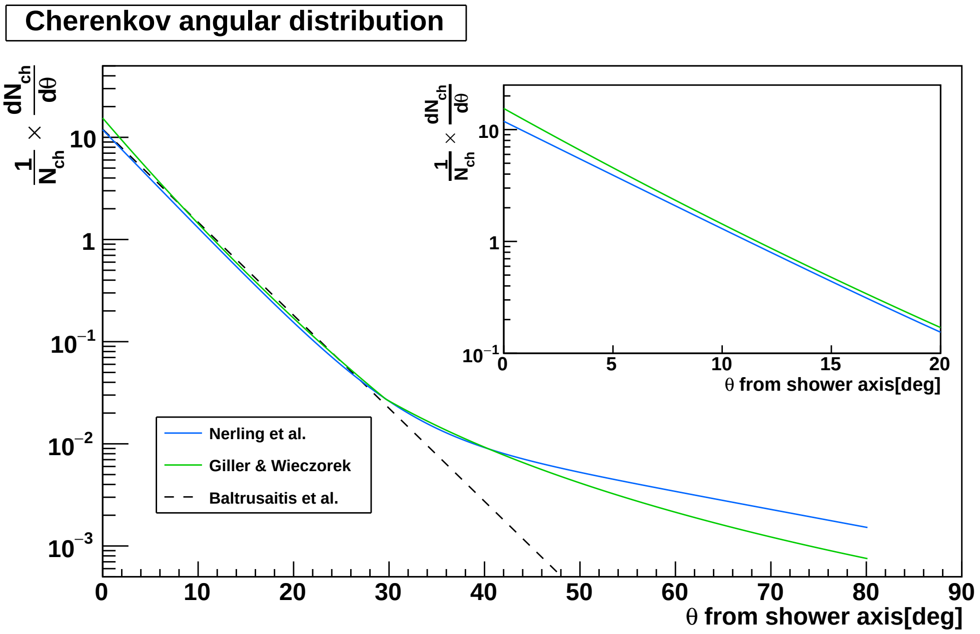

FIGURE 5.38: Angular distribution of Cherenkov photons comparison of Nerling et al. [46], Giller & Wieczorek [101] and Baltrusaitis et al. [102] description. Parameterizations with the shower age = 1, height = 5 km are shown in both description.

The differences in reconstructed energy and X_{max} using Nerling et al. [46] and Giller & Wieczorek [101] Cherenkov mode are shown in Fig. 5.39. Same reason as fluorescence yield study, the systematic shifts in the energy scale and X_{max} have the energy dependence. In consequence, we estimate that the systematic uncertainties due to the Cherenkov model have also the energy dependence and the maximum uncertainties are $\pm$ 4 % in the energy scale and $\pm$ 12 g/cm^2 in the X_{max} measurement at lower energy region.

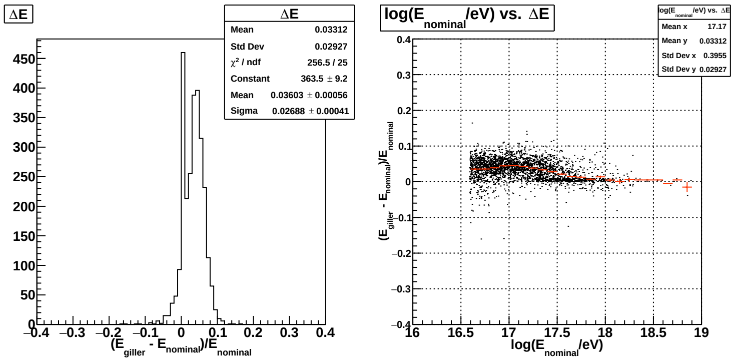

(A) Comparison of energy to Giller & Wieczorek [101] Cherenkov model

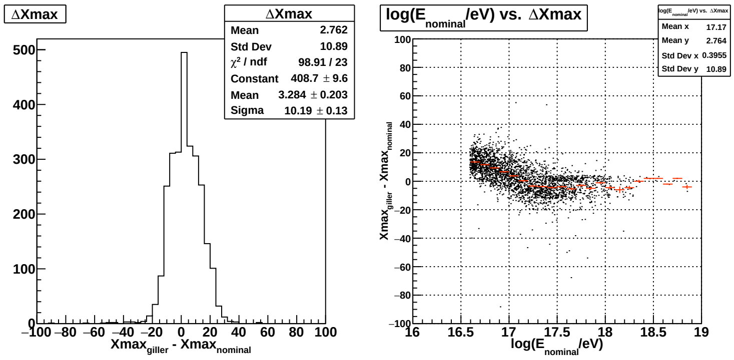

(B) Comparison of X_{max} to Giller & Wieczorek [101] Cherenkov model

FIGURE 5.39: Reconstructed energy and X_{max} comparison with Nerling et al. [46] and Giller & Wieczorek [101] Cherenkov model

5.7.4 Atmospheric Parameters

VAOD

The atmospheric effect is dominated by the amount of aerosols. In this analysis, we adopt a value of the horizontal attenuation length, which is 30 km i.e., VAOD = 0.04. As discussed in Sec. 2.6.2, the widths of VAOD distribution are + 0.025, -0.015 respectively. Here we estimate the systematic uncertainties for atmospheric attenuation by shifting these values from nominal one. Fig. 5.40 - 5.41 the results of differences for energies and X_{max}, respectively. The systematic uncertainties for energies ansd X_{max} due to the atmospheric aerosols are $^{+2.5}_{-1.5}$ % and ± 1 g/cm^2, respectively.

Atmospheric Profile

Another effect comes from the atmospheric profile, i.e., the pressure and density of the atmosphere as a function of height. As discussed in Sec. 2.6.1, we adopt the atmospheric profiles database provided by the GDAS. When we reconstruct the observation data using an atmospheric database that uses NOAA National Weather Service radiosonde data instead of the GDAS, it can be estimated the systematic uncertainties due to the atmospheric profiles. Here we use both radiosonde database measured at ELKO and SLC sites for comparison. We found to be ± 1% and ± 1 g/cm^2 for the systematic uncertainties for energy and X_{max} due to the atmospheric profiles.

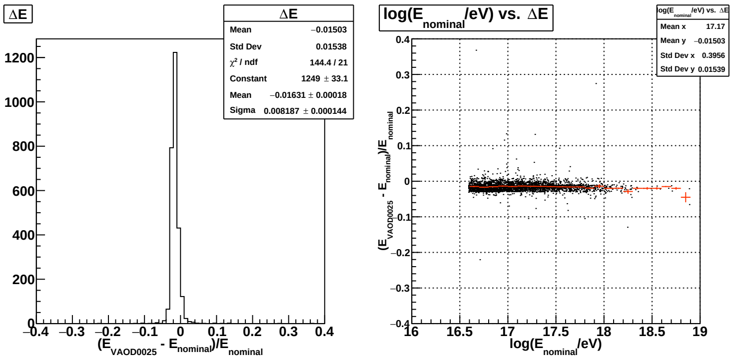

(A) Comparison to -0.015 shifted in VAOD

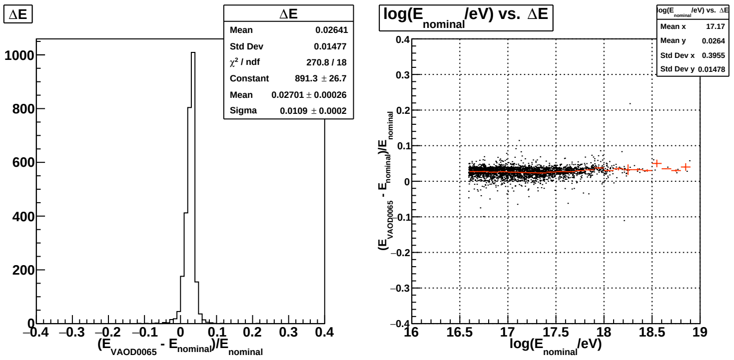

(B) Comparison to +0.025 shifted in VAOD

FIGURE 5.40: Reconstructed energy comparison with the VAOD shifted $^{+0.025}_{-0.015}$ from nominal value.

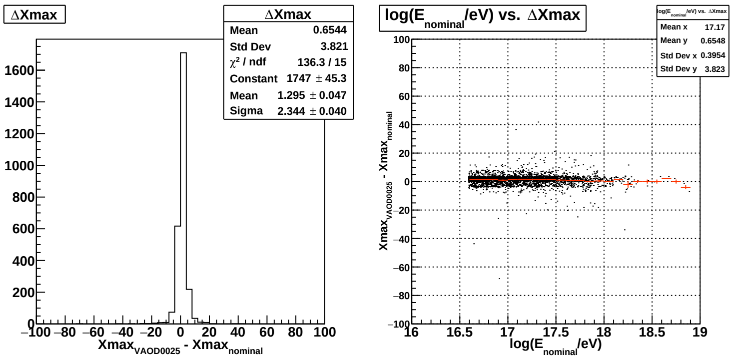

(A) Comparison to -0.015 shifted in VAOD

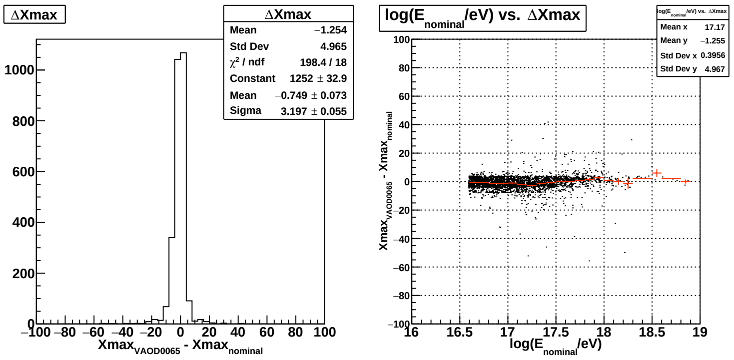

(B) Comparison to +0.025 shifted in VAOD

FIGURE 5.41: Reconstructed $X_{\max}$ comparison with the VAOD shifted $^{+0.025}_{-0.015}$ from nominal value.

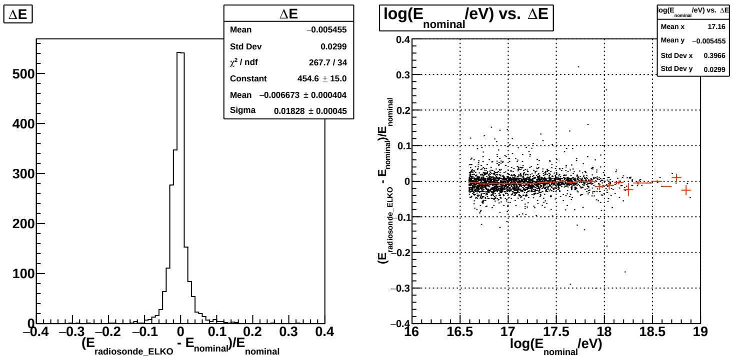

(A) Comparison to radiosonde measured at ELKO site

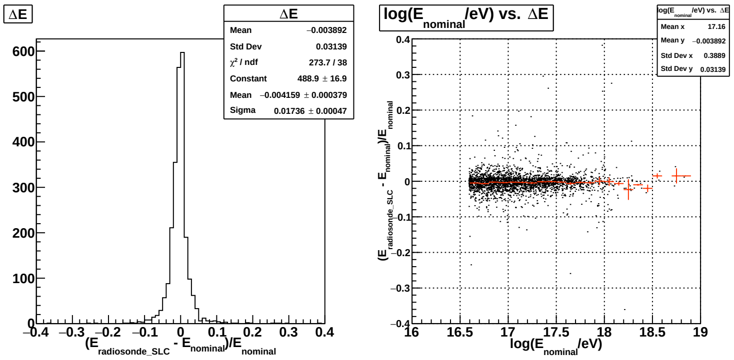

(B) Comparison to radiosonde measured at SLC site

FIGURE 5.42: Reconstructed energy comparison with the radiosonde atmospheric profile.

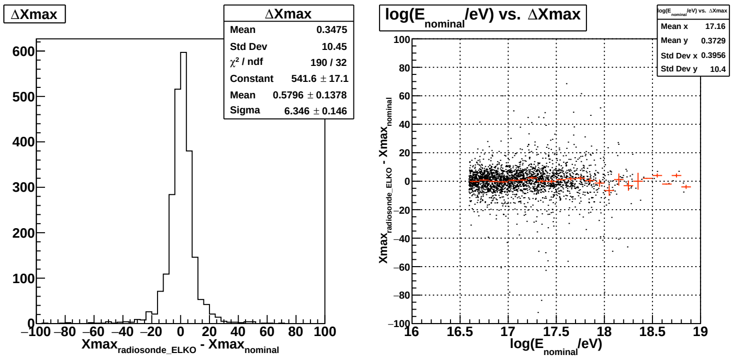

(A) Comparison to radiosonde measured at ELKO site

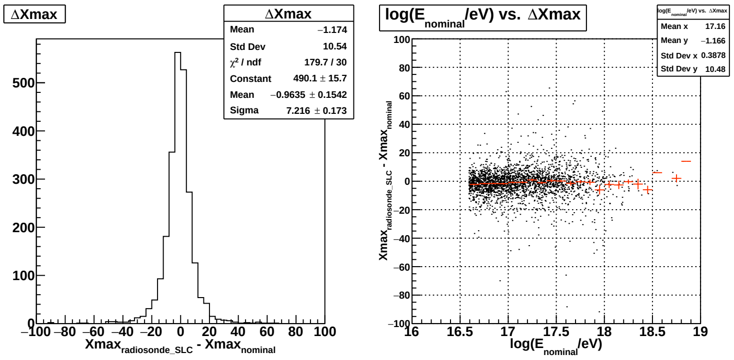

(B) Comparison to radiosonde measured at SLC site

FIGURE 5.43: Reconstructed X_{max} comparison with the radiosonde atmospheric profile.

5.7.5 Missing Energy Correction

As discussed in Sec. 4.4.3, we apply the missing energy correction assuming the H4a composition model [12]. Consequently, this correction depends on the composition assumption. Thus, the discrepancy of missing energies between primary protons and irons can be systematic uncertainties. The maximum discrepancy from H4a assumption curve and predicted missing energy curve is 6 % at $10^{16.5}$ eV, then we estimate the systematic uncertainty due to the missing energy as 6 % in the energy scale and 3 g/cm^2 in the X_{max} measurement.

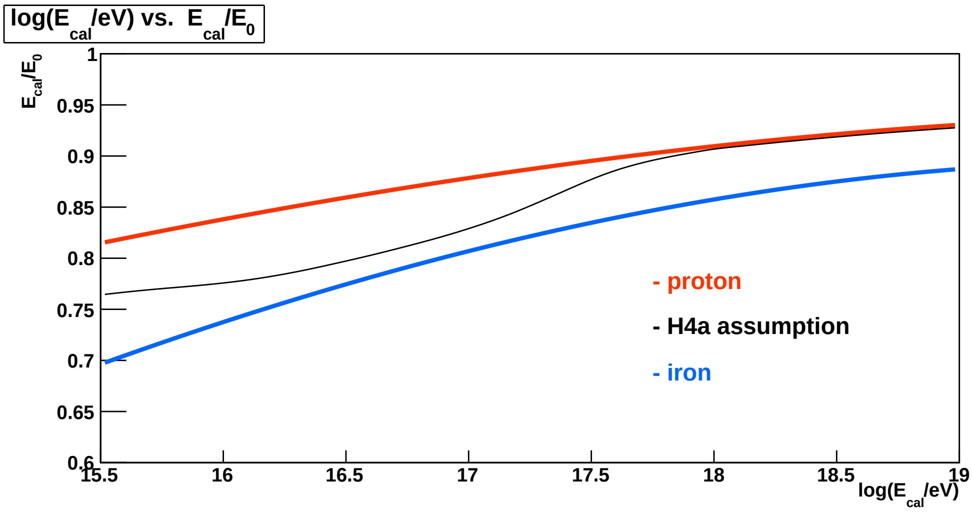

FIGURE 5.44: Missing energy correction assuming the H4a composition model [12].

5.7.6 Total Systematic Uncertainties

Adding all contributions uncertainties in quadrature, we summarized the total systematic uncertainties on the energy scale and X_{max} measurement in Table. 5.4. The total systematic uncertainties as a function of energy are also shown in Fig. 5.45 and 5.46.

Sources	Energy	X_{max}
Photonic Scale	10 %	5 g/cm^2
Relative Time of FD and SD	0	3.5 g/cm^2
Fluorescence yield	3 to 10%	5 to 1 g/cm^2
Cherenkov model	5 to 1 %	12 to 5 g/cm^2
Atmosphere	$^{+2.7}_{-1.8}$ %	1.4 g/cm^2
Missing energy	6 %	3 g/cm^2
Total	12.6 to 15.7 %	15.7 to 7.8 g/cm^2

TABLE 5.4: Summary of systematic uncertainties in energy, X_{max} measurements. Lines with multiple entries represent the values at the low and high end of the considered energy range ($\simeq 10^{16.5}$ eV and $\simeq 10^{18.5}$ eV, respectively).

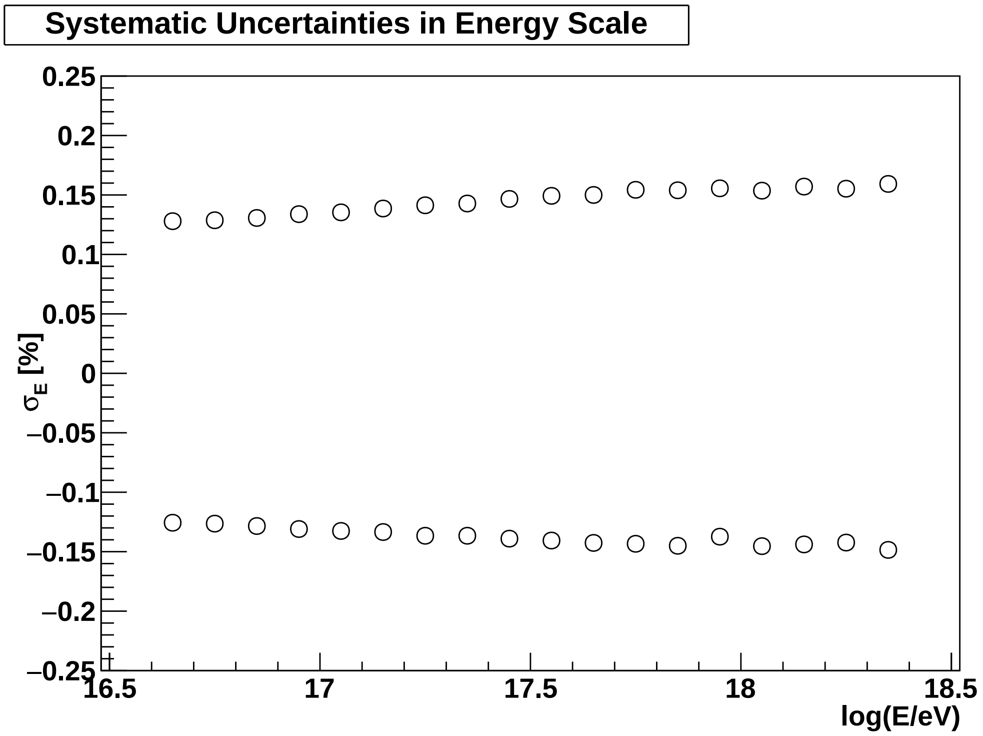

FIGURE 5.45: Systematic uncertainties in the energy scale as a function of energy. Quadratic sum of all contributions are presented.

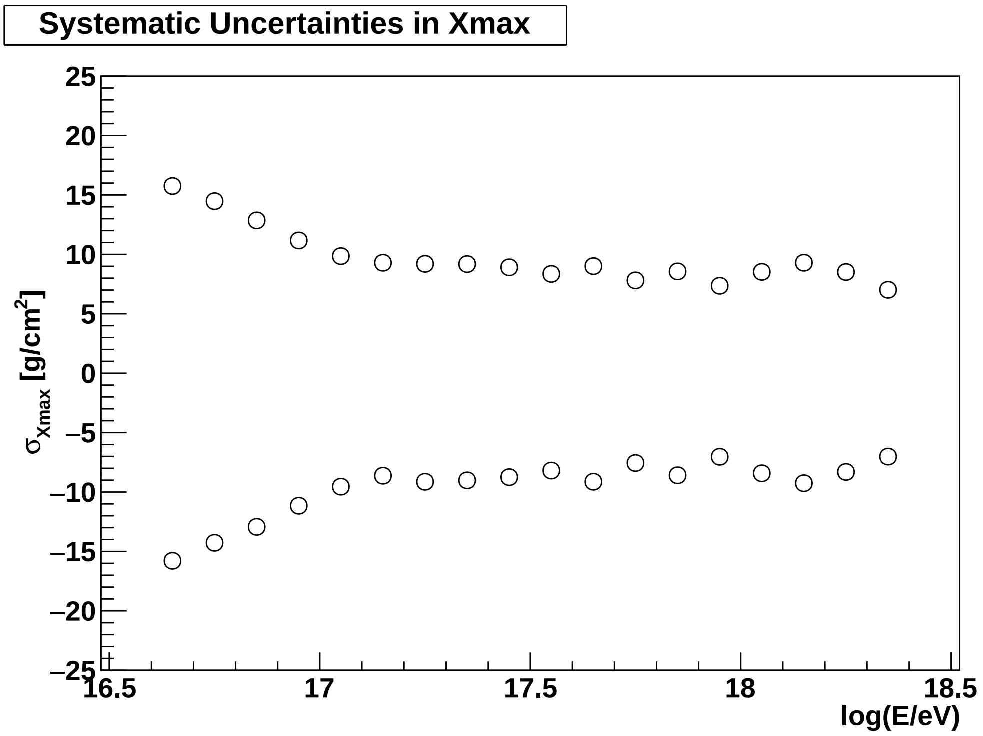

FIGURE 5.46: Systematic uncertainties in X_{max} as a function of energy. Quadratic sum of all contributions are presented

5.8 Comparison with Other Measurements

5.8.1 Energy Spectrum Measurements

The uncertainty of the energy scale is propagated into the flux measurement by $\sigma_J/J = |\gamma - 1|\sigma_E/E$ [103], where the flux is described as $J \propto E^{-\gamma}$. Using the values shown in Fig. 5.45, the systematic uncertainties in the flux measurement are obtained: $\sigma_J^{\mathrm{sys,E}}/J \approx 23\%$, for $E < 10^{17}$ eV, $\sigma_J^{\mathrm{sys,E}}/J \approx 30\%$, for $E > 10^{17}$ eV. Fig. 5.47 shows the observed spectrum by TALE hybrid detector with systematic error denoted by gray band. In addition, other spectra measured by TALE monocular mode [26], IceTop [24], Yakutsk [16],Tunka [20], KASCADE-Grande [15], and Pierre Auger Observatory [104] are shown for comparison. Their results are compatible with the TALE hybrid spectrum within its systematic uncertainties. The observed spectral indices and the break point energy, which is related with the 2nd knee, are summarized in Table. 5.5.

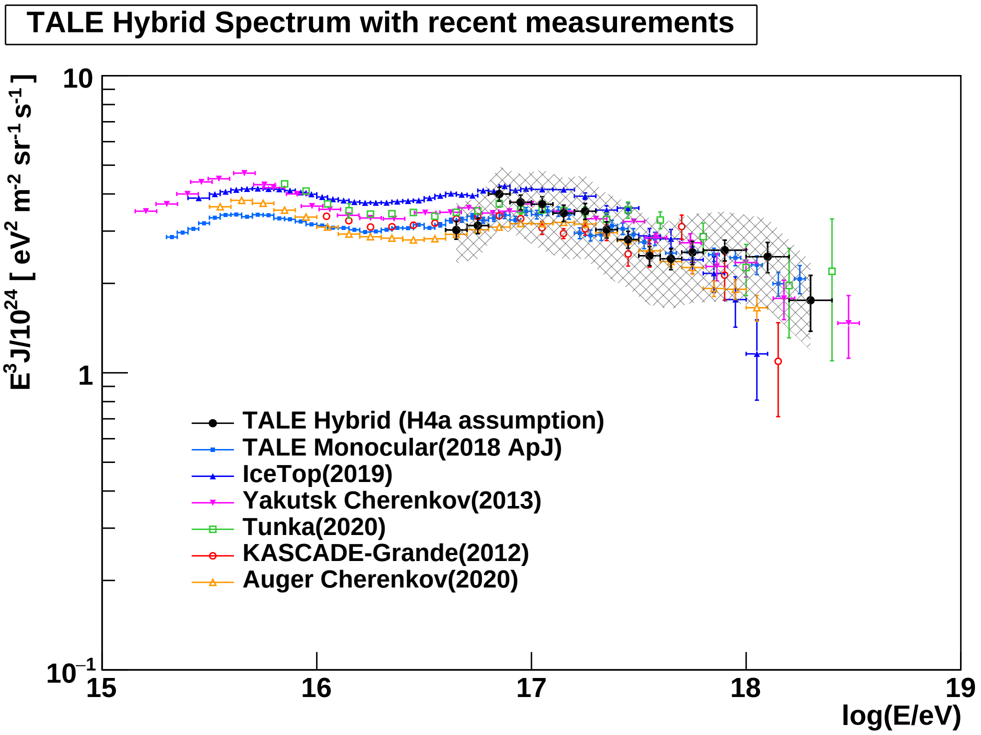

FIGURE 5.47: TALE hybrid energy spectrum with systematic band. For comparison, TALE monocular mode [26], IceTop [24], Yakutsk [16], KASCADE-Grande [15], and Auger Cherenkov-dominated data [104] results are shown.

	γ_1	$\log_{10}(E_{\mathrm{break}}/\mathrm{eV})$	γ_2
TALE Hybrid	-2.81 ± 0.01	17.04 ± 0.01	-3.26 ± 0.03
IceTop [105]	-2.91 ± 0.01	17.1 ± 0.1	-3.37 ± 0.08
Yakutsk [16]	-2.92 ± 0.03	∼ 17.1	-3.24 ± 0.04
Tunka [20]	-2.99 ± 0.01	∼ 17.5	-3.29 ± 0.09
KASCADE-Grande [15]	-2.95 ± 0.05	16.92 ± 0.10	-3.24 ± 0.08
Auger [104]	-2.91 ± 0.01	17.22 ± 0.03	-3.36 ± 0.03

TABLE 5.5: Fit parameters of broken power law fit by other measurements.

5.8.2 Mass Composition Measurements

Fig. 5.48 shows the X_{max} elongation plot observed by the TALE hybrid detector with systematic error denoted by gray band. The TA hybrid detector measurement [11] [106], HiRes/MIA [107], and Auger [28] results are also shown for comparison. As we see, the observed mean X_{max} are smoothly connected to the mean X_{max} measured by the TA hybrid detector at EeV energies. As well, the TALE hybrid data is consistent with the HiRes/MIA result. However, a discrepancy between the results from the Auger and this work can be seen in lower energies. The origin of this discrepancy remains unclear and requires additional research.

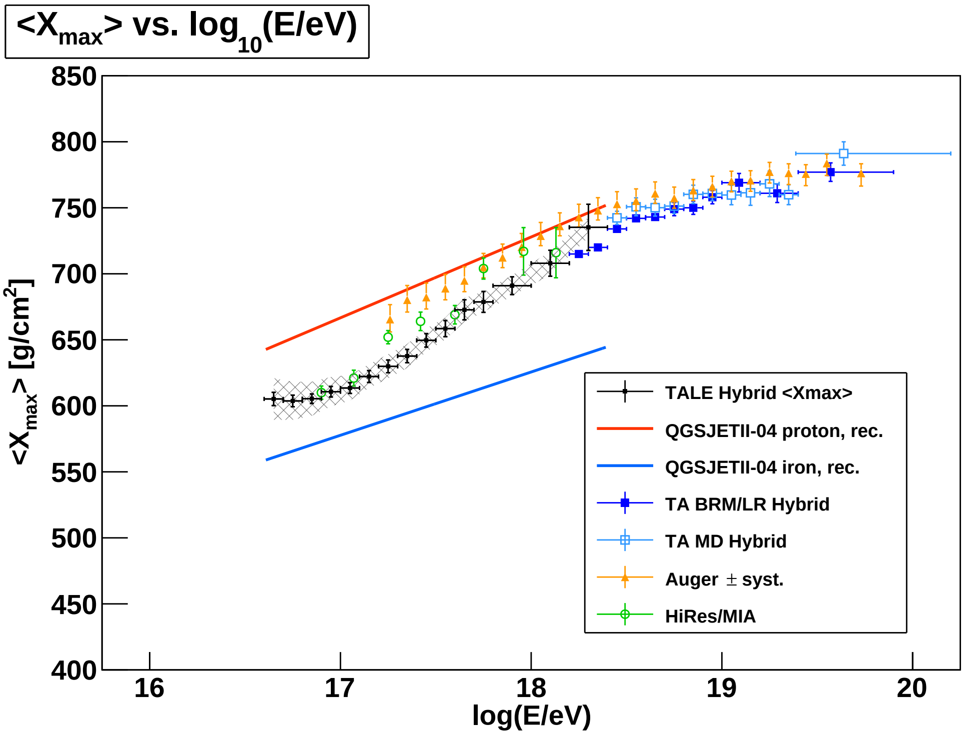

FIGURE 5.48: TALE hybrid $\langle X_{\mathrm{max}} \rangle$ with systematic band. For comparison, 8.5 yrs TA BRM/LR hybrid [11], 7 yrs TA MD hybrid [106], HiRes/MIA [107], and Auger [28] results are shown. The Auger data are take from public data page on [108].

For further comparison with particle detection based experiments, we display a mean logarithmic mass plot. From the observed X_{max}, the mean ln$A$ can be determined by,

$$\langle \ln A \rangle = \frac{X_{\mathrm{max}}^{\mathrm{data}} - X_{\mathrm{max}}^{\mathrm{proton}}}{X_{\mathrm{max}}^{\mathrm{iron}} - X_{\mathrm{max}}^{\mathrm{proton}}} \cdot \ln A_{\mathrm{iron}}, \tag{5.13}$$

where $X_{\mathrm{max}}^{\mathrm{data}}$ is the mean X_{max} observed by experiments, $X_{\mathrm{max}}^{\mathrm{proton/iron}}$ are the mean X_{max} for the proton and the iron primaries obtained by MC simulation, and $\ln A_{\mathrm{iron}}$ is the natural logarithm of the iron atomic mass. Note that $X_{\mathrm{max}}^{\mathrm{proton/iron}}$ are evaluated by own MC of each experiment. Fig. 5.49 shows the mean ln$A$ as a function of energy. The mean ln$A$ measured by the TALE hybrid detector are shown as black dots with systematic error denoted by gray band. As we see, the photon detection based measurements (Tunka, Yakutsk, TA / TALE and Auger) are consistent with each other, while a discrepancy with particle detection based experiments (KASCADE and IceTop) is seen. Since the mean ln$A$ measured by the KASCADE and IceTop are based on the muon detection, this discrepancy might be explained by the muon puzzle as discussed in Sec. 1.1.3.

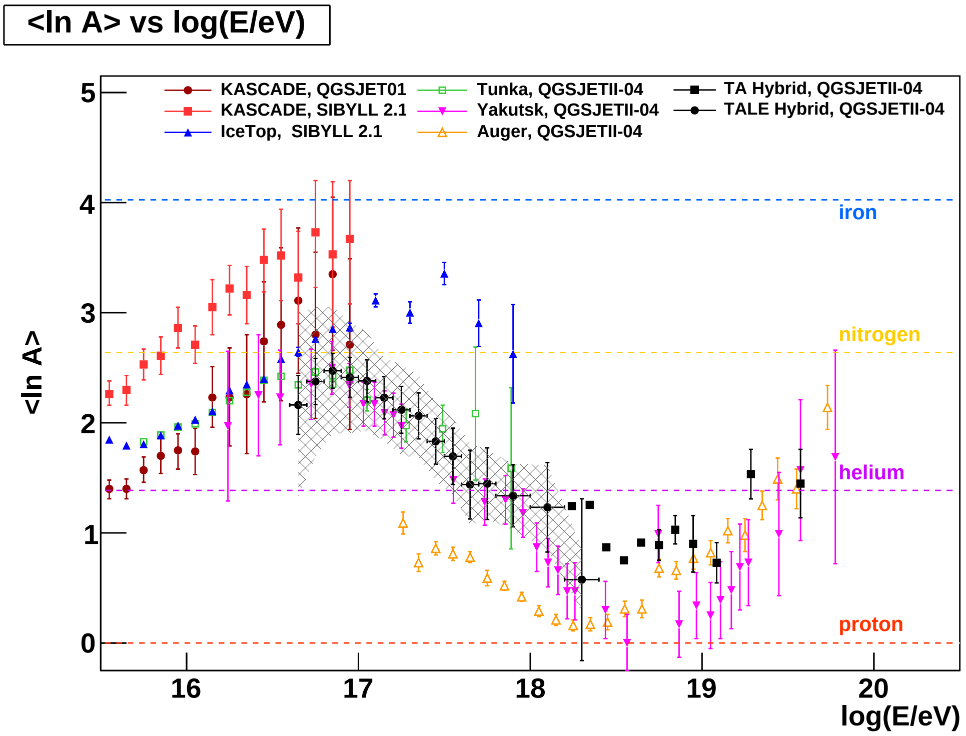

FIGURE 5.49: ⟨ln$A$⟩ measured by the TALE hybrid detector with systematic band. For comparison, two interpretations by KASCADE [109], IceTop [24], Tunka [21], Yakutsk [110], Auger [28], and 8.5 yrs TA BRM/LR hybrid [11] results are shown.

Chapter 6

Conclusions

In order to study the properties of cosmic rays, the Telescope Array experiment has started stable observations in 2008 with the Hybrid Detectors, which are composed of 38 fluorescence detectors located in three sites and 507 surface detectors with 1.2 km spacing covered with 700 km^2 of effective area. In addition, resolving the transition of cosmic ray sources from the galactic to extragalactic origin, the Telescope Array Low energy Extension (TALE) has started with the same detection technique as the TA since November 2017.

This dissertation is focused on studying the cosmic ray mass composition and energy spectrum in the energy range of $10^{16.5}$ - $10^{18.5}$ eV, where could be signatures of the transition of cosmic rays sources from galactic to extragalactic origin. Knowing the composition and spectrum features of cosmic rays at this distinctive energy region represents an important constraint on the galactic-extragalactic transition models. For this purpose, we analyze more than 2 years of data collected by the TA Middle Drum FD and the TALE hybrid detector.

To reach the results of cosmic ray mass composition and energy spectrum below 10^{17} eV, we are necessary to precisely reconstruct events that are dominated by the Cherenkov light. As the Cherenkov light is treated as noise for the fluorescence light in the previous standard FD measurements, this aggressively using the Cherenkov light such as fluorescence light is a breakthrough approach for the FD measurements. This approach is required the more careful treatment of the Cherenkov light properties are needed than ever. However, the time durations of Cherenkov dominated shower are too short for stand-alone geometry reconstruction, even if we reconstruct the hybrid data (events observed by both the FD and SD). For this reason, we apply the Profile Constrained Geometry Fit (PCGF) reconstruction to the hybrid data for the first time. This reconstruction achieved resolutions of 0.5° in zenith angle and azimuthal angle, less than 30 g/cm^2 in $X_{\max}$, and 10 % in energy. In addition, a hybrid Monte Carlo simulation was developed, making use of existing SD and FD simulations. The validity of these simulations has been verified by Data/MC comparisons, ensuring that our MC simulations reproduce the hybrid data with reasonable agreements.

In the mass composition analyses, we firstly compared the observed mean $X_{\max}$ with the expected ones estimated by the MC simulations for primary protons or irons using the QGSJetII-04 hadronic interaction model. The elongation rate of data mean $X_{\max}$ shows a clear break at the energy of $\log_{10}(E/\mathrm{eV}) = 17.06 \pm 0.09$, indicating the start of a transition from heavy to light composition. In addition, the all of $X_{\max}$ distributions from the data were compared to the corresponding proton, iron, and mixture of both $X_{\max}$ distributions in each energy bin. We performed statistical tests, and we got quantifying the same results and showed compatibility with mass composition getting lighter with increasing the cosmic ray energies. Lastly, in the mean ln$A$ plot, our result shows the mass composition is getting from intermediate mass to light component with increasing cosmic ray energies.

In the energy spectrum analysis, we confirmed the 2nd knee structure at $\log_{10}(E/\mathrm{eV})$ = 17.04 ± 0.01 in the measured spectrum, with a softening the spectral index from γ_1 = -2.81 ± 0.01 to γ_2 = -3.26 ± 0.03. The results are consistent with our previous measurements by the TA SD, TA FD, and TALE FD monocular mode. Both break features in the elongation rate and the energy spectrum are likely correlated, and imply to be corresponding to the end of heavy components of galactic cosmic rays and the start of light components of extragalactic cosmic rays.

Appendix A

X_{max} distributions with mixture composition fit

Fig. A.1 - A.4 show the measured X_{max} distributions compared with the best fit mixed distributions contributing of proton and iron for each energy bin.

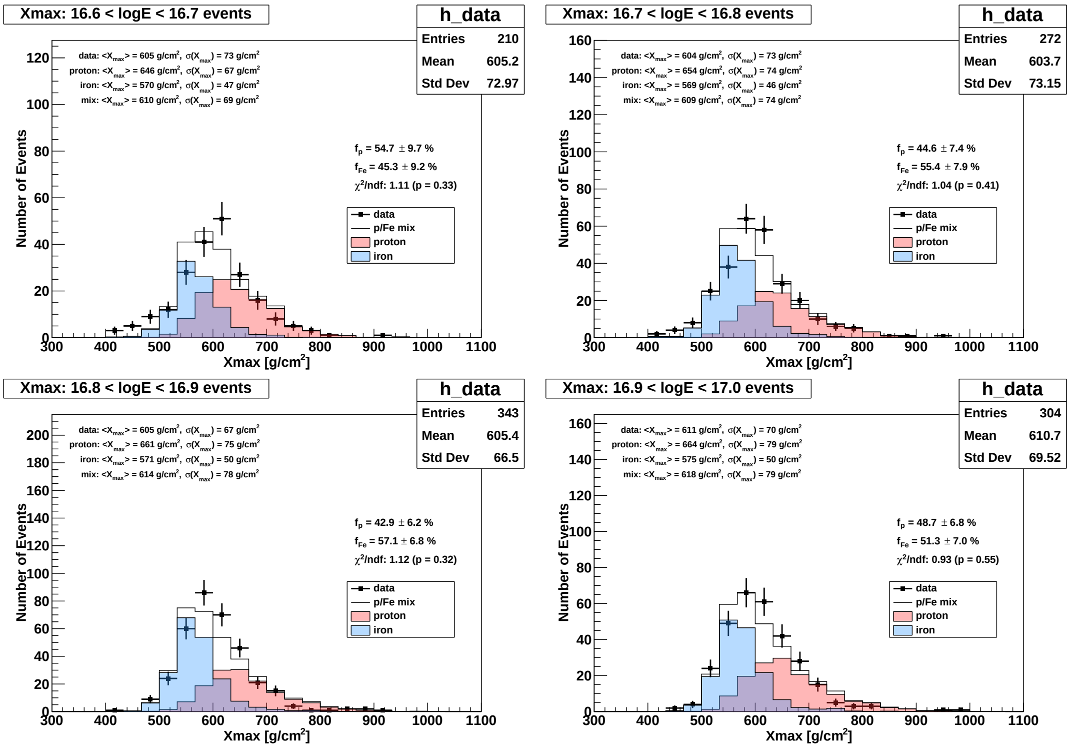

FIGURE A.1: X_{max} distribution for data and mixture of proton MC and iron MC for energy greater than $10^{16.6}$ eV and less than $10^{17.0}$ eV. In each figure, the data is shown with points, the mixture fit is shown by solid line with red filled proton MC and blue filled iron MC.

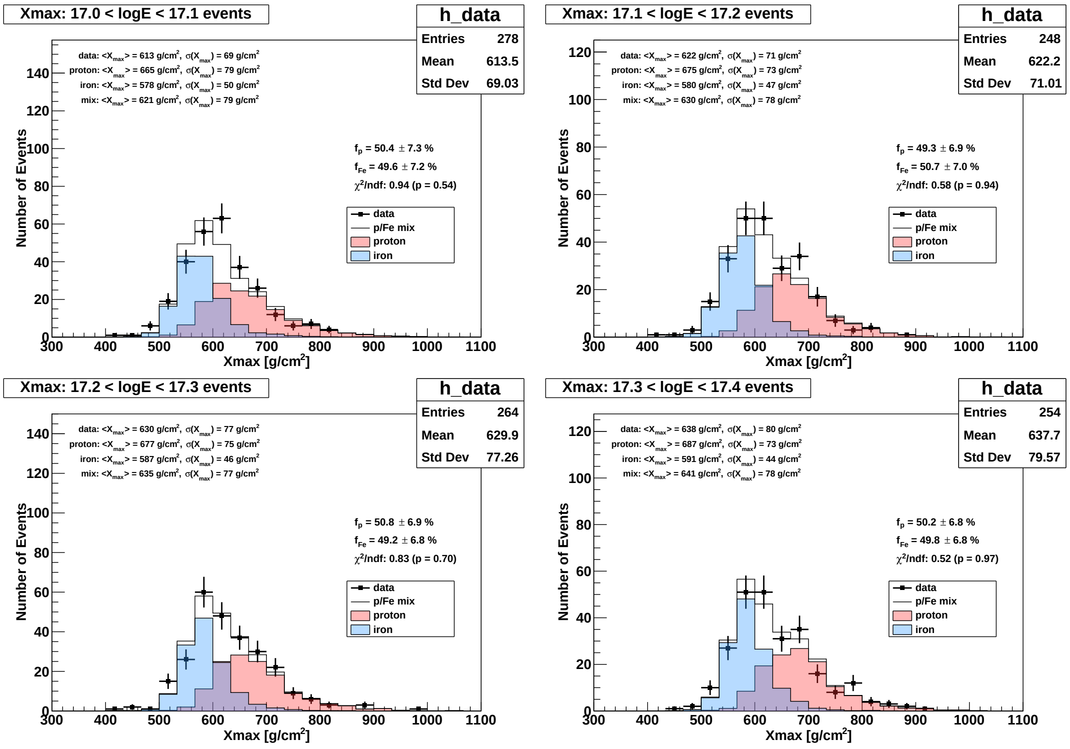

FIGURE A.2: $X_{\max}$ distribution for data and mixture of proton MC and iron MC for energy greater than $10^{17.0}$ eV and less than $10^{17.4}$ eV. In each figure, the data is shown with points, the mixture fit is shown by solid line with red filled proton MC and blue filled iron MC.

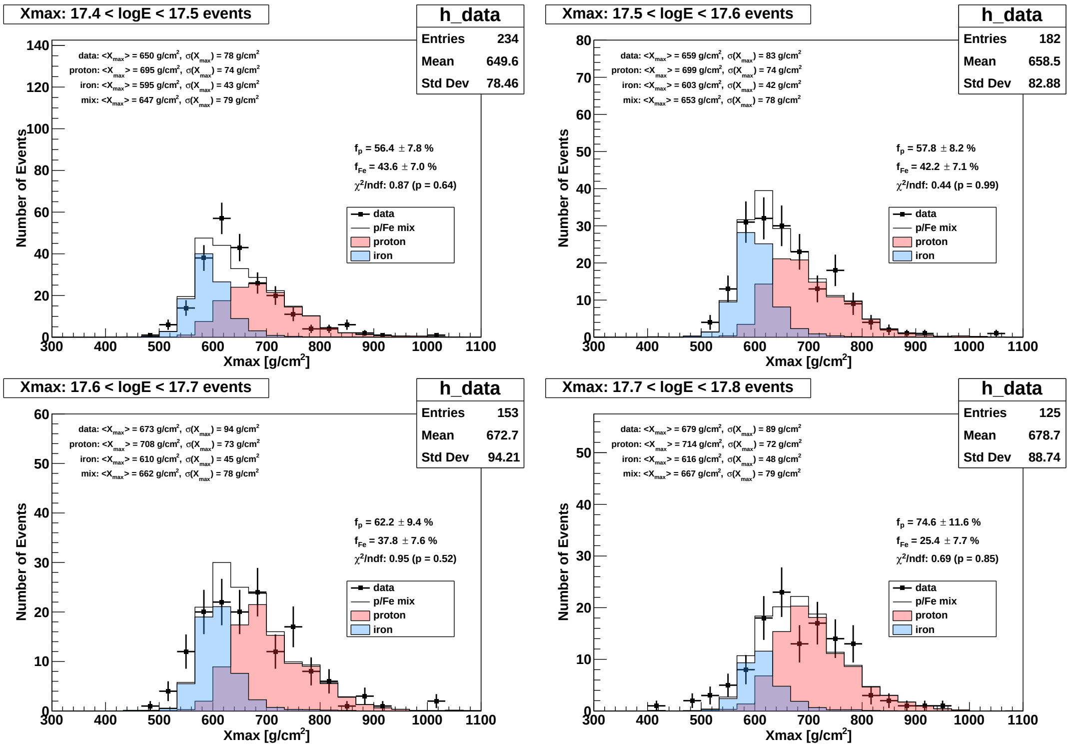

FIGURE A.3: $X_{\max}$ distribution for data and mixture of proton MC and iron MC for energy greater than $10^{17.4}$ eV and less than $10^{17.8}$ eV. In each figure, the data is shown with points, the mixture fit is shown by solid line with red filled proton MC and blue filled iron MC.

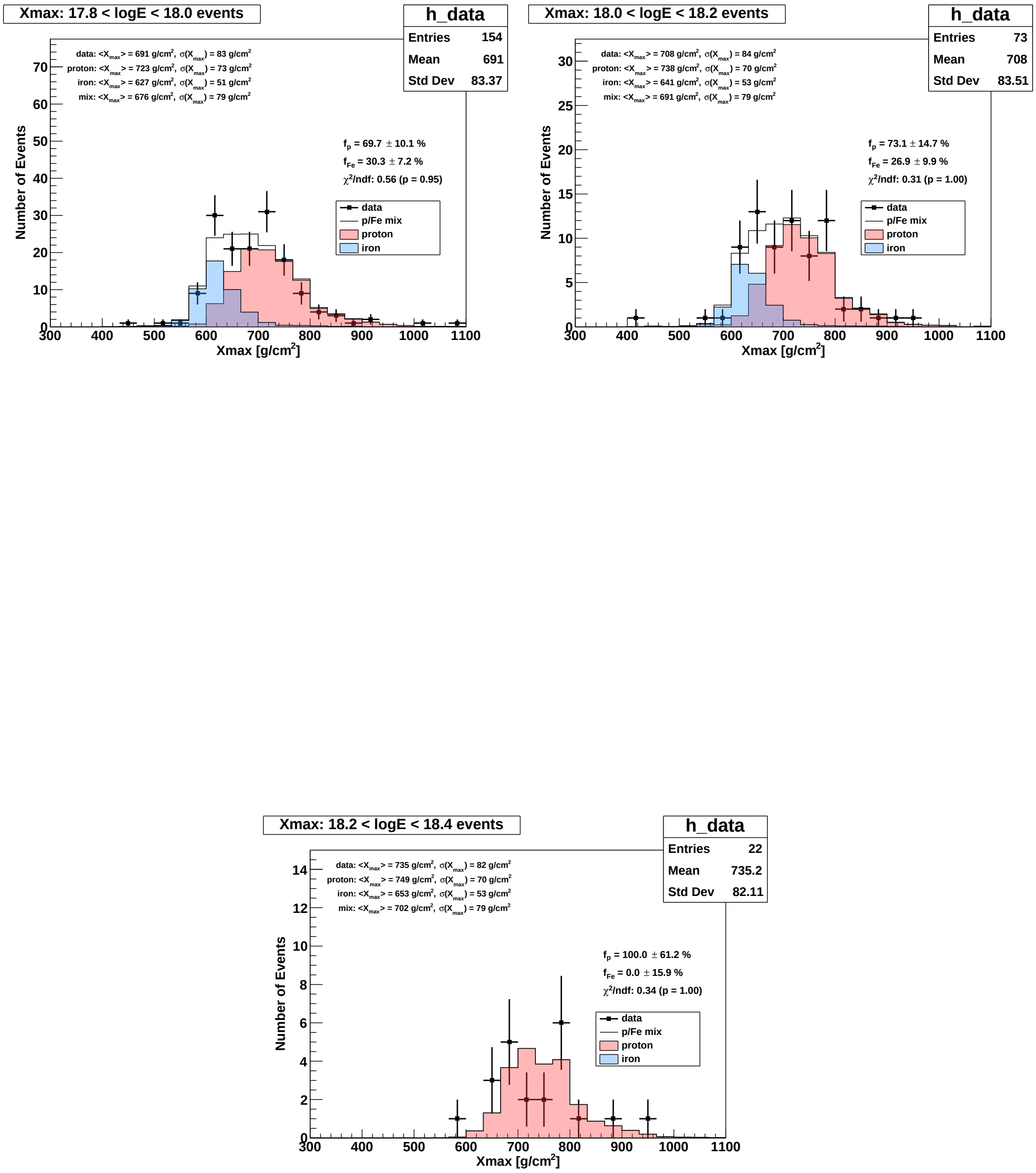

FIGURE A.4: $X_{\max}$ distribution for data and mixture of proton MC and iron MC for energy greater than $10^{17.8}$ eV and less than $10^{18.4}$ eV. In each figure, the data is shown with points, the mixture fit is shown by solid line with red filled proton MC and blue filled iron MC.

Bibliography

[1] V. Hess. “Über Beobachtungen der durchdringenden Strahlung bei sieben Freiballonfahrten”. In: *Phys. Z* 13 (Jan. 1912).

[2] W. F. Hanlon. *Updated cosmic ray spectrum*. accessed Dec. 31, 2021. URL: `https://web.physics.utah.edu/~whanlon/spectrum.html`.

[3] C. Patrignani et al. “Review of Particle Physics”. In: *Chin. Phys. C* 40.10 (2016), p. 100001. DOI: `10.1088/1674-1137/40/10/100001`.

[4] S. Ostapchenko. “Monte Carlo treatment of hadronic interactions in enhanced Pomeron scheme: I. QGSJET-II model”. In: *Phys. Rev. D* 83 (2011), p. 014018. DOI: `10.1103/PhysRevD.83.014018`. arXiv: `1010.1869 [hep-ph]`.

[5] Karl-Heinz Kampert and Michael Unger. “Measurements of the Cosmic Ray Composition with Air Shower Experiments”. In: *Astropart. Phys.* 35 (2012), pp. 660–678. DOI: `10.1016/j.astropartphys.2012.02.004`. arXiv: `1201.0018 [astro-ph.HE]`.

[6] H. P. Dembinski et al. “Report on Tests and Measurements of Hadronic Interaction Properties with Air Showers”. In: *EPJ Web Conf.* 210 (2019). Ed. by I. Lhenry-Yvon et al., p. 02004. DOI: `10.1051/epjconf/201921002004`. arXiv: `1902.08124 [astro-ph.HE]`.

[7] H. P. Dembinski. “The Muon Puzzle in High-Energy Air Showers”. In: *Phys. Atom. Nucl.* 82.6 (2020). Ed. by M. N. Strikhanov, A. M. Galper, and A. A Petrukhin, pp. 644–648. DOI: `10.1134/S1063778819660165`.

[8] Alexander Aab et al. “Observation of a Large-scale Anisotropy in the Arrival Directions of Cosmic Rays above 8×10^{18} eV”. In: *Science* 357.6537 (2017), pp. 1266–1270. DOI: `10.1126/science.aan4338`. arXiv: `1709.07321 [astro-ph.HE]`.

[9] R. U. Abbasi et al. “Indications of Intermediate-Scale Anisotropy of Cosmic Rays with Energy Greater Than 57 EeV in the Northern Sky Measured with the Surface Detector of the Telescope Array Experiment”. In: *Astrophys. J. Lett.* 790 (2014), p. L21. DOI: `10.1088/2041-8205/790/2/L21`. arXiv: `1404.5890 [astro-ph.HE]`.

[10] R. U. Abbasi et al. “Indications of a Cosmic Ray Source in the Perseus-Pisces Supercluster”. In: (Oct. 2021). arXiv: `2110.14827 [astro-ph.HE]`.

[11] R. U. Abbasi et al. “Depth of Ultra High Energy Cosmic Ray Induced Air Shower Maxima Measured by the Telescope Array Black Rock and Long Ridge FADC Fluorescence Detectors and Surface Array in Hybrid Mode”. In: *Astrophys. J.* 858 (2018), p. 76. DOI: `10.3847/1538-4357/aabad7`. arXiv: `1801.09784 [astro-ph.HE]`.

[12] T. K. Gaisser, T. Stanev, and S. Tilav. “Cosmic Ray Energy Spectrum from Measurements of Air Showers”. In: *Front. Phys. (Beijing)* 8 (2013), pp. 748–758. DOI: `10.1007/s11467-013-0319-7`. arXiv: `1303.3565 [astro-ph.HE]`.

[13] B. Peters. “Primary cosmic radiation and extensive air showers”. In: 22.4 (Nov. 1961). DOI: `10.1007/BF02783106`.

[14] *KASCADE Home Page*. URL: `https://kcdc.iap.kit.edu/information/aboutKASCADE/`.

[15] A. Haungs et al. “High-energy cosmic rays measured with KASCADE-Grande”. In: *PoS* EPS-HEP2013 (2013). Ed. by Ronald Cintra Shellard, p. 398. DOI: `10.22323/1.180.0398`. arXiv: `1308.1485 [astro-ph.HE]`.

[16] S. P. Knurenko et al. “Cosmic ray spectrum in the energy range 1.0E15-1.0E18 eV and the second knee according to the small Cherenkov setup at the Yakutsk EAS array”. In: (Oct. 2013). arXiv: `1310.1978 [astro-ph.HE]`.

[17] Stanislav Knurenko and Igor Petrov. “Mass Composition of Cosmic Rays at Ultra High Energies by Yakutsk Data”. In: *J. Phys. Conf. Ser.* 632.1 (2015), p. 012098. DOI: `10.1088/1742-6596/632/1/012098`.

[18] A. A. Ivanov, S. P. Knurenko, and I. Ye Sleptsov. “Measuring extensive air showers with Cherenkov light detectors of the Yakutsk array: The energy spectrum of cosmic rays”. In: *New J. Phys.* 11 (2009), p. 065008. DOI: `10.1088/1367-2630/11/6/065008`. arXiv: `0902.1016 [astro-ph.HE]`.

[19] Sergey Ostapchenko. “Status of QGSJET”. In: *AIP Conf. Proc.* 928.1 (2007). Ed. by S. Mani Tripathi and Richard E. Breedon, pp. 118–125. DOI: `10.1063/1.2775904`. arXiv: `0706.3784 [hep-ph]`.

[20] N. M. Budnev et al. “The primary cosmic-ray energy spectrum measured with the Tunka-133 array”. In: *Astropart. Phys.* 117 (2020), p. 102406. DOI: `10.1016/j.astropartphys.2019.102406`. arXiv: `2104.03599 [astro-ph.HE]`.

[21] V. V. Prosin et al. “Results from Tunka-133 (5 years observation) and from the Tunka-HiSCORE prototype”. In: *EPJ Web Conf.* 121 (2016). Ed. by P. Piattelli et al., p. 03004. DOI: `10.1051/epjconf/201612103004`.

[22] *IceCube Home Page*. URL: `https://icecube.wisc.edu/`.

[23] M. G. Aartsen et al. “The IceCube Neutrino Observatory: Instrumentation and Online Systems”. In: *JINST* 12.03 (2017), P03012. DOI: `10.1088/1748-0221/12/03/P03012`. arXiv: `1612.05093 [astro-ph.IM]`.

[24] M. G. Aartsen et al. “Cosmic ray spectrum and composition from PeV to EeV using 3 years of data from IceTop and IceCube”. In: *Phys. Rev. D* 100.8 (2019), p. 082002. DOI: `10.1103/PhysRevD.100.082002`. arXiv: `1906.04317 [astro-ph.HE]`.

[25] Dmitri Ivanov. “Energy Spectrum Measured by the Telescope Array”. In: *PoS* ICRC2019 (2019), p. 298. DOI: `10.22323/1.358.0298`.

[26] R. U. Abbasi et al. “The Cosmic-Ray Energy Spectrum between 2 PeV and 2 EeV Observed with the TALE detector in monocular mode”. In: *Astrophys. J.* 865 (2018), p. 74. DOI: `10.3847/1538-4357/aada05`. arXiv: `1803.01288 [astro-ph.HE]`.

[27] Pedro Abreu et al. “Energy spectrum of cosmic rays measured using the Pierre Auger Observatory”. In: *PoS* ICRC2021 (2021), p. 324. DOI: `10.22323/1.395.0324`.

[28] Alexey Yushkov. “Mass Composition of Cosmic Rays with Energies above $10^{17.2}$ eV from the Hybrid Data of the Pierre Auger Observatory”. In: *PoS* ICRC2019 (2019), p. 482. DOI: `10.22323/1.358.0482`.

[29] Alexander Aab et al. “The Pierre Auger Observatory Upgrade - Preliminary Design Report”. In: (Apr. 2016). arXiv: `1604.03637 [astro-ph.IM]`.

[30] Alexander Aab et al. “The Pierre Auger Cosmic Ray Observatory”. In: *Nucl. Instrum. Meth. A* 798 (2015), pp. 172–213. DOI: 10.1016/j.nima.2015.06.058. arXiv: 1502.01323 [astro-ph.IM].

[31] T. Pierog et al. “EPOS LHC: Test of collective hadronization with data measured at the CERN Large Hadron Collider”. In: *Phys. Rev. C* 92 (3 2015), p. 034906. DOI: 10.1103/PhysRevC.92.034906. URL: https://link.aps.org/doi/10.1103/PhysRevC.92.034906.

[32] Felix Riehn et al. “Hadronic interaction model Sibyll 2.3d and extensive air showers”. In: *Phys. Rev. D* 102.6 (2020), p. 063002. DOI: 10.1103/PhysRevD.102.063002. arXiv: 1912.03300 [hep-ph].

[33] H. Bethe and W. Heitler. “On the Stopping of fast particles and on the creation of positive electrons”. In: *Proc. Roy. Soc. Lond. A* 146 (1934), pp. 83–112. DOI: 10.1098/rspa.1934.0140.

[34] J. Matthews. “A Heitler model of extensive air showers”. In: *Astropart. Phys.* 22 (2005), pp. 387–397. DOI: 10.1016/j.astropartphys.2004.09.003.

[35] T.K.Gaisser and A.M.Hillas. “Reliability of the Method of Constant Intensity Cuts for Reconstructing the Average Development of Vertical Showers”. In: vol. Proceedings of 15th International Cosmic Ray Conference (Plovdiv, Bulgaria) 8. 1977.

[36] W. Heitler. *The quantum theory of radiation*. Vol. 5. International Series of Monographs on Physics. Oxford: Oxford University Press, 1936.

[37] Markus Risse. “Properties of extensive air showers”. In: *Acta Phys. Polon. B* 35 (2004). Ed. by Marek Jezabek and Henryk Wilczynski, pp. 1787–1798. arXiv: astro-ph/0402300.

[38] Koichi Kamata and Jun Nishimura. “The Lateral and the Angular Structure Functions of Electron Showers”. In: *Progress of Theoretical Physics Supplement* 6 (Feb. 1958), pp. 93–155. ISSN: 0375-9687. DOI: 10.1143/PTPS.6.93.

[39] K. Greisen. “Cosmic ray showers”. In: *Ann. Rev. Nucl. Part. Sci.* 10 (1960), pp. 63–108. DOI: 10.1146/annurev.ns.10.120160.000431.

[40] S. Lafebre et al. “Universality of electron-positron distributions in extensive air showers”. In: *Astropart. Phys.* 31 (2009), pp. 243–254. DOI: 10.1016/j.astropartphys.2009.02.002. arXiv: 0902.0548 [astro-ph.HE].

[41] D. Heck et al. *CORSIKA: a Monte Carlo code to simulate extensive air showers.* 1998.

[42] Ralph Engel, Dieter Heck, and Tanguy Pierog. “Extensive Air Showers and Hadronic Interactions at High Energy”. In: *Annual Review of Nuclear and Particle Science* 61.1 (2011), pp. 467–489. DOI: 10.1146/annurev.nucl.012809.104544.

[43] B. Keilhauer et al. “Nitrogen fluorescence in air for observing extensive air showers”. In: *EPJ Web Conf.* 53 (2013). Ed. by K. H. Kampert et al., p. 01010. DOI: 10.1051/epjconf/20135301010. arXiv: 1210.1319 [astro-ph.HE].

[44] R. Abbasi et al. “Air fluorescence measurements in the spectral range 300-420 nm using a 28.5-GeV electron beam”. In: *Astropart. Phys.* 29 (2008), pp. 77–86. DOI: 10.1016/j.astropartphys.2007.11.010. arXiv: 0708.3116 [astro-ph].

[45] F. Kakimoto et al. “A Measurement of the air fluorescence yield”. In: *Nucl. Instrum. Meth. A* 372 (1996), pp. 527–533. DOI: 10.1016/0168-9002(95)01423-3.

[46] Frank Nerling et al. “Universality of electron distributions in high-energy air showers: Description of Cherenkov light production”. In: *Astropart. Phys.* 24 (2006), pp. 421–437. DOI: `10.1016/j.astropartphys.2005.09.002`. arXiv: `astro-ph/0506729`.

[47] M. Nagano et al. “New measurement on photon yields from air and the application to the energy estimation of primary cosmic rays”. In: *Astropart. Phys.* 22 (2004), pp. 235–248. DOI: `10.1016/j.astropartphys.2004.08.002`. arXiv: `astro-ph/0406474`.

[48] M. Ave et al. “Measurement of the pressure dependence of air fluorescence emission induced by electrons”. In: *Astropart. Phys.* 28 (2007), pp. 41–57. DOI: `10.1016/j.astropartphys.2007.04.006`. arXiv: `astro-ph/0703132`.

[49] P. A. Cherenkov. “Visible luminescence of pure liquids under the influence of γ-radiation”. In: *Dokl. Akad. Nauk SSSR* 2.8 (1934), pp. 451–454. DOI: `10.3367/UFNr.0093.196710n.0385`.

[50] David Newton, J. Knapp, and A. A. Watson. “The Optimum Distance at which to Determine the Size of a Giant Air Shower”. In: *Astropart. Phys.* 26 (2007), pp. 414–419. DOI: `10.1016/j.astropartphys.2006.08.003`. arXiv: `astro-ph/0608118`.

[51] The CTA Consortium. *Science with the Cherenkov Telescope Array*. WORLD SCIENTIFIC, 2019. DOI: `10.1142/10986`. eprint: `https://www.worldscientific.com/doi/pdf/10.1142/10986`.

[52] Vladimír Novotný. “Measurement of the spectrum of cosmic rays above $10^{16.5}$ eV with Cherenkov-dominated events at the Pierre Auger Observatory”. In: *PoS* ICRC2019 (2019), p. 374. DOI: `10.22323/1.358.0374`.

[53] Vladimír Novotný. “Measurement of the energy spectrum of cosmic rays using Cherenkov-dominated data at the Pierre Auger Observatory”. PhD thesis. Charles U., 2020.

[54] K.Suga. “Methods for observing extremely large extensive air showers”. In: *Proc. 5th, Interamerican Symp, La Paz, (eds. I. Escobar et al.), 2, XLIX- 1-5.* (1962). URL: `https://cir.nii.ac.jp/ja/crid/1370287385181765766`.

[55] T Hara, F Ishikawa, and S Kawaguchi. “DETECTION OF THE ATMOSPHERIC SCINTILLATION LIGHT FROM AIR SHOWERS.” In: *Acta Phys. Acad. Sci. Hung. 29: Suppl. 3, 369-76.* (Jan. 1970). URL: `https://www.osti.gov/biblio/4663098`.

[56] H. Kawai et al. “Telescope array experiment”. In: *Nucl. Phys. B Proc. Suppl.* 175-176 (2008). Ed. by Kwong Sang Cheng et al., pp. 221–226. DOI: `10.1016/j.nuclphysbps.2007.11.002`.

[57] T. Abu-Zayyad et al. “The Cosmic Ray Energy Spectrum Observed with the Surface Detector of the Telescope Array Experiment”. In: *Astrophys. J. Lett.* 768 (2013), p. L1. DOI: `10.1088/2041-8205/768/1/L1`. arXiv: `1205.5067 [astro-ph.HE]`.

[58] Dmitri Ivanov et al. “Recent measurement of the Telescope Array energy spectrum and observation of the shoulder feature in the Northern Hemisphere”. In: *PoS* ICRC2021 (2021), p. 341. DOI: `10.22323/1.395.0341`.

[59] T. Abu-Zayyad et al. “The Energy Spectrum of Ultra-High-Energy Cosmic Rays Measured by the Telescope Array FADC Fluorescence Detectors in Monocular Mode”. In: *Astropart. Phys.* 48 (2013), pp. 16–24. DOI: `10.1016/j.astropartphys.2013.06.007`. arXiv: `1305.6079 [astro-ph.HE]`.

[60] R. U. Abbasi et al. “The energy spectrum of cosmic rays above $10^{17.2}$ eV measured by the fluorescence detectors of the Telescope Array experiment in seven years”. In: *Astropart. Phys.* 80 (2016), pp. 131–140. DOI: `10.1016/j.astropartphys.2016.04.002`. arXiv: `1511.07510 [astro-ph.HE]`.

[61] T. Abu-Zayyad et al. “The Energy Spectrum of Telescope Array’s Middle Drum Detector and the Direct Comparison to the High Resolution Fly’s Eye Experiment”. In: *Astropart. Phys.* 39-40 (2012), pp. 109–119. DOI: `10.1016/j.astropartphys.2012.05.012`. arXiv: `1202.5141 [astro-ph.IM]`.

[62] T. Abu-Zayyad et al. “Energy Spectrum of Ultra-High Energy Cosmic Rays Observed with the Telescope Array Using a Hybrid Technique”. In: *Astropart. Phys.* 61 (2015), pp. 93–101. DOI: `10.1016/j.astropartphys.2014.05.002`. arXiv: `1305.7273 [astro-ph.HE]`.

[63] R. U. Abbasi et al. “The hybrid energy spectrum of Telescope Array’s Middle Drum Detector and surface array”. In: *Astropart. Phys.* 68 (2015), pp. 27–44. DOI: `10.1016/j.astropartphys.2015.02.008`.

[64] R. U. Abbasi et al. “Study of Ultra-High Energy Cosmic Ray composition using Telescope Array’s Middle Drum detector and surface array in hybrid mode”. In: *Astropart. Phys.* 64 (2015), pp. 49–62. DOI: `10.1016/j.astropartphys.2014.11.004`. arXiv: `1408.1726 [astro-ph.HE]`.

[65] Douglas Bergman. “Combined Fit of the Spectrum and Composition from Telescope Array”. In: *PoS* ICRC2019 (2019), p. 190. DOI: `10.22323/1.358.0190`.

[66] R. U. Abbasi et al. “Search for Large-scale Anisotropy on Arrival Directions of Ultra-high-energy Cosmic Rays Observed with the Telescope Array Experiment”. In: *Astrophys. J. Lett.* 898.2 (2020), p. L28. DOI: `10.3847/2041-8213/aba0bc`. arXiv: `2007.00023 [astro-ph.HE]`.

[67] R. U. Abbasi et al. “Testing a Reported Correlation between Arrival Directions of Ultra-high-energy Cosmic Rays and a Flux Pattern from nearby Starburst Galaxies using Telescope Array Data”. In: *Astrophys. J. Lett.* 867.2 (2018), p. L27. DOI: `10.3847/2041-8213/aaebf9`. arXiv: `1809.01573 [astro-ph.HE]`.

[68] Rasha Abbasi et al. “The status of the TALE surface detector array and TALE infill project”. In: *PoS* ICRC2021 (2021), p. 255. DOI: `10.22323/1.395.0255`.

[69] R. U. Abbasi et al. “Surface detectors of the TAx4 experiment”. In: *Nucl. Instrum. Meth. A* 1019 (2021), p. 165726. DOI: `10.1016/j.nima.2021.165726`. arXiv: `2103.01086 [astro-ph.IM]`.

[70] Mathew Potts, Charles Jui, et al. “Monocular Energy Spectrum using the TAx4 Fluorescence Detector”. In: *PoS* ICRC2021 (2021), p. 343. DOI: `10.22323/1.395.0343`.

[71] Yuichiro Tameda et al. “Trigger electronics of the new fluorescence detectors of the Telescope Array experiment”. In: *Nucl. Instrum. Meth. A* 609 (2009), pp. 227–234. DOI: `10.1016/j.nima.2009.07.093`.

[72] H. Tokuno et al. "New air fluorescence detectors employed in the Telescope Array experiment". In: *Nucl. Instrum. Meth. A* 676 (2012), pp. 54–65. DOI: 10.1016/j.nima.2012.02.044. arXiv: 1201.0002 [astro-ph.IM].

[73] Monica Gene Allen. "Ultra High Energy Cosmic Ray Energy Spectrum and Composition using Hybrid Analysis with Telescope Array". PhD thesis. University of Utah, 2012. URL: http://www.telescopearray.org/media/theses/mallen_thesis.pdf.

[74] *Analog Device 8-Bit 20 MSPS, 60 mW Sampling A/D Converter*. accessed Nov. 13, 2021. URL: https://www.analog.com/media/en/technical-documentation/data-sheets/AD775.pdf.

[75] *NOAA/ESRL Radiosonde Database*. URL: https://ruc.noaa.gov/raobs/General_Information.html.

[76] *Global Data Assimilation System*. URL: https://www.ncei.noaa.gov/products/weather-climate-models/global-data-assimilation.

[77] *National Oceanic and Atmospheric Administration, Global Data Assimilation System (GDAS)*. URL: https://ready.arl.noaa.gov/gdas1.php.

[78] Takayuki Tomida et al. "The atmospheric transparency measured with a LIDAR system at the Telescope Array experiment". In: *Nucl. Instrum. Meth. A* 654 (2011), pp. 653–660. DOI: 10.1016/j.nima.2011.07.012. arXiv: 1109.1196 [astro-ph.IM].

[79] R. Abbasi et al. "Techniques for measuring atmospheric aerosols at the high resolution fly's eye experiment". In: *Astropart. Phys.* 25 (2006), pp. 74–83. DOI: 10.1016/j.astropartphys.2005.11.006. arXiv: astro-ph/0512423.

[80] Takafumi Uehama et al. "Measurement of atmospheric transparency in Telescope Array using Central Laser Facility". In: *PoS* ICRC2019 (2020), p. 442. DOI: 10.22323/1.358.0442.

[81] Takayuki Tomida et al. "The atmospheric transparency of Telescope Array observation site by the CLF". In: *PoS* ICRC2021 (2021), p. 217. DOI: 10.22323/1.395.0217.

[82] A Ferrari et al. "FLUKA: A Multi-Particle Transport Code". In: (Dec. 2005). DOI: 10.2172/877507. URL: https://www.osti.gov/biblio/877507.

[83] W R Nelson, H Hirayama, and D W.O. Rogers. "EGS4 code system". In: (Dec. 1985). URL: https://www.osti.gov/biblio/6137659.

[84] M. Kobal. "A thinning method using weight limitation for air-shower simulations". In: *Astroparticle Physics* 15.3 (2001), pp. 259–273. DOI: https://doi.org/10.1016/S0927-6505(00)00158-4.

[85] D. S. Gorbunov, G. I. Rubtsov, and Sergey V. Troitsky. "Air-shower simulations with and without thinning: Artificial fluctuations and their suppression". In: *Phys. Rev. D* 76 (2007), p. 043004. DOI: 10.1103/PhysRevD.76.043004. arXiv: astro-ph/0703546.

[86] B. T. Stokes et al. "Dethinning Extensive Air Shower Simulations". In: *Astropart. Phys.* 35 (2012), pp. 759–766. DOI: 10.1016/j.astropartphys.2012.03.004. arXiv: 1104.3182 [astro-ph.IM].

[87] T. Abu-Zayyad et al. "CORSIKA Simulation of the Telescope Array Surface Detector". In: (Mar. 2014). arXiv: 1403.0644 [astro-ph.IM].

[88] J. Allison et al. “Geant4 developments and applications”. In: *IEEE Transactions on Nuclear Science* 53.1 (2006), pp. 270–278. DOI: 10.1109/TNS.2006.869826.

[89] R. U. Abbasi et al. “Monocular Measurement of the Spectrum of UHE Cosmic Rays by the FADC Detector of the HiRes Experiment”. In: *Astropart. Phys.* 23 (2005), pp. 157–174. DOI: 10.1016/j.astropartphys.2004.12.006. arXiv: astro-ph/0208301.

[90] T. Fujii et al. “An event reconstruction method for the Telescope Array Fluorescence Detectors”. In: *AIP Conf. Proc.* 1367.1 (2011). Ed. by Hiroyuki Sagawa et al., pp. 149–152. DOI: 10.1063/1.3628732.

[91] Tareq Ziad AbuZayyad. “The Energy Spectrum of Ultra High Energy Cosmic Rays”. PhD thesis. University of Utah, 2000. URL: http://www.telescopearray.org/media/papers/tareq_thesis.pdf.

[92] R. U. Abbasi et al. “First observation of the Greisen-Zatsepin-Kuzmin suppression”. In: *Phys. Rev. Lett.* 100 (2008), p. 101101. DOI: 10.1103/PhysRevLett.100.101101. arXiv: astro-ph/0703099.

[93] John A. Nelder and Roger Mead. “A Simplex Method for Function Minimization”. In: *Comput. J.* 7 (1965), pp. 308–313.

[94] Roger J. Barlow and Christine Beeston. “Fitting using finite Monte Carlo samples”. In: *Comput. Phys. Commun.* 77 (1993), pp. 219–228. DOI: 10.1016/0010-4655(93)90005-W.

[95] R. Brun and F. Rademakers. “ROOT: An object oriented data analysis framework”. In: *Nucl. Instrum. Meth. A* 389 (1997). Ed. by M. Werlen and D. Perret-Gallix, pp. 81–86. DOI: 10.1016/S0168-9002(97)00048-X.

[96] Greg Daveid Furlich. “OBSERVATION OF THE GZK SUPPRESSION WITH THE TELESCOPE ARRAY FLUORESCENCE TELESCOPES AND DEPLOYMENT OF THE TELESCOPE ARRAY EXPANSION”. PhD thesis. University of Utah, 2020.

[97] Douglas Chase Rodriguez. “THE TELESCOPE ARRAY MIDDLE DRUM MONOCULAR ENERGY SPECTRUM AND A SEARCH FOR COINCIDENT SHOWERS USING HIGH RESOLUTION FLY’S EYE HIRES-1 MONOCULAR DATA”. PhD thesis. University of Utah, 2020.

[98] R. U. Abbasi et al. “Measurement of the Flux of Ultra High Energy Cosmic Rays by the Stereo Technique”. In: *Astropart. Phys.* 32 (2009), pp. 53–60. DOI: 10.1016/j.astropartphys.2009.06.001. arXiv: 0904.4500 [astro-ph.HE].

[99] T. Abu-Zayyad et al. “TA Energy Scale : Methods and Photometry”. In: *Proceedings of the 32nd International Cosmic Ray Conference*. 2011, pp. 250–253. DOI: 10.7529/ICRC2011/V02/1270. URL: http://icrc2011.ihep.ac.cn/paper/proc/v2.pdf.

[100] Luan B. Arbeletche and Vitor De Souza. “Parametrization of the angular distribution of Cherenkov light in air showers”. In: *Eur. Phys. J. C* 81.2 (2021), p. 195. DOI: 10.1140/epjc/s10052-021-08971-7. arXiv: 2007.13812 [astro-ph.HE].

[101] M. Giller and G. Wieczorek. “Influence of the scattered Cherenkov light on the width of shower images as measured in the EAS fluorescence experiments”. In: *Astropart. Phys.* 31 (2009), pp. 212–219. DOI: 10.1016/j.astropartphys.2009.01.003.

[102] R. M. Baltrusaitis et al. “THE UTAH FLY’S EYE DETECTOR”. In: *Nucl. Instrum. Meth. A* 240 (1985), pp. 410–428. DOI: 10.1016/0168-9002(85)90658-8. URL: http://www.telescopearray.org/images/papers/1985/Baltrusaitis%20et%20al%20-%20The%20Flys%20Eye.pdf.

[103] Dmitri Ivanov. “Energy spectrum measured by the telescope array surface detector”. PhD thesis. Rutgers U., Piscataway, 2012. DOI: 10.7282/T3K35SG3.

[104] Vladimír Novotný. “Measurement of the energy spectrum of cosmic rays using Cherenkov-dominated data at the Pierre Auger Observatory”. PhD thesis. Charles U., 2020.

[105] M. G. Aartsen et al. “Measurement of the cosmic ray energy spectrum with IceTop-73”. In: *Phys. Rev. D* 88.4 (2013), p. 042004. DOI: 10.1103/PhysRevD.88.042004. arXiv: 1307.3795 [astro-ph.HE].

[106] Jon Paul Lundquist. “Study of UHECR Composition Using Telescope Array’s Middle Drum Detector and Surface Array in Hybrid Mode”. In: *PoS* ICRC2015 (2016), p. 441. DOI: 10.22323/1.236.0441.

[107] T. Abu-Zayyad et al. “Measurement of the Cosmic-Ray Energy Spectrum and Composition from 10^{17} to $10^{18.3}$ eV Using a Hybrid Technique”. In: *The Astrophysical Journal* 557.2 (2001), pp. 686–699. DOI: 10.1086/322240. URL: https://doi.org/10.1086/322240.

[108] *Pierre Auger Observatory, Data and Tables*. URL: https://www.auger.org/science/public-data/data.

[109] T. Antoni et al. “KASCADE measurements of energy spectra for elemental groups of cosmic rays: Results and open problems”. In: *Astropart. Phys.* 24 (2005), pp. 1–25. DOI: 10.1016/j.astropartphys.2005.04.001. arXiv: astro-ph/0505413.

[110] Stanislav Knurenko and Igor Petrov. “Mass composition of cosmic rays above 0.1 EeV by the Yakutsk array data”. In: *Adv. Space Res.* 64.12 (2019), pp. 2570–2577. DOI: 10.1016/j.asr.2019.07.019. arXiv: 1908.01508 [astro-ph.HE].